THÈSE de DOCTORAT DE L'UNIVERSITÉ JEAN MONNET SAINT-ÉTIENNE
Membre de l'Université de LYON

Ecole Doctorale : Sciences, Ingénierie, Sante (ED SIS N° 488)

Spécialité de doctorat : Physique (domaine scientifique 2)

Soutenue publiquement le 27/06/2024, par :

Kacper BIŁKO

N° d'ordre NNT: 2024STET030

Advancements in CERN's Radiation Monitoring and Data Analysis Solutions for Radiation to Electronics applications

Devant le jury composé de :

Yacine Kadi	**Président**
Prof., CERN	
Frédéric Wrobel	**Rapporteur**
Prof., Université de Montpellier	
Eamonn Daly	**Rapporteur**
Dr., Agence Spatiale Européenne	
Marta Bagatin	**Examinatrice**
Prof., Université de Padoue	
Yacine Kadi	**Examinateur**
Prof., CERN	
Sylvain Girard	**Directeur de thèse**
Prof., Université Jean Monnet	
Rubén García Alía	**Co-Encadrement de thèse**
Dr., CERN	

Contents

Acknowledgments

I would like to express my deepest gratitude to those who made this PhD journey possible.

Firstly, I extend my heartfelt thanks to my PhD supervisors, Rubén García Alía and Sylvain Girard, for their exceptional mentoring and guidance throughout this project. The swift completion of the project wouldn't have been possible without the endorsement of CERN leaders, Simone Gilardoni and Francesco Cerutti.

Special thanks to Diego Di Francesca for his expertise and guidance related to Distributed Optical Fibre Radiation Sensors, to Mario Sacristan and Giuseppe Mazzola for their help with Monte Carlo simulations, to Sławosz Uznański for providing me with data from the FGClite controllers, and to Carlo Cazzaniga for familiarizing me with silicon detector setup.

I am also deeply grateful to my colleagues Andrea Coronetti, Ivan Slipukhin, Ygor Aguair, Matteo Cecchetto, and Mario Sacristan, whose support during my experimental activities was indispensable. In this context, I would like to acknowledge the experts at the external research institutes where my experiments were carried out: Yolanda Morilla, Pedro Martín-Holgado, Ulli Köster, Manon Letiche, Camille Belanger-Champagne, Alex Hands, and Heikki Kettunen. Your help in the execution of my experiments was crucial to the success of this PhD.

Thank you to Francesc Salvat Pujol for his FLUKA Preex and physics support, and to Anton Lechner for insightful discussions related to the LHC arcs.

Lastly, I am grateful to Reyes Alemany Fernandez for her help in carrying out beam loss tests in LEIR, and to Markus Widorski for providing LINAC3-related FLUKA simulations.

To my nearest and dearest outside the professional domain, your unwavering support and encouragement have been immensely appreciated. Thank you for always being there.

Authored journal publications

[1] Kacper Biłko et al. "CERN Super Proton Synchrotron Radiation Environment and Related Radiation Hardness Assurance Implications". In: *IEEE Transactions on Nuclear Science* 70.8 (Aug. 2023), pp. 1606–1615. ISSN: 1558-1578. DOI: 10.1109/TNS.2023.3261181.

[2] Kacper Biłko et al. "Radiation Environment in the Large Hadron Collider During the 2022 Restart and Related RHA Implications". In: *IEEE Transactions on Nuclear Science* 71.4 (Apr. 2024), pp. 607–617. ISSN: 0018-9499, 1558-1578. DOI: 10.1109/TNS.2023.3328145. (Visited on 04/22/2024).

[3] Kacper Biłko et al. "Mixed-Field Radiation Monitoring and Beam Characterization Through Silicon Diode Detectors". In: *IEEE Transactions on Nuclear Science* 71.4 (Apr. 2024), pp. 777–784. ISSN: 0018-9499, 1558-1578. DOI: 10.1109/TNS.2024.3350342. (Visited on 04/22/2024).

[4] Kacper Biłko et al. "Ultra-Large Silicon Diode for Characterizing Low-Intensity Radiation Environments". In: *IEEE Transactions on Nuclear Science* 71.4 (Apr. 2024), pp. 770–776. ISSN: 0018-9499, 1558-1578. DOI: 10.1109/TNS.2023.3337839. (Visited on 04/22/2024).

[5] Kacper Bilko et al. "CHARM High-energy Ions for Micro Electronics Reliability Assurance (CHIMERA)". In: *IEEE Transactions on Nuclear Science* (2024), pp. 1–1. ISSN: 0018-9499, 1558-1578. DOI: 10.1109/TNS.2024.3358376. (Visited on 01/29/2024).

Authored proceedings

[1] Kacper Biłko, Ruben García Alía, and Jean-Baptiste Potoine. "Automated Analysis of the Prompt Radiation Levels in the CERN Accelerator Complex". en. In: *Proc. 13th International Particle Accelerator Conference (IPAC'22), Bangkok, Thailand, 12-17 June 2022*. JACOW Publishing, Geneva, Switzerland, July 2022, pp. 736–739. ISBN: 978-3-95450-227-1. DOI: 10.18429/JACoW-IPAC2022-MOPOMS043. (Visited on 07/05/2023).

[2] K. Bilko et al. "Overview of Total Ionizing Dose Levels in the Large Hadron Collider during 2022 restart". In: *Proc. IPAC'23*. IPAC'23 - 14th International Particle Accelerator Conference. JACoW Publishing, Geneva, Switzerland, May 2023, pp. 4008–4011. ISBN: 978-3-95450-231-8. DOI: 10.18429/jacow-ipac2023-thpa047.

Coauthorshiped publications and proceedings

[1] Rubén García Alía et al. "Fragmented High-Energy Heavy-Ion Beams for Electronics Testing". In: *IEEE Transactions on Nuclear Science* 70.4 (Apr. 2023), pp. 486–495. ISSN: 1558-1578. DOI: 10.1109/TNS.2022.3210403.

[2] Rubén García Alía et al. "Heavy Ion Energy Deposition and SEE Intercomparison Within the RADNEXT Irradiation Facility Network". In: *IEEE Transactions on Nuclear Science* 70.8 (Aug. 2023), pp. 1596–1605. ISSN: 1558-1578. DOI: 10.1109/TNS.2023.3260309.

[3] Alessia Ciccotelli et al. "Energy deposition studies for the LHCb insertion region of the CERN Large Hadron Collider". In: *Physical Review Accelerators and Beams* 26.6 (June 2023). Art. no. 061002. DOI: 10.1103/PhysRevAccelBeams.26.061002. (Visited on 07/05/2023).

[4] D. Prelipcean et al. "Radiation levels produced by the operation of the Beam Gas Vertex monitor in the LHC tunnel at IR4". In: *Proc. IPAC'23*. IPAC'23 - 14th International Particle Accelerator Conference. JACoW Publishing, Geneva, Switzerland, May 2023, pp. 4578–4581. ISBN: 978-3-95450-231-8. DOI: doi:10.18429/jacow-ipac2023-thpl082.

[5] E. Johnson, Kacper Bilko, et al. "Beam delivery of high-energy ion beams for irradiation experiments at the CERN Proton Synchrotron". In: *Proc. IPAC'23*. IPAC'23 - 14th International Particle Accelerator Conference. JACoW Publishing, Geneva, Switzerland, May 2023, pp. 297–300. ISBN: 978-3-95450-231-8. DOI: 10.18429/jacow-ipac2023-mopa115.

[6] A. Waets, Kacper Bilko, et al. "Heavy Ion Beam Characterization for Radiation Effects Testing at CERN using Monte Carlo Simulations and experimental benchmarking". In: *Proc. IPAC'23*. IPAC'23 - 14th International Particle Accelerator Conference. JACoW Publishing, Geneva, Switzerland, May 2023, pp. 5106–5109. ISBN: 978-3-95450-231-8. DOI: doi:10.18429/jacow-ipac2023-thpm128.

[7] M. Delrieux, Kacper Bilko, et al. "Production of slow extracted beams for CERN's East Area at the Proton Synchrotron". In: *Proc. IPAC'23*. IPAC'23 - 14th International Particle Accelerator Conference. JACoW Publishing, Geneva, Switzerland, May 2023, pp. 257–260. ISBN: 978-3-95450-231-8. DOI: doi:10.18429/jacow-ipac2023-mopa099.

[8] Andreas Waets et al. "Very-High-Energy Heavy Ion Beam Dosimetry using Solid State Detectors for Electronics Testing". In: *IEEE Transactions on Nuclear Science* (2024), pp. 1–1. ISSN: 1558-1578. DOI: 10.1109/TNS.2024.3350667.

[9] Mario Sacristán Barbero et al. "Characterization of Fragmented Ultra-high Energy Heavy Ion Beam and its Effects on Electronics Single Event Effect Testing". In: *IEEE Transactions on Nuclear Science* (2024). Conference Name: IEEE Transactions on Nuclear Science, pp. 1–1. ISSN: 1558-1578. DOI: 10.1109/TNS.2024.3396737. (Visited on 05/06/2024).

List of the performed scientific experiments within PhD activity

This PhD includes data from multiple test campaigns, where the PhD student either led the silicon detector irradiations (PSI, CNA, GSI) or coordinated the entire test campaign (ILL, TRIUMF, RADEF, CERN), as listed in Tab. 1.

Table 1: Performed scientific experiments (test campaigns) in the frame of this PhD work

facility	location	particle type(s)	role
PSI-PIF	Villigen, Switzerland	protons	responsible for the silicon detector experiment
CNA	Seville, Spain	proton and alpha beams	responsible for the silicon detector experiment
ILL-PF1B	Grenoble, France	cold neutrons	responsible for the silicon detector experiment, test campaign leader
GSI-SIS18	Darmstadt, Germany	very high energy ^{238}U ions	responsible for the onsite execution of silicon detector experiment
TRIUMF	Vancouver, Canada	atmospheric-like neutrons and high-energy protons	author of the scientific proposal, leading the experiments [full coordination]
ILL-PN1	Grenoble, France	^{235}U fission products, protons and light ions	author of the scientific proposal, leading the experiments [full coordination]
RADEF	Jyvaskyla, Finland	high-energy heavy ions	author of the scientific proposal, leading the experiments [full coordination]
CERN-SPS	Geneva, Switzerland	radiation produced by accelerator	coordination and deployment of the passive dosimeters along SPS
CERN-LINAC3	Geneva, Switzerland	radiation produced by accelerator	responsible for the silicon detector experiment
CERN-CHIMERA CERN-HEARTS	Geneva, Switzerland	very high energy lead ions	responsible for the silicon detector experiment for intensity beamline characterization
CERN-LEIR	Geneva, Switzerland	radiation produced by accelerator	responsible for the silicon detector experiment
CERN-building 865	Prevessin-Moens, France	atmospheric radiation	responsible for the silicon detector experiment
CERN-CHARM	Geneva, Switzerland	mixed-field radiation	responsible for the silicon detector experiment

List of conference presentations

The thesis is largely based on the student's publications and proceedings, disseminated during scientific conferences:

- RADECS 2022 – poster presentation,
- IPAC 2023 – poster presentation,
- NSREC 2023 – two oral and poster presentations,
- RADECS 2023 – poster presentation.

Abbreviations

ALPS A Logarithmic Position System.

ATLAS A Toroidal LHC ApparatuS.

BLM Beam Loss Monitor.

CALLAB CALibration LABoratory.

CERN European Organization for Nuclear Research.

CHARM Cern High energy AcceleRator Mixed field facility.

CHIMERA CHARM High-energy Ions for Micro Electronics Reliability Assurance.

CMS Compact Muon Solenoid.

CNA Centro Nacional de Aceleradores.

COTS Commercial-Off-The-Shelf.

dcum CUMulated Distance.

DD Displacement Damage.

DOFRS Distributed Optical Fibre Radiation Sensor.

DS Dispersion Supressor.

DUT Device Under Test.

FGClite Function Generator Controller light.

FPGA Field Programmable Gate Array.

FWHM Full Width at Half Maximum.

GCR Galactic Cosmic Ray.

HEARTS High-Energy Accelerators for Radiation Testing and Shielding.

HEH High-Energy-Hadron.

HEHeq High-Energy-Hadron-equivalent.

ILL Institut Laue-Langevin.

IP Interaction Point.

IR Insertion Region.

LEIR Low Energy Ion Ring.

LET Linear Energy Transfer.

LHC Large Hadron Collider.

LINAC3 Linear Accelerator 3.

LS Long Shutdown.

LSS Long Straight Section.

MOSFET Metal–Oxide–Semiconductor Field-Effect Transistor.

NXCALS NeXt Cern Accelerator Logging Service.

PC Power Converter.

PHD Pulse Height Deficit.

PIPS Passivated Implanted Planar Silicon.

PLC Programmable Logic Controller.

PMMA Poly(methyl methacrylate) aka plexiglass.

PS Proton Synchrotron.

PSB Proton Synchrotron Booster.

PSD Pulse Shape Discrimination.

PSI Paul Scherrer Institut.

R2E Radiation to Electronics.

RADEF RADiation Effects Facility.

RADFET Radiation Sensing Field Effect Transistor.

RadMon CERN Radiation Monitor.

RADNEXT RADiation facility Network for the EXploration of effects for indusTry and research.

RF Radio-Frequency.

RHA Radiation Hardness Assurance.

RPL Radio-Photo-Luminescence.

RPLd Radio-Photo-Luminescence dosimeter.

RR civil engineering designation for underground works on beam path with a main usage for power converters.

SEC Secondary Emission Chamber.

SEE Single Event Effect.

SEU Single Event Upset.

SPE Solar Particle Event.

SPS Super Proton Synchrotron.

SRAM Static Random Access Memory.

TCL Target Collimator Long.

THNeq THermal-Neutron-equivalent.

TID Total Ionizing Dose.

TRIUMF TRI-University Meson Facility.

VHE Very-High-Energy.

Chapter 1

Introduction

Ionizing radiation of different origins is present everywhere. At the ground level, it is due to cosmic rays and decays of naturally present compounds, e.g. radon. In the solar system, the main source of radiation arises from the sun's activity. However, in addition to natural radiation, there are multiple artificial, human-induced, sources. Examples of such are particle accelerators, where fractional beam losses induce radiation showers. In high-energy and high-intensity accelerators even a small amount of losses leads to a radiation field in its immediate surroundings. Depending on the beam energy, the secondary radiation field consists of multiple particle species at various energies (mixed-field radiation).

Unavoidably, this is the case also in the CERN (European Organization for Nuclear Research) accelerator complex, illustrated in Fig. 1.1. Whereas the primary concern of radiation is human safety (Radiation Protection), within this work, the focus is on the safety of the electronic systems, as the radiation impacts electronics both through cumulative (Total Ionizing Dose, Displacement Damage) and stochastic effects (Single Event Effect, SEEs). At relatively low levels the primary concern is SEEs, especially in the case of distributed commercial critical systems. With the increasing levels, the cumulative levels start to play a role. Therefore, a radiation environment needs to be characterized, with various radiation monitors, to provide further assessments concerning radiation effects.

The higher the energy and intensity of a beam in the accelerator, the higher radiation levels can occur, posing a threat to the reliability of the installed electronic systems. Therefore, at CERN the primary concern is for electronic systems installed at the Large Hadron Collider (LHC) [1, 2] and the Super Proton Synchrotron (SPS) [3, 4], the two largest CERN accelerators.

The SPS, in the past exploited for weak interaction studies through the proton-antiproton inter-

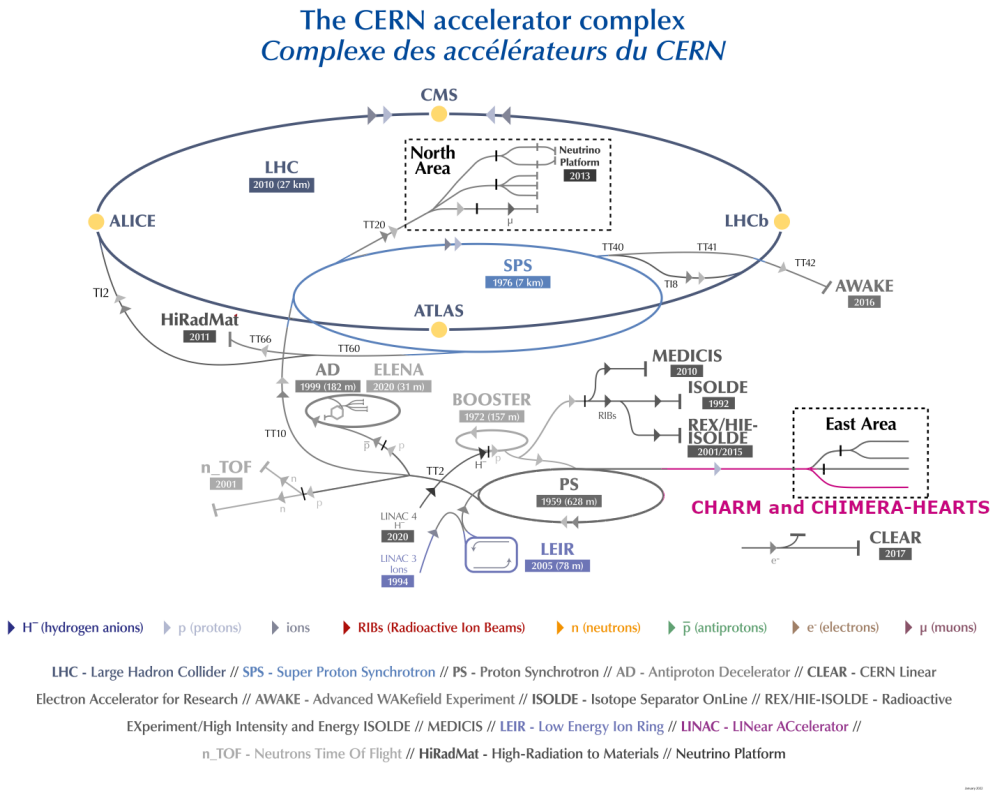

Figure 1.1: CERN accelerator complex. Coloured regions, i.e. LHC, SPS, LEIR, LINAC3, CHARM/CHIMERA-HEARTS correspond to accelerators/facilities covered in this thesis. Adapted from [5].

actions (Nobel prize in 1984) [6–10]), is currently the largest CERN injector, which supplies beam to experiments (AWAKE [11], HiRadMat [12], North Area Fixed Target [13]) and the LHC [1]. It is further described in Chapter 5.1. Most of the time the accelerator is operated with the proton beam accelerated between momenta of 16 GeV/c (typically injection energy) and 450 GeV/c (extraction energy for LHC beams). With such high energies and injected beam intensities of $\sim 10^{13}$ protons, even small beam losses can lead to a severe radiation environment. The LHC, the largest collider worldwide, described in Chapter 5.2, spans over a total circumference of 26.7 km, accelerates protons between 450 GeV/c – 6800 GeV/c in the two counter-circulating beams, and collides them in the centers of 4 experiments. Additionally, both LHC and SPS are operated with heavy-ion particle beams, however, the related radiation levels analysis is beyond the scope of this work, as they are significantly lower in the great majority of the locations, with the exceptions of regions with dominating heavy-ion specific beam loss mechanisms such as Bound-Free-Pair Production [14].

Through radiation-induced electronic system failures, the radiation might interrupt the operation of the accelerators, leading to downtime, defined as the period when the accelerator cannot be operated. In fact, radiation effects on electronics were the major source of the LHC downtime during

its first years of operation [15], in the so-called LHC Run 1, mainly covering the 2011 and 2012 years [16]. This resulted in the need to implement urgent mitigation measures to ensure the fulfillment of the scientific objectives of the accelerator infrastructure. Such measures, coordinated by the Radiation to Electronics (R2E) project at CERN, mainly consisted of relocating and shielding accelerator equipment sensitive to radiation effects on electronics [17]. In both cases, the mitigation effort, carefully prioritized through radiation level and equipment sensitivity studies, required a significant cost and time investment, primarily due to the associated cabling and civil engineering activities. Such mitigation measures were implemented during the so-called Long Shutdown (LS)1 (2013 and 2014) [18], as well as throughout Run 2 (2015-2018) [17]. These mitigation efforts were complemented by a more systematic approach towards the design and qualification of radiation-tolerant electronics systems, based on Commercial-Off-The-Shelf (COTS) microelectronics components [19]. Except for 2015 [20], the mitigation and prevention (i.e. through radiation tolerant design and qualification) efforts resulted in an acceptable rate of radiation-induced system failures during Run 2, albeit with an increased (but still acceptable) impact in 2018 due to a combination of enhanced radiation levels in several critical locations as well as possible cumulative damage contributions.

It is worth mentioning at this stage that the radiation effects in electronics affecting the LHC operation typically come in the form of functional interrupts in critical systems that trigger a so-called beam dump, consisting in the safe extraction of the beam from the accelerator, therefore avoiding potential severe damage of the accelerator infrastructure due to inadequate handling of the energy stored in it. In some cases, such functional interrupts can be removed by remotely resetting the concerned equipment. However, other cases require a manual reset or electronics board replacement, adding extra downtime on top of the 2-3 hours required to re-establish the stable beam conditions in the LHC and restart the collisions for physics data production.

Therefore, to a first quantified approximation, the impact of radiation effects on the availability and performance of the LHC can be measured through the number of beam dumps triggered by radiation effects on electronics. This quantity is typically expressed per unit integrated luminosity, which is proportional to the number of collisions produced in the detector regions of the accelerator. The evolution of this important figure-of-merit throughout Run 2 and Run 3 can be seen in Fig. 1.2, providing a quantitative view of the qualitative description above.

In the case of an SPS, an example of radiation-induced failures is the SPS Access System, containing industrial Programmable Logic Controller (PLC) I/O cards, that despite not being installed in the direct proximity of the SPS beamline, were affected by radiation failures during the 2021 operation, leading to 121 h of downtime [21]. Another example of an SPS system that could cause accelerator issues is A Logarithmic Position System (ALPS), used to measure the position of a beam in the accelerator via 216 Beam Position Monitors [22].

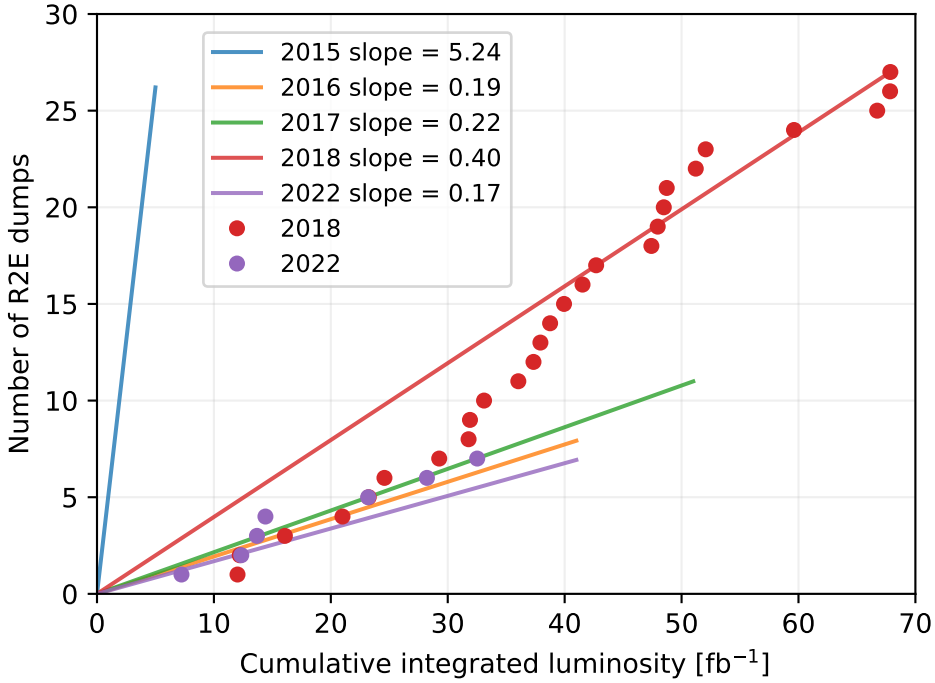

Figure 1.2: Radiation-induced interruptions of the LHC as a function of CMS integrated luminosity.

Its front-end Field Programmable Gate Array (FPGA) boards are based on radiation-qualified COTS and are installed directly under the accelerator's magnets. Following the studies presented in this thesis [4], locations requiring mitigation measures were identified and reported prior to system failures, hence enabling preventive maintenance actions.

The aforementioned experiences of radiation impact on electronics lead to the definition of the CERN Radiation Hardness Assurance (RHA) strategy [19, 23], consisting of two main pillars: i) knowledge about the expected radiation environment, that is obtained through beam monitoring and simulations and ii) radiation tolerant design and qualification of electronic systems. The CERN in-house designs are mostly based on COTS components that require radiation tests, both at the component (before the system design), and at a system level. In the case of CERN, the latter is performed in Cern High energy AcceleRator Mixed field facility (CHARM) [24]. The radiation field, produced via the spallation reaction with a target, mimics the mixed radiation field that can be encountered along the CERN accelerator infrastructure.

Whereas the focus of the thesis is not on RHA methodologies and related testing, the presented studies can complement already existing RHA guidelines. Within this study, two main, interlinked, topics are being investigated, as illustrated in Fig. 1.3. The first one, described in Chapter 5, is

related to the comprehensive analysis of the recent radiation levels in the LHC and SPS accelerators profiting from the already existing available radiation monitors, namely Beam Loss Monitors (BLMs) [25], CERN Radiation Monitors (RadMons) [26, 27], and Distributed Optical Fibre Radiation Sensors (DOFRSs) [28, 29]. Enhanced knowledge and findings may lead to the updates or redefinitions of the present RHA guidelines, e.g. due to unexpected radiation levels in some locations.

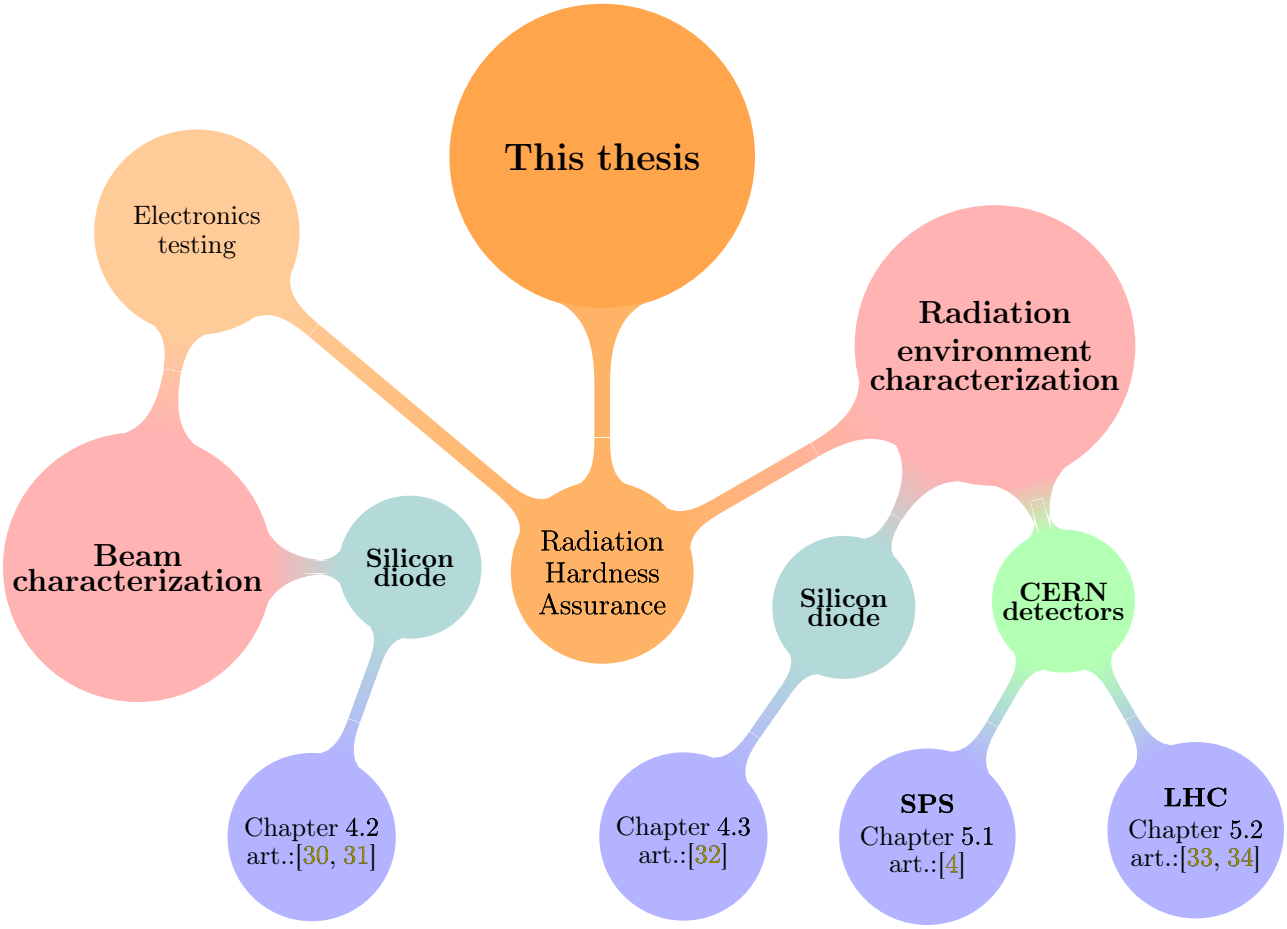

Figure 1.3: Mind map describing the content of this PhD, with the links between the chapters and authored publications. Content highlighted with **bold** is covered in this work.

The second part of the thesis, covered in Chapter 4, introduces silicon solid-state detectors that have two primary roles concerning the RHA. Primarily, due to enhanced sensitivity to radiation, they are intended as new monitors for the CERN's mixed-field radiation environment [35], to complement existing solutions such as RadMons, e.g. in very low radiation environments, which however can still impact electronic systems. This detector aims to improve the overall RHA procedure through the characterization of radiation in the direct proximity of electronic systems, focusing on the impact of the accelerator parameters (e.g. beam destination in the SPS). The second role of the detector is

more in line with the conventional silicon diode applications [36, 37] and targets beam characterization, both in well-established facilities during RHA-related irradiation tests, to verify the quality of the provided beam, as well as a beam monitor in the new facilities, e.g. within the scope of CERN's CHIMERA (CHARM High-energy Ions for Micro Electronics Reliability Assurance) and HEARTS (High-Energy Accelerators for Radiation Testing and Shielding) projects [30, 38–40], aimed at delivering Very-High-Energy (VHE) heavy ions to CHARM with the goal of electronics testing.

This PhD work targets applied and engineering aspects, providing a comprehensive picture from hundreds of GBs of radiation data (from silicon and other detectors) thanks to both existing and self-developed state-of-the-art software, related to data handling (data engineering) and its analysis, further described in Chapter 3. Therefore, the presented work can be considered horizontal, and each of the branches could lead to at least a few separate PhD theses.

Chapter 2

State of the art

In this chapter, the scope of the research together with a review of the existing studies are presented, in the two main thesis branches, related to the silicon diode detectors (Chapter 2.1) and CERN radiation environment (Chapter 2.2).

2.1 Part 1 - characterization of beams and radiation fields

One of the two main branches of the thesis refers to the silicon state detectors and their applications in the context of the RHA, to i) characterize beams used for electronics testing, and ii) characterize the radiation environments to which electronics is/will be exposed. The choice of silicon is motivated by the fact that this semiconductor is used in typical electronic systems, therefore interaction mechanisms of the environment with the detector will be similar to the ones in electronic systems [41, 42]. Radiation monitoring could be also performed by other solid-state detectors, made of germanium or diamond [43, 44], however, in such cases, the similarity in reaction channels with electronics might not be preserved. Moreover, radiation can be characterized by other detectors such as scintillators or ionization chambers but the link with electronics is even weaker.

Profiting from the similarity of the silicon solid-state detectors with electronics, in this thesis, the capabilities and limitations of silicon detectors are presented, focusing on the applications related to the characterization of the beamlines used for electronic testing (mono-energetic) and radiation field characterization (ground level, mixed-field CHARM, accelerators). The silicon detectors are commercially produced by Canberra and operated with current-sensitive preamplifiers.

The silicon detectors are widely used for beam characterization, particularly proton and heavy-ion ones [37, 45]. There are several past studies demonstrating their use for radiation characterization, e.g. atmospheric [46] or mixed-field [36]. They also serve as a benchmark tool between SEE testing

methods alternative to heavy ions, e.g. through laser [47] or pulsed X-rays [48]. Due to their simplicity, they are used to benchmark Monte Carlo codes [49–52], that are later employed to simulate deposited energies (thus potential radiation effects) in electronic components.

The silicon detectors are mostly used in combination with charge-sensitive preamplifiers, however, despite generally worse detector energy resolution, use with CIVIDEC fast current-sensitive preamplifiers [53, 54] allows to characterize (e.g. measure flux) of more intense beams, identify pile-up events, or exploit current profiles for contamination detection, through Pulse Shape Discrimination (PSD). As to what concerns the detectors themselves, similar Passivated Implanted Planar Silicon (PIPS) Canberra silicon detectors are used mainly for heavy-ion beam characterizations [37, 55–57].

Within this thesis, the objective will be to characterize Canberra detectors in a very broad range of beams (low/high energy protons, low/high energy heavy ions, thermal neutrons, gamma rays), and demonstrate capabilities of beam characterization (spectral, flux, etc.) and radiation monitoring. The main novelty arises from the use of commercial Canberra PIPS detectors to characterize the mixed-field radiation environment related to the accelerator operation (LINAC3, LEIR accelerators, described Chapter 5).

The motivation behind the selection of silicon solid-state detectors for CERN R2E applications is outlined below.

- Silicon is a fundamental material in electronics, and exploiting a silicon detector for radiation characterization will enable a direct link to the radiation effects in electronics due to the same reaction channels, e.g. for intermediate or high energy neutrons [51].
- Silicon detectors are more sensitive than the ionization chambers or SRAM-based solutions due to the mass of the sensitive material.
- Silicon detectors can be exploited both for beam characterization and radiation monitoring, due to the active readout.
- Silicon detectors are cheaper than the diamond equivalents and show better stability during irradiations.
- Silicon detectors do not require external cooling (as compared to germanium detectors).
- Silicon detectors are fast enough to disentangle contributions on an event-by-event basis, enabling the retrieval of the energy deposition spectrum, as opposed to a single value (e.g. dose). This is exploited in benchmarks against Monte Carlo codes.

- The required instrumentation (power supplies, digitizer, cabling) is simple and relatively compact. Therefore, the system can be shipped and operated in external institutes during test campaigns.

2.2 Part 2 - CERN accelerator's radiation environment

As already highlighted, each particle accelerator produces radiation fields of its own kind, with unique properties. Radiation depends not only on the machine layout but also on the operational parameters, therefore understanding underlying dependencies is crucial in the environment characterization within RHA. In particular, to foresee and plan mitigation measures prior to the radiation-induced issues and to ensure the correctness of the estimates for future radiation levels on which radiation tolerant designs are based, it is critical to understand the distribution of the radiation field along the accelerator and its evolution in time.

Similar considerations are made in the other radiation environments where the electronics systems are operated. An example of such an environment is space [58] where systems are exposed continuously to Galactic Cosmic Rays (GCRs) [59] and to time-discrete Solar Particle Events (SPEs) [60]. Depending on the orbit, systems might be also affected by protons and electrons trapped in the inner and outer Van Allen belts [61]. At the earth's orbits, a significant contribution is due to protons trapped in the belts. Whereas of smaller intensity, heavier ions from GCR are of high relevance for SEEs due to their high LET values, capable of inducing errors through direct ionization, as opposed to protons that typically only upset electronics through indirect ionization.

Enhanced systems reliability often involves larger costs due to radiation-hard designs. Therefore, often trade-off is made, taking into account the criticality of a system. For example, space or avionics systems are required to be redundant enough not to encounter "hard" (destructive) unexpected effects, that could lead, in the worst case, to the loss of a satellite or an aircraft accident. Whereas in the case of accelerators majority of the systems are of lesser importance, there are systems (e.g. beam extraction) whose failure might lead to severe damage to scientific infrastructure. Accelerators differ between themselves in terms of operation settings, e.g. beam energy, beam intensity, or beam optics. In a great simplification, for all hadron accelerators, the main source of radiation, i.e. interaction/loss of the beam particle with the surrounding elements, is the same. However, the machines differ in terms of processes that induce the losses, hence particle showers, and their magnitude. Therefore, it is important to understand the related beam loss mechanisms and their relation with both operational settings and the induced radiation, as that allows to define reliability requirements for future designs, optimizing costs, and machine availability.

Compared with the space environment, radiation produced due to beam losses in the largest

CERN accelerators does not include heavier ions and the vast majority of the SEEs are due to nuclear reactions induced by hadrons. While comparing annual levels of hadrons above 20 MeV, the fluence at ground level is about $2 \times 10^5\,\mathrm{cm}^{-2}$/year, which is 4 orders of magnitude below the value at the International Space Station [24]. Around the LHC, this value can be lower than $10^5\,\mathrm{cm}^{-2}$/year, and exceed $10^{11}\,\mathrm{cm}^{-2}$/year closer to experimental regions [24].

In this thesis, the radiation levels in the two largest CERN accelerators, the LHC and the SPS, are analyzed in detail. Concerning the LHC, the focus is on the 2022 year, which is the first one after LS2 (2019-2021), during which important changes were made which could impact the radiation levels. The key objective of this work is to detect any unexpected changes in radiation levels that occurred as compared with the Run 2 operation (2015-2018), and more particularly, with its last year - 2018. Focusing on the regions that are relevant for electronic systems, any significant difference is highlighted, and wherever possible, investigated. As to what concerns SPS analysis, the focus is on the year 2021, however, a large fraction of 2022 is covered too. In the SPS the focus is on the arc sectors, which contain the periodic magnet arrangement and constitute a large fraction (about 74%) of the total SPS circumference. In both LHC and SPS, the focus is on exploiting the capabilities of the already deployed monitoring infrastructure, to provide a comprehensive view of radiation distribution profiting from the advantages of separate detectors.

The current knowledge about the LHC radiation environment (from the electronics point of view) is primarily a result of the intensified effort arising from radiation issues encountered at the beginning (2012-2013) of the LHC operation [17]. In particular, Run 2 (2015-2018) involved multiple studies, starting from the very comprehensive analysis of the Total Ionizing Dose (TID) by BLM [62] or High-Energy-Hadron-equivalent (HEHeq) by CERN Radiation Monitors (RadMons) [63]. The radiation levels at the two large CERN experiments, CMS and ATLAS, were also investigated [2, 64]. Over 70% of the LHC circumference, constituting so-called arc sectors (with periodic magnet arrangement), was analyzed in detail and presented in [65–67]. Collimation regions were investigated through the combined efforts of the BLM radiation measurements and FLUKA Monte Carlo simulations [68, 69]. Often, the radiation is assessed purely based on FLUKA simulations [70, 71], however, this does not allow for the detection of changes in the radiation field, e.g. due to the impact of operational parameters.

Within this thesis, the aim concerning the LHC accelerator (Chapter 5.2) is to focus on the most recent, not yet analyzed, radiation measurements (2022, the first year after the accelerator restart), primarily the dose from the BLM, and perform a comparison with the past (mainly 2018) data. This is critical to ensure that i) assumptions and analyses made in Run 2 are still valid, and ii) no significant radiation anomalies were detected.

Until 2018, the primary source of information about SPS radiation was activation survey measurements and passive Radio-Photo-Luminescence (RPL) dosimeter measurements [72], both performed by CERN's Radio-Protection group. However, in both cases, the links to the RHA and electronics were not straightforward. Radiation measurements by RPL dosimeters often involved multiple years of operation, and the impact of smaller periods (beam recommissioning, impact of the settings) could not be resolved. In the case of activation surveys, the measured quantity is not equivalent to the one relevant for electronic systems, and the activation strongly depends on the material budget (and its type) and the very recent operation, thus is not necessarily representative of the prompt radiation levels during the year.

The first studies aiming at the investigation of dose profiles measured by active BLMs were performed in 2016 [73]. The study, however, i) focused on the operation in the years (2011-2015), which involved significantly less LHC operation ii) didn't investigate BLM data in detail (loss evolution within a cycle, different monitor positions, correctness of logging), iii) didn't profit from the additional radiation monitors (as they were not yet deployed).

Previous FLUKA Monte Carlo studies [74] assumed multiple simplifications such as i) beam losses due to interaction with the residual gas, ii) losses happening at the top SPS energy (which will be demonstrated not to be the case), and iii) loss (residual gas) profile corresponding to residual activation measurements. The second one would be the case only if all material budget was constant along the accelerator and operation at the end of the year was representative for the entire year.

Within this thesis, the goal is to exploit radiation measurements from the SPS accelerator (Chapter 5.1) and investigate the source of beam losses, through the time occurrence within a cycle. As of 2021, this became possible due to the BLM high-frequency data logging. Moreover, this study is the first one that links already known and investigated beam loss mechanisms [75] and resulting radiation levels. Additionally, profiting from the recently (2020) installed DOFRS, for the first time in the SPS, the BLM measurements are further complemented by fiber distributed monitoring.

Chapter 3

Materials, Tools and Methods

This chapter introduces the minimum knowledge needed to understand the thesis' content and the used nomenclature. Chapter 3.1 gives a short overview of the interactions between various radiative fields and silicon and defines the quantities used to assess the risk of electronics failures. As the thesis is strongly engineering-oriented, Chapter 3.2 provides a comprehensive view of the used radiation detectors, whereas Chapter 3.3 discusses the developed software.

3.1 Theoretical introduction

3.1.1 Radiation - silicon interactions

The main compound of electronic components, including the detectors used in this study, is silicon. Therefore, this chapter synthesizes the interactions of particles used in the thesis, such as protons, heavy ions, and neutrons.

The probability of a particle undergoing an interaction with a target nuclei is described by a concept cross-section (σ), that has a dimension of surface area.

3.1.1.1 Neutrons

As neutral particles, neutrons interact only with nuclei, through a strong force.

Elastic nuclear scattering, denoted as *A(n,n)A*, is a process that does not involve the production of new particles or target/projectile excitation. In this interaction type, the particles exchange kinetic energy and their directions change according to four-momentum conservation. Instead, **nonelastic processes**, include fission, radiative capture, and all nuclear reaction channels. They lead to the excitation of nuclei or the emission of new particles. Nonelastic reactions include **fission** (n,f)

and **radiative capture** (n,γ). Nuclear fission occurs for heavy elements and therefore is negligible for silicon.

As depicted in Fig. 3.1, depending on the neutron energy, different processes dominate. Low-energy neutrons interact with silicon through radiative capture and the cross section decreases proportionally-inversed to the neutron's velocity. At a certain energy (tens of keV), other nonelastic processes start to occur (due to nuclei structure, thus energy threshold), forming a so-called resonance region, where a cross-section has multiple peaks. At the end of the resonance region, the different nonelastic reaction channels (producing secondary products with LETs relevant for SEEs induction) superimpose and can no longer be distinguished. Therefore, the cross-section curve becomes smooth.

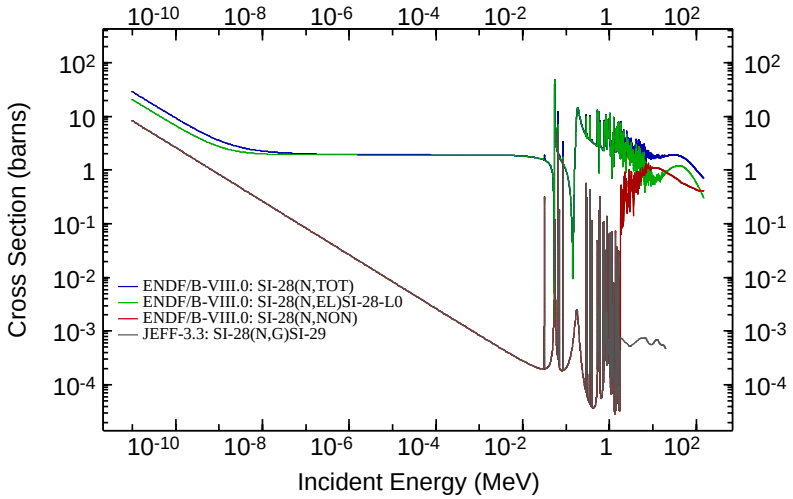

Figure 3.1: Cross section for the interactions of neutrons with ^{28}Si. The blue curve denotes the total cross-section, the green trace corresponds to the elastic interactions, and the red translates into nonelastic interactions, including radiative capture (grey trace). Peaks visible above 0.01 MeV correspond to the nuclear resonances originating from the nuclei structure. The data were extracted from ENDF and JEFF databases and were plotted via [76].

3.1.1.2 Charged particles: protons and ions

As compared to neutrons, protons and heavier ions, as charged particles, can interact with atoms also through the Coulomb force, both with the electrons and nucleus. The processes can be classified into three main categories:

- Coulomb scattering on electron potential from the target atom,
- strong force nuclear interactions with nucleus,
- slowing down due to ionization, i.e. collisions with target electrons.

As opposed to neutrons, charged particles are affected by a repulsive Coulomb force between nuclei, therefore nuclear reactions have a certain threshold energy. In general, ions undergo the same reactions as protons, however, the thresholds for nuclear interactions are higher due to a higher Coulomb barrier between nuclei. Additionally, due to a complex structure, consisting of multiple hadrons, among nonelastic processes, break up of nuclei into lighter fragments (**fragmentation**) is possible.

3.1.1.3 Photons

Photons interact with silicon through the following processes:

- **Rayleigh scattering** – elastic deflections of the photons without change of its energy;
- **photoelectric effect** – absorption of the entire photon's energy and emission of an electron from the inner shell, and sometimes, Auger electron;
- **Compton scattering** – deflection of photon by the electrons from outer shells, with a partial reduction of photon's energy;
- **photonuclear reactions** – nonelastic reactions of a photon with nuclei (γ, ...), resulting in the absorption of a photon by nuclei and emission of hadrons (p, n);
- **pair production** – in the presence of external mass (nuclei or atom's electron) a photon can decay to a pair of electron/positron or muon/antimuon.

The cross-sections as a function of a photon's energy are illustrated in Fig. 3.2. In this study, the gamma rays of 1.17 MeV and 1.33 MeV, produced by a radioactive decay of ^{60}Co, were exploited for calibration purposes. For these energies, the most frequent interaction is Compton scattering.

3.1.2 R2E quantities

In this study, among various physical quantities describing the radiation environment, the focus is on the dose, which is relevant for assessing Total Ionizing Dose (TID) cumulative effects, and High-Energy-Hadron-equivalent (HEHeq) fluence, relevant for assessing SEEs risks.

The dose is defined as absorbed energy in exposed material and is given in Grays (Gy), where 1 Gy corresponds to an energy of 1 J deposited in 1 kg of matter.

Following Eq. (3.1), the HEHeq fluence is defined as a time-integrated flux of hadrons above 20 MeV with the weighted ($w(E)$, defined based on the RadMon's Toshiba SRAM response) contribution of

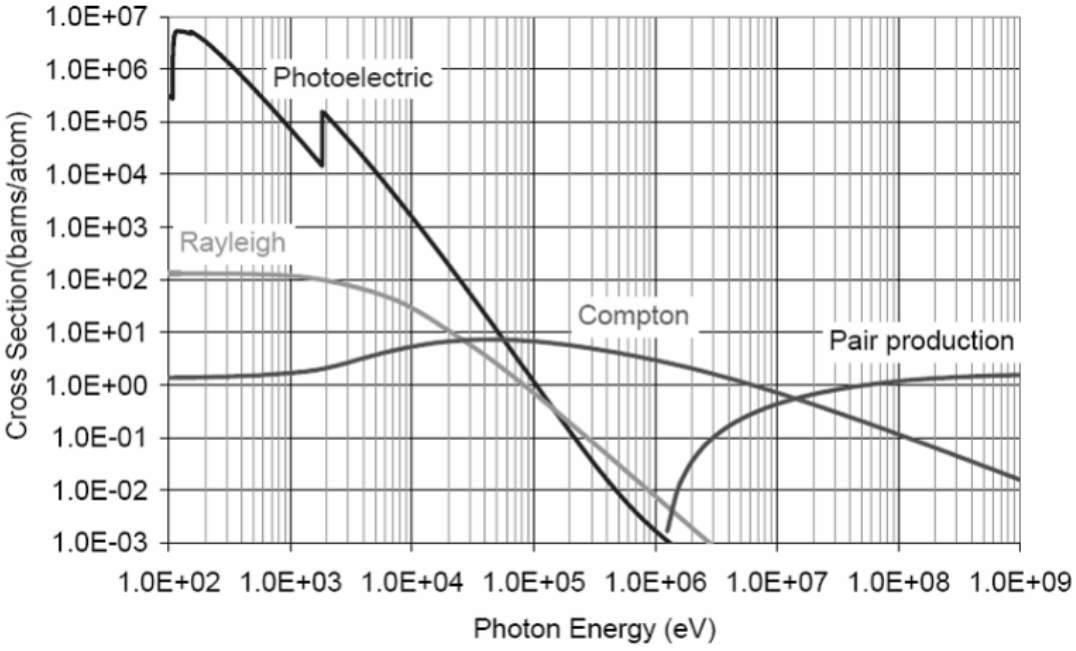

Figure 3.2: Partial cross section for the gamma rays interaction in silicon. Image credit: [77].

0.2 MeV – 20 MeV neutrons [71], as given by Eq. (3.1).

$$\Phi_{\mathrm{HEHeq}} = \int_{20\mathrm{MeV}}^{\infty} \frac{\mathrm{d}\phi_{\mathrm{HEH}}(E)}{\mathrm{d}E}\mathrm{d}E + \int_{0.2\mathrm{MeV}}^{20\mathrm{MeV}} w(E)\frac{\mathrm{d}\phi_n(E)}{\mathrm{d}E}\mathrm{d}E \tag{3.1}$$

In the case of electronics containing compounds with high cross-section for thermal-neutron interactions (involving charged particle emission), such as ^{6}Li or ^{10}B, the quantity used to assess the risks is called thermal-neutron-equivalent fluence. At low neutron energies, the total cross-section scales with the inverse of the neutron's velocity ($\sigma \sim v^{-1} \sim E^{-1/2}$). Therefore, a given THNeq fluence, calculated according to Eq. (3.2), describes such a spectral neutron field, that would induce the same number of interactions (captures) as the same fluence of thermal neutrons (25.3 meV).

$$\Phi_{\mathrm{THNeq}} = \int_{0}^{\infty} \sqrt{\frac{25.3\,\mathrm{meV}}{E}}\frac{\mathrm{d}\phi_n(E)}{\mathrm{d}E}\mathrm{d}E \tag{3.2}$$

Another quantity, used in this thesis is LET, describing the average amount of energy $\mathrm{d}E_x$ that is lost by an ionizing particle in matter (density ρ) per unit path-length $\mathrm{d}x$, as given by Eq. (3.3).

$$\mathrm{LET} = \frac{1}{\rho}\left|\frac{\mathrm{d}E_x}{\mathrm{d}x}\right| \tag{3.3}$$

3.1.3 Detection of particles with silicon detector

Semiconductor materials can be exploited for radiation monitoring purposes due to the presence of an energy gap between the valence and conduction electronic bands. Radiation might induce transitions between the bands. Therefore, the resulting change in the concentration of free charge carriers (electrons and holes) can provide information about the amount of deposited energy. In the case of silicon, around 3.6 eV (at room temperature) is needed to induce a direct transition between these bands. The indirect transitions, although having a low probability, require photon energy as low as the forbidden band gap (1.1 eV).

Often silicon is doped with more (n-type doping) or fewer (p-type doping) valence electrons compared to intrinsic silicon to create layers with opposite majority charge carriers (electrons and holes). When these layers are brought into contact, the diffusion of carriers will create the depletion region at the junction between layers. The depletion region is broadened by the external electric field, called reverse bias, applied to the semiconductor. In such a depletion region there are almost no free charge carriers. When a particle or photon interacts with silicon, it may cause ionization of the material, resulting in the creation of multiple electron-hole pairs. The number of pairs created is proportional to the deposited energy and is measured thanks to the bias, which ensures the movement of electrons and holes towards the cathode and anode, respectively.

In the case of silicon diode used for particle detection, the structure, also called P-I-N diode, typically consists of three silicon regions, as it is schematically represented in Fig. 3.3. The first and last regions are very thin. They are heavily doped, n- and p-type, to ensure the ohmic contact at the junction between the semiconductor and metal electrodes. Between them, an intrinsic silicon region with minimal (or no) doping is located. It serves as the sensitive volume of the detector. Reversed-bias voltage applied to the n- and p-type regions broadens the depletion region throughout the entire intrinsic region. The excessive carriers are removed from their respective doping regions, leaving a stationary space charge. Consequently, the majority of excessive carriers are removed and the current flow (called leakage current) is minimal. It is due to the random charge excitation in the depletion region, induced by thermal (temperature dependency) or photoelectric effects (illumination dependency). Therefore, each change in the measured current can be attributed to the electron-hole pairs induced by the radiation, with the total induced charge being proportional to the deposited energy.

While the principle of radiation detection, relying on ionization, is similar to ionization chambers, silicon detectors are significantly more sensitive due to their higher material density and the lower energy required to produce electron-hole pairs in silicon compared to the ionization of a gas molecule.

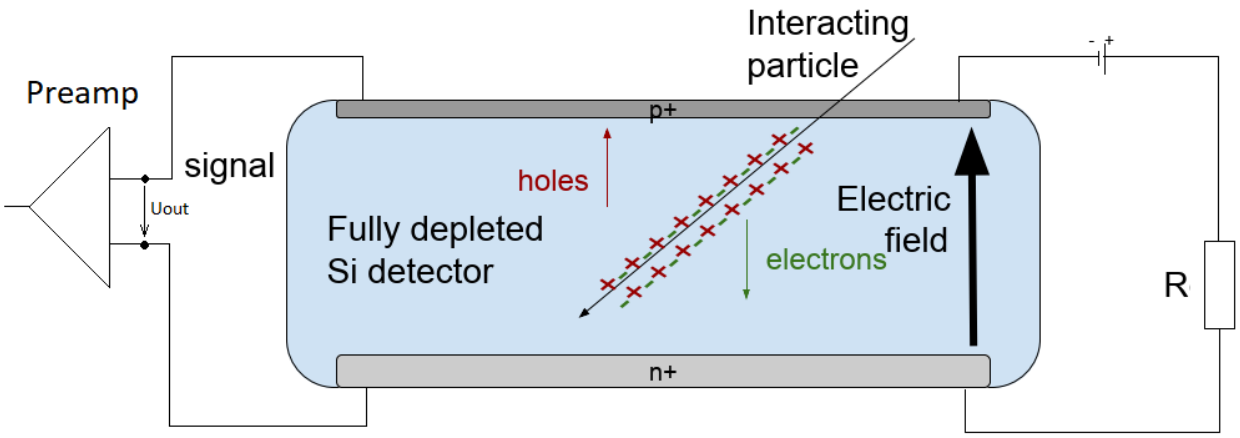

Figure 3.3: Schematic representation of a silicon PIN diode used as a radiation monitor. For clarity reasons, the Bias tee separating AC (signal) and DC (bias) signals, is not included in the scheme.

3.2 Hardware

3.2.1 CERN Radiation detectors

This section introduces active and passive solutions used for assessment of the radiation environment in the CERN accelerator complex by the R2E activity. Fig. 3.4 illustrates a region of the SPS, with all the described systems deployed.

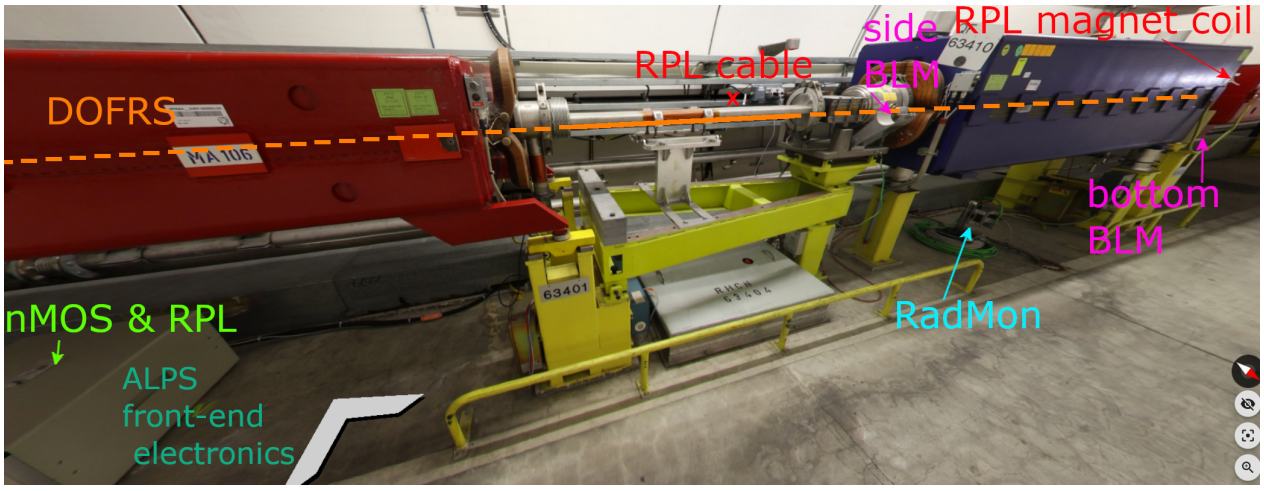

Figure 3.4: Standard positions of the radiation sensors in the SPS arc sections, with the electronic rack of the ALPS system (with RPLd on top, ∼0.9 m distance from the beamline), directly exposed to the mixed-field radiation. Behind the magnets, at the cable tray (∼1.3 m distance), as of 2021 the DOFRS monitor is installed. Before 2021, the dose was assessed by the RPLds (∼1 m distance), in each arc half-period one installed at the cable tray, and one at the magnet coil. Each arc half-period contains one BLM, installed either at the side of the beamline (∼30 cm distance) or under the first dipole magnet, as in the presented location. Additionally, in some half-periods RadMons are deployed under the magnets.

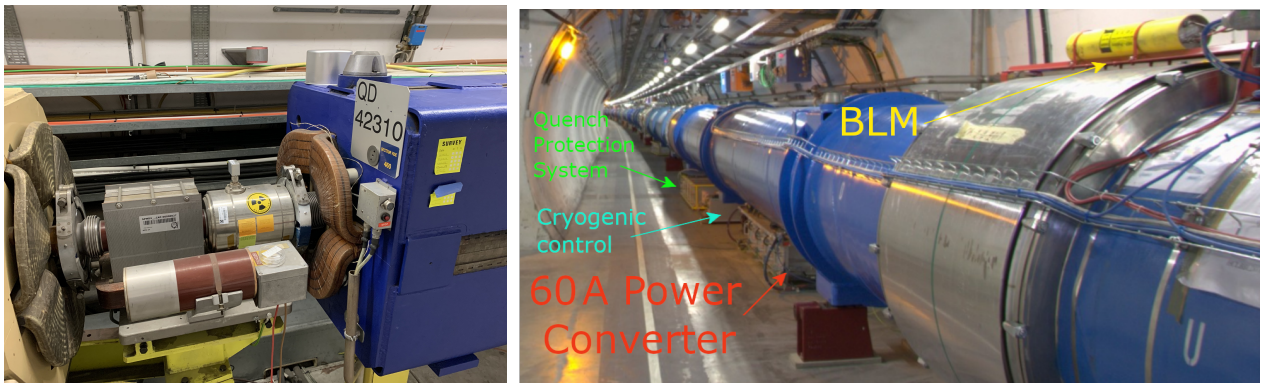

(a) SPS (b) LHC

Figure 3.5: Beam Loss Monitors installed in the SPS and the LHC.

3.2.1.1 Beam Loss Monitor (BLM)

The Beam Loss Monitoring system is a pillar of the machine protection solutions in the CERN accelerator complex. In the LHC, the system is a part of machine interlock, meaning that if signals are not within the accepted range, the particle beam is not permitted to be in the machine, resulting in a safe beam disposal at dedicated blocks (referred to as a beam dump). Whereas multiple types of beam instrumentation are exploited within the Beam Loss Monitoring system, the core are Ionization Chamber Beam Loss Monitors (BLMs), depicted in Fig. 3.5.

Inside the chambers, as depicted in Fig. 3.6, several parallel plates collect the charge produced through the ionization. In the case of the SPS, each chamber contains 30 of plates, with 5 mm separation. Each monitor is filled with approximately 1 dm^3 of air at 1.1 bar pressure (room temperature), and biased at 800 V. As opposed to the SPS, BLMs in the LHC contain 50 aluminum plates, separated by 5 mm and biased at 1.5 kV. The chamber volume is filled with 1.5 dm^3 of nitrogen gas at 1.1 bar [78].

The Beam Loss Monitoring system in the SPS consists of approximately 270 BLM units [79], distributed along the entire accelerator. In the LHC, over 3600 detectors are deployed. It has to be noted that the readout system installed in the SPS is less advanced than the one in the LHC [25, 80], and therefore provides limited accuracy and time resolution. In the SPS, the logging can be retrieved within 5 ms, whereas in the LHC 40 µs is achievable.

Although the main purpose of the system is machine protection, rather than dosimetry, it also plays an essential role in the active monitoring of the radiation environment, mainly due to the time resolution, significantly better as compared with other monitors. After a dedicated data processing [81], BLMs provide very detailed information about dose distribution and time evolution along the accelerator [65, 66].

(a) SPS (b) LHC

Figure 3.6: Insides of the ionization chamber BLMs installed in the SPS and the LHC. Credit: SY-BI-BL [78].

3.2.1.2 Distributed Optical Fibre Radiation Sensor (DOFRS)

Another monitoring system used to monitor radiation in the CERN accelerator complex is based on the P-doped silica optical fibers [82, 83], with the example depicted in Fig. 3.7. The detection

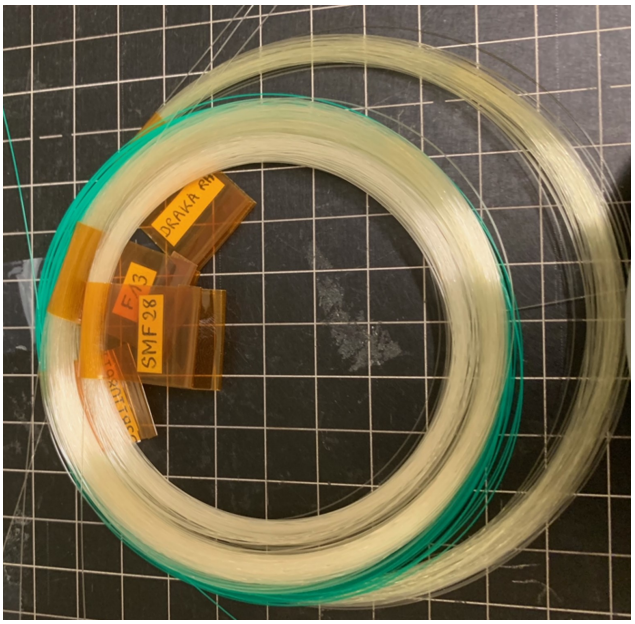

Figure 3.7: Example of the optical fibers that were characterized to be used within the DOFRS system.

mechanism is based on the Radiation-Induced Attenuation (RIA) phenomenon [28]. As the ionizing radiation impacts the fiber, it creates point defects in its core and cladding regions. These defects attenuate transmitted light, and therefore based on the attenuation profile, the radiation profile can be retrieved. For the best optical fibers such as the ones containing Phosphorus in their cores, the RIA linearly evolves with the TID (up to 500 Gy) without dose rate or temperature dependence in the ranges of interest for CERN. The system includes optical time domain reflectometry devices, that inject and measure periodically infrared light pulses injected into the fibers. Through a time-of-flight technique, exploiting the delay between the production of a pulse and the arrival time of the backscattered signal resulting from the pulse interaction with the silica material at a given location

(Rayleigh scattering), it is possible to reconstruct the 1D loss distribution along the deployed fiber, and after calibration, to obtain the 1D dose distribution. The readout in the DOFRS is performed periodically, and therefore the system can be used to monitor not only the spatial radiation profile but also its time evolution.

The first CERN's accelerator covered with DOFRS was the PSB [29]. Later, the system was successively deployed to cover the PS and the entire SPS (2021). During the LHC post-shutdown restart in 2022, the system was operational in the Dispersion Supressor regions of Insertion Regions 1, 5, and 7.

The fiber path usually follows the cable tray position. Therefore, the lateral distance from the beamline might vary between different regions. In the arc sectors of the SPS it can be assumed that the lateral position with respect to the beamline is preserved.

3.2.1.3 Radio-Photo-Luminescence dosimeter (RPLd)

Despite being a passive system, i.e. completely independent from the power supply and other connectivity, RPLds play a crucial role in the CERN dosimetric activities, mainly thanks to their broad detection range (1 Gy – 10^6 Gy) and easiness of deployment thanks to their small size (cylinder of 8.5 mm height and 1.5 mm diameter).

The principle of the RPLds relies on the two phenomena induced by radiation in the Ag-doped alkali-phosphate glass ($AlNa_3O_8P_2$:Ag), i.e. luminescence light emission due to RPL centers and glass darkening due to color centers. The concentration of these centers can be related to the absorbed dose. During the dose reading process, UV light (365 nm) stimulates the RPL centers, causing them to emit orange luminescent light known as RPL light. Simultaneously, the formation of color centers alters the transparency of the glass, shifting it from clear to yellow, brown, and eventually nearly black at high doses. For low dose range, up to 300 Gy, the RPL response is linear with the dose until reaching saturation around 1 kGy due to the glass darkening induced by an increased number of color centers. Therefore, it is necessary to use a second measurement to avoid ambiguity in the RPL light measurement. At CERN, light transmission measurement is used in the saturation region to reduce the uncertainty and to identify between the low-dose and high-dose ranges. Examples of irradiated RPLds are depicted in Fig. 3.8.

In the frame of this PhD, during the 2022 operation, several RPL dosimeters were deployed in the SPS to i) study the dose levels at the electronic equipment positions, ii) investigate the attenuation coefficients between the cable tray and the equipment level.

(a) darkening due to colour centres

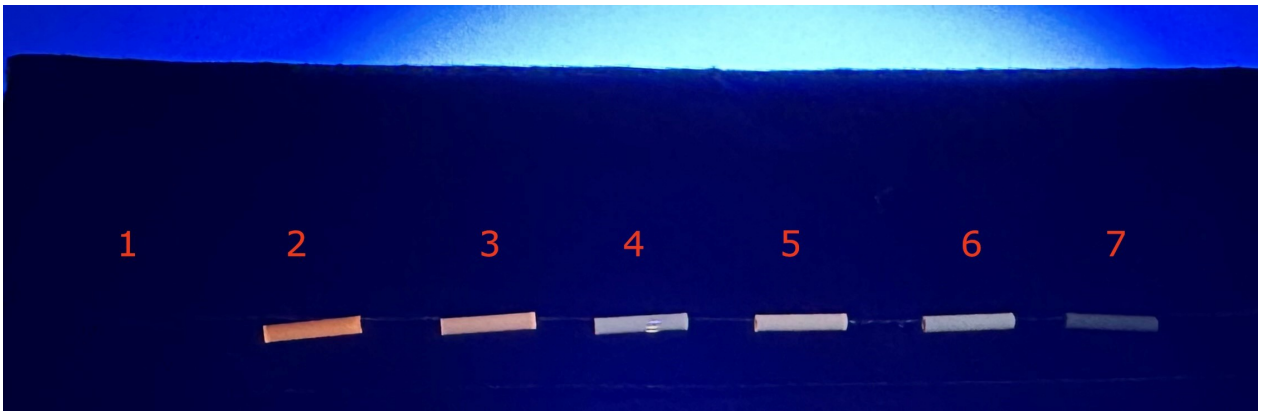

(b) luminescence

Figure 3.8: An example of the RPLds exposed to radiation in the LHC, together with darkening and luminescence phenomena.

3.2.1.4 RadMon

The CERN accelerator complex is equipped with hundreds of dedicated radiation monitors called RadMons [26, 27], with the example pictured in Fig. 3.9.

The RadMon is based on COTS components. Its main advantage is the capability of measuring not only dose(SiO_2), but also other quantities, such as HEHeq-, 1-MeV-silicon-neutron-equivalent-, and THNeq-, fluencies; relevant for characterizing radiation environment with the focus on its effects on electronics.

The dose is monitored through a floating gate [84] transistor or Radiation Sensing Field Effect Transistors (RADFETs), in older RadMon versions [85]. Ionizing radiation leads to the production of electron-hole pairs. The generated electrons can become trapped in the insulating oxide layer of the MOSFET, resulting in a shift of a threshold voltage, i.e. minimum voltage required to enable the flow of charges between the source and drain terminals. The increase of the voltage is proportional to the absorbed dose.

1-MeV-silicon-neutron-equivalent fluence, relevant for the assessment of DD, is measured by a p-i-n diode. The DD in the silicon leads to the increase of the diode's forward voltage, and thanks to

Figure 3.9: RadMon with RPLd installed in the SPS.

the calibration the damage created by a particle can be compared with the effect induced by 1 MeV neutrons.

The THNeq and HEHeq fluencies are measured by a combination of two SRAMs, manufactured by Cypress (technology 90 nm) and Toshiba (technology 0.4 um). As opposed to the Toshiba memory, the sensitivity of Cypress memory to thermal neutrons is negligible compared to its HEHeq sensitivity. Therefore, by combining the measurements and cross-sections of both memories, the HEHeq and THNeq fluencies can be retrieved.

3.2.2 Silicon solid-state detectors

Chapter 3.1.3 introduced the concept of silicon solid-state detectors in the context of radiation detection. This chapter describes the hardware implementation of such a radiation detector setup based on the commercial Passivated Implanted Planar Silicon (PIPS) detectors manufactured by Canberra and pictured in Fig. 3.10. Within this work, measurements from four detectors of two models are presented. The larger detector has an active silicon volume of 50 cm^2x500 µm, and will be denoted as *large*. The smaller detectors, herein referred to as *small*, have an exposed surface of 0.5 cm^2 and thickness of 300 µm. The main characteristics of the detectors, together with the reversed bias voltage required to obtain a full depletion, are listed in Tab. 3.1. Both detectors were

(a) small **(b)** large

Figure 3.10: Silicon detectors used in the presented work.

Table 3.1: Specification of the used silicon detectors. Detectors I-III will be denoted as small, and IV as large.

Ref.	Model	Lot number	Nominal bias (V)	Thickness (mm)	Exposed Si surface (cm^2)	Sheet
I	FD 50-14-300 RM	3184.318.119.14	110	0.3	0.5	[86]
II	FD 50-14-300 RM	3705.326D.377.21	60	0.3	0.5	[87]
III	FD 50-14-300 RM	3705.326D.378.18	60	0.3	0.5	[88]
IV	PD 5000-75-500 AM	3560.317A.24.1	130	0.5	50	[89]

operated with one of the two CIVIDEC preamplifiers: C1-HV or C2-HV. The certified gain was equal to 21.7 dB and 43.9 dB, respectively. The preamplifiers, in addition to amplification, include a bias tee. The amplified output signal was digitized with the CAEN DT5751 1GS/s digitizer. The bias voltage was provided by a Keithley 2410 Source Measurement Unit. The schematic experimental setup is depicted in Fig. 3.11.

Whereas the exposed detector surface of detectors (I-III) is equal to 0.5 cm^2, this model of detectors is known to have some silicon active volume under the steel case [37]. As will be shown in Chapter 4.1.4, based on the ratio of direct ionization events from i) heavy-ions directly punching silicon and ii) heavy-ions degraded by the case before the interaction [57], it is estimated that $\approx$0.27 cm^2 of active silicon surface is located below the case.

Each energy deposition event is recorded as a voltage trace over time $V(t)$. After the conversion (R=50 Ω impedance) to current, the signal is integrated to retrieve the number of the collected charges. This step assumes that the setup does not encounter signal losses and that the gain g is equal to the one specified by CIVIDEC. In the following step, the total deposited energy is calculated as the measured number of charges multiplied by the energy that is needed to create an e-hole pair in silicon (W$\approx$3.6 eV). On top of that, the obtained deposited energy value is further multiplied by a k correction factor, arising from an energy

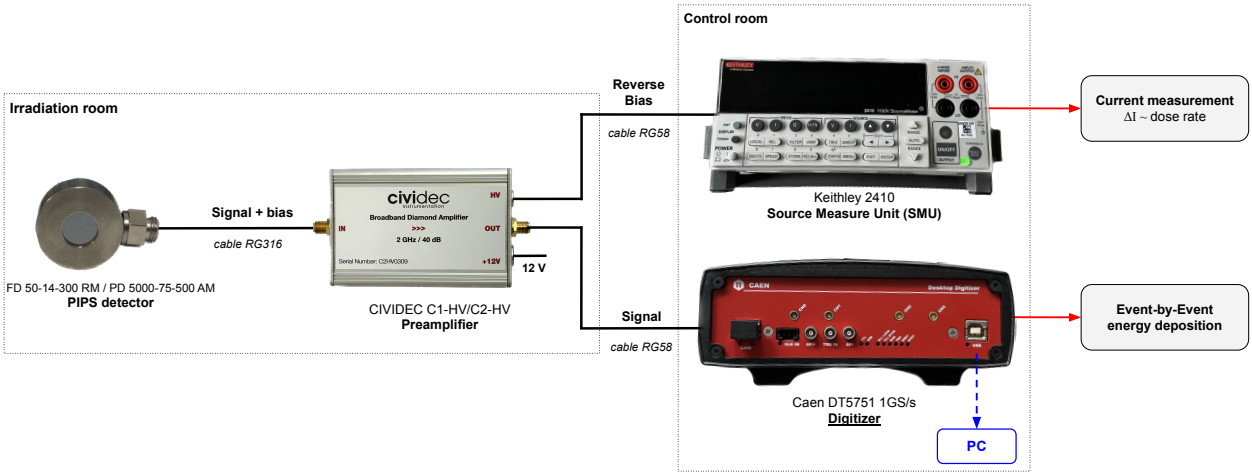

Figure 3.11: The scheme of the silicon diode experimental setup. It consists of a silicon diode detector, power supplies, preamplifier, and digitizer.

calibration under conditions that allow for very accurate control of the deposited energy in the diode. This is described by Eq. (3.4).

$$E_{dep} = k \cdot W \frac{Q}{e} = k \frac{W}{ge} \int I(t)\, dt \tag{3.4}$$

Each energy deposition event inducing a voltage transient above a threshold is acquired and saved to a binary file, which is processed according to Chapter 3.3.2.

3.3 Software tools

3.3.1 Apache Spark and radiation data processing

Devices and equipment related to the accelerators' operation log data to the NeXt Cern Accelerator Logging Service (NXCALS) [90], the successor of the old Oracle-based CALS service. This includes the BLM, RadMon, and DOFRS systems. One of the main advantages of NXCALS, is the extraction API built on top of Apache Spark [91], a unified open-source analytics engine for big data, allowing to perform studies on a dedicated cluster.

The developed R2E analysis tools, schematically depicted in Fig. 3.12, are designed to profit from the available Apache Spark engine for efficient radiation data processing. First, the scripts perform transformations of the data such that they can be used for dosimetry purposes, an example of which is the baseline subtraction, particularly important in low radiation regions, that compensates for systematic error caused by the digitization of analog signals and related nonzero value of the current despite lack of the radiation. Later, for each monitor type and each of the accelerators, the transformed data is aggregated (e.g. integrated, time-averaged) to compress the data size, while preserving the information level relevant for R2E

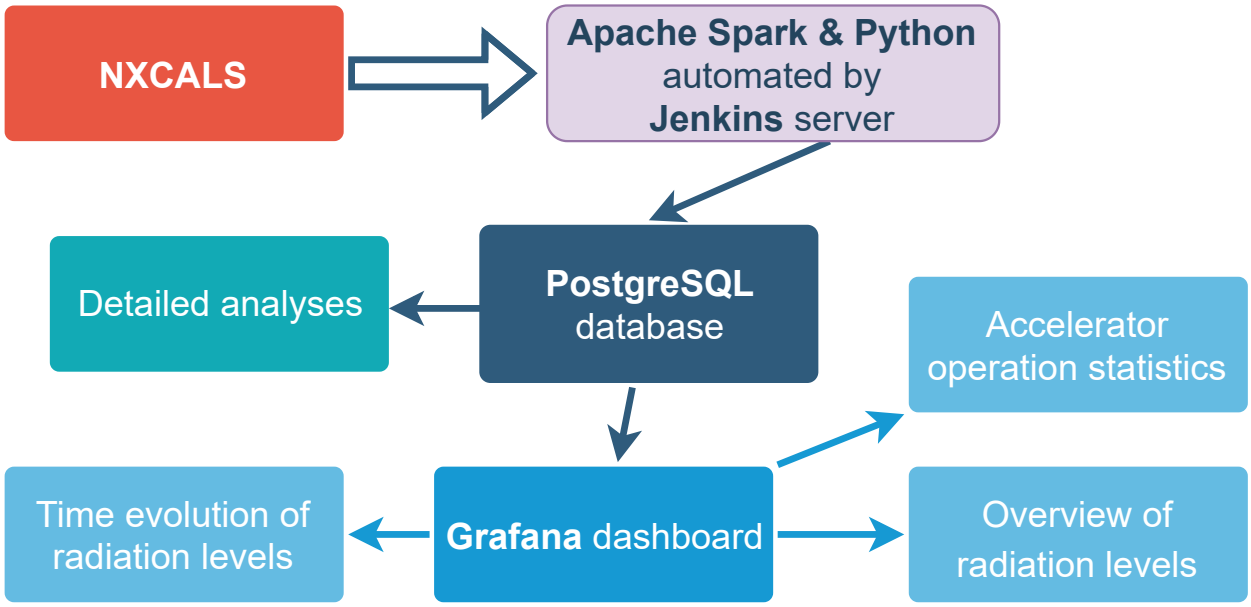

Figure 3.12: Scheme of the data pipeline put in place to automate the radiation data analysis. Source: [81].

applications.

For each accelerator and each monitor type, a dedicated script was developed, profiting from the efficient Python libraries (PySpark, Pandas [92], Numpy [93]). The scripts are executed periodically by a Jenkins automation server on the Apache Spark cluster (included in NXCALS) consisting of several thousands of CPU cores. Whenever possible, the algorithms were designed to profit from the parallelized execution offered by Apache Spark.

3.3.2 Silicon detector data processing

The digitizer is controlled by the CAEN Wave Dump software. In case of a high event rate, exceeding the transfer rates available via USB 2.0, a buffer of the digitizer might reach saturation. Provided that the saturation of the digitizer does not exist, each transient with the amplitude exceeding a given software threshold is saved in the binary file with 1 ns resolution. An example of a transient signal induced by a high-energy heavy ion is depicted in Fig. 3.13. To a first approximation, the area above the baseline is proportional to the released charge, hence the deposited energy. Such a period, related to a single device trigger, lasting a few hundred nanoseconds (usually 500 ns), is called a *frame*. The frames are then post-processed with two types of analysis codes, developed as a part of the thesis. Both of them read binary files created by WaveDump software, and process frames on a sequential basis. The goal of both codes, being the analysis of frames, is the same, however, due to different execution speeds they are used in different scenarios.

The algorithm implemented in C++, listed in Appendix A, is designed and optimized for performance. The code is used during test campaigns to provide real-time insights about the radiation field during irradiation and data acquisition, as the execution times are fast (a few seconds per gigabyte of data).

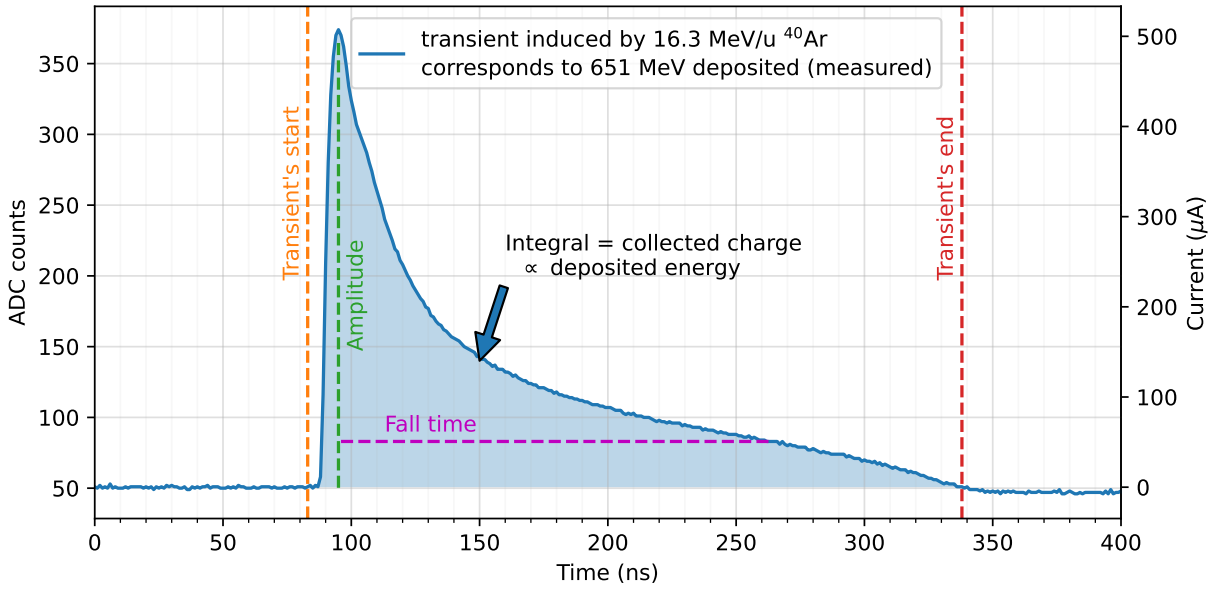

Figure 3.13: Example of energy deposition event, *frame*, as measured by a silicon diode and acquired via CAEN Wave Dump.

Later, after completing the test campaign, the results are analyzed with a Python script, which contains slightly different algorithms and additional features, such as pile-up detection. It also allows easier comparison with different facilities or testing conditions, due to object-oriented design.

3.3.3 Particle transport codes

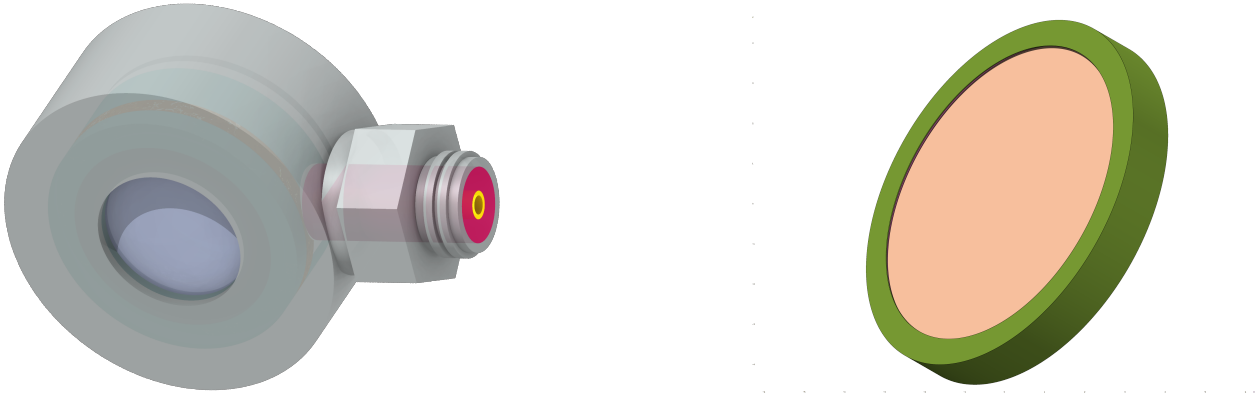

(a) small **(b)** large

Figure 3.14: Models of the detectors implemented in the FLUKA code. Colors, particularly for large detector, do not reflect reality.

3.3.3.1 FLUKA

FLUKA is a Monte Carlo-based particle transport code [94–96], with roots in the 1960s, written in Fortran. It plays a critical role in radiation protection and energy deposition assessments. It has a Graphical User Interface (GUI), called FLAIR [97], which significantly facilitates the preparation of an input file. Whereas this thesis is oriented towards measurements, several FLUKA simulation results are included, for benchmarking purposes. One of the advantages arising from FLAIR is the ability to build accurate geometries, for example, silicon detectors, as illustrated in Fig. 3.14.

3.3.3.2 Geant4

Geant4 is another Monte Carlo particle transport code, implemented in C++, with an open-source license. Due to implementation in a modern objective language, as compared to Fortran, the toolkit offers more flexibility in designing applications and custom particle treatment. Profiting from that fact, a G4SEE tool was developed [51], enabling detailed studies of energy depositions in simple geometries. In this thesis, it was used to investigate which neutrons contribute to which regions of the energy deposition spectra.

Chapter 4

Characterization of irradiation beams and radiation fields

This chapter, written based on the work presented in [30–32], focuses on the previously introduced silicon detectors, highlighting their calibration in multiple particle fields, later applied to both direct (beam) and indirect (secondary product, i.e. radiation) characterization.

The calibration section begins with the analysis of the detectors' response in the reference proton/^{4}He beams, providing a conversion between the charge measured on an event-by-event basis, and the deposited energy. Linked to the deposited energy, however, in the longer time frames ($\sim$s), the following section shows the relationship between the measured amplitude of the bias current and the dose rate that the diode is exposed to. Next, the response of the detectors in proton beams is presented, as a showcase of the nuclear interactions in silicon induced by high-energy hadrons. The latter are the most critical constituents of the accelerator's mixed field in terms of radiation-induced electronic failures. Last, the indirect measurements of thermal neutrons are presented, as neutrons of such low energies are highly present in the accelerator's shielded regions, due to increasing thermalization along with the increasing distance from the radiation source and their high penetration capabilities in concrete/soil.

Profiting from calibration covered in Chapter 4.1, Chapter 4.2 shows use cases of the small silicon detector in applications related to comprehensive beam characterization. In the beginning, it is shown how the diode can be used for flux monitoring in the CHIMERA-HEARTS beamline, providing heavy ion beams for electronic testing with high penetration depths while preserving high LET values. Later, it is demonstrated how the leakage current calibration and measurements can be used to characterize proton/neutron beams in terms of dose rates. Chapter 4.2.3 shows how the detector can be exploited for a spatial beamline characterization, while there is a possibility of remote detector alignment.

As to what concerns the characterization of the radiation fields, Chapter 4.3 shows how the setup can be used to provide insights from the radiation fields, focusing on low-intensity environments, such as cosmic-

ray induced neutrons or some accelerators' environments, where other solutions (e.g. SRAM-based) are not sensitive enough.

4.1 Detectors calibration

4.1.1 Energy calibration with low energy proton and alpha beams

Each energy deposition event is recorded as a voltage trace over time. After the conversion (R=50 Ω impedance) to current, the signal is integrated to retrieve the number of the collected charges. This step assumes that the setup does not encounter signal losses and the amplification is equal to the one specified by CIVIDEC. In the following step, the total deposited energy is calculated as the measured number of charges multiplied by the energy that is needed to create an electron-hole pair in silicon (W≈3.6 eV). On top of that, the obtained deposited energy value is further multiplied by a k correction factor, as given in Eq. (3.4), arising from a calibration.

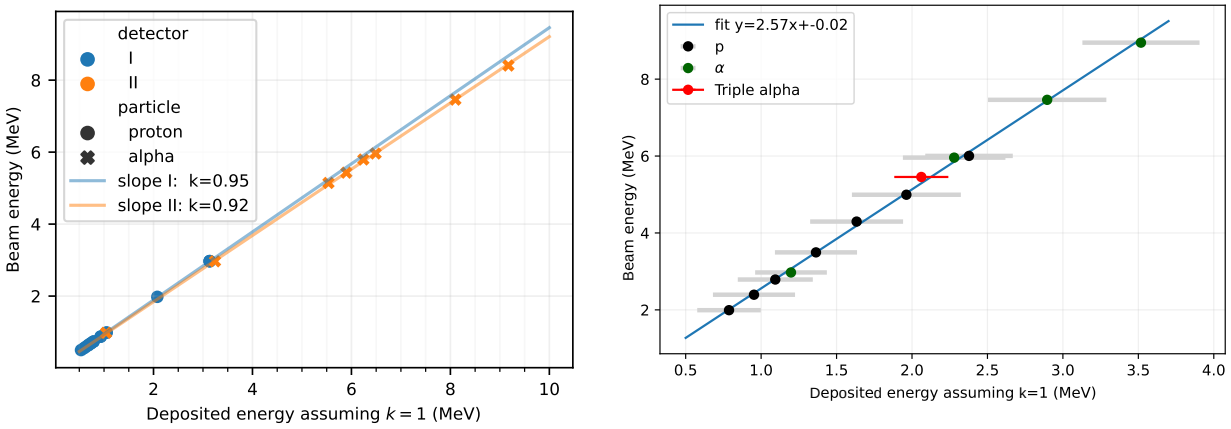

(a) small detectors (I-III)

(b) large detector (IV), with the σ of measured direct ionization peak

Figure 4.1: Total deposited energy (equal to the beam energy) as a function of the measured deposited energy that assumes on average 3.6 eV to create a single e-hole pair and setup parameters according to the specification. The calibration was performed for both small (I and II) and large detectors, listed in Tab. 3.1. The slope of each fit corresponds to a correction factor k that should be applied to the measurements in a similar energy regime.

For both small (I-II) and large (IV) detectors, the calibrations were performed in the 3MV Tandem accelerator at CNA under vacuum conditions, as depicted in Fig. 4.1 [98, 99]. In the case of small detector I, the calibration involved a proton beam with 10 energies between 0.5 MeV and 2.97 MeV, also exploitable for electronics testing [54]. Detector II was calibrated with an alpha beam of 4 different energies between 2.97 MeV and 8.95 MeV. The obtained k factors are equal to 0.95 in the case of small detector I, and 0.92 for small detector II. The factors are similar and the difference is likely due to the detectors themselves (e.g. due to the irradiation history and/or doping difference). As it has been reported [100], the value might depend on the depositing particle type. Within the accuracy of the presented setup, there is no evidence that the

difference in k factors comes from the different particle types used during the calibration (proton, alpha), mainly thanks to a very thin dead layer (below 50 nm). Calibration for the large detector was performed in the same facility, with both p and ^{4}He particle beams. To reduce the event rate, a polyethylene collimator, depicted in Fig. 4.2 was used, which could compromise the measured setup energy resolution, given that the triple-alpha source irradiation (with no collimation) led to a narrower peak than in the case of monoenergetic particle beams.

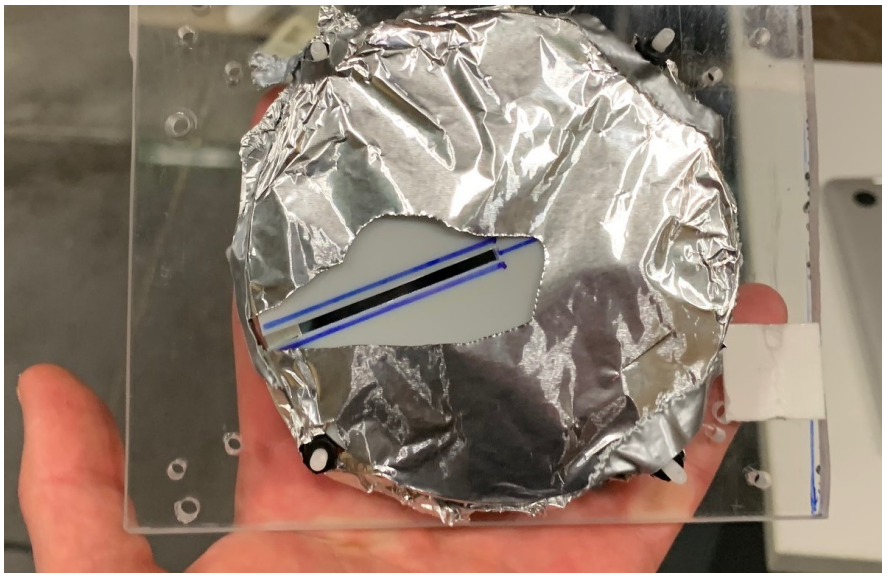

Figure 4.2: Collimator used to reduce event rate during large detector energy calibration. The aperture extends between the center of the detector and its case, providing a representative sample of events profiting from the radial symmetry.

In this work, the evolution of the k factor as a function of irradiation history was not experimentally investigated. It cannot be excluded that it changes with the accumulation of DD or TID. For small detectors it was observed that the leakage current increased along with the detector's history and the energy resolution degraded, likely due to DD effect [101]. The latter is illustrated in Fig. 4.3. As the preamplifier has been installed outside a vacuum chamber, potentially leading to additional signal attenuation from a vacuum feedthrough on the raw signal, the k factors cannot be directly compared with calibrations depicted in Fig. 4.1.

The tests included a triple-alpha (^{239}Pu, ^{241}Am, ^{244}Cm) source calibration, depicted in Fig. 4.4. However, given the energy resolution of the setup, it is not possible to disentangle each of the ^{4}He energies in the measured deposition spectrum. According to the manufacturer specification, the energy resolution of the detector itself, in terms of Full Width at Half Maximum (FWHM), is equal to 67 keV for alpha particles of 5486 keV. The Full Width at Half Maximum (FWHM) is factor 10 lower than the measured value. One of the reasons could be i) an alpha source (used by the manufacturer) with a smaller energy spread, ii) use of a different readout chain, in particular a charge-sensitive amplifier. The latter could improve the resolution significantly at the cost of a worse time resolution. In the targeted radiation environments (accelerators), a

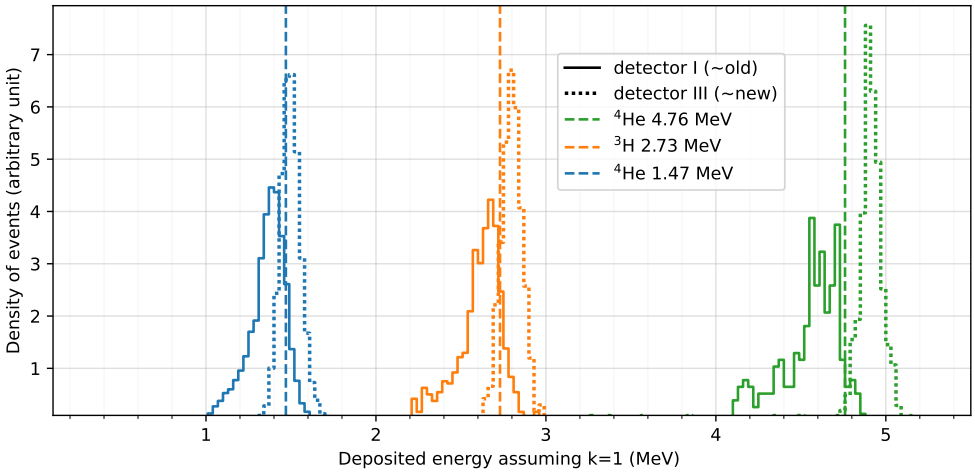

Figure 4.3: Measured energy deposition spectra for ^{3}H and ^{4}He ions, as collected at PN1 instrument, further described in Chapter 4.1.4, by small detectors. Detector III wasn't previously irradiated, as opposed to detector I, which had encountered multiple irradiations with various particle types (mixed field, low and high energy protons). The larger width of the direct ionization peaks for detector I is likely due to the detector's irradiation history. Vertical lines correspond to the beam's energy, i.e. true deposited energy. Calibration for detector III yields $k < 1$, whereas for detector I, it is $k > 1$.

very good time resolution is essential to discard false pulses, resembling particle interactions, that are induced by high-frequency noise, e.g. due to magnet operation.

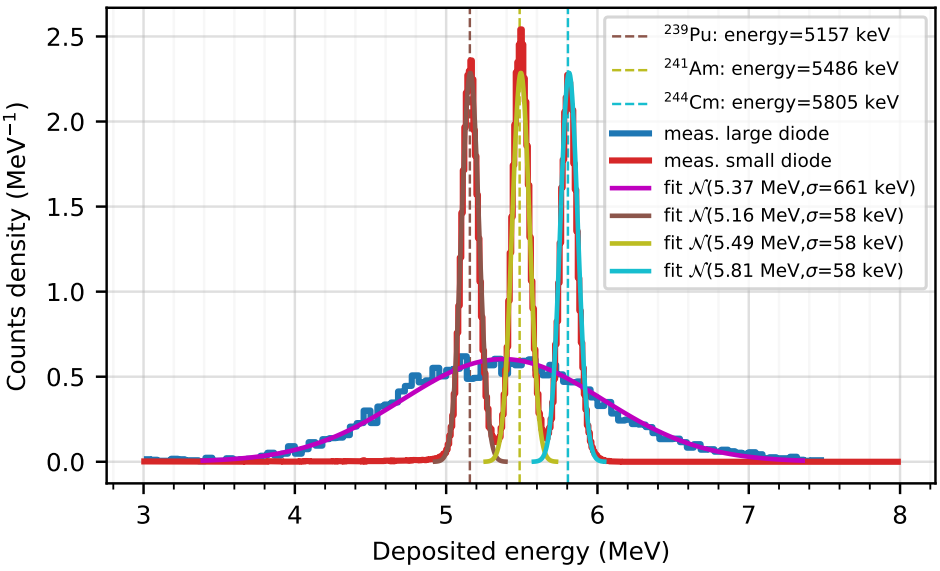

Figure 4.4: Measured energy deposition distribution with triple-alpha (^{239}Pu, ^{241}Am, ^{244}Cm) source as measured by the large detector listed in Tab. 3.1. The energy resolution of the large detector (with the current-sensitive preamplifier and described readout chain) is worse compared to the small detector.

4.1.2 Dose-rate calibration with gamma rays

The current that is measured at the preamplifier's bias output is directly proportional to the dose rate. Profiting from this fact, a calibration of the setup (detector II, IV) against gamma rays from ^{60}Co was performed. During the tests, the beam was not collimated and the detectors were covered with an aluminum foil. The reference dose-rate measurements in the facility were obtained using PTW 30010 Farmer ionization chamber (volume 0.6 cm^3, with 4.55 mm-thick polymethylmethacrylate build-up cap). The measurements with the linear fit are depicted in Fig. 4.5. The retrieved current to dose-rate conversion is equal to 6.17×10^4 Gy/s/A for a small detector, and 3.7×10^2 Gy/s/A for a large detector. It has to be noted that the small detectors

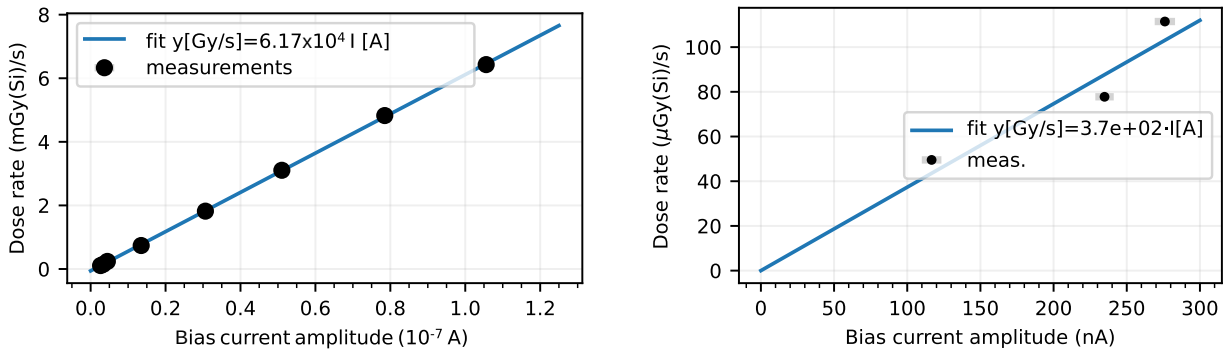

(a) detector small (I-III) **(b)** detector large (IV)

Figure 4.5: Dose-rate (in Si) as a function of the leakage current amplitude under the Co-60 irradiation.

contain a case, that partially covers the active silicon region. During the calibration with gammas, the case helps in reaching the electron equilibrium, which wouldn't be achieved if pure 300 um-thick silicon was used, as there wouldn't be enough material for electron build-up. The electron equilibrium was achieved in the reference condition, in the used ionization chamber. According to performed FLUKA Monte Carlo simulations under irradiation with photons of 1 MeV, the measured dose would be approximately 30% lower as compared with the dose in thicker silicon volume (in electron equilibrium). While considering only the active region itself and without surroundings, the respective dose would be factor 3.3 underestimated.

The calibration is useful for dose rate estimations in high-radiation environments, where the use of event-by-event acquisition mode is not feasible due to pile-ups. There are, however, a few important limitations. In the case of large diode, the calibration curve has only two points (and enforced crossing through the origin), therefore the obtained results have significant uncertainty. Another limitation arises from the silicon thickness, which is not enough to reach full electron equilibrium during the calibration (possible overestimation). In the case of small diode, the impact of the case is relatively more important. The uncertainty of the dose rate measurements in a mixed-field is within 41%, as the calibration could introduce 30% overestimation due to electron-equilibrium condition and the case collimation (assuming worst-case of 0.35 cm^2 shielded surface) could reduce the active silicon volume by 41%, leading to a dose rate underestimation. However, in the accelerator's mixed field, e.g. in CHARM, the expected deviation would be lower due to the highly penetrating nature of the radiation.

4.1.3 High-energy protons

The setup allows retrieving each single energy deposition event (created by a single hitting particle). Depending on the beam type, the resulting energy deposition spectra provide information concerning the beam energy spread and the interaction of the environment with silicon, the latter being essential also for Monte Carlo simulations benchmarking. Examples of energy deposition histograms collected with the aforementioned proton beams are depicted in Fig. 4.6.

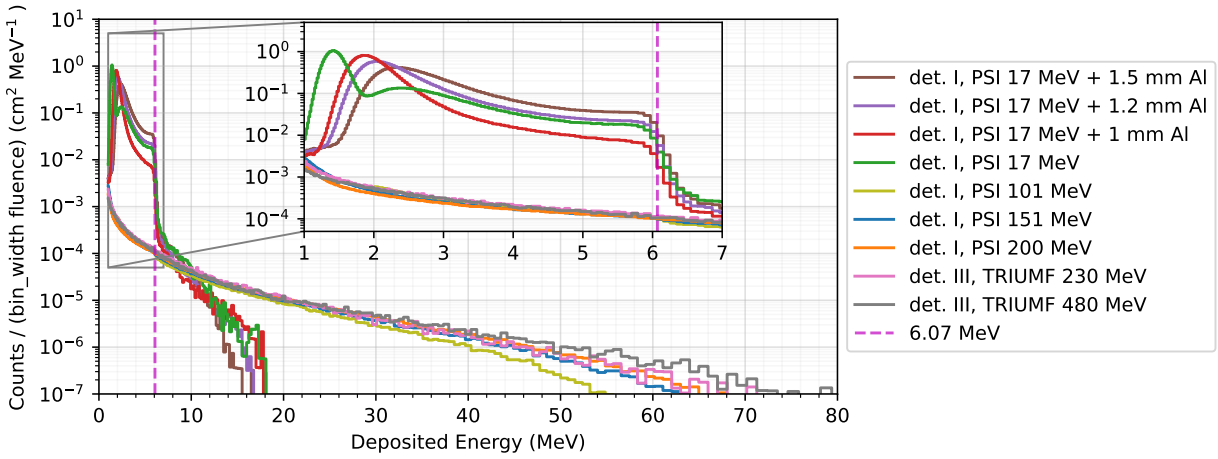

Figure 4.6: Energy deposition spectra under proton irradiations as measured by detector I (PSI-PIF) and detector III (TRIUMF-PIF). Additionally, at 6.07 MeV a vertical dashed line is displayed, which indicates the maximum energy that a proton can deposit in 300 μm of silicon through direct ionization. In the case of PSI, energies below 70 MeV were obtained through the degradation of 70 MeV beam, as opposed to energies above 100 MeV that were obtained via degradation of 200 MeV primary beam. In TRIUMF, the beams were not degraded and correspond to primary energy extracted from the cyclotron.

There is a good agreement between the ~200 MeV spectra measured in PSI and TRIUMF. With the decreasing energy, there are fewer open nuclear reaction channels, with lower energy transferred to secondaries, and therefore fewer high-energy deposition events. In the case of significantly degraded beams, the majority of the measured events are due to proton direct ionization and were not measured by the high-energy proton beam, due to their lower LET. Moreover, due to the energy degradation and associated beam energy spread, some protons do and some do not deposit their entire energy in the silicon, leading to the step at 6 MeV, which corresponds to the maximum energy that can be deposited via direct ionisation by protons in the thickness of the small diode. The step can be used as an ad-hoc calibration in the radiation environment with a significant presence of protons, for example when the presented calibration is not valid due to additional cable attenuation.

4.1.4 Heavy ions

Heavy ions are of high relevance for SEE electronic testing in space applications due to their capabilities of depositing high energies in small silicon volumes. In this thesis, small detectors (II and III) were exploited for heavy-ion beam characterization within CHIMERA-HEARTS activity, as will be shown in Chapter 4.2. Along with the exploitation of the detector for the beam characterization, calibration irradiations, aiming at the detector characterization, were performed.

The typical response of the detector to heavy ions is depicted in Fig. 4.7. In the case of ions having a range in silicon not exceeding the detector's thickness, i.e. having a Brag peak within silicon volume, the energy deposition spectrum contains a low energy tail due to energy deposition by lighter fragments (present in a beam, produced in the diode case, or in the silicon due to nonelastic reactions) and a prominent peak, around the ion's kinetic energy, caused by the ions depositing their entire energy through the direct ionization. In the case of ions with a range in silicon exceeding the detector's thickness, for example, ^{238}U of 600 MeV/u, the energy deposition spectrum contains events induced by fragments or due to nonelastic processes. However, the peak caused by direct ionization is not at the largest energy depositions, as fragments can have higher LET than the primary beam. Moreover, for higher beam energies, with penetration capabilities exceeding the diode case, there is a possibility of observing a second direct ionization peak due to ions that have higher stopping power due to energy degradation in the diode case and active silicon region present under the case, as observed in a previous study [37]. Additionally, due to Pulse Height Deficit (PHD) effects, the energy calibration obtained with reference protons or helium ions does not result in correct values of the deposited energy. Therefore, to study the small detector's response to heavy ions, dedicated heavy-ion calibration runs were performed.

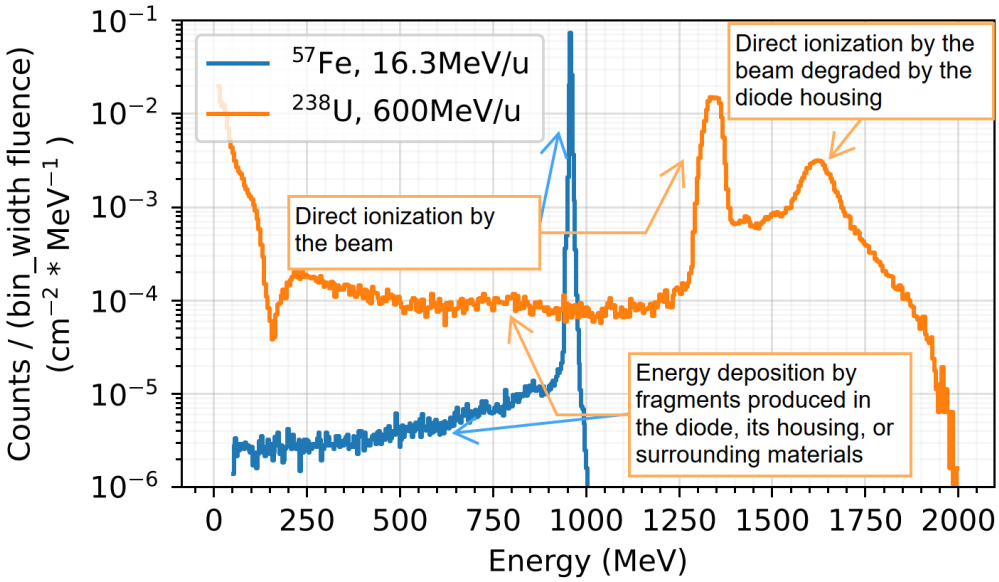

Figure 4.7: An example of energy deposition spectra induced by high-energy heavy ions in small detector. ^{57}Fe ions at that energy have a range in silicon below the detector's thickness, such that the entire ion's kinetic energy could be deposited via direct ionization. On the other hand, ^{238}U were highly energetic with the range exceeding the detector's thickness. Image source: [57].

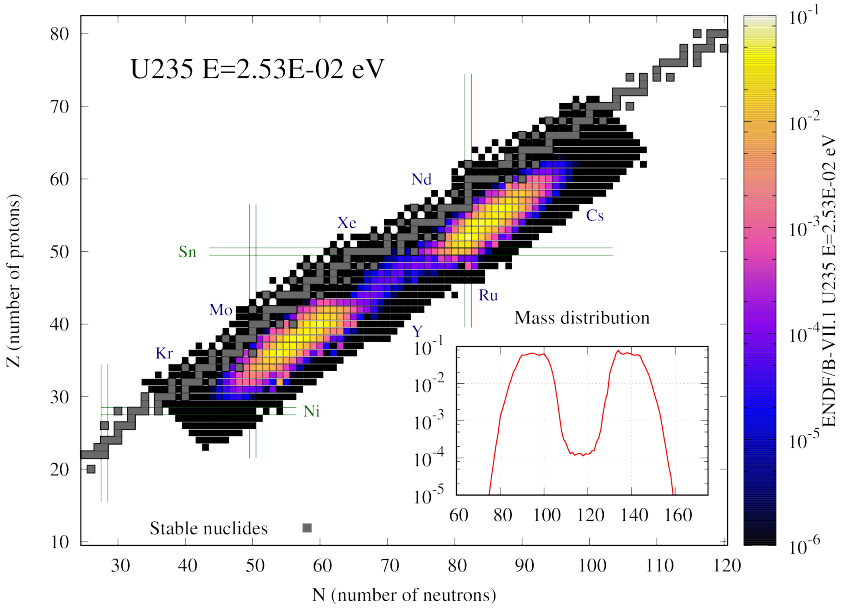

Figure 4.8: Schematic distribution of fragments produced via ^{235}U fission. *This plot was used with the permission of the United Kingdom Atomic Energy Authority. All rights reserved.* Image source: [102].

4.1.4.1 ^{235}U fission products

The first set of heavy-ion calibration irradiations (in vacuum) with the small diode (III) was performed in ILL at the Lohengrin spectrometer (PN1) where fission products can be delivered to DUT [103, 104]. During the experiment, a ^{235}U target was used [105]. The target material was covered with thin nickel foil and was installed on the titanium frame [106]. Additionally, some ^{10}B and ^{6}Li were installed close to the target. A schematic representation of ^{235}U fission products yield is illustrated in Fig. 4.8. In addition to the fission products, several light ions, produced from the elements near the target, can be produced. The list of used ions is included in Tab. 4.1. Before reaching DUT, the fragments are separated by magnetic and electrostatic deflectors [107], with respect to their $\frac{A}{Q}$ and the velocity, i.e. $\frac{E_{kin}}{A}$. Due to the thickness of the Ni-foil, most of the fission products have a charge of $Q = 20$. That is the equilibrium charge state reached by ions of a given velocity traversing the Ni cover foil. Initially, lower-charged ions will predominantly strip electrons off while initially, higher-charged ions will predominantly capture more electrons while traversing the foil.

Profiting from the light ions ($A < 5$), a calibration for detector III was performed, similarly to that described in Chapter 4.1. The calibration for detector II was not applied, as the setup arrangement was different than during typical tests. First, the amplifier was installed outside of the vacuum chamber, thus the attenuation from the vacuum feed-through could lead to a stronger impact on the detector signal, as compared with the CNA calibrations, where the preamplifier was installed in a vacuum. Second, the majority of irradiations were performed with an additional 3 dB attenuator, due to limitation on the dynamic range of the digitizer. The calibration is presented in Fig. 4.9. The factor of $k = 0.967$, is higher than for other detectors, which means that the measured value needs to be multiplied by a higher number to retrieve the true deposited energy.

Table 4.1: Projectiles used during detector calibration during PN1 experiment, together with the particle's kinetic energy, creating reaction channel, and the physical source of the element.

projectile	energy (MeV)	reaction	source
p	0.58	^{14}N(n, p)^{14}C	^{14}N absorbed on/in titanium frame
^{7}Li	0.84	^{10}B(n, ^{4}He)^{7}Li*	^{10}B deposited close to the target
^{7}Li	1	^{10}B(n, ^{4}He)^{7}Li	^{10}B deposited close to the target
^{4}He	1.47	^{10}B(n, ^{4}He)^{7}Li*	^{10}B deposited close to the target
^{4}He	1.75	^{10}B(n, ^{4}He)^{7}Li	^{10}B deposited close to the target
p	1.82	^{59}Ni(n, p)^{59}Co	^{59}Ni produced in the nickel foil covering the target through ^{58}Ni(n, γ)^{59}Ni
^{4}He	2.04	^{6}Li(n, ^{4}He)^{3}H	^{6}Li deposited close to the target
^{3}H	2.73	^{6}Li(n, ^{4}He)^{3}H	^{6}Li deposited close to the target
^{4}He	4.76	^{59}Ni(n, ^{4}He)^{56}Fe	^{59}Ni produced in the nickel foil covering the target through ^{58}Ni(n, γ)^{59}Ni
^{4}He	8	^{235}U ternary fission	^{235}U target
^{4}He	11	^{235}U ternary fission	^{235}U target

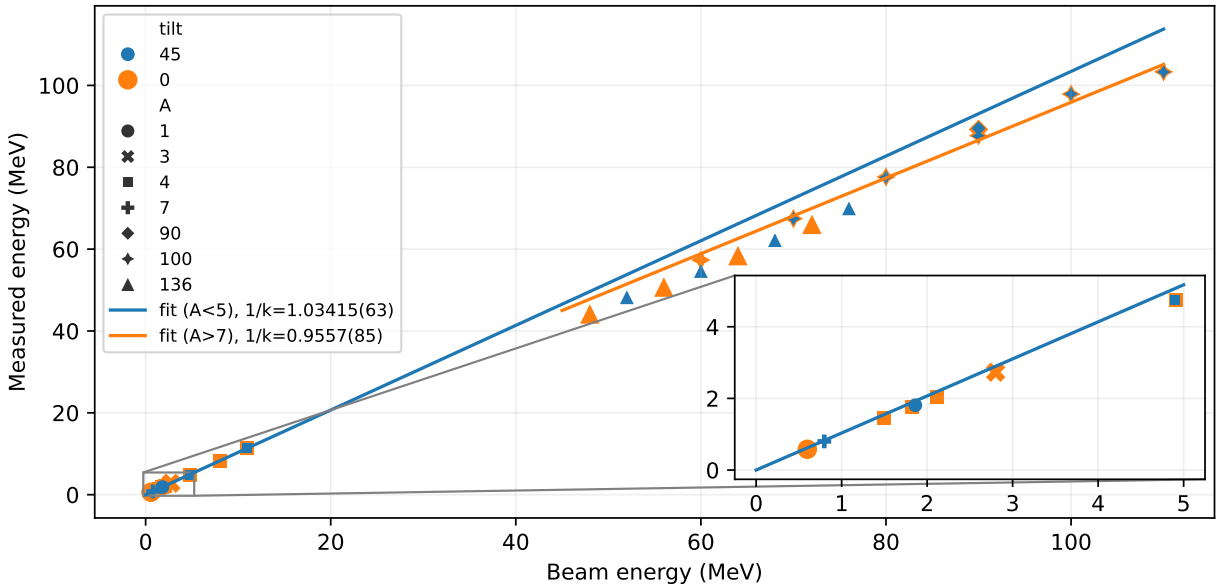

Figure 4.9: Beam energy (fully deposited in silicon) as a function of measured deposited energy (assuming $k = 1$ and amplification according to the manufacturer) for small detector (III). The linear fit was performed for beams with $A \leq 4$ and no tilt. The deviation from the calibration curve increases both with the increasing A and the beam's kinetic energy.

This might be because the amplifier was installed outside of a vacuum chamber and a feed-through could have additionally attenuated the signal. After the calibration with ions ($A < 5$), the small detector (III) was irradiated with the fission products ($A > 7$). Given 3 independent variables (mass A, kinetic energy E_{kin}, and charge Q) the instrument does not allow the selection of a unique fragment, but rather a composition

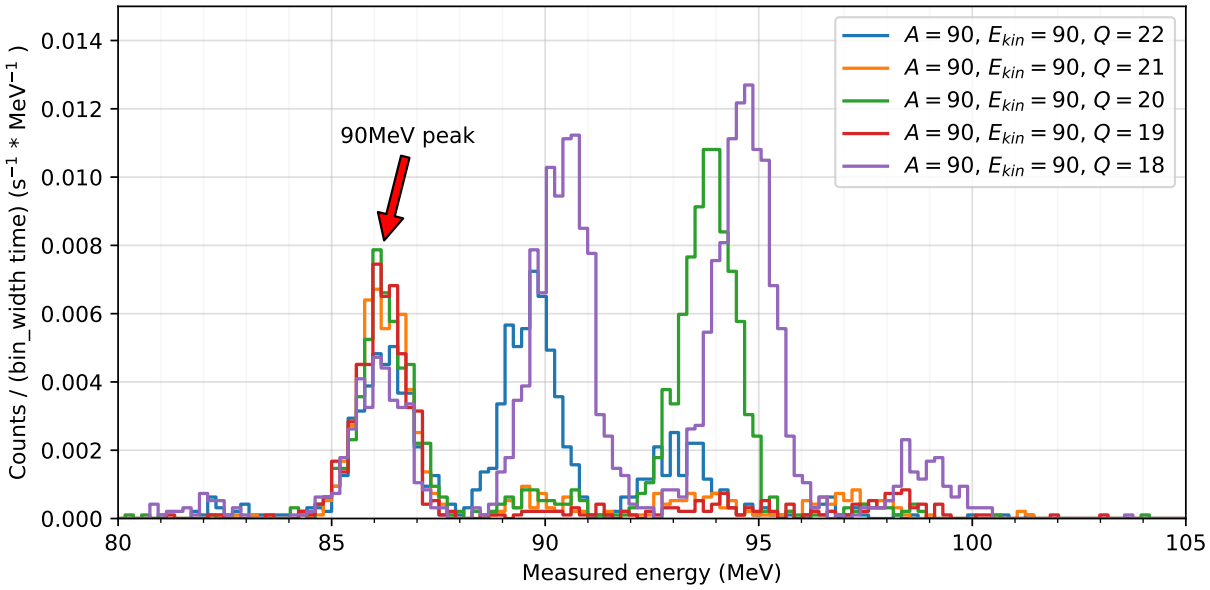

Figure 4.10: Measured energy deposition spectra with a fixed mass (A) and energy (E_{kin}) parameters. Peak present at all the runs (charge states $Q = \{18, ..., 22\}$) at the same position corresponds to the "true" $E_{kin} = 90\,\mathrm{MeV/u}$.

of fragments meeting separators' conditions ($\frac{A}{q}$ and $\frac{E_{kin}}{q}$) (within the acceptance range). This ambiguity is not observed for light ions. The calibration for heavier elements started with irradiation with a fixed mass and energy (A, E) and varying charge state (Q). The peak, illustrated in Fig. 4.10, that is present for all the configurations at the same location corresponds to the products having indeed $A = 90$ and $E = 90$, and can be used as a reference for other runs.

An example of an energy deposition spectrum is depicted in Fig. 4.11. The separator settings corresponded to parameters of $A = 100$, $Q = 20$, and $E_{kin} = 100$. However, in addition to the peak by fragments of 100 MeV, there are other peaks as among the fission products there are other products that meet the separator condition.

Despite the total energy deposition by the ions, the related measured energies were reduced due to various effects such as i) Pulse Height Deficit (PHD) [108, 109], ii) loss of the energy in the detector's dead layer. This deviation is illustrated in Fig. 4.9. The latter, however, is negligible, as there was no observable difference in the deposited energies while tilting the detector by 45°, therefore increasing the energy deposited in the dead layer by 41%. Hence, the dominant effect is related to the PHD, and the deviation (underestimation of the deposited energy) from the calibration curve for p/^{4}He increases both with the increasing atomic number A, hence Z (that is more relevant due to dependence in Bethe-Boch formula), and the kinetic energy E.

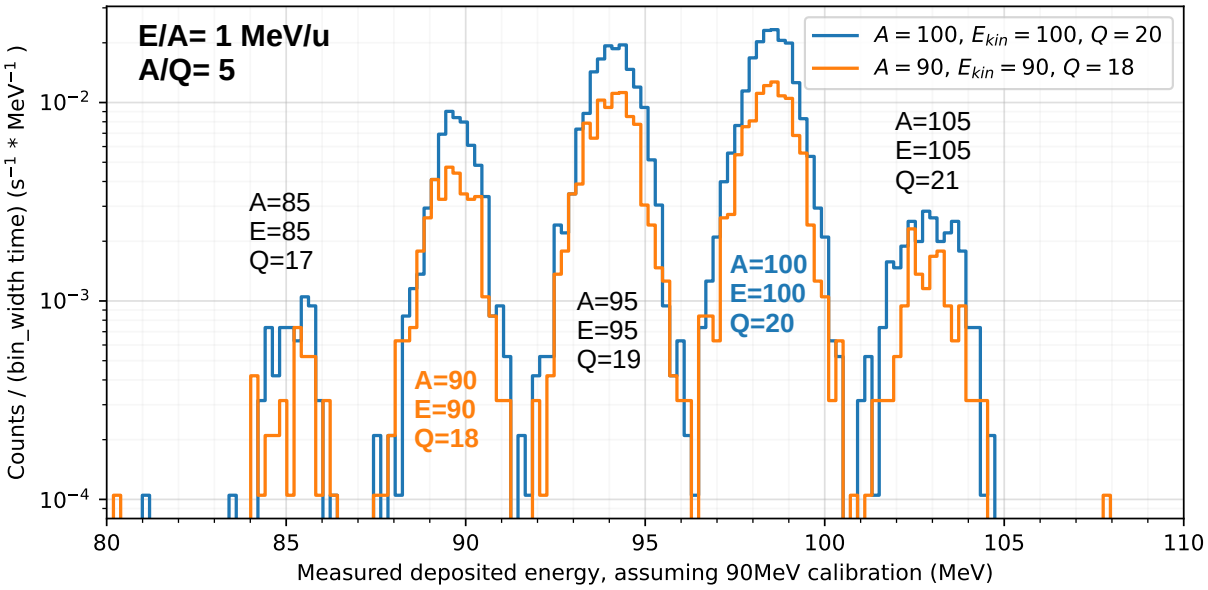

Figure 4.11: Measured energy deposition spectra with small detector, for two configurations of $(A, Q, E) = (100, 20, 100)$ and $(90, 18, 90)$, leading to the same separator settings ($\frac{A}{Q} = \frac{90}{18} = \frac{100}{20} = 5$, $\frac{E}{A} = \frac{90}{90} = \frac{100}{100} = 1$).

4.1.4.2 Mono-energetic heavy ions

The studies of the small detector response were continued in RADEF [110], thanks to beamtime granted by RADNEXT project [57]. Unfortunately, the small detector (III) was partially malfunctioning due to an unknown issue. For several energies, the direct ionization peak was split into two smaller peaks. The problem did not exist with the same readout chain and a different small detector (kindly provided by the facility). Qualitatively, the higher the LET was, the higher the difference between peak positions could be observed. For low-LET ions, the difference could not be resolved, however, the broadening of the main peak was observed (compared with other measurements not covered within this work). The effect was geometric, as the peak ratio was affected by a detector tilt and irradiated silicon region (as observed when testing with a very small beam spot). Dust or dirt at the detector's surface could explain such an effect, but, the detector was cleaned and no dirt could be observed. Moreover, similar behavior could be observed for backside irradiations. Therefore, it is assumed that some part of the detector has different properties, either due to i) the manufacturing process, or more likely ii) due to its history (non-uniform irradiation, transport damage). Therefore, collected data has to be treated with some mistrust. Fig. 4.12 depicts a calibration for heavy ions in the 9.3 MeV/u to 22 MeV/u range.

4.1.4.3 Active surface measurements

As indicated in the previous studies [30, 37], the small detector (II) has some sensitive volume covered by a case. Given homogeneous irradiation over the entire detector, the covered sensitive surface can be estimated by comparing the count of direct ionization events between two peaks, the primary one caused by the direct silicon hits, and the secondary one by the ions with degraded energy due to passage through the case.

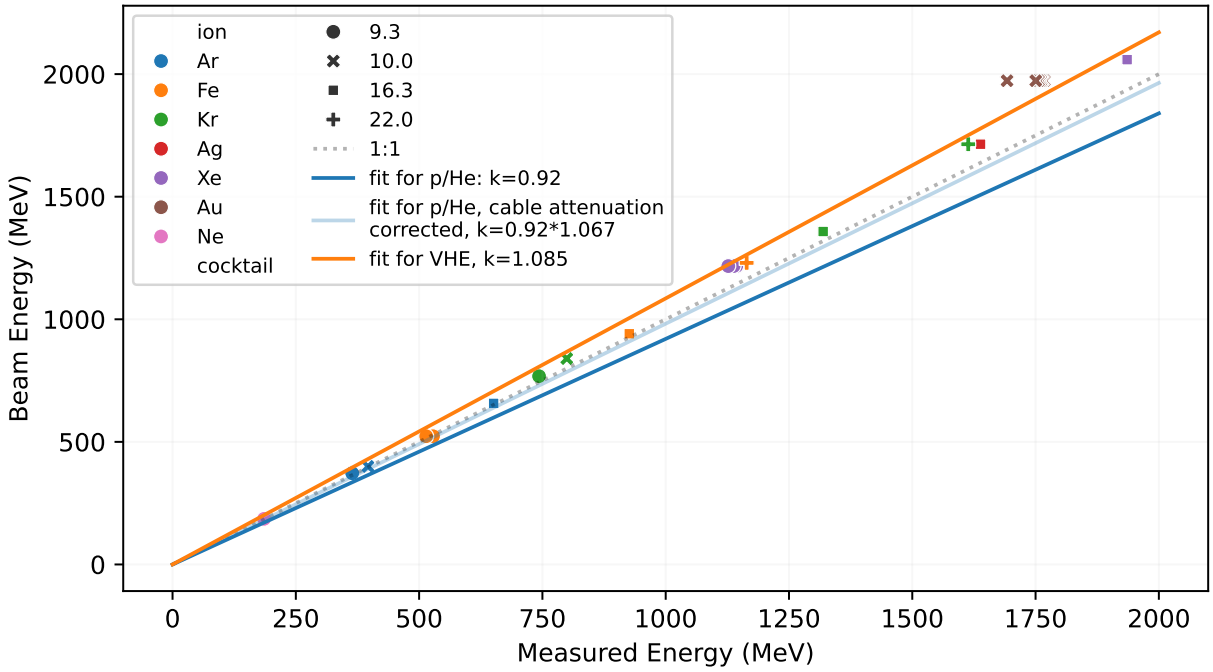

Figure 4.12: Beam energy as a function of measured energy (assuming $E_{eh} = 3.6\,\mathrm{eV}$).

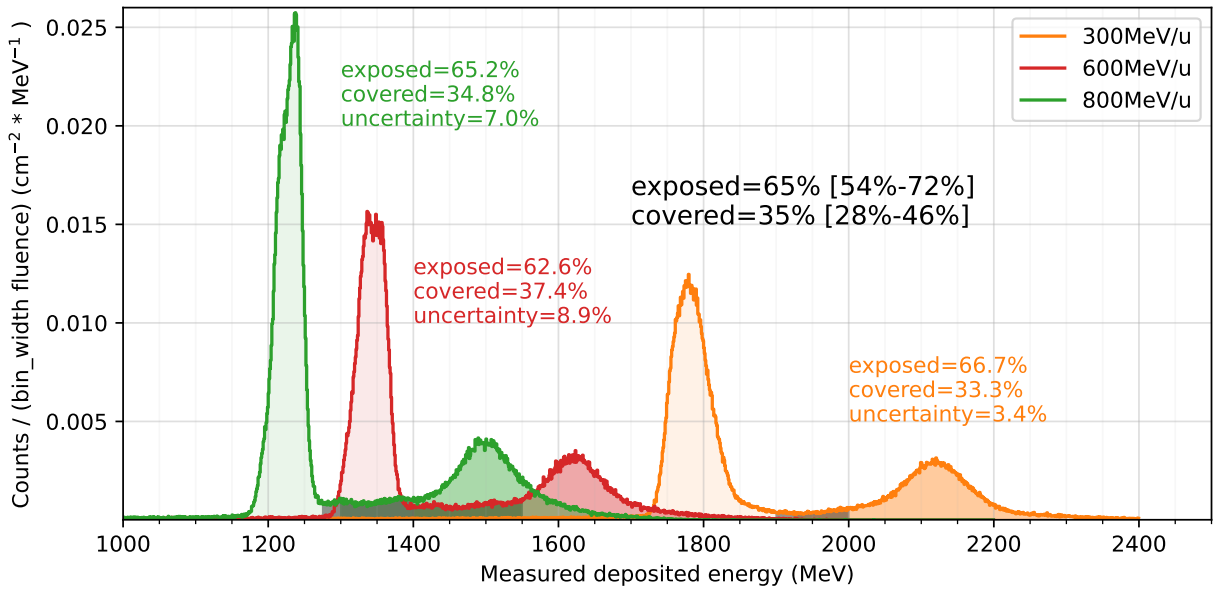

Figure 4.13: Energy deposition spectrum by ^{238}U ions. Based on the ratio of the number of events in the main and secondary peaks, the covered active surface was estimated ($s_{\mathrm{covered}} \approx 0.27\,\mathrm{cm}^2$).

$$s_{\mathrm{covered}} = \frac{n_{\mathrm{degraded}}}{n_{\mathrm{direct}}} s_{\mathrm{exposed}} \tag{4.1}$$

Profiting from the high-energy ^{238}U beam of 300 MeV/u, 600 MeV/u and 800 MeV/u, and the energy deposition spectrum depicted in Fig. 4.13, the uncovered surface (s_{exposed} =0.5 cm^2) is estimated to be a 65% of the total active surface, following Eq. (4.1). The total active surface is therefore estimated to be around 0.77 cm^2.

4.1.4.4 Dead-layer measurements

High-LET ion beams can be used to estimate the thickness of a dead layer in a detector (d), as the energy deposited in that layer (E_{dead}) is proportional to the ion's path length, that can be modified by a detector's tilt (θ), as given by linearity relation described in Eq. (4.2).

$$E_\theta \sim -d\rho LET\frac{1}{\cos\theta} \tag{4.2}$$

Fig. 4.14 depicts the deposited energy (assuming $k = 1$) as a function of tilt for ^{197}Au ion at 1973 MeV (LET at surface 85.6 MeV/(mg/cm^2), according to the facility). As expected, the detector's tilt led to a decrease in the direct ionization peak position. At 0°, the two peaks, previously mentioned, are visible. For calculation purposes, the one at lower energy was selected. The manufacturer specifies that the dead layer has a thickness below 50 nm. At 60°, the ion doubles its path length in the dead layer. Therefore, the position of the direct ionization peak is expected to shift about 1 MeV towards lower energy at 60° incidence angle, which could be barely detectable given the setup's energy resolution. Yet, for an unknown reason,

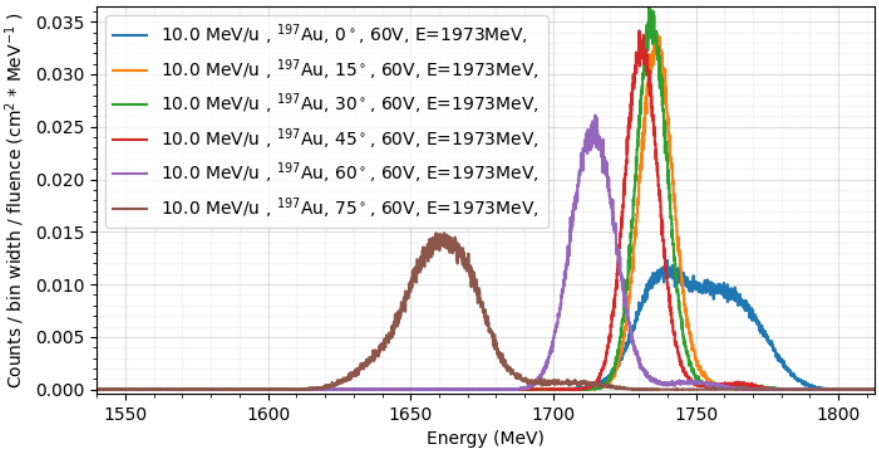

Figure 4.14: Measured energy deposition spectra in small detector for different tilts. For the calculations, the peak value is considered.

the direct ionization peak moved about 25 MeV as compared to normal and 60° incidence angle. One of the explanations could be the high-energy delta rays that escape the sensitive volume or the strong impact of the ion track path on the charge collection efficiency. However, no certain explanation has been found so far. Following Eq. (4.2), a linear regression was performed (Fig. 4.15), that would result in the unrealistic dead layer thickness of 1.36 um. The measured value significantly exceeds the value provided by the manufacturer

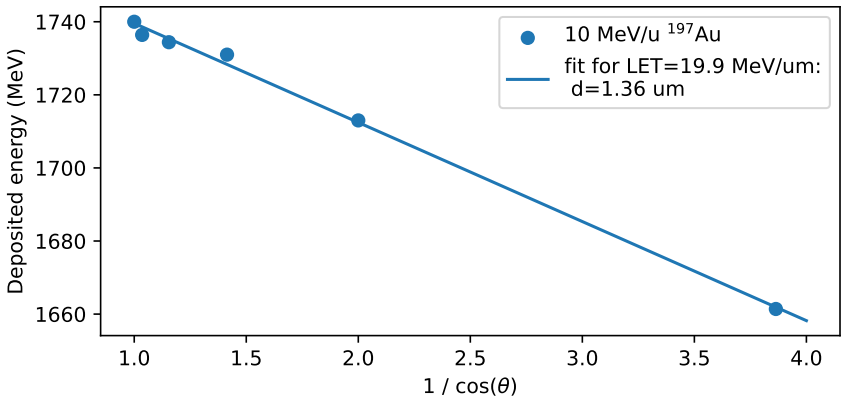

Figure 4.15: Measured deposited energy (direct ionization peak) in small detector as a function of detector's tilt.

(<50 nm). As the mechanism is unknown, and the detector showed unexplainable geometric dependencies, the dead-layer measurements are given for future benchmarks and unless confirmed, should not be trusted. Ideally, measurements should be performed with a charge-sensitive preamplifier (to increase energy resolution) and low-energy protons or ^{4}He, to reduce heavy-ion specific effects that might increase recombination.

4.1.5 Thermal neutrons

Thermal neutrons are a relevant ingredient of the high-energy accelerator mixed-field radiation environment [111]. This is particularly the case in the shielded accelerator areas, where they are a source of soft errors in electronic systems, leading to multiple accelerator issues [21]. The characterization of the thermal radiation component is therefore essential in the CERN accelerator environment, and within this subsection, the capabilities of the small detector in combination with a ^{6}Li converter, employed also for beam characterization in the CERN neutron Time Of Flight (nTOF) [112, 113], are presented.

The detection of thermal neutrons with pure silicon is not optimal, as the cross-section for a thermal neutron capture is low, 169 mb [114], and the energy deposited by the related gamma radiation might be below setup's detection limit. The capture cross-section would correspond to a single interacting thermal neutron per 5200 crossing a small silicon detector at normal incidence. The case of the diode detector contains multiple alloys (stainless steel, brass), and therefore acts as a thermal neutron capture booster. The enhanced event rate, is however not useful, as the very accurate detector model, and its composition, remain the company's confidential information.

To detect thermal neutrons in a controlled manner, the most straightforward approach is to use materials with high thermal-neutron interaction cross-section, such as ^{157}Gd, ^{3}He, ^{10}B, ^{113}Cd or ^{6}Li. Particularly materials that emit light ions are of interest. The ions interact via direct ionization, leading to a peak in the energy deposition distribution (assuming small energy straggling in air and location of the entire Bragg peak within a silicon volume), as opposed to a spectrum from γ/β radiation. Therefore, the candidates for the converter materials are ^{10}B (σ_{th} ≈3800 b, reactions: Eq. (4.1.4) and Eq. (4.1.5)) and ^{6}Li (σ_{th} ≈940 b, reaction Eq. (4.1.3)).

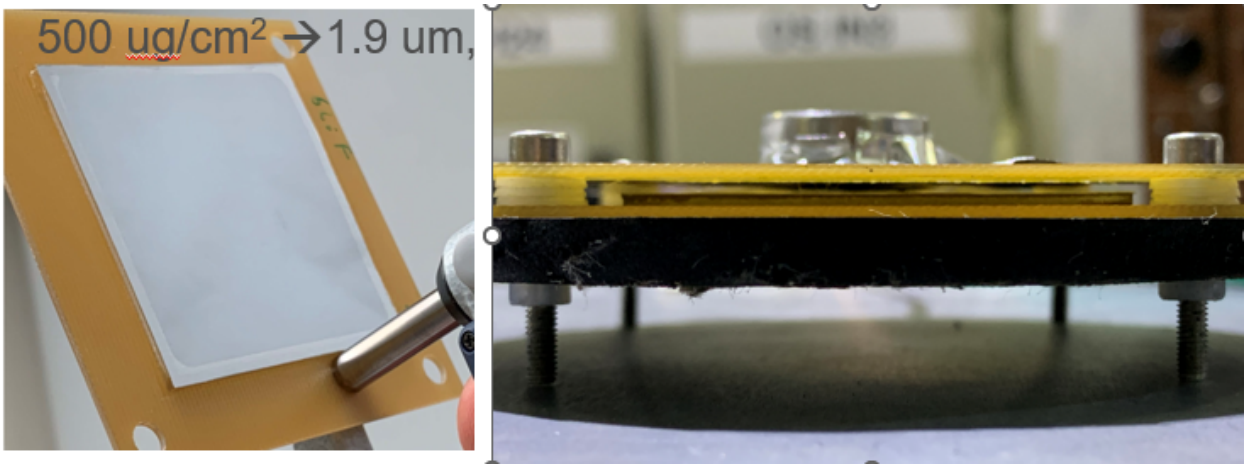

Figure 4.16: ^{6}Li thermal neutron converter with the silicon diode.

Whereas the first one has a 4-times higher reaction cross-section, the resulting ^{4}He/^{7}Li have a short range in air, making it difficult to work with the presented silicon detector setup. ^{6}Li produced in reaction Eq. (4.1.3), however, in addition to alpha particle, emits a ^{3}H, that has a relatively long range in air. Within this work,

a ^{6}Li converter [112, 113] is used to enhance the smallś detector sensitivity.

$$\mathrm{n} + {}^{6}\mathrm{Li} \longrightarrow {}^{3}\mathrm{H}\,(2.73\,\mathrm{MeV}) + {}^{4}\mathrm{He}\,(2.05\,\mathrm{MeV}) \tag{4.1.3}$$

$$\mathrm{n} + {}^{10}\mathrm{B} \longrightarrow {}^{7}\mathrm{Li}\,(1.0\,\mathrm{MeV}) + {}^{4}\mathrm{He}\,(1.78\,\mathrm{MeV}) \tag{4.1.4}$$

$$\mathrm{n} + {}^{10}\mathrm{B} \longrightarrow \gamma\,(0.48\,\mathrm{MeV}) + {}^{4}\mathrm{He}\,(1.47\,\mathrm{MeV}) + {}^{7}\mathrm{Li}\,(0.84\,\mathrm{MeV}) \tag{4.1.5}$$

(a) collimator **(b)** zoom for the aperture

Figure 4.17: A small ^{10}B-rubber collimator with an aperture of approximately 1.6 mm diameter. As illustrated, due to the material property and drilling process the aperture size is a significant source of uncertainty.

A proof of concept for thermal neutron detection was performed at the PF1B instrument (Polarised cold neutron beam facility), at the Institute Laue-Langevin (ILL). The interaction cross section for cold neutrons is higher than for thermal neutrons, as it scales with the inverted velocity. A foil with lithium fluoride (95% enriched ^{6}Li) (surface density of 500 µg/cm^2, resulting in a layer thickness of 1.9 µm) was installed in front of the small detector. To reduce the activation and event rate, a ^{10}B-rubber collimator was used. The setup is depicted in Fig. 4.16. Given the suppleness of rubber, the aperture of the collimator (diameter of 1.6 mm), depicted in Fig. 4.17, was an important source of uncertainty.

The measured energy deposition spectrum is depicted in Fig. 4.18. For benchmark purposes, FLUKA Monte Carlo simulations were performed, with the primary beam consisting of a mono-energetic thermal-neutron beam. The simulation geometry is illustrated in Fig. 4.19. The larger width of the measured ^{3}H peak might be due to the impact of the gamma rays, produced in ^{10}B collimator, as each of the energy deposition events by ^{6}Li/^{4}He is accompanied by the energy depositions by low energy gamma rays, that standalone would be below to the detection limit. In the simulation, due to its sequential nature, both ^{3}H and γ energy deposition events cannot happen simultaneously.

The rate of events with a converter was significantly higher than without it. While aligning the number of measured and simulated events for a tritium peak (2 MeV to 3 MeV), the measured flux would be equal to ϕ_{THNeq}=4.8 × 10^{8} n/cm^2/s. This is consistent with the analytical flux calculation presented in Appendix B,

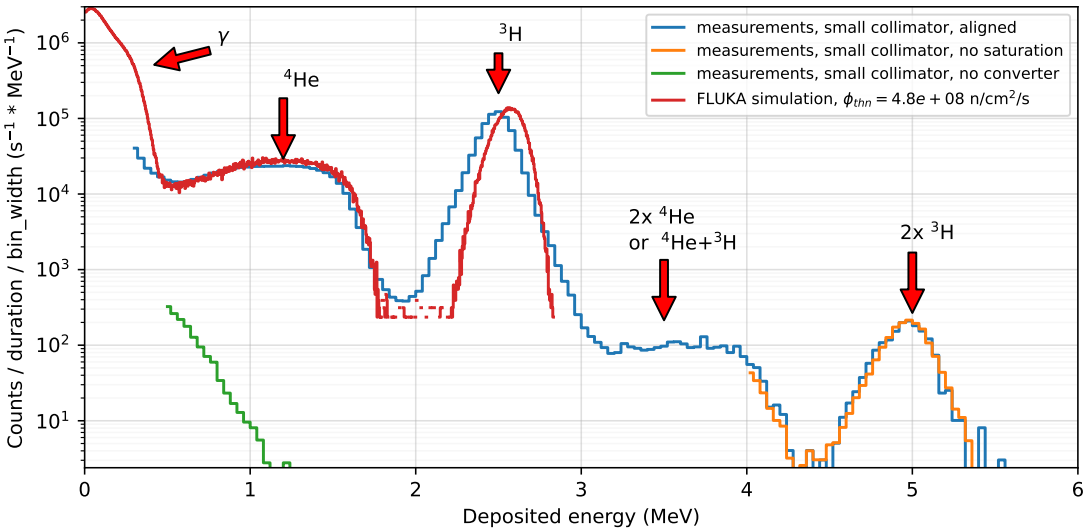

Figure 4.18: Simulated and measured energy deposition spectra for neutron irradiation with ^{6}Li converter, together with a reference measurement.

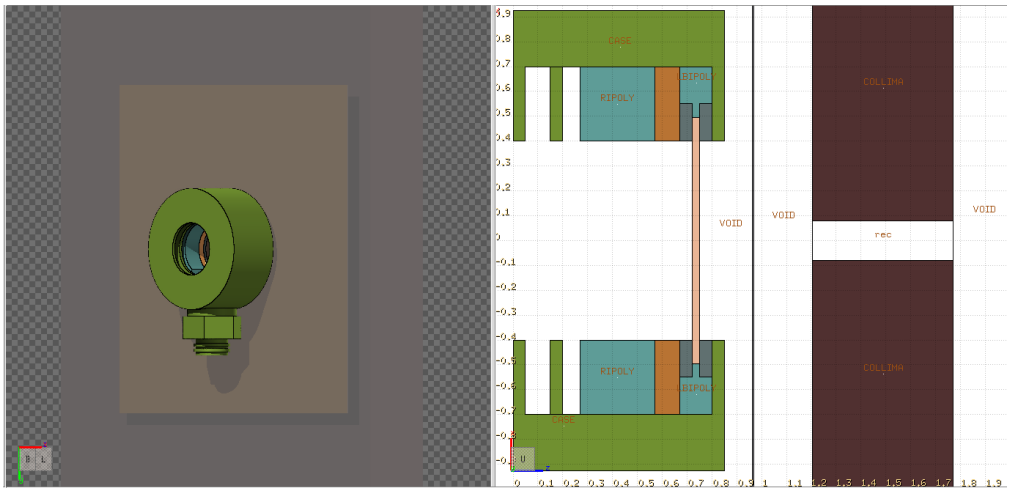

Figure 4.19: FLUKA model of the silicon detector with the ^{6}Li converter and ^{10}B collimator.

which can be exploited to retrieve the flux value without performing Monte Carlo simulations. Usually, the flux is assessed with an activation of Au foil. Such measurements for the performed runs are not available. Although the large diode is significantly more sensitive, the detection of the thermal neutrons (via ^{6}Li converter) with the current setup would be challenging due to the poor setup energy resolution, making it harder to identify ^{3}H peak on top of the mixed-field spectrum. The second constraint is the setup detection limit, which could prevent peak detection in noisy environments. These potential limitations, however, would need to be confirmed via experimental measurements, and if applicable, mitigated e.g. through the use of a charge-sensitive preamplifier, that could increase the setup's energy resolution.

4.2 Beam characterization

4.2.1 Flux monitoring

One of the main characteristics of particle beams is particle flux. Accurate measurements are usually the responsibility of a hosting facility. However, during radiation testing, it is a good practice to perform basic beam cross-checks. In beams consisting of charged particles, one of the approaches is to use a silicon diode and retrieve a number of relevant counts, induced only by the primary beam particles, per time. Knowing the active surface of the detector, the number of events can be converted to the flux, hence delivering fluence.

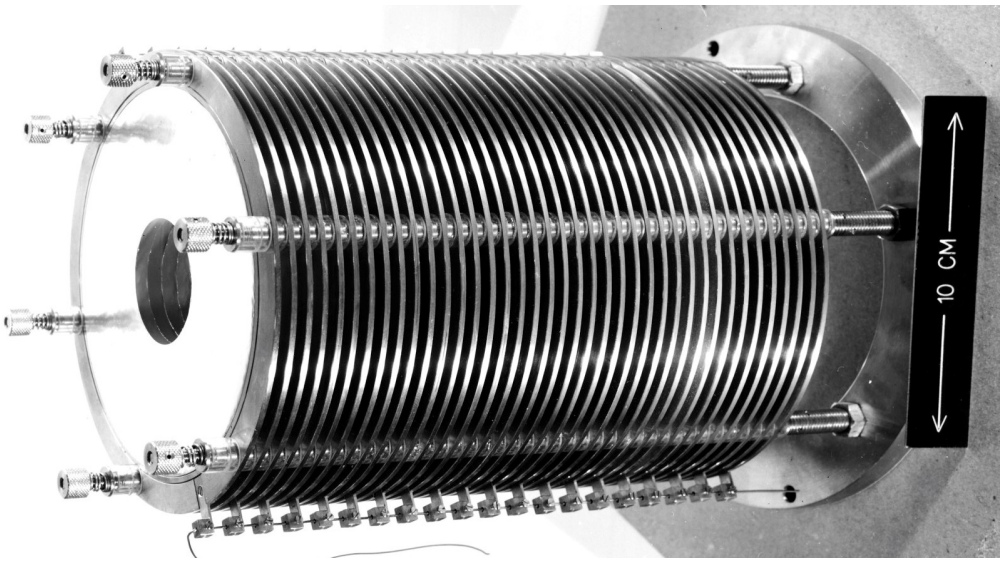

Figure 4.20: An example of an inner part of a Secondary Emission Chamber (SEC) consisting of several aluminum plates. Image credit: CERN.

Within this work, it is demonstrated how the small diode detector was exploited for flux measurements of the CHIMERA-HEARTS beamline, in particular for absolute calibration of the SEC [115], providing only relative intensity measurements. It is an instrument permanently installed in the beamline, consisting of several aluminum plates, as illustrated in Fig. 4.20. A charged beam impacting the plates leads to the production of secondary electrons that are collected thanks to the applied high voltage. The measured current is proportional to the passing beam intensity. However, for the heavy-ion beams the analytical conversion was not derived, therefore the instrument response (divided by the signal gain) was compared with the response of small detector (II), installed at the beam center, 30 m downstream of the SEC device (CERN code: XSEC70). Whereas the procedure was repeated for all the beam energies due to energy-dependent attenuation in air and the energy-dependent response of SEC, in this section the focus is on demonstrating the principle for 1 GeV/u extracted beam. The corresponding simulated value at the small detector is about 605 MeV/u [30].

There are some limitations to the following approach. As described in Chapter 4.1.4, the detector has a

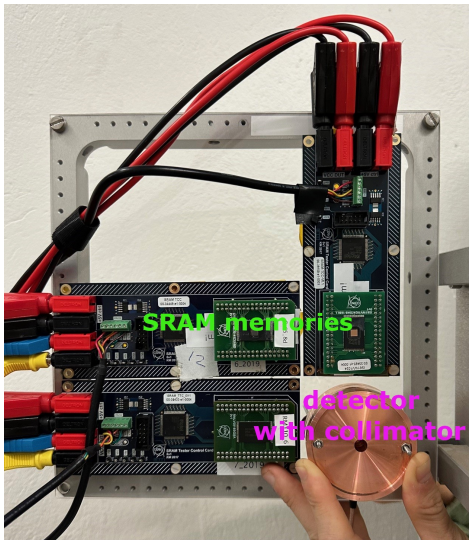

(a) small detector (II) with 3 stacked copper collimators, each one of 1 cm thickness and 7 mm aperture (diameter)

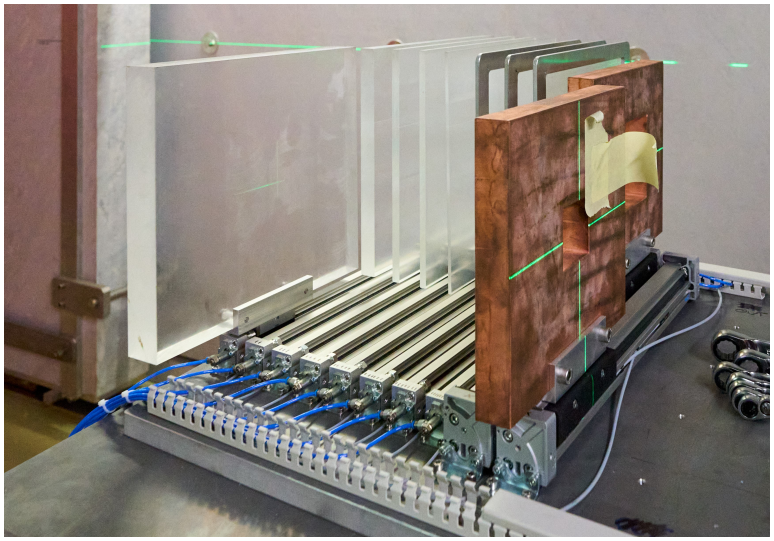

(b) table with PMMA degraders (thicknesses: 40 mm, 20 mm, 10 mm, 8 mm, 4 mm, 2 mm, 1 mm and 0.5 mm) and copper collimators ($10x10\,cm^2$ and $5x5\,cm^2$), Image credit: CERN.

Figure 4.21: Experimental setup during the CHIMERA-HEARTS SEC flux cross-calibration.

partially shielded active silicon area. Depending on the beam properties, the particles might be stopped or punch-through the case, leading to a different effective active silicon surface. Often, this limitation can be mitigated via the analysis of an energy deposition spectrum, as the different material budget, due to case penetration, implies different deposited energy. In the HEARTS 2023 operation, this was mitigated by three identical copper collimators, each 1 cm-thick, of 28 cm^2-circular surface, and 0.385 cm^2 aperture, installed on top of the detector. For the considered beam energy that provided enough material budget to range out the ions before reaching the detector. The second limitation is related to the event acquisition rate of the digitizer, about 30 kHz for 500 ns events, due to the bandwidth of the USB 2.0 link between the digitizer and PC. With dedicated firmware settings, the limitation can be mitigated as the number of trigger events is stored in the data, providing information about how many events were lost due to buffer saturation. An example of the procedure is illustrated in Fig. 4.22. The third limitation is related to the validation of the calibration only for particular settings of beamline magnets due to the impact on the beam spatial profile. The SEC measures the total beam intensity, however, the small detector probes the intensity in a given spot (beam center) of space. Therefore, once the beam spatial profile gets modified, the calibration will not be valid. This limitation could be mitigated using another device measuring spatial beam profile, however, that is beyond this work.

Due to the presence of fragments, not all the transients measured by the detector are caused by the primary beam. Therefore, only events close to the direct ionization peak are considered for calibration, as depicted in Fig. 4.23a. Nonelastic energy deposition events between the primary beam and silicon are highly unlikely, therefore it is assumed that events outside the direct ionization peaks are fragments which are excluded from the calculation. Moreover, the pile-up is neglected, as the contribution is negligible (few %, as depicted in Fig. 4.23a). Given the highly colinear relationship between the small diode and the SEC, illustrated in

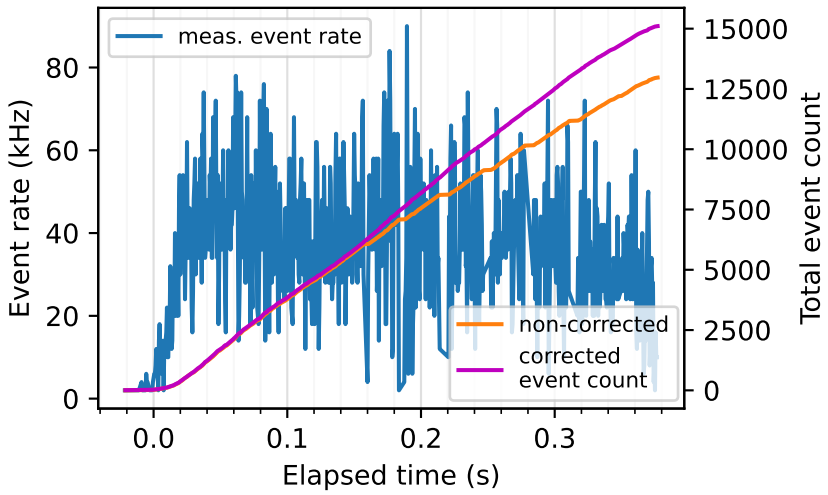

Figure 4.22: An example of a spill recorded with the digitizer through the event count rate (1 ms binning), together with the raw total event count, and event count that was corrected to compensate for the buffer saturation.

Fig. 4.23b, the dominant source of uncertainty is associated to the classification between events caused by a primary beam (with a requested LET) and the rest, i.e. fragments and degraded beam. For 1 GeV/u (extracted) beam, this error is within 20% (worst case scenario). However, the uncertainty increases with the reduction of beam energy due to beam straggling and further fragmentation.

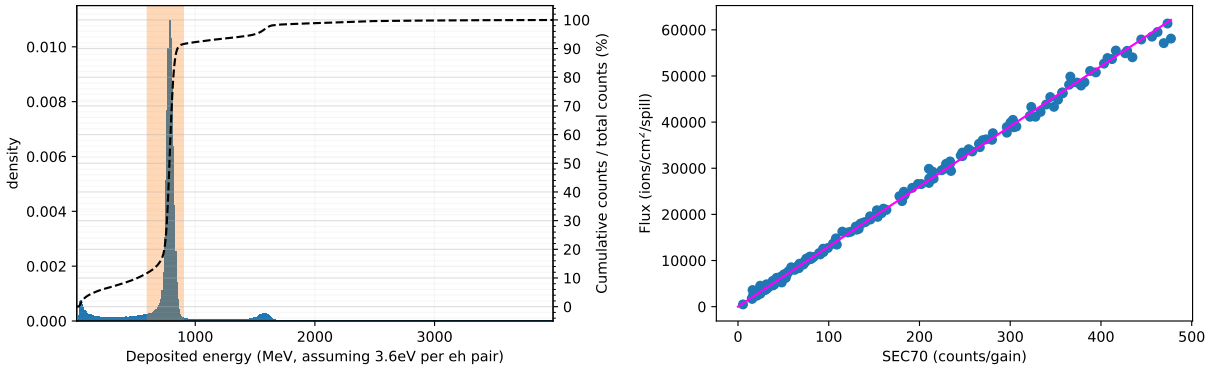

(a) energy deposition spectrum **(b)** measured flux vs SEC response

Figure 4.23: Calibration of the SEC instrument for 1 GeV/u (extracted) beam to the flux measured by a small detector (II), within CHIMERA-HEARTS activity. Only events in the highlighted energy deposition region were included to exclude fragments present in the beam. Pile-up events were neglected for simplicity reasons (introduced error of few %).

Electronics testing usually requires beams with LET values higher than 13 MeV/(mg/cm^2), as provided by the 1 GeV/u (extracted) beam. The increase (exceeding 40 MeV/(mg/cm^2)) can be achieved by the beam degradation through the PMMA slabs. The degrader system is illustrated in Fig. 4.21b. Together with the

LET increase, the use of degraders induces further beam fragmentation, as depicted in Fig. 4.24, therefore for each of the configurations, a flux calibration procedure was performed. The measured ratio between the intensity of primary ions at the exit and the entry of the degrader system is illustrated in Fig. 4.25. With the increasing thickness, there is more probability for ions to undergo nonelastic processes (fragmentation), therefore the intensity of primary ions decreases. The transmission measurements, especially those for thicker configuration, hence higher LET, are affected by uncertainty related to the classification of events.

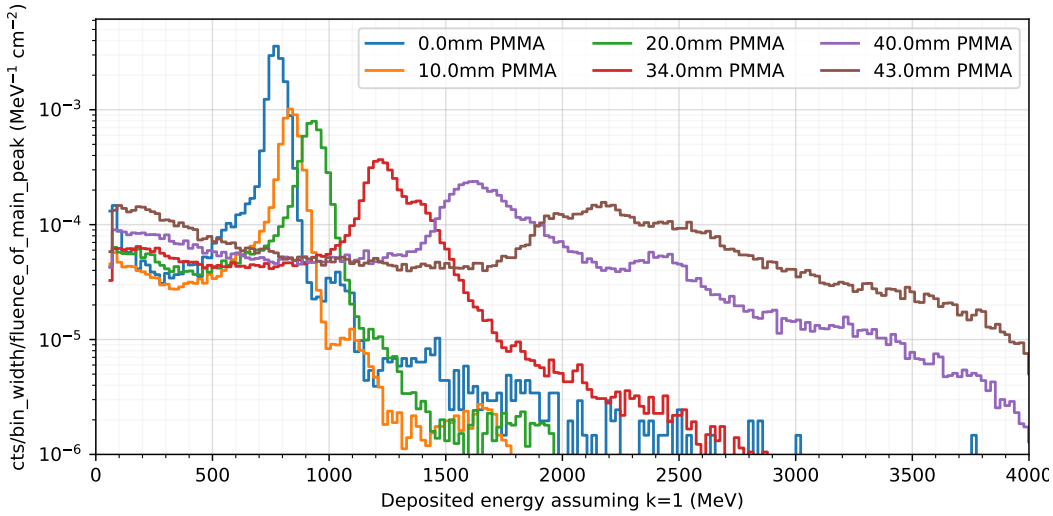

Figure 4.24: Measured energy deposition spectra for 1 GeV/u (extracted energy, about 605 MeV/u at the degrader) beam for selected PMMA degrader thicknesses. With the increasing thickness, the LET of the beam increases, leading to higher deposited energy through direct ionization (main peak shifts towards higher energies). This, however, leads to further beam straggling and induces additional beam fragmentation (i.e. direct ionization peak is less prominent).

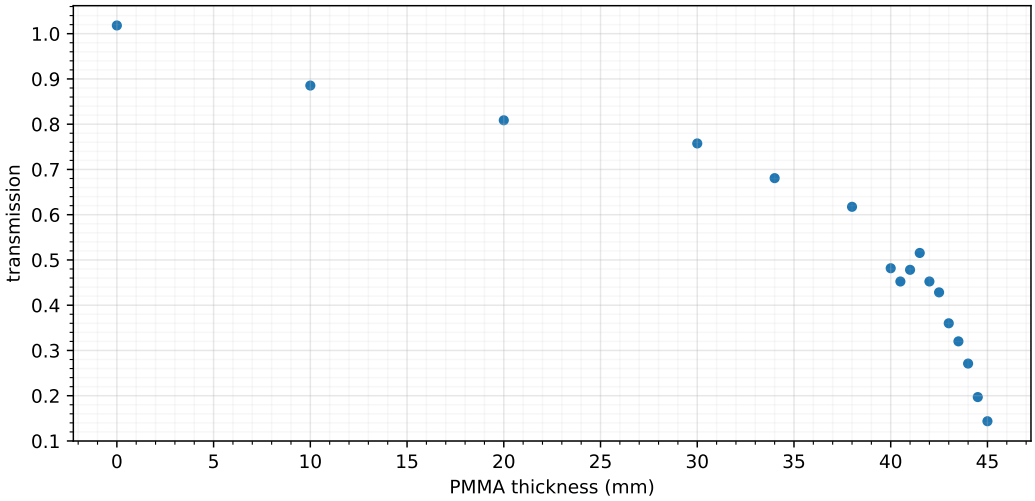

Figure 4.25: Transmission (survival) of 1 GeV/u (extracted energy, about 605 MeV/u at the degrader) beam as a function of the PMMA degrader thickness.

4.2.2 Dose/Dose-rate measurements

Profiting from the dose rate calibration, through the leakage current measurements, the setup can be exploited for a beam characterization, in terms of absolute delivered dose and its time variability.

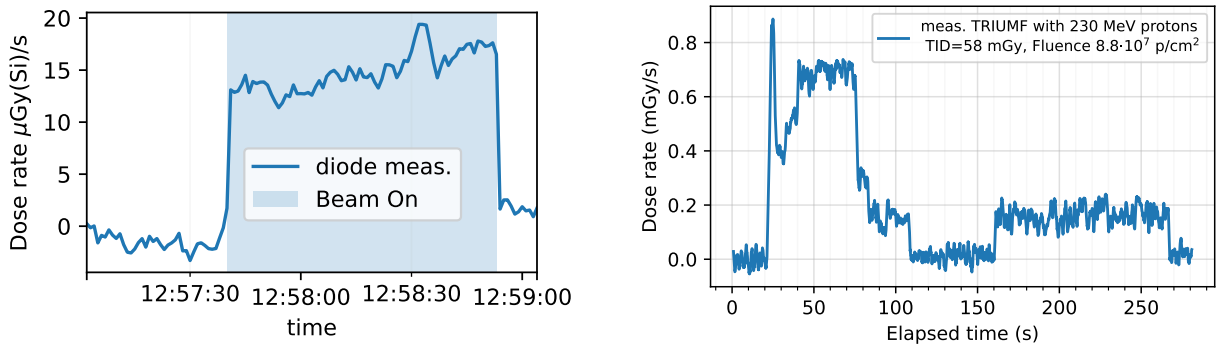

(a) large diode + neutrons

(b) small diode + protons

Figure 4.26: Measured dose rate during neutron irradiation at BL1B, TRIUMF, with atmospheric-like spectrum. The mean neutron flux (>10 MeV) during the run was 2.2×10^5 n/cm^2/s.

Fig. 4.26b depicts the dose rate during 230 MeV-proton irradiation at TRIUMF-PIF. Over the irradiation with the total fluence of 8.8×10^7 cm^{-2}, the measured dose was 58.0 mGy. Assuming the LET of the beam is equal to 3.37 MeVcm^2/g [116], the expected dose is 47.4 mGy, within 19% agreement with the measurement.

According to the FLUKA Monte Carlo simulations for 230 MeV protons, the case could lead up to 3.4% higher dose as compared with uncovered silicon volume. The higher measured value could arise from the uncertainty of the current - dose rate coefficient, as explained in Chapter 4.1.2.

In general, the aforementioned calibration is a good approximation for particles that are capable of penetrating the diode case without significant energy loss. The estimated uncertainty for such mixed fields is within 41%, arising from the difference in the exposed/covered silicon volumes and electron equilibrium during calibration. In the mixed field where there is a significant presence of thermal neutrons, the case would act as a converter and the related deposited dose would be significantly larger as compared with pure silicon.

4.2.3 Spatial beam characterization

The diode can be also used to assess the spatial properties of the beam if no better instruments are available. This technique is, however, rather inefficient, as it requires multiple flux measurements in the different positions with respect to the beam's center.

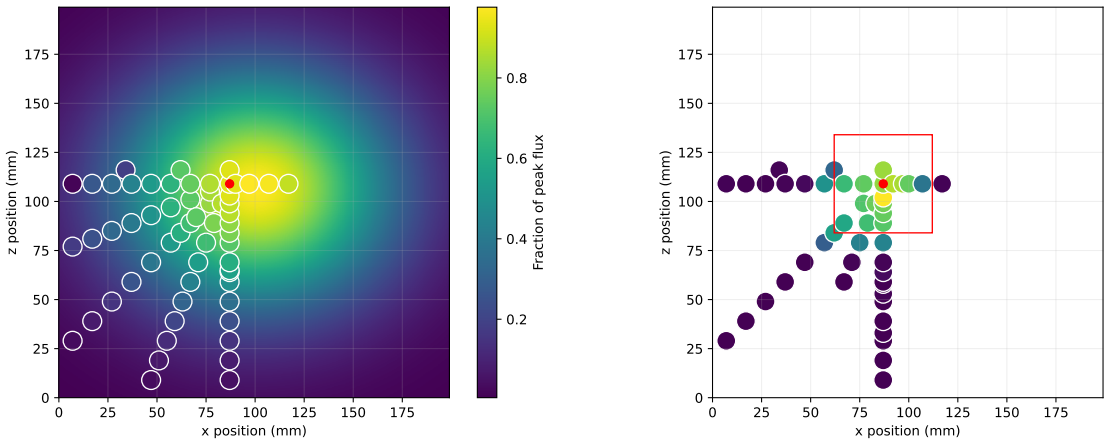

(a) no collimation **(b)** collimation

Figure 4.27: Spatial beam profile measurements with small diode (points), together with a standard bivariate normal fit ($x_0 = 101\,\text{mm}$, $z_0 = 106\,\text{mm}$, $\sigma_x = 69\,\text{mm}$, $\sigma_z = 60\,\text{mm}$) in the non-collimated case. The red point $(x, z) = (87\,\text{mm}, 109\,\text{mm})$ corresponds to the assumed beam center $(x', z') = (0, 0)$, as given by the alignment, before the measurements. The red rectangle would be a collimator's aperture assuming ideal alignment.

A proof-of-concept has been performed during CHIMERA-HEARTS [30] operation in 2023, with a PS extraction energy of 650 MeV/u. It relies on a remotely movable table that swipes the diode in a plane perpendicular to a beam and builds a 2-dimensional map of the total registered events. It was assumed that during multiple spills the intensity-normalized beam spatial profile was preserved and the only difference could be the absolute number of ions delivered to the testing position, i.e. intensity. This is a fair assumption, as the spatial beam profile is primarily driven by the focusing strength of the quadrupole magnets, which was kept constant during the scanning. Fig. 4.27, in the form of a 2-dimensional histogram, illustrates the relative beam intensity in one-quarter of the space, for runs i) without further collimation (Fig. 4.27a), and ii) with $5x5\,\text{cm}^2$ mask (Fig. 4.27b), illustrated in Fig. 4.21b. Following the fit from the first case, it was 14 mm off-center horizontally. The beam shape was $\sigma_z = 60\,\text{mm}$ vertically and $\sigma_x = 69\,\text{mm}$ mm horizontally. This approach, however, might yield results with a non-negligible uncertainty, as the spatial symmetry assumption is not valid. The following procedure could be improved by extending the scan to the full (x,z) phase space for both collimated and non-collimated cases. Eq. (4.2.1) describes the reconstructed spatial intensity beam profile with reference to the maximum measured value ($\phi_{\text{meas.max}}$). The coordinates (x,z) describe the position of the detector on a movable table, with $(x_0, z_0) = (87\,\text{mm}, 109\,\text{mm})$ being the beam center if the alignment was errorless, whereas (x', z') coordinates have origin $(x', z') = (0, 0)$ at the alleged beam center $(x_0, z_0) = (87\,\text{mm}, 109\,\text{mm})$. It is assumed that there is no correlation between x and z

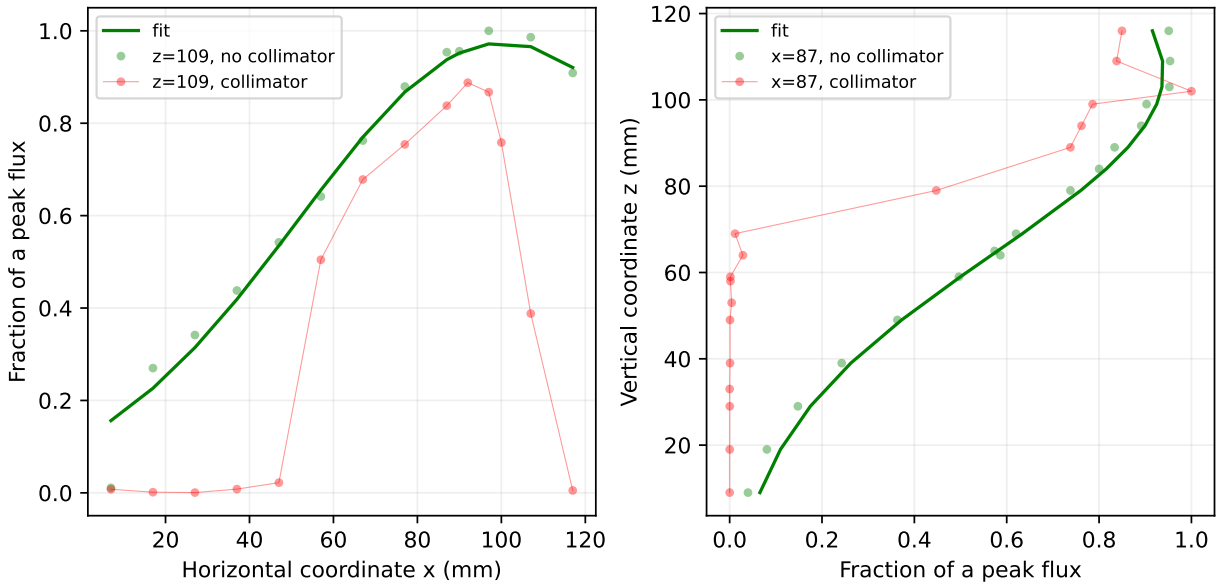

Figure 4.28: Horizontal and vertical beam profiles for HEARTS 650 MeV/u (extracted, corresponding to around 140 MeV/u at the detector position [30]) beam as measured with small detector, together with a bivariate normal fit, as given by Eq. (4.2.1).

variables ($\rho \to 0$).

$$
\begin{aligned}
\phi_{650\,\mathrm{MeV}}(x,z) &= \frac{c}{2\pi\sigma_x\sigma_z\sqrt{1-\rho^2}} \\
&\quad \exp\left\{-\frac{1}{2(1-\rho^2)}\left[\left(\frac{x-\mu_x}{\sigma_x}\right)^2+\left(\frac{z-\mu_z}{\sigma_z}\right)^2-2\rho\frac{(x-\mu_x)(z-\mu_z)}{\sigma_x\sigma_z}\right]\right\} \\
&\overset{\rho\to 0}{=} \phi_{\max}\cdot\exp\left\{-\frac{1}{2}\left[\left(\frac{x-\mu_x}{\sigma_x}\right)^2+\left(\frac{z-\mu_z}{\sigma_z}\right)^2\right]\right\} \\
&\approx 0.976\cdot\phi_{\mathrm{meas.max}}\cdot\exp\left\{-\frac{1}{2}\left[\left(\frac{x-101\,\mathrm{mm}}{69\,\mathrm{mm}}\right)^2+\left(\frac{z-106\,\mathrm{mm}}{60\,\mathrm{mm}}\right)^2\right]\right\} \\
&\approx 0.976\cdot\phi_{\mathrm{meas.max}}\cdot\exp\left\{-\frac{1}{2}\left[\left(\frac{x'-14\,\mathrm{mm}}{69\,\mathrm{mm}}\right)^2+\left(\frac{z'+3\,\mathrm{mm}}{60\,\mathrm{mm}}\right)^2\right]\right\}
\end{aligned}
\tag{4.2.1}
$$

Whereas not the most time-efficient, this subsection proves how small detector was (and can be) exploited to provide insights about spatial beam properties. One of the advantages is event-by-event energy deposition information, providing not only spatial information but also energy deposition spectrum, enabling to investigate which regions start to be dominated by fragments.

4.2.4 Spectral beam characterization

During data acquisition with the setup, the entire frames are saved to the file. There is no data reduction, such as on-fly integration. This feature can be exploited for Pulse Shape Discrimination (PSD) [53, 117], for example in terms of amplitude, fall time, or even comparisons of entire pulse shapes. The differences in pulse shapes arise from differences in the energy deposition, e.g. depth in silicon or LET of the ionizing particle, resulting in different measured charge collections (current) [118, 119]. Therefore, the differences can be exploited to discriminate events caused by particles varying in terms of the kinetic energy or the species. However, in most of the cases, the differences are not observable due to the finite setup resolution. PSD is particularly relevant for beam purity characterization, e.g. in cyclotron facilities, where multiple ions are accelerated within the same cocktail and there is a chance of extracting more than one ion species in case of slightly incorrect settings.

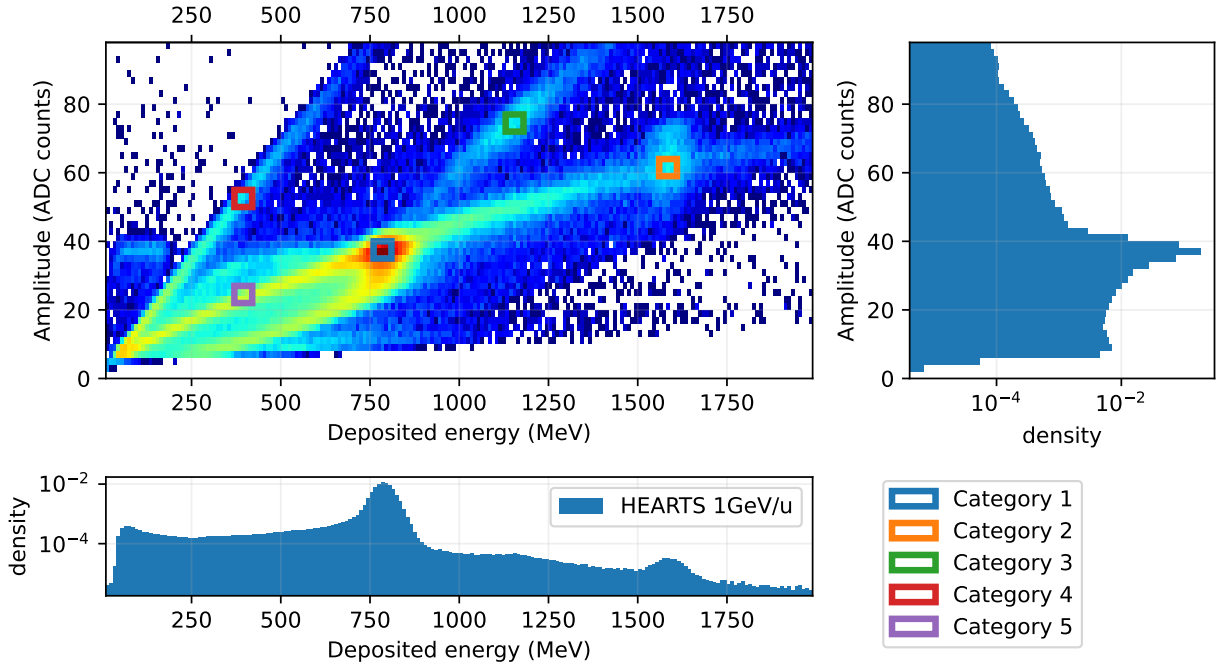

Figure 4.29: Heatmap representation of transients' amplitude as a function of the measured deposited energy for CHIMERA-HEARTS 1 GeV/u (extracted) beam. Clear pile-up events (22.6% of events), i.e. transients with at least 2 peaks, were excluded. Five categories, regions of higher local densities, were selected for further consideration. The color is proportional to the logarithm of the number of counts in each heatmap bin.

As an example of the PSD application, illustrated in Fig. 4.29, is the discrimination of the events caused by a nominal 1 GeV/u (extracted) beam from the events induced by fragments or degraded beam. This, as explained in Chapter 4.2.1, is important to provide accurate intensity calibration of the SEC instrument with the aforementioned CHIMERA-HEARTS activity. Fig. 4.29 depicts amplitudes of the measured transients as a function of the related deposited energies (proportional to transients' integrals), with five categories of

events (arbitrary selection based on the local clusters). The averaged pulse transients corresponding to the categories are illustrated in Fig. 4.30.

- Category 1 - energy depositions by a primary beam through the direct ionization
- Category 2 - pile-up with two ions depositing energy with a time difference of a few nanoseconds that cannot be distinguished based on the multiple peaks
- Category 3 - unknown origin
- Category 4 - (probably) light fragments produced in the beamline or within copper collimators
- Category 5 - (probably) nuclear reactions induced in silicon by the primary beam or fragments

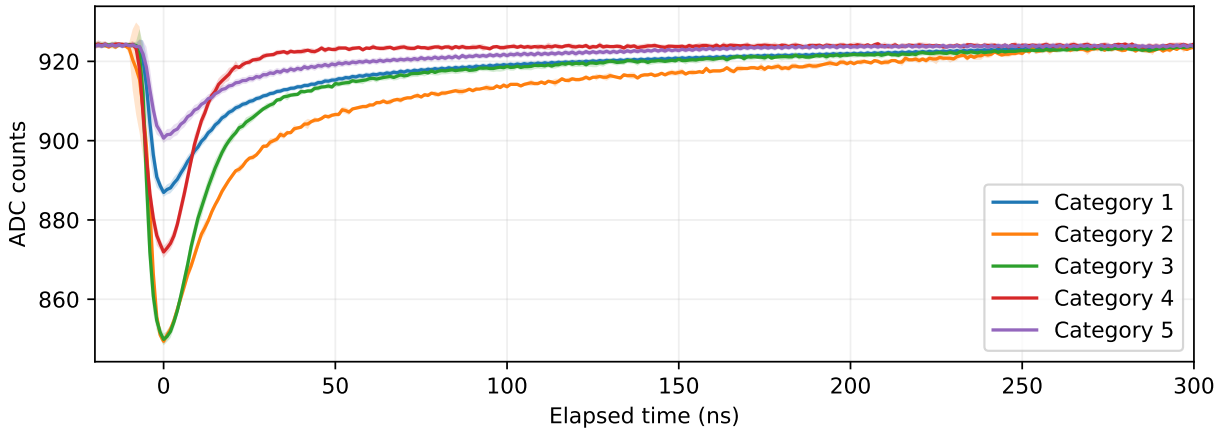

Figure 4.30: Averaged measured transients corresponding to the five regions (categories) highlighted in Fig. 4.29.

For the SEC cross-calibration, only Category 1 and Category 2 (extended to all pile-ups) should be considered. Category 5 can be neglected, as usually nuclear reactions by heavy ions are significantly less probable than the energy deposition by direct ionization, and therefore the error is negligible.

4.3 Radiation field characterization with silicon diodes

4.3.1 Atmospheric-like spectral neutron fields

The targeted working environment, such as LHC-shielded alcoves, is neutron-dominated. To demonstrate the detection capabilities in the several neutron fields, the tests were performed at: the Am-Be source (11.8 TBq in August 2014 [120]), located in CALibration LABoratory (CALLAB) at CERN [121]; at a CERN surface building under the exposure to atmospheric radiation; at the spallation neutron facility TRIUMF-BL1B [122–125]; and at the CERN accelerator environment, close to the Linear Accelerator 3 (LINAC3) [126]. The simulated energy spectra for these fields are depicted in Fig. 4.31 [127–129].

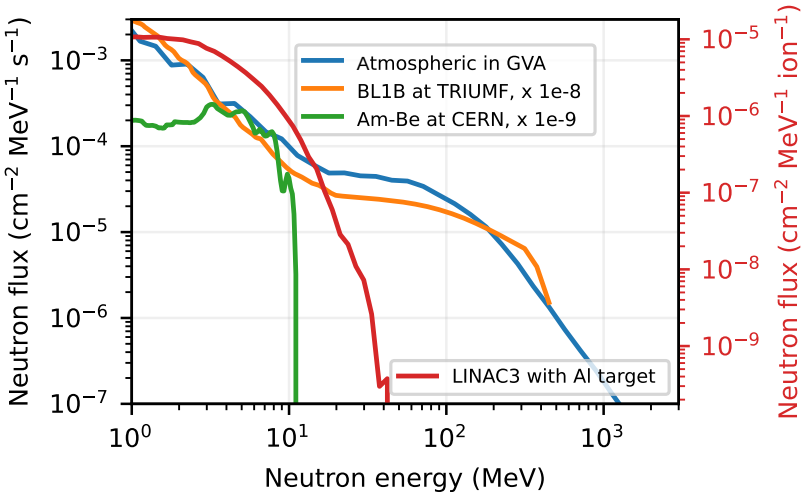

Figure 4.31: Simulated neutron flux spectra for i) atmospheric field extracted from MAIRE tool [127, 129] for Geneva coordinates, ii) spallation neutron field at TRIUMF (BL1B), iii) AmBe source at CERN [121], iv) 4.2 MeV/u $^{16}O^{8+}$ions impacting Al-target at LINAC3 (CERN).

The detector has been acquiring data for 55 days in an indoor location at CERN, at the ground level, as depicted in Fig. 4.32. The building has two floors and the experiment took place on the top one. The surface of the detector was covered with aluminum foils to shield the detector from visible light.

The measured energy deposition spectrum is depicted in Fig. 4.34. Over that period, 1035 energy deposition events above 10 MeV were recorded. The measurement was benchmarked against FLUKA Monte Carlo simulations, which contained a detailed detector geometry (Fig. 3.14a) and neutron beam with the energy spectrum retrieved through the MAIRE toolkit, accounting for the local latitude, longitude, and altitude [129]. The simulation, however, did not account for the energy resolution of the considered detector, therefore the simulated energy deposition spectrum was convoluted (blurring) with a Gaussian profile whose variance was approximately equal to the variance measured for a monoenergetic beam. The obtained agreement between both curves is very good, within 25% while considering the measured vs. simulated (further convoluted) event rate above 10 MeV of deposited energy, as listed in Tab. 4.2.

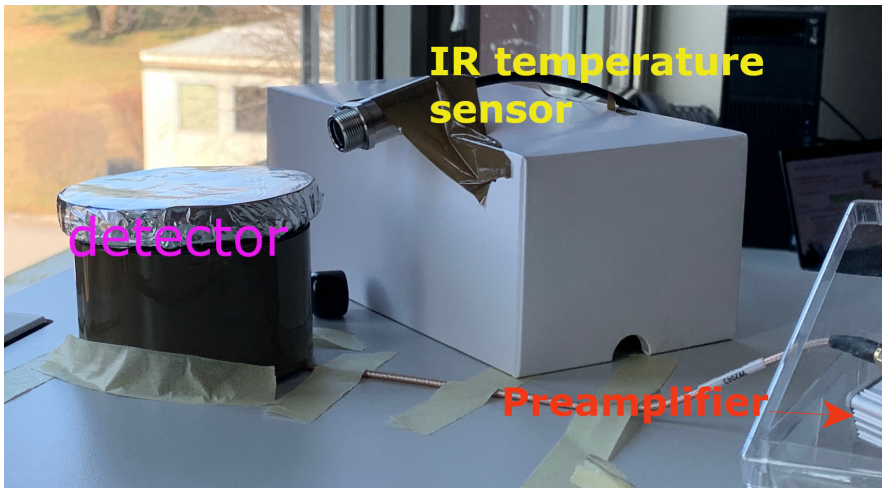

Figure 4.32: Experimental setup during the acquisition with the cosmic-induced radiation. Temperature measurements by the IR sensor are beyond the scope of this work.

Table 4.2: Statistics of registered counts under the exposure to i) ground-level radiation (Atm. GVA), ii) TRIUMF-BL1B spallation neutrons, together with a normalized event count and FLUKA Monte Carlo simulations for ground-level neutron spectrum. Flux in TRIUMF-BL1B was reduced from the maximum available to avoid pile-ups. The normalized event count considers the number of events above 10 MeV of deposited energy (E_d) divided by the fluence of neutrons above kinetic energy (E_{kin}) of 10 MeV (simulated in the case of atmospheric experiments and measured in case the TRIUMF one).

	Counts $E_d > 4$MeV	Counts $E_d > 10$MeV	Count rate $E_d > 10$MeV	Fluence $E_{kin} > 10$MeV	**Normalised event count $\mathbf{E_d > 10}$ MeV**
Atm. Geneva	0.17	1.0	2.2×10^{-4}	3.0	**3.4**
TRIUMF-BL1B	25	490	2.0×10^{3}	1400	**3.5**
Atm. sim.	2.3	91	N/A	350	**2.6**
Atm. sim. convoluted	380	95	N/A	350	**2.7**
unit	10^5 counts	10^3 counts	counts/s	10^4 cm^{-2}	**counts/cm^{-2}**

Additionally, simplified simulations of the atmospheric-neutron spectrum impacting the diode silicon volume were performed using the Geant4-based toolkit, G4SEE [51]. As opposed to FLUKA simulations, the G4SEE ones did not include the diode case due to current toolkit limitations. Profiting from a detailed scoring we investigated which neutrons (kinetic energy) contribute to the deposited energy spectrum. Considering the region above the detection limit of the setup, energy deposition events above ∼12 MeV are driven primarily by neutrons with kinetic energies between 10-100 MeV.

Profiting from beamtime provided via RADNEXT [57], irradiations of the large detector at TRIUMF-BL1B were performed. The neutron beam is obtained via the 480 MeV proton beam impacting on a lead

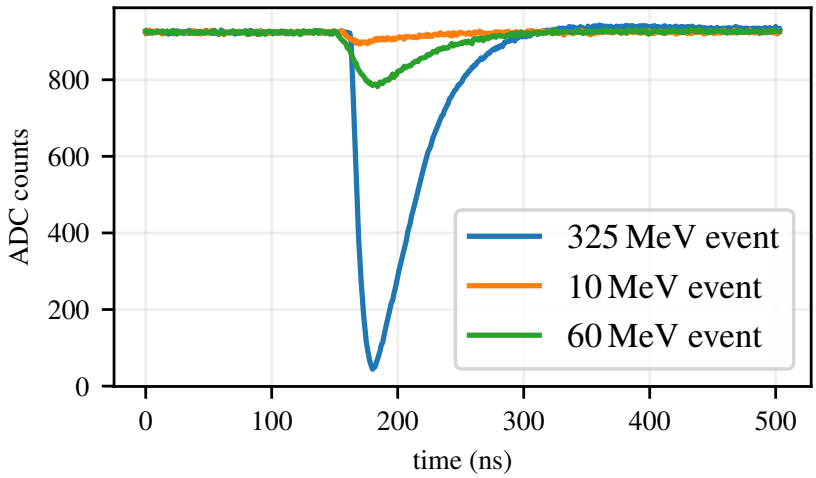

Figure 4.33: Examples of the registered single energy deposition events, registered during the exposure to the atmospheric radiation.

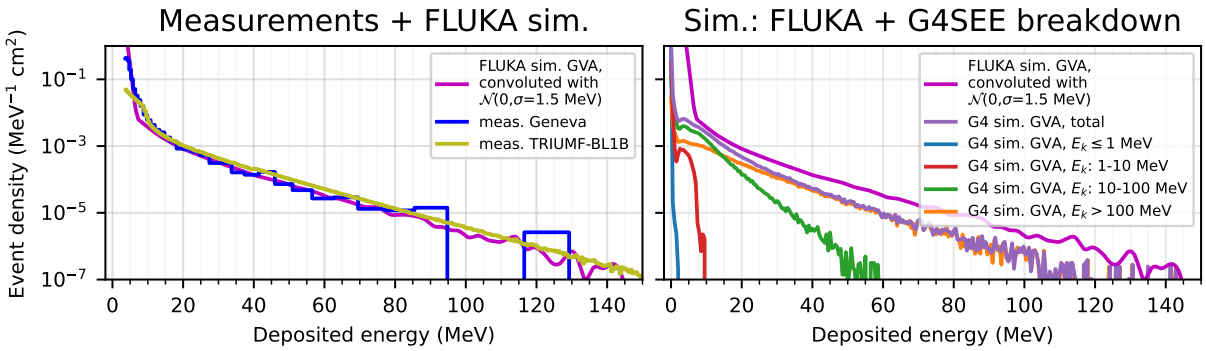

Figure 4.34: Measured (on the left) and simulated (on the right) energy deposition spectra over the exposure to the atmospheric radiation. The FLUKA simulated energy deposition spectrum is depicted in both subplots. The measurements were performed at CERN, over 55 days, whereas the FLUKA Monte Carlo simulations took as input the atmospheric spectrum retrieved by MAIRE and provided the energy deposited in the silicon. Additionally, to imitate diode energy response (low resolution), the simulated energy deposition spectrum has been convoluted with the normal distribution of $\sigma = 1.5$ MeV. The deposited energy per a single event reached up to 325 MeV (Fig. 4.33).

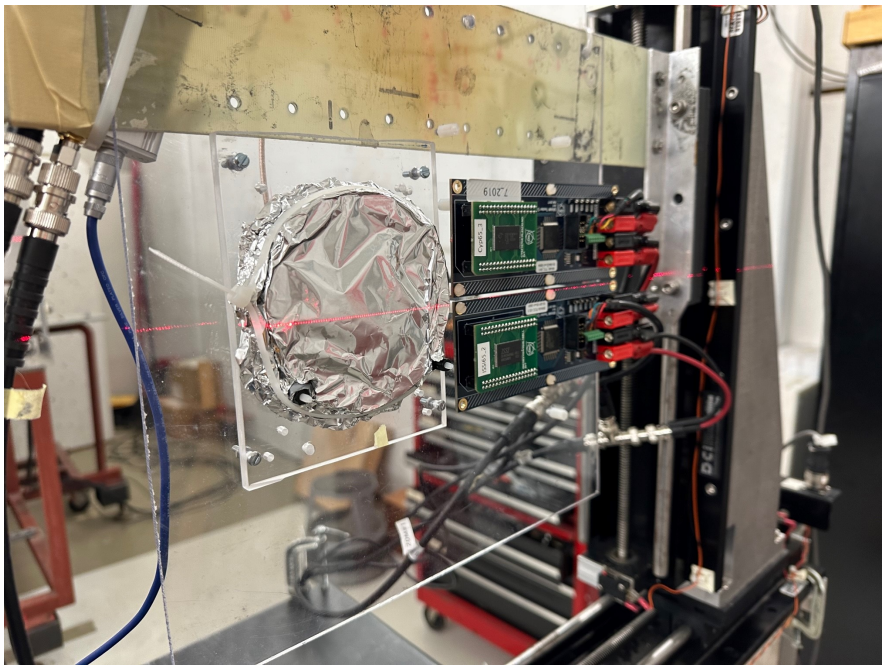

Figure 4.35: Silicon detector and two SRAM memories during experimental tests at TRIUMF-BL1B, aiming in demonstrating the enhanced detection capabilities once compared with SRAM solutions.

target, through spallation reaction [122]. The related neutron spectrum resembles an atmospheric one, with the cut-off due to the maximum kinetic energy of the protons (480 MeV), as depicted in Fig. 4.31.

The measured energy deposition spectrum is illustrated in Fig. 4.34, and as expected, it is similar to the one measured at the ground level - within 3%, as listed in Tab. 4.2, while considering both neutron kinetic and deposited energies above 10 MeV.

In addition to the aforementioned large silicon diode, irradiations at TRIUMF involved also the small diode, and several SRAM memories, with a setup example as shown in Fig. 4.35. As listed in Tab. 4.3, the detection sensitivity of the large silicon diode exceeds the tested SRAM solutions by 5 orders of magnitude.

Fig. 4.36 depicts a detection cross-section as calculated for the large diode detector, considering the number of measured events per delivered fluence. As opposed to SRAMs, the cross-section for the diode is a function that depends on the selected limit of the measured deposited energy. The small diode (with the analogous readout chain) has a significantly lower detection limit (around 200 keV), however, due to smaller silicon volume is overall less sensitive at the atmospheric-like neutrons detection. At lower threshold energies, the cross-section scales with the ratio of silicon volumes. The higher the threshold, the worse the rescaled cross-section agreement between the two diodes. This is due to a larger Si-range of secondary products, carrying energy outside the sensitive volume.

In addition, as described in Chapter 4.2.2, the detector can be exploited for dose rate measurements. An example of measured dose rate during TRIUMF-BL1B irradiation is depicted in Fig. 4.5. The provided flux

Table 4.3: Measured detection cross-sections under irradiation with TRIUMF-BL1B neutron beam.

	Reference	Date code	Size (Mbit)	σ (cm^2)	$\frac{\sigma_{diode}}{\sigma}$
large diode (bias: 130 V)	3560.317A.24.1			0.21	1.00
large diode (bias: 170 V)	3560.317A.24.1			0.30	0.70
small diode	3705.326D.378.18			0.022	9.6
ISSI 40nm	IS61WV204816BLL-10TLI	1650	32	6.6×10^{-7}	3.2×10^5
Cypress 65nm	CY62167GE30-45ZXI	1731	16	2.0×10^{-6}	1.1×10^5
Cypress 90nm	CY62157EV30LL-45ZSXI	1843	8	1.3×10^{-6}	1.6×10^5
Cypress 90nm	CY62167EV30LL-45ZXA	1731	16	6.8×10^{-7}	3.1×10^5

of neutrons with kinetic energies E_k >10 MeV was 2.2×10^5 $n_{>10MeV}/cm^2/s$, leading to the deposited dose of 7×10^{-11} Gy/($n_{>10MeV}/cm^2$) under the exposure to atmospheric-like neutrons. However, due to the limited number of points at the Co-60 calibration, this result has a large uncertainty.

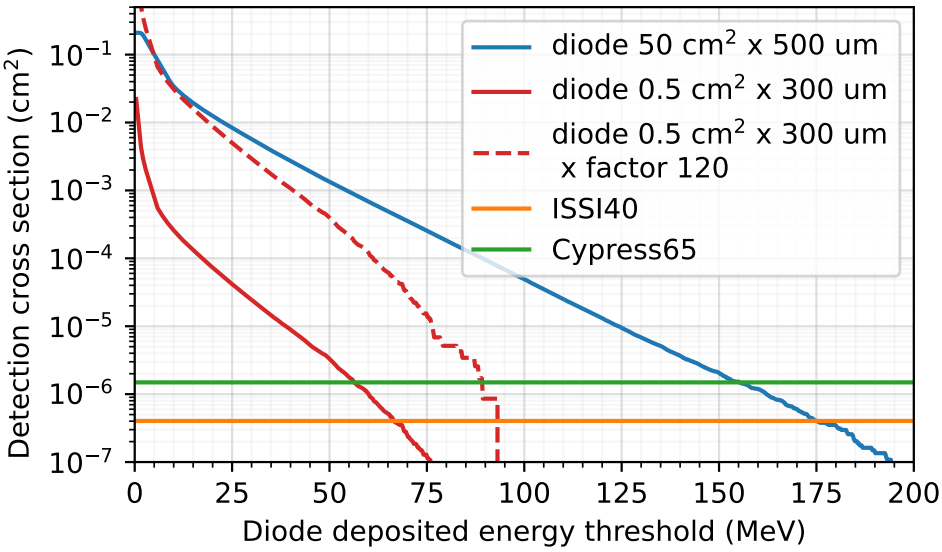

Figure 4.36: Detection cross-section as a function of the threshold deposited energy, for the large silicon diode, as measured at TRIUMF-BL1B with an atmospheric-like neutron beam. For comparison purposes, the analogous curve for a smaller, 0.5 cm^{2}x300 μm, silicon diode was depicted, together with the measured cross-sections for ISSI and Cypress-65 nm memories (listed in Tab. 4.3). A dashed line corresponds to the detection cross section for a small diode rescaled according to the volume ratio (x120) compared to the large detector.

4.3.2 Accelerator radiation environment

4.3.2.1 Linear Accelerator 3 (LINAC3)

To demonstrate the use case for the silicon diode focusing on accelerator applications, an experiment at one of CERN's accelerators, the LINAC3, was performed. The aim was to measure the response of multiple radiation detector types under the radiation field that would be produced in case of the sudden loss of a 4.2 MeV/u $^{16}O^{8+}$ beam on a magnet or other beamline element. For this reason, different target materials were installed inside the accelerator's vacuum chamber and exposed to the $^{16}O^{8+}$ beam. Focusing on the target made of Al, a benchmark between BatMon (battery-powered RadMon) and the silicon diode was performed. The setup is depicted in Fig. 4.37. The produced radiation field consisted primarily of neutrons, with the simulated spectrum depicted in Fig. 4.31.

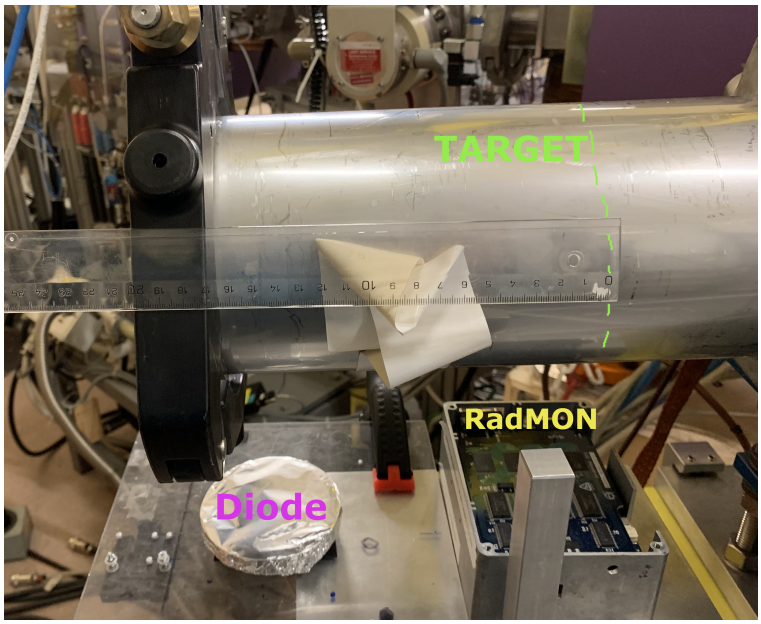

Figure 4.37: Silicon diode and BatMon (battery-powered RadMon) used during LINAC3 experiments aiming in measuring radiation due to loss of an 4.2 MeV/u $^{16}O^{8+}$ beam on a beamline element. The Al-target, mocking a beamline element, was installed inside a vacuum chamber.

During 4320 s of data acquisition, approximately 6.6×10^{13} ions reached the 0.5 mm Al-target. The energy of the oxygen ions at the target was 4.2 MeV/u. The produced secondary radiation field consisted of neutrons and gamma rays, with the simulated neutron energy spectrum depicted in Fig. 4.31. The measured energy deposition spectrum is depicted in Fig. 4.38, and compared with the FLUKA Monte Carlo simulations. The gamma rays do not contribute to the measured energy deposition spectra (below the acquisition threshold). The measurement event rate is factor 2.2 lower than the simulated one, however, the energy deposition profiles match well. The difference could be due to approximations used in the simulations or an overestimated number of ions that reached the target (due to reduced transmission). The measured spectrum below ~4 MeV could be affected by the detection limit of the setup. The silicon diode detected 2636 events with the deposited energy above 2 MeV (41 events above 10 MeV deposited). At the same time, BatMon

(battery-powered RadMon) measured 0 SEUs (HEHeq $<5 \times 10^6\,\mathrm{cm}^{-2}$) and dose below the detection limit of the floating gate transistor (below 5 mGy) [84]. This demonstrates how the diode detector could efficiently complement RadMon, particularly through the enhancement in detection capabilities. The increased sensitivity could be exploited in CERN's very low radiation areas where RadMons are not sensitive enough to retrieve meaningful statistics over short time periods. Profiting from the information about an entire energy deposition spectrum, the diode could be also deployed in the regions, where radiation levels are assessed with Monte Carlo simulations, for their validation. Despite the highlighted advantages, the diode detector is significantly more expensive and harder to deploy as compared to the SRAM-based solutions (such as RadMon), therefore the use of diodes in a spatially distributed manner is not foreseen.

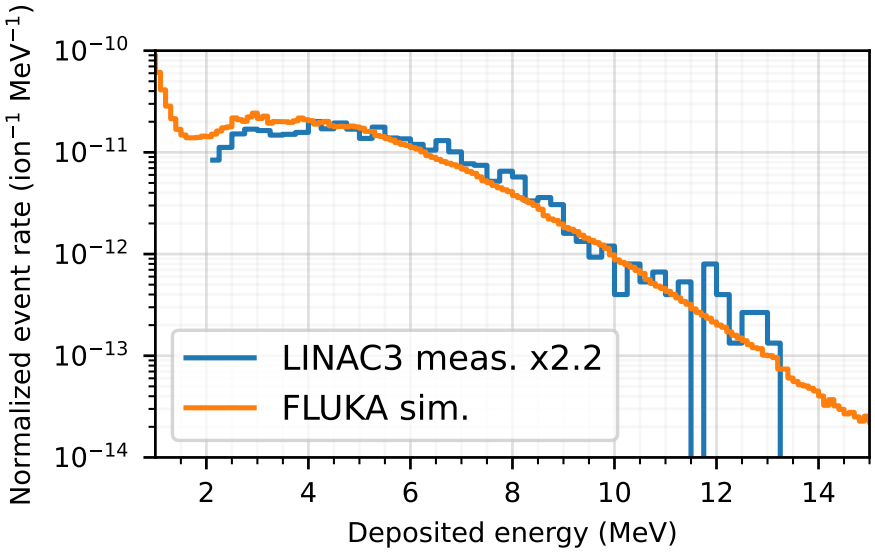

Figure 4.38: Measured and simulated energy deposited in the silicon diode as per primary $^{16}O^{8+}$ion impacting the Al-target in the LINAC3 at CERN. Measured values were multiplied by 2.2 for visibility purposes.

4.3.2.2 Low Energy Ion Ring (LEIR)

LEIR [130] is the second accelerator in the ion's chain, receiving the beam from LINAC3 at 4 MeV/u, and after acceleration to approximately 70 MeV/u (depending on the ion), sending it to the PS for the further acceleration.

For most of the ion operation, the accelerators are supplied with lead beams. However, within the OXY4LHC project [131], the aim is to provide an oxygen beam to the LHC. As the lighter ions have higher ranges in matter and stronger fragmentation capabilities (due to a smaller Coulomb barrier), the radiation levels in the chain needed to be evaluated. Following the dedicated studies in LINAC3, described in Chapter 4.3.2.1, this section covers diode measurements of the radiation at the LEIR accelerator, intending to compare oxygen and lead operations. It has to be noted, that the measurements were the first radiation assessment performed in LEIR within the R2E activity, leading to the discovery of the main radiation source in the accelerator.

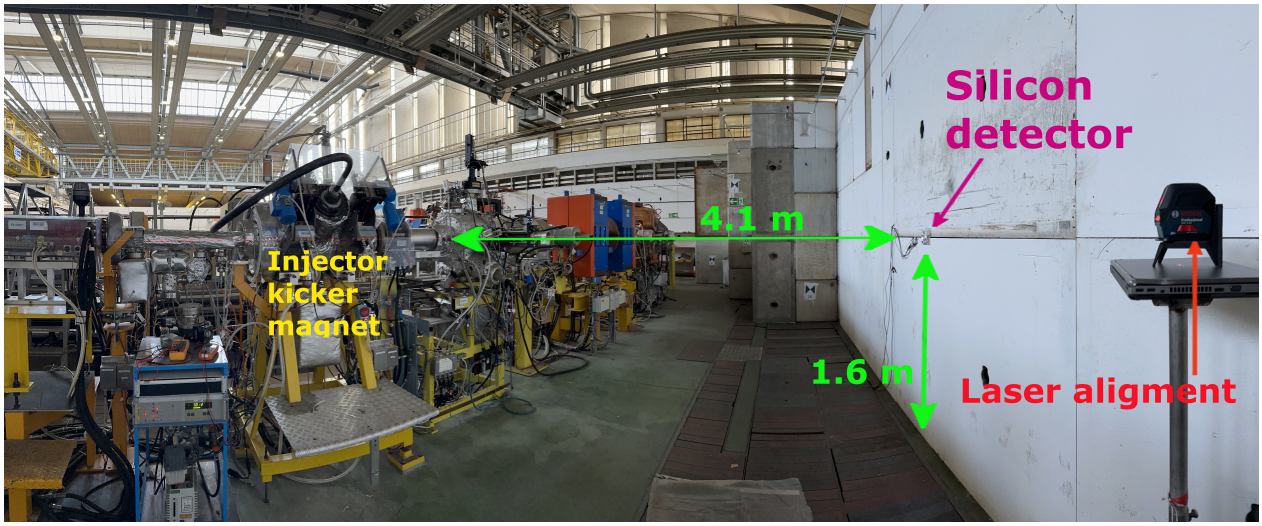

Figure 4.39: Diode setup during the experiment at LEIR.

The large detector (IV, according to Tab. 3.1) was installed close to the injector kicker magnet (CERN code: ER.SEH10). It was biased with 170 V, 40 V above the recommended value to increase the detection limit by increasing the current's amplitude (faster charge collection). The selected location was arbitrary and driven by the installation requirements, i.e. cabling should not interfere with the standard LEIR accesses. Moreover, to reduce the impact of the expected EMC interferences, the detector was installed 4.2 m from the beamline, ~7 cm below the beam plane. The installation (front-end) is depicted in Fig. 4.39. The back end was installed close to the access doors, behind a concrete shielding.

The LEIR is operated mainly with two cycle types: *long*, lasting 3.6 s (CERN's name: *NOMINAL*), and *short*, lasting 2.4 s (CERN's name: *EARLY*). Because of multiple injections, the accelerated intensity is approximately factor 4x larger as compared to a single injection *short* cycle (lasting 2.4 s), pictured in Fig. 4.40a. In 2023, *long* cycles used only the $^{208}Pb^{54+}$ beam, whereas *short* exploited both $^{208}Pb^{54+}$ and $^{16}O^{4+}$.

Since the restart of lead operation in mid-August 2023, several periods with higher measured event rates were identified, with unknown origin. Later, it was found out that these periods were also visible by the CERN's radioprotection ionization chamber (CERN code: PAXP.203), permanently installed at the LEIR's visitor platform (the opposite side of the accelerator, distant about 30 m) for radiation protection.

After performing a detailed study, it was identified that these radiation peaks coincide with a completed fill of the LHC with a heavy-ion beam. This is because after larger accelerators no longer require a beam, the destination of the beam needs to be changed manually to the LEIR's dump. If that is not done, the beam is not extracted and circulates until the magnetic field is sustained. It is particularly visible for a *long* cycle consisting of 7 injections from LINAC3, as depicted in Fig. 4.40b. Yet, as pictured in Fig. 4.40 by dashed traces, most of the intensity is lost in the accelerator before the beam reaches the top energy (67 MeV/u for $^{16}O^{4+}$, 72.2 MeV/u for $^{208}Pb^{54+}$).

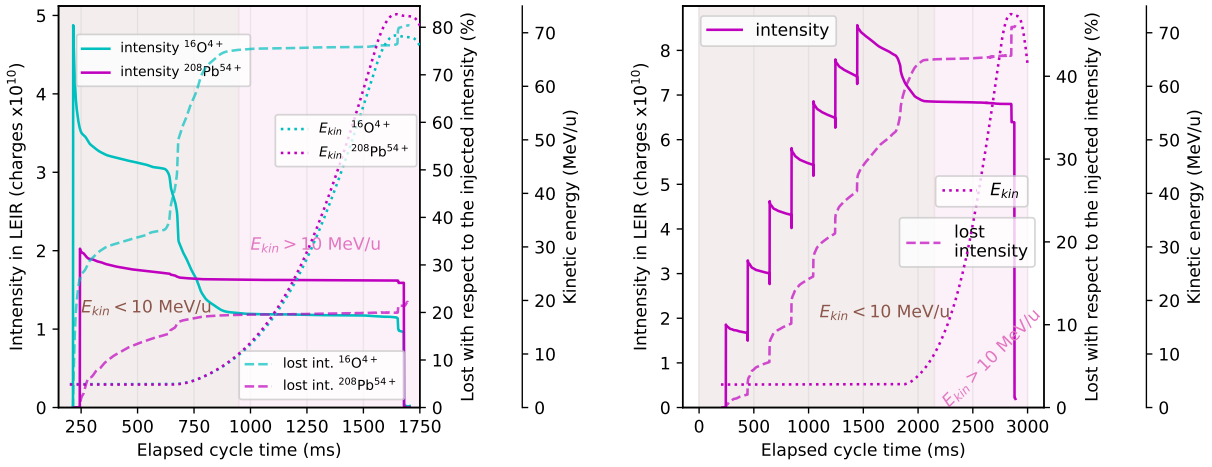

(a) *short* cycles for $^{208}Pb^{54+}$ and $^{16}O^{4+}$ **(b)** *long* cycle for $^{208}Pb^{54+}$

Figure 4.40: Averaged annual intensity for two types of LEIR cycles as measured by the ring Beam Current Transformer. Together with the intensity and the ion's kinetic energy, an averaged loss (cumulative sum of the derivative of the averaged intensity trace, excluding injections and extraction, with the inverted sign) evolution is depicted.

For further analysis an arbitrary threshold of 10 MeV/u was considered. Below it, the beam is lost during injection, RF-capture, and at the beginning of acceleration (uncaptured beam). Above, the losses mostly happen at the flat top (accelerated beam). The time evolution of the lost intensity, for losses both below and above 10 MeV/u is pictured in Fig. 4.41.

It illustrates the cumulative number of the measured energy deposition events, with at least 10 MeV deposited. This arbitrary energy threshold was selected to: i) mitigate the impact of the setup's detection limit, as the ADC trigger is applied on the signal's amplitude, not the integral; ii) focus on the energy depositions triggered by hadrons, that dominate the electromagnetic radiation's component at that (and higher) energy. The counts' time evolution resembles the evolution of the intensity that is lost above 10 MeV/u, implying that the dominant source of radiation is losses at energy above the threshold of 10 MeV/u, which translates

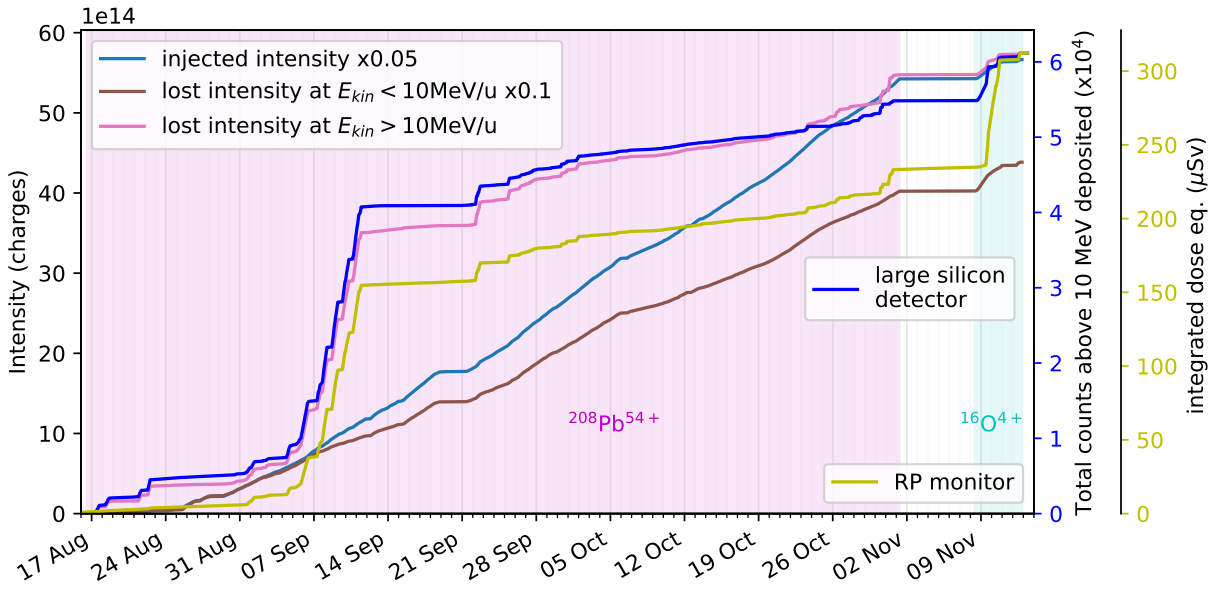

Figure 4.41: Total injected and lost LEIR's intensity as a function of time, together with the large detector counts. Lost intensity was split into categories, depending on the ion's kinetic energy at the loss time. For benchmark purposes, an integrated equivalent dose was depicted, as measured by an ionization chamber (CERN code: PAXP.203) located at the visitor's platform (about 30 m distant from the silicon detector). The unproportionally larger response of the ionization chamber during $^{16}O^{4+}$ run might be due to differences in the beam loss locations.

effectively to losses at top energy. Whereas the presented diode measurements are from a single location, the evolution of the dose equivalent, measured by an ionization chamber on the opposite side of LEIR (south-east corner, at the visitor's platform), follows the same trend. This further supports the hypothesis that the LEIR's radiation is driven by the accelerated, non-extracted beam, that is lost within a ring (precise loss distribution unknown).

The measured energy deposition spectra, for $^{208}Pb^{54+}$ and $^{16}O^{4+}$ operations, are depicted in Fig. 4.42. Due to encountered issues, such as power cuts or laptop-enforced restarts, only 84% of the 2023 accelerator operation (in terms of the injected intensity) was monitored by the silicon diode. However, the missing part had no impact on the analysis. While considering events above 10 MeV depositions normalized to the acquisition time, the rate of events during $^{208}Pb^{54+}$ ($^{16}O^{4+}$) in time was 44x (67x) larger than atmospheric one. It has to be pointed out that as the driving factor is intensity losses, not constant in time, the time normalization is not optimal. While considering normalization per the lost ion above 10 MeV/u, the rate of events for $^{208}Pb^{54+}$ was factor 5 higher, compared to the $^{16}O^{4+}$ operation. It has to be pointed out that conclusions are location-dependent. For example, while applying the same normalization for the ionization chamber dose equivalent measurements, the worst-case dose rate equivalent was factor 2 larger for the $^{16}O^{4+}$ operation, i.e. resulting in a factor 10 difference compared to the diode measurements.

The LEIR use case of the silicon detector proved its excellent capabilities in the accelerator environment,

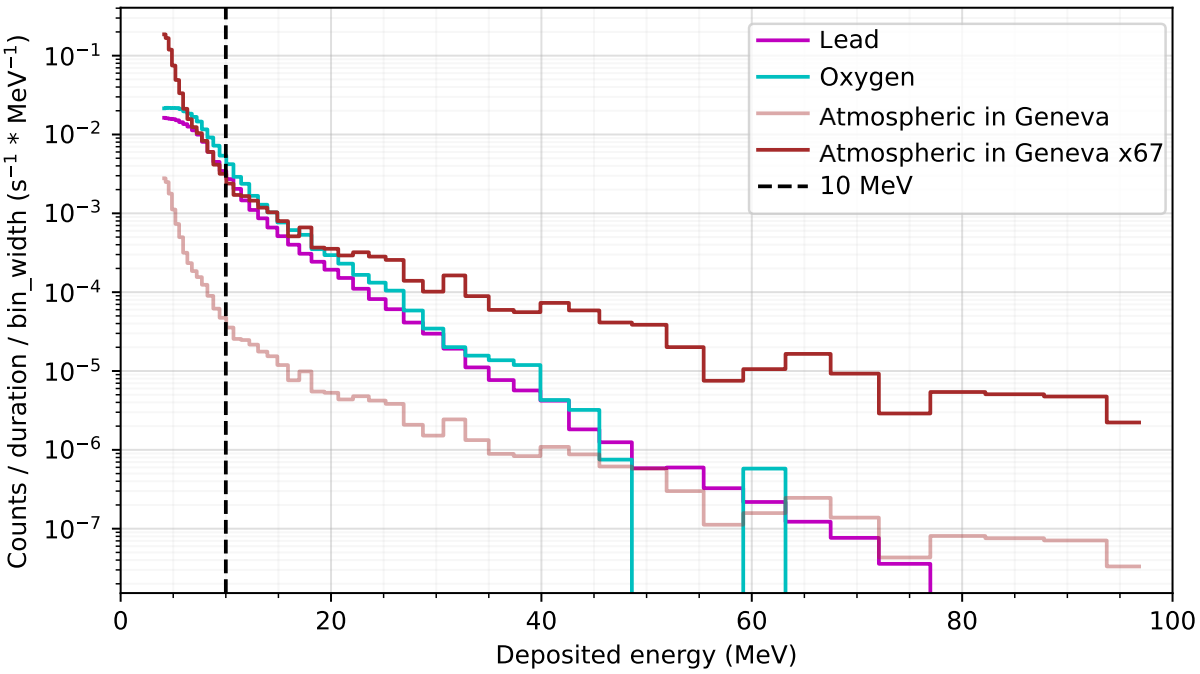

Figure 4.42: Measured energy deposition spectra during LEIR $^{208}Pb^{54+}$ and $^{16}O^{4+}$ runs. For comparison purposes, a measured atmospheric energy deposition spectrum is depicted.

linking the silicon detectors (Chapter 4) with the CERN's accelerator environment (Chapter 5). Thanks to the provided expertise, for the first time, the origin of radiation in LEIR, i.e. accelerated beam lost within the ring for cycles not extracted towards the PS or the LEIR dump, was defined. This led to discussions concerning the dynamic destination implementation in the LEIR accelerator which would ensure that the beam is extracted to the dedicated external dump in case larger accelerators do not request a beam. This will lead to a significant reduction of the radiation in the LEIR accelerator.

4.3.2.3 CHARM

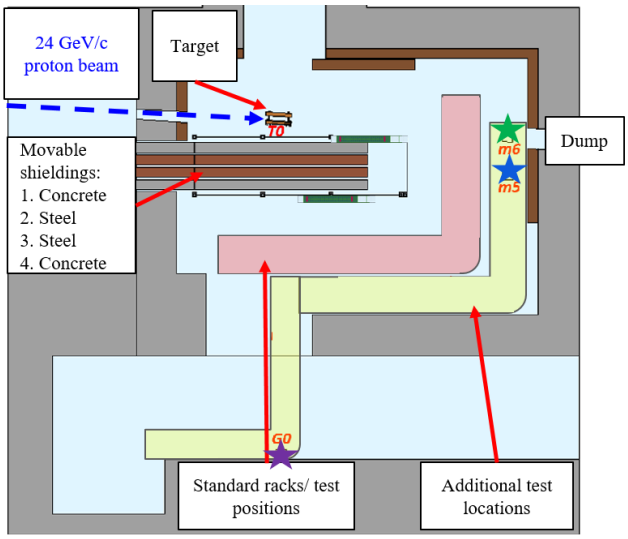

(a) schematic top view drawing of the facility with marked G0 testing position.

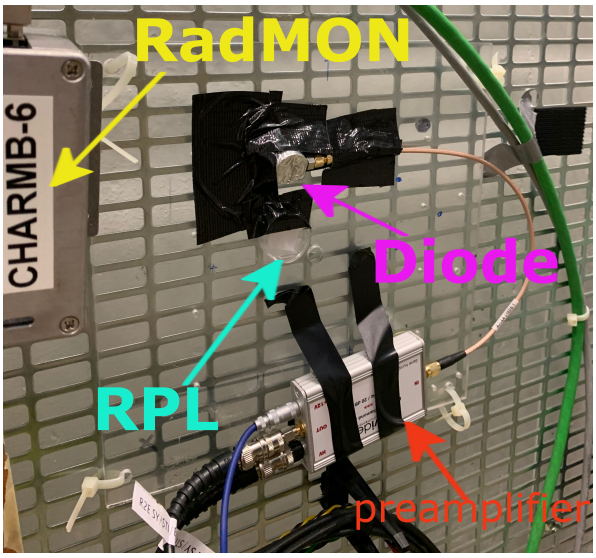

(b) small diode detector, together with a nearby RPL and RadMon, during tests in CHARM's G0 position

Figure 4.43: Schematic representation of CHARM with experimental setup used during the tests.

The CHARM facility [24] is part of CERN's PS East Area [132]. It provides a mixed-field through a spallation reaction between a 24 GeV/c proton beam extracted from PS and a target, most frequently a copper one. In addition to the target selection, the facility allows the modification of the particle spectral composition through the shielding arrangement. It contains several standard test locations, varying in terms of particle spectra and intensity. In this paragraph, measurements acquired with detector (I) in the G0 position are presented. During tests, the copper target was used and no shielding was in place. The schematic drawing with the highlighted G0 testing position is depicted in Fig. 4.43a. The experimental setup, consisting of detector, RadMon, and RPLd, is pictured in Fig. 4.43b.

The simulated particle energy spectrum for the dominant constituents (hadrons) is illustrated in Fig. 4.44 [133, 134]. During these tests, the small detector was used with 20 dB CIVIDEC preamplifier, resulting in a detection limit at about 5 MeV of deposited energy. Electromagnetic radiation components (electrons and photons) usually deposit lower energies in 300 µm, therefore it was neglected in FLUKA simulation benchmarks.

The cumulative radiation levels (for constant settings) are proportional to the number of Protons deposited On Target (POT). Each spill typically contains around 6×10^{11} POT. Measured and simulated (for the selected hadrons) energy deposition spectra are depicted in Fig. 4.45, confirming very good agreement obtained in a past study [36].

Concerning dose measurements, the leakage current was measured only during several spills, not throughout the entire CHARM run (one week). Within the selected 11 spills, chosen among those depicted in Fig. 4.46, corresponding to 6.49×10^{12} POT, the detector measured 10.96 mGy (1.69×10^{-15} Gy/POT). As the CHARM configuration was constant, extrapolating the following result to the entire one-week run, yields

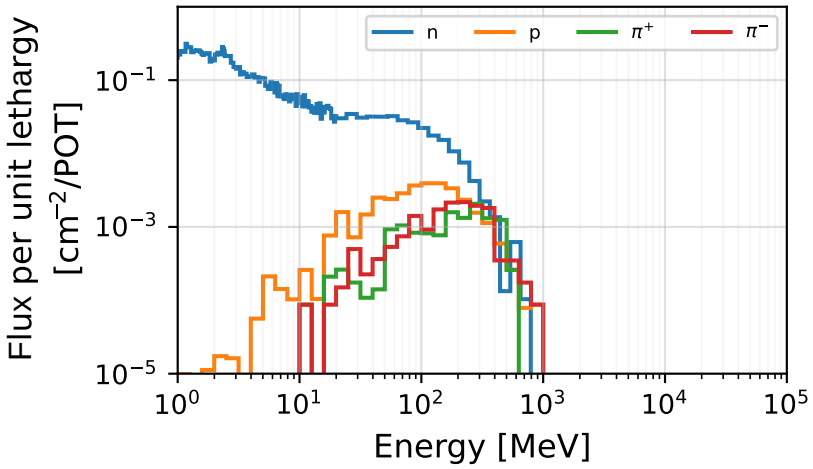

Figure 4.44: Simulated particle spectra, for the dominating particle species, in G0, for CHARM configuration with the copper target, and no shielding in place. Due to logarithmic binning over few decades, the flux figure is normalized per unit lethargy, i.e. $\frac{\mathrm{d}\phi}{\mathrm{d}(\log E)} = E\frac{\mathrm{d}\phi}{\mathrm{d}E}$ (divided by the energy bin width and multiplied by the mean value of the energy bin in the logarithmic representation, being the geometric mean value of bin's start and end values.)

(36.04 ± 0.82) Gy. Additionally, over the corresponding CHARM one week run, the RPLd was installed in the direct proximity of small detector, as shown in Fig. 4.43b. During the irradiation, the RPLd measured 32.6 Gy, that considering the POT=2.13×10^{16} p, corresponds to a dose rate of 1.53×10^{-15} Gy/POT (copper target and no shielding). At the same time the nearby RadMon measured 26.9 Gy (1.26×10^{-15} Gy/POT).

The agreement of the extrapolated dose measurement by small detector is within 25% with RadMon and within 10% once compared with the RPLd.

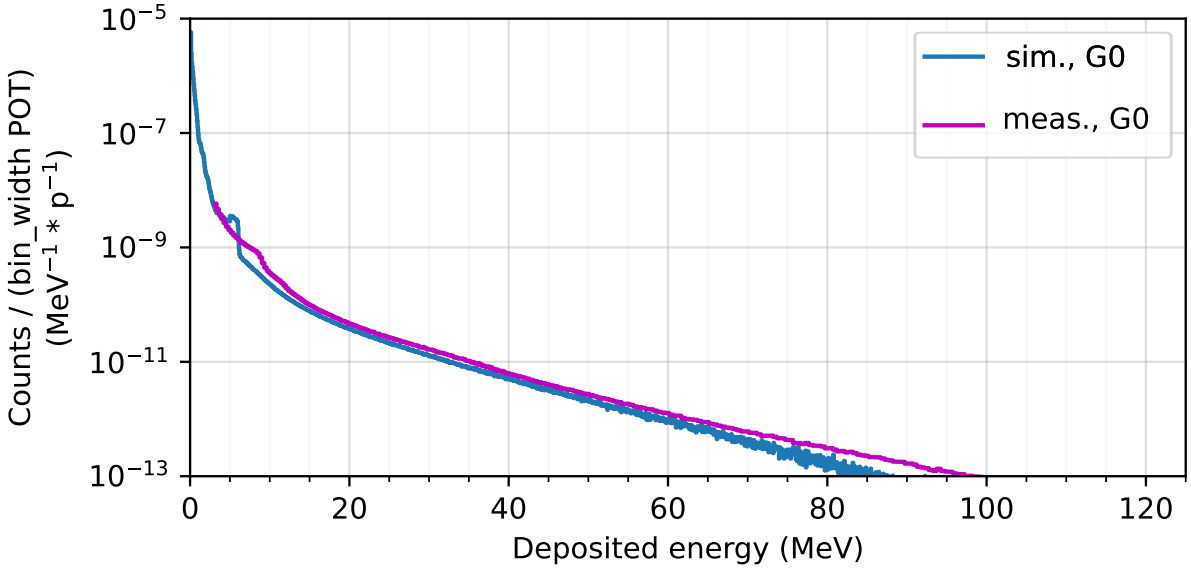

Figure 4.45: Measured energy deposition spectra in testing positions G0, as measured by small detector (I) at CHARM for the Cu target and no shielding in use. The traces were normalized to the delivered Protons on Target (POT). Additionally, simulated energy deposition distribution was depicted, as retrieved via the FLUKA Monte Carlo simulations, considering circular beam composed of particle spectra shown in Fig. 4.45.

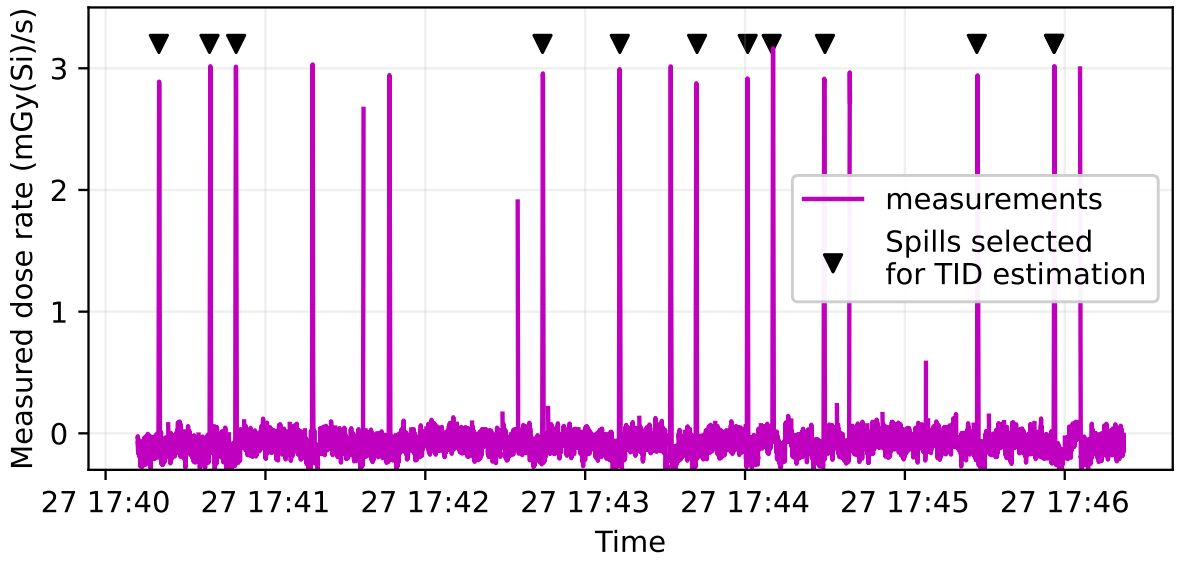

Figure 4.46: Dose rate over time as measured by the small detector (I) in the G0 position (CHARM configuration: no shielding in place with the Cu target). Due to a limitation of the Source Measure Unit (no measurement while accessing buffered data), only selected spills were captured entirely and thus used for TID estimation.

4.4 Summary

- The energy calibration enabled further data exploitation, particularly in the case of the large detector, whose correction versus the analytical value was nonnegligible ($k = 2.57$). Values for small detectors were significantly closer to the analytical value $k = 1$ (k=0.93 to 0.97). There were small differences within the small detectors, implying potential changes in the calibration along the detectors' irradiation history or differences in the manufacturing process.
- Dose rate vs leakage current calibration for the small detector, applied to proton and mixed-field radiation, lead to values close to analytical calculation (19%) and measurements with other dosimeters (10% difference with RPLd, RadMon).
- It was demonstrated how the detector behaves under heavy-ion irradiations, particularly how the calibration factor k increases (e.g. due to larger recombination at higher LET values). With the help of a high-energy heavy-ion beam, the shielded active silicon surface was estimated to be about $0.27\,\mathrm{cm}^2$, while the non-shielded surface is $0.5\,\mathrm{cm}^2$.
- A method for enhancing the capabilities of thermal neutron detection, with the use of ^{6}Li converted, was demonstrated. This is crucial for future detector applications in the monitoring of radiation environment in the CERN accelerator complex, where thermal neutrons are of high relevance, as their relative contribution increases with the shielding thickness. The method was shown to be suitable to be exploited in the air due to the range of tritium ions.
- The versatility of the detectors (and the related setup) was further exploited to demonstrate beam characterization capabilities, focusing on CHIMERA-HEARTS activities, where the small detector has been a crucial instrument, used for flux absolute calibration of the existing beamline instrumentation.
- In terms of radiation monitoring, the targeted use cases involve locations with relatively low radiation, where other solutions, such as SRAM-based RadMons, are not sensitive enough to collect meaningful statistics in short periods, for example, related to particular accelerator settings. Profiting from the atmospheric radiation (actual one, and obtained through spallation) it was demonstrated how the large detector can be used to characterize low radiation environments, even caused by atmospheric neutrons. The measured increase of sensitivity with respect to SRAM solutions exceeded 5 orders of magnitude. This was further confirmed in the radiation field produced at one of the CERN accelerators (LINAC3) where the large detector was capable of measuring thousands of energy deposition events, whereas RadMon measured none.
- The great potential of the large detector was further proved in another CERN accelerator, LEIR, during a standard operation. Not only did the detector manage to address the question of how the radiation levels will change with an ion change, but what's more important, it detected higher event rates that happened in some short periods. It turned out, that these were significant beam losses due to the non-optimal design of a control system, allowing for beam disposal within a ring, without extraction to a dedicated dump.

Chapter 5

High-energy accelerator losses and radiation levels

This chapter introduces the two largest CERN accelerators, SPS and LHC, focusing on the prompt radiation levels, mainly dose. It has been written based on the authored publications [4, 34]. In the beginning, a reader is familiarised with technical aspects: accelerator layout and the related nomenclature. Later, the typical accelerator operation is described. The following sections describe beam loss mechanisms (for the main operation modes), and linked to that, radiation levels along the accelerators. The sections are concluded with short summaries, that highlight the most relevant findings and conclusions.

5.1 Super Proton Synchrotron

5.1.1 SPS layout

The SPS [135] is a circular accelerator of almost 6912 m circumference, consisting of 6 sextants, as illustrated in Fig. 5.1. Each sextant consists of a Long Straight Section (LSS) and two arcs, at the two sides of the LSS. The accelerator is organized in 2 × 108 half-periods (determined by the main quadrupole magnet locations), each of ∼32 m extension. Every sextant contains 36 half-periods – 8 attributed to the LSS and 14 to each of the arcs. Assuming that $X = (1, ..., 6)$ denotes the sextant's number, the Arc-, LSS, Arc+ would span over half-periods X00-X13, X14-X21, X22-X35, respectively. Based on Sextant 1, this convention is illustrated in Fig. 5.2. Furthermore, within this work, the naming is such that ArcNM would contain both arcs (Arc$N$+, Arc$M$−) between LSSN and LSSM.

Each LSS poses a specific functionality related to the accelerator operation. In LSS1, the beam is injected and scraped (cleaned from off-momentum particles). In LSS2, the beam is slowly extracted (i.e. over multiple turns) towards the TT20 beamline, which supplies particles to Fixed Target experiments in the North Area [13]. LSS3 houses the radio-frequency cavities responsible for the beam bunching and acceleration.

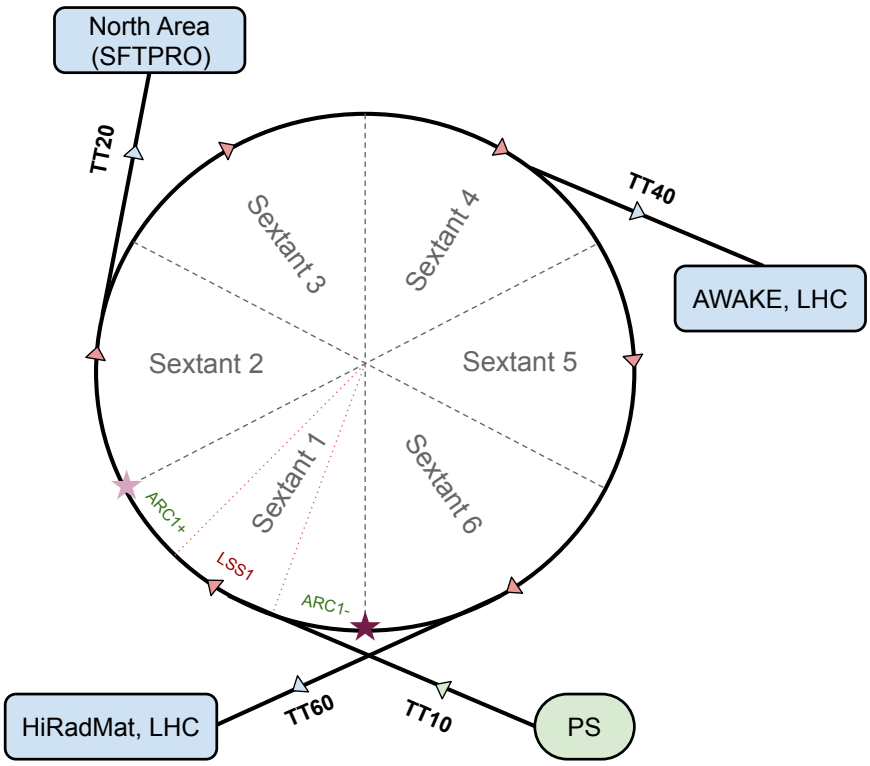

Figure 5.1: Schematic layout of the SPS with both injection (TT10) and extraction transfer lines (TT20, TT40, TT60).

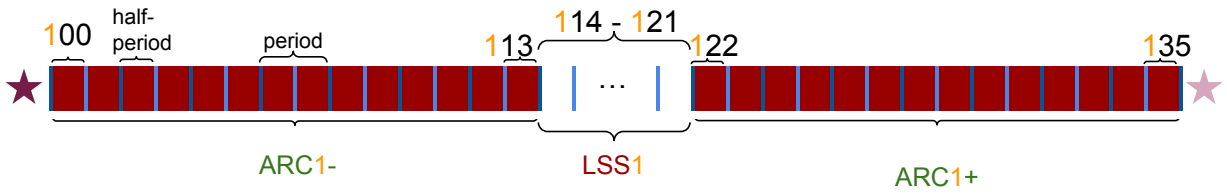

Figure 5.2: Schematic drawing of Sextant 1 with highlighted half-periods that limit ARC1-, LSS1, and ARC1+. The same naming convention is applicable to all Sextants. The stars at the beginning of ARC1- and at the end of ARC1+ correspond to the locations marked in Fig. 5.1.

Then, in both LSS4 and LSS6, the beam is fast extracted (i.e. within a single turn) towards the LHC or the SPS experiments. In the case of LSS4, through the TT40 extraction line, the beam is provided both to the counterclockwise circulating beam of the LHC and to the AWAKE experiment [11], whereas LSS6, via TT60 transfer line, supplies the beam to the clockwise-circulating beam of the LHC and the HIRADMAT facility [12]. Lastly, as of 2021, LSS5 hosts the internal beam dump [136], which allows for a safe abort of the beam from the ring.

5.1.2 SPS operation

The SPS accelerator operates in cycles, each one lasting between a few and a few tens of seconds, depending on the beam user. The main beam users correspond to SFTPRO (Fixed Target experiments in the North Area), LHC, and HiRadMat. Examples of the SPS cycles for the most common beam users are depicted in Fig. 5.3. Most of the time, the accelerator is operated with protons, although in some years operation with heavier ions is performed, typically for a few weeks. Each year, the majority of the injected protons are sent

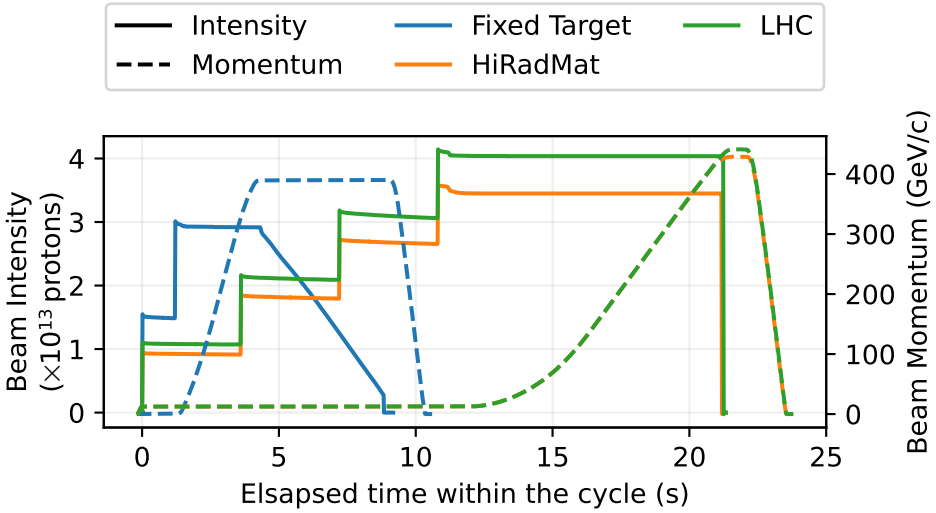

Figure 5.3: Examples of the SPS cycles, in terms of beam intensity and beam momentum, for the most common beam users: North Area experiments (SFTPRO), LHC, and HiRadMat experiment. The SFTPRO beam is extracted slowly, i.e. over multiple turns, whereas, for the other users, the fast extraction takes place (single turn).

to the North Area Fixed Target experiments (more than 85%), with the rest being shared mainly among LHC and HiRadMat (a few percent of the annual injected intensity). The statistics of the cycles and related intensities are listed in Tab. 5.1.

Table 5.1: Statistics of the injected intensities (I.I.) to the SPS with the breakdown among the main beam users.

	Unit	SFTPRO	LHC	HiRadMat	other
Typical Injected Intensity (I.I.)	10^{13}p	3.5-4	3-3.8	3-3.8	-
Typical Cycle Duration	s	10	22	22	-
Momentum at Injection	GeV/c	14	26	26	-
Momentum at Extraction	GeV/c	400	450	440	-
Total I.I. 2017	10^{17}p	141.7	7.5	2.0	0.9
Total I.I. 2018	10^{17}p	186.1	8.0	0.5	0.8
Total I.I. 2021	10^{17}p	105.0	0.4	4.1	7.9
Total I.I. 2022 until 17.05 (TS1)	10^{17}p	9.7	4.6	0.03	6.0
Total I.I. 2022 until 13.09 (TS2)	10^{17}p	156.2	9.3	0.13	6.1

5.1.3 Beam Loss Mechanisms

In the SPS sectors, the occurring beam loss mechanisms are not only determined by the amount of injected intensity and the beam energy, but also by the beam user, and therefore by both the related beam and accelerator parameters. The most relevant beam loss mechanisms, in terms of radiation levels, are listed below.

Following the occurrence in the cycle, the first losses will happen at the injection, as the shape of a batch from PS does not entirely match the SPS RF buckets [137]. The parts of the beam that were not captured into RF buckets, so-called uncaptured beam, drift along the RF buckets [75], populating the kicker gap and leading to additional losses when kicker magnets are switched on, i.e. at fast extraction or successive injections. However, the majority of the uncaptured beam is lost at the very beginning of acceleration. Another example of a mechanism related to off-momentum losses is the transition crossing, happening only for SFTPRO cycles due to lower injection energy. As depicted in Fig. 5.4, the related beam losses during 2022 corresponded to 1.1% of the total injected intensity.

The other set of mechanisms is related to the transverse properties of a beam, in terms of physical dimensions, as the aperture of the beamline is limited. Particularly, in the SPS, the vertical aperture is smaller as compared to the horizontal one, and several bottleneck locations were identified [138]. Apart from the aperture, other factors affecting the losses are optics functions ($\beta_{x,y}$ and dispersion D_x, [139]), determined by the magnet properties. In addition to the beam emittance, these functions have a direct impact on the macroscopic beam size.

Along the energy ramping, and despite the decreasing beam's emittance (a parameter that links the optic functions with the physical transverse shape of a beam), the impact of dispersion is increasing. This might lead to beam losses, particularly in the locations where the local maxima of dispersion function coincidences with the aperture limitations.

After the completed acceleration, beam losses during the extraction are foreseen. Once the slow extraction starts, we excite a resonance and increase the beam shape to shave it deliberately using an electrostatic septum, which by design touches the beam and induces beam loss in LSS2, leading to high radiation levels in the LSS2 and several following periods. The extraction towards the North Area takes place of several 100,000 turns.

The beam losses during the fast extraction are significantly lower. In the gap between the bunched beam, the fast pulsed magnets rise and extract the beam within a single turn.

Several other beam loss mechanisms are present during the SPS operation. An example of such is the interaction of the beam with the residual gas molecules that are present in the vacuum chamber. This mechanism is dominant in the LHC arc sectors, however, despite the lower vacuum quality in the SPS, the other beam loss mechanisms induced by beam-machine interactions (particularly those occurring at low energy) overshadow the residual-gas contribution.

The detailed analysis of beam loss mechanisms is outside the scope of this work, and the loss mechanisms are indirectly investigated by means of measured radiation levels, particularly with respect to their occurrence

in SPS cycles. As the losses in the SPS energy regime are initiated by inelastic interactions, higher beam energy leads to more radiation showers, and therefore higher radiation levels per unit lost proton. However, the measurements of dose are not directly proportional to the amount of beam losses.

To illustrate when the losses occur, the main cycles (SFTPRO, and LHC that is analogous to the HiRadMat) were divided with respect to the beam momentum, into *Injection*, *Acceleration*, and *Top Energy* periods. Additionally, for SFTPRO cycles, within *Acceleration* period, a *Transition* crossing subperiod has been defined.

Fig. 5.4 and Fig. 5.5 represent the normalized beam intensity decrease rate, due to beam losses/extraction/dump. To visualize how the related losses impact radiation levels, the plots are supported by normalized dose rate measurements from BLMs along the ring.

It is expected that the majority of dose related to beam losses due to uncaptured beam occur within the *Injection* period, or at the very beginning of the *Acceleration* period. This is the main beam loss mechanism for the LHC beams. The expected exceptions are: i) LSS1, where the beam is scraped, ii) LSS5, where the beam is safely removed at the dump, and iii) LSS4, where the beam is fast extracted towards the LHC. As LSS6 also supplies a beam to the LHC, an open point is the lack of a similar trend, i.e. the losses at the *Top Energy* are not observable. One of the explanations could be a different BLM positioning.

For SFTPRO beams, as expected, the mean dose measured in LSS2 (beam extraction) and LSS5 (safe beam disposal) are dominated by the *Top Energy* period. Additionally, the arc sectors following these LSSs, i.e. 23 and 56, present analogous behavior, implying the impact of LSS functionality on the radiation levels seen in the following arcs.

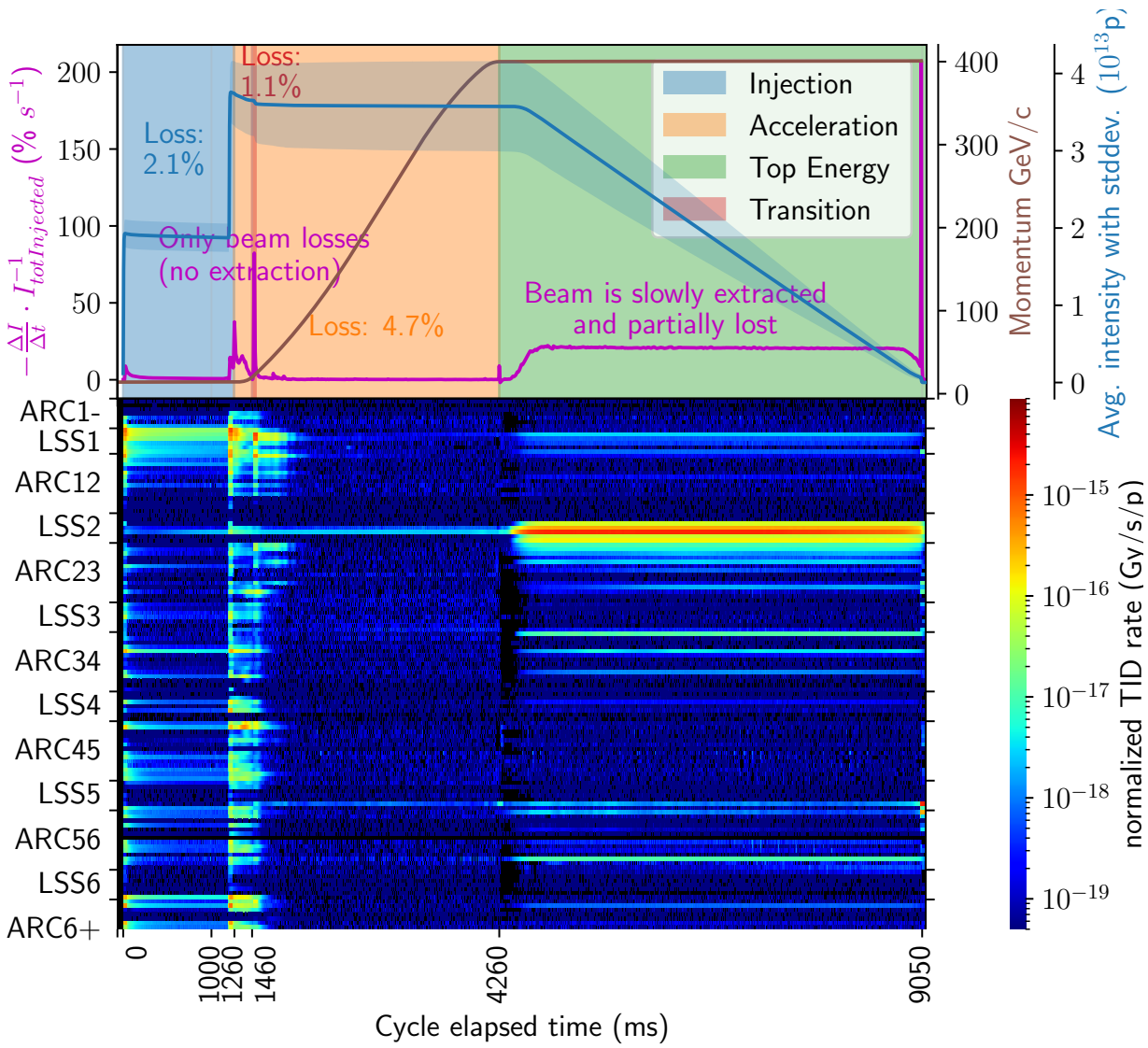

Figure 5.4: The intensity loss rate normalized to the total injected intensity, as measured in 2022 during SFTPRO cycles. The loss rate includes lost, extracted, and dumped protons. For comparison purposes, the beam momentum, together with an averaged beam intensity and its standard deviation is depicted. Only cycles with at least 10^{13} protons injected were considered. In these cycles, 2.1% of the total injected intensity was lost in the machine during the *Injection* period and 4.7% during the *Acceleration* phase (including 1.1% lost at *Transition* crossing). The bottom plot illustrates the injected-intensity normalized dose rate values along the accelerator as measured by the side BLMs in 2022 (until 13.09) during SFTPRO cycles.

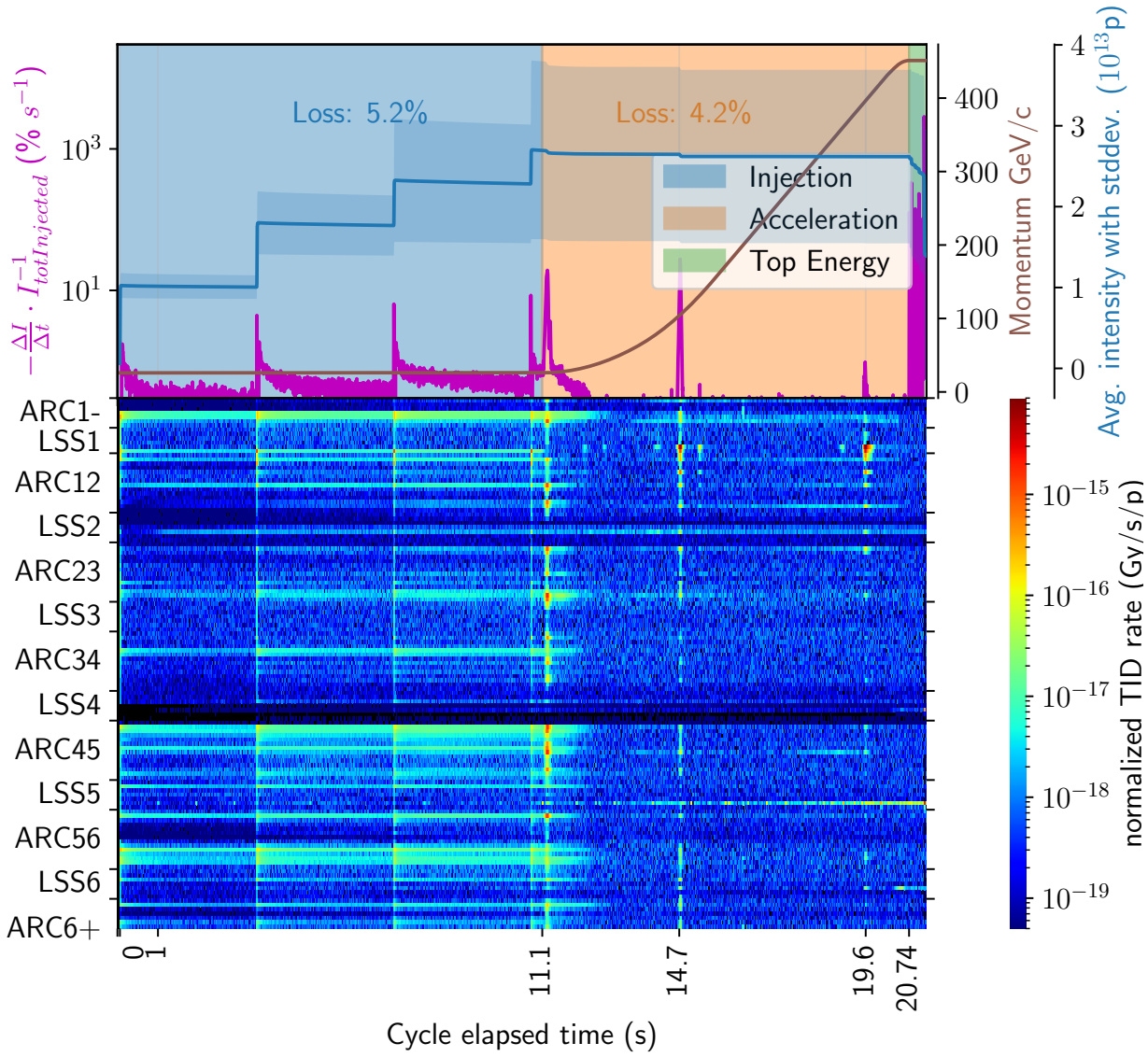

Figure 5.5: The intensity loss rate normalized to the total injected intensity, as measured in 2022 during LHC cycles. The loss rate includes lost, extracted, and dumped protons. For comparison purposes, the beam momentum, together with an averaged beam intensity and its standard deviation is depicted. Only cycles without dump occurring before the *Top Energy* period were considered. In these cycles, 5.1% of the total injected intensity was lost in the machine during the *Injection* period and 4.2% during the *Acceleration* phase (at the very beginning of acceleration due to uncaptured beam, and during the beam scrapping at 14.7/19.6 s.). The bottom plot illustrates the injected-intensity normalized dose rate values along the accelerator as measured by the side BLMs in 2022 (until 13.09) during the LHC cycles.

5.1.4 Radiation levels in 2021

5.1.4.1 Long Straight Sections

In LSS1, during 2022 operation, the highest radiation levels, reaching several tens of kGy, have been measured close to the beam momentum scraper (period 117-118), responsible for intercepting off-momentum particles, and close to the internal dump block (half-period 114) likely due to horizontal aperture bottleneck. In the LSS2, the radiation levels, reaching several hundreds of kGy, are mainly caused by the particles that are lost during the process of the slow-beam extraction, as depicted in Fig. 5.4.

LSS4 and LSS6 are analogous with each other in terms of the expected dominating radiation source term, which is the loss of the particles during fast extraction to the LHC, HiRadMat or AWAKE. However, as depicted in Fig. 5.5, this is not the case, and the dose values in these LSSs are dominated by the losses due to the uncaptured SFTPRO beams, with the dose values reaching up to few hundreds Gy.

In LSS5, as of 2021, the dominating radiation source are the particle showers due the disposal of beams on the dedicated beam dump, leading to dose levels up several tens of kGy.

5.1.4.2 Arc

In the arc sections, the main magnets are arranged in a periodic manner, with one focusing quadrupole followed by 4 bending dipoles, one defocusing quadrupole, and 4 bending dipoles. These 10 magnets constitute two arc half-periods (one period). Within the arc periods, the arrangement of the majority of radiation monitors (and passive dosimeters) resembles the main magnets' periodicity. As opposed to the LHC [67], in

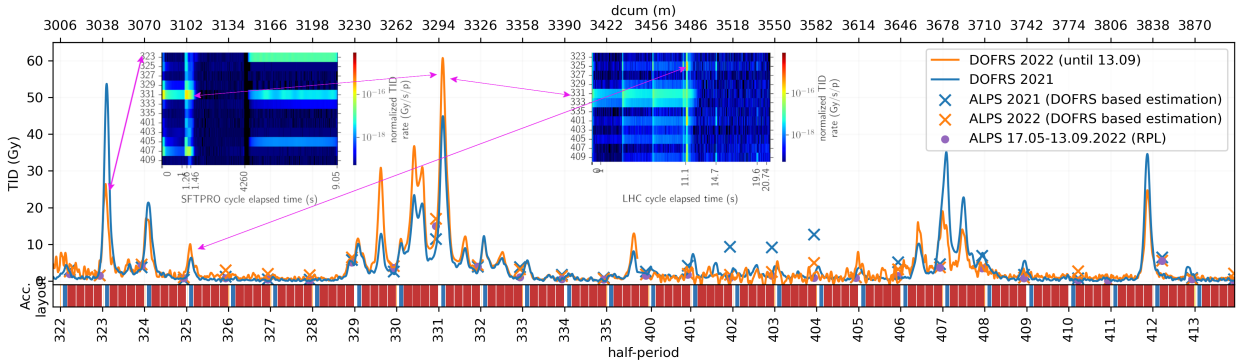

Figure 5.6: TID (Gy in SiO_2, 2 m spatial resolution) in the arc sector 34 as measured by DOFRS in the years 2021 and 2022 (until September), with the schematic magnet layout. Additionally, the dose levels at the ALPS equipment are depicted, by means of RPL measurements from 2022; together with DOFRS-based estimates for 2021 and 2022. By focusing Fig. 5.4 and Fig. 5.5 on the arc sector 34, the detailed radiation peak analysis can be performed. For example, in 2022 the peak in half-period 323 was due to North Area cycles, with the majority of the dose registered during the Top Energy. The peak in half-period 325, was driven by the LHC cycles and happened at the beginning of acceleration, likely due to the loss of the uncaptured beam. The peak in 331 is due to the SPS vertical aperture restriction [138], and the losses can be observed for both SFTPRO and LHC cycles.

the SPS arc sectors the interactions of the residual gas with a beam are not the dominating loss mechanism. If

that was the case, in the presented dose breakdowns (Fig. 5.4 and Fig. 5.5) the majority of contribution in the arc sectors would come from the Top Energy (for SFTPRO) and Acceleration (for LHC) periods, whereas, in all arc sectors, except sector 23, the majority of the losses occur at *Injection* or early acceleration, likely due to uncaptured beam. Moreover, the impact of the LSS1/LSS2 functionality (scrapping/slow extraction), by means of similar loss occurrence within a cycle, can be observed in several locations along the machine.

An example of the dose measurements performed by the DOFRS in 2021 and 2022 are illustrated in Fig. 5.6, together with the dose estimates at the ALPS front-end racks. Supporting DOFRS measurements with the BLM measurements allow for a detailed analysis of radiation peaks, particularly by means of their origin and time evolution.

Multiple other radiation peaks have been identified, particularly in the arc sectors 12 (periods: 122-124, 128), 45 (422-425) and 61 (622-626, 632-634, 113), and are depicted in Fig. 5.7. The maximum measured dose values, at the arc cable tray, exceed 800 Gy, as measured by DOFRS with 1 m spatial resolution in half-period 113 during 2022. Whereas the BLMs are installed at the same positions in each half-period, it can be observed that those values are not linearly proportional to the DOFRS measurements, due to i) local shielding (e.g. from corrector magnets), ii) different loss mechanisms, or iii) issues (e.g. calibration) with either of the monitors.

Studies of the arc radiation environment are critical for the protection of the electronic systems to estimate the dose levels that the equipment, such as ALPS, encountered. The radiation levels measured in nearby locations are used in combination with empiric and/or simulation scaling factors to estimate the dose directly at the equipment position. The passive dosimeters provide accurate dose measurements, the spatial pattern of the localised dose peaks strongly depends on accelerator parameters, and therefore, only active monitoring systems allow for instantaneous mitigation actions related to electronics protection.

5.1.5 Summary

The main points concerning the analysis of SPS radiation levels in 2021 and 2022 are summarized below.

- For the first time a comprehensive study of the SPS radiation environment was performed, focusing on the driving beam loss mechanism. It was shown, that in the majority of the SPS locations, beam losses happen at the low (injection) energy, due to the uncaptured beam. It was measured that the beam extraction in LSS2 is inducing beam losses not only locally, but in several half-periods across the ring.
- Another novelty arises from the recently deployed DOFRS. The data, processed and analyzed for the first time in the scope of this work, allow for spatial monitoring of the dose along the accelerator. It was shown how the system can be exploited not only for beam diagnostics (together with BLMs) but also for the assessment of radiation levels on electronic systems.
- Based on the analysis of beam losses, it was shown that in the SPS arcs beam-residental gas interactions are not the dominant source of radiation, as opposed to the LHC.

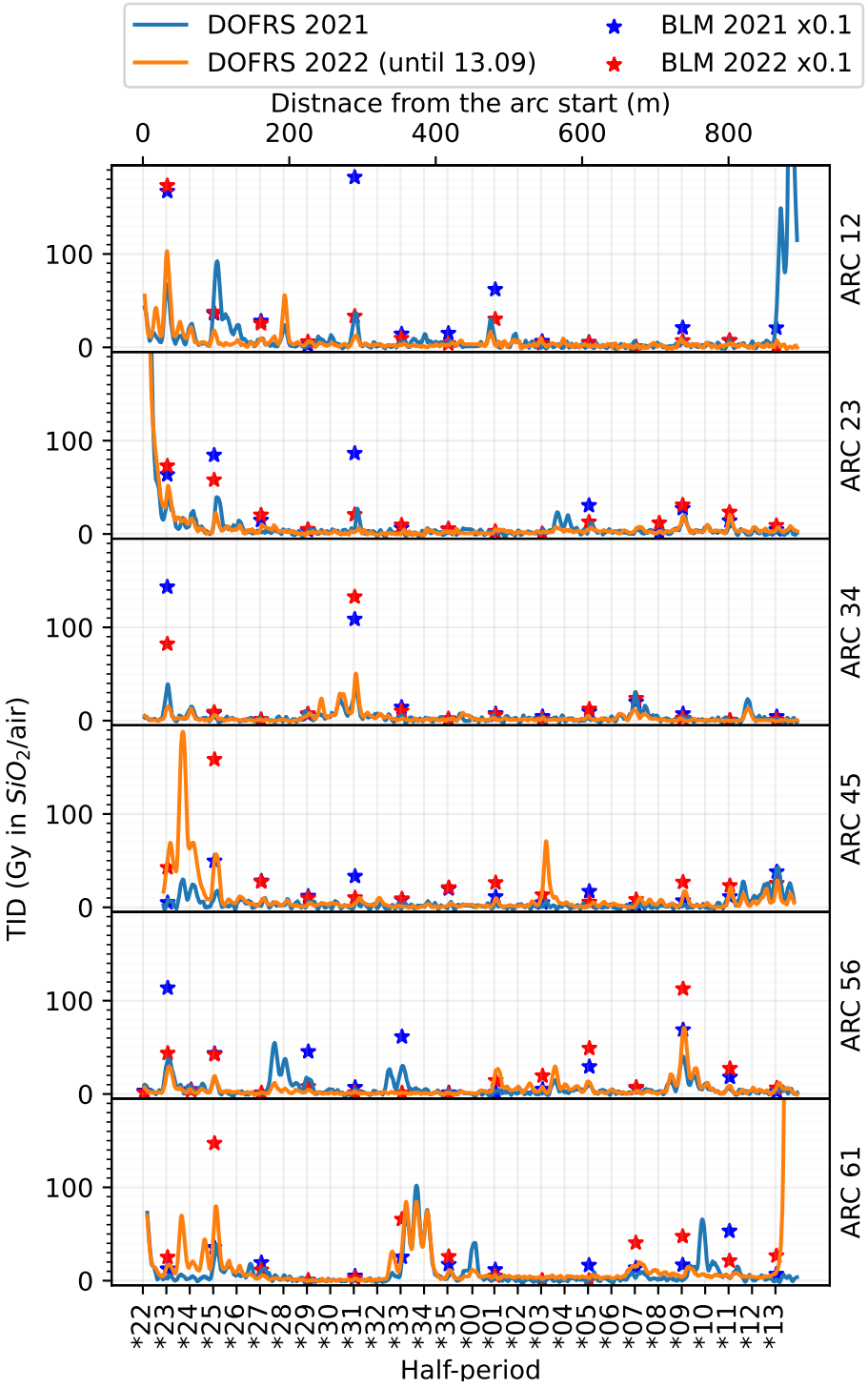

Figure 5.7: TID along SPS arc sectors as measured in 2021 and 2022 (until 13.09) by the DOFRS (dose in silica, 2 m spatial resolution) and BLMs (dose in air). For visibility purposes, the measurements by BLMs were divided by a factor 10.

5.2 Large Hadron Collider

5.2.1 LHC layout

The LHC has a circumference of nearly 27 km, and consists of 8 Insertion Regions (IRs), that are interconnected with 8 arc sections, through the Dispersion Supressor (DS) regions [140]. Each IR hosts, in its center, either an experiment or a system essential for the accelerator operation (e.g. collimators). The center of each IR is called the Interaction Point (IP). Each IR consists of a Long Straight Section (LSS), with two DS regions at both ends. A schematic drawing of the LHC is illustrated Fig. 5.8. Each of the sectors is arranged

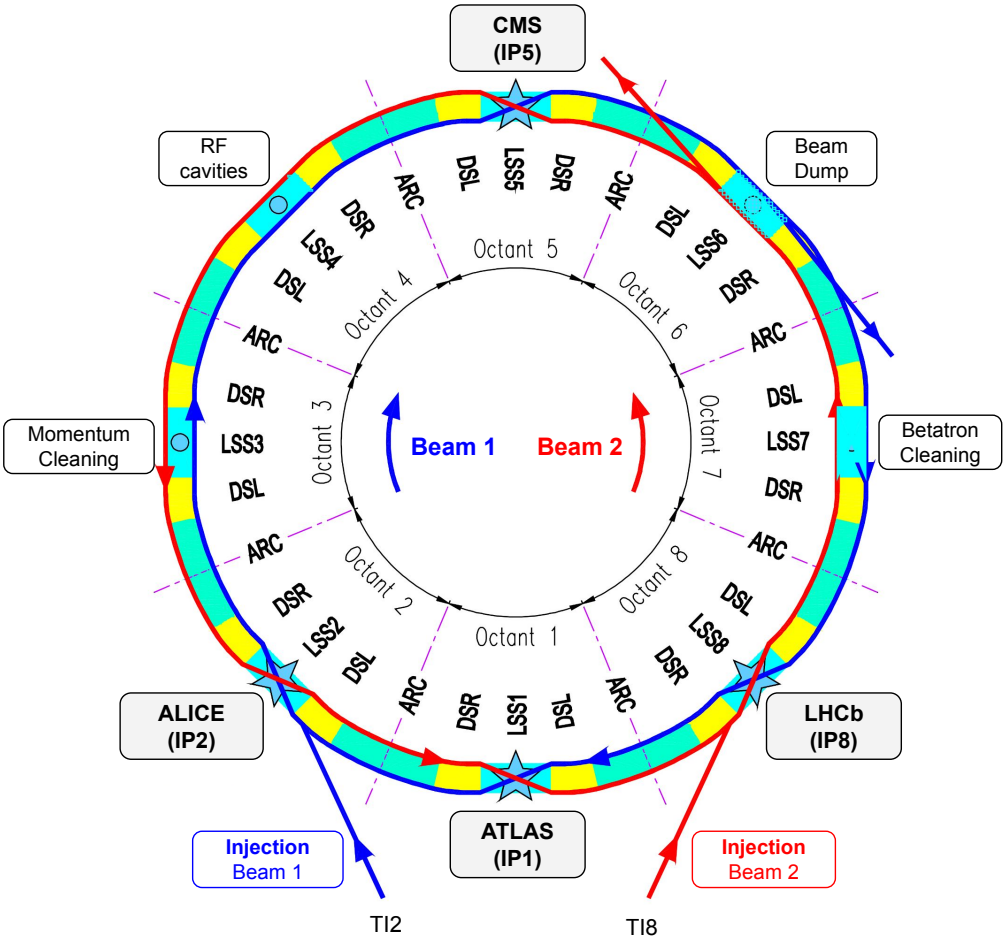

Figure 5.8: Layout of the LHC with the two counter circulating beams. Adapted from [140].

in so-called half-cells defined by the main quadrupole magnets. For example, the DS region starts in the 8^{th} and ends in the 11^{th} half-cell (inclusive). The LSS spans until the 7^{th} half-cell on both sides of an IP. The arc spans between the 12^{th} half-cells (numbering until 34^{th}) of two neighboring IRs. The role of DS regions is to interconnect and match the beam optics between LSSs and arcs, by reducing the horizontal beam dispersion through dedicated magnet settings. Arc sectors, through the dipole magnets, are responsible for the bending

and transport of beams between IRs.

LSS1 hosts the ATLAS experiment [141], one of the two high-luminosity experiments. The second one, CMS, is installed in LSS5 [142]. Additionally, LHC houses two smaller experiments, ALICE [143] and LHCb [144], located at the center of LSS2 and LSS8, respectively. Additionally, IR2 features an injection system for beam 1. The second beam, circulating counterclockwise, is injected in IR8.

The remaining four IRs are not hosting experiments but are critical for the operation of the accelerator. LSS3 and LSS7 contain collimators [145], used to remove particles that do not meet the desired acceptance in terms of momentum (IR3) or transverse position (IR7). LSS4 is responsible for beam acceleration, hosting RF cavities [146], and multiple other beam instruments. LSS6 functionality is dedicated to the beam dump system, allowing for a safe beam extraction [147].

5.2.2 LHC operation

The LHC is operated in fills, with each fill being defined as the period between the first beam injection and beam extraction. A typical LHC fill, depicted in Fig. 5.9, consists of several beam injections from the SPS, happening with a beam energy of 450 GeV. Later, after the accomplished injection phase, the beam is accelerated (ramped up) up to almost 7 TeV (6.5 TeV in 2018, 6.8 TeV in 2022). At the top energy, the accelerator is adjusted to provide colliding beams to the 4 experiments. Once the intensity or quality of beams is no longer optimal, or in case of an issue, the beams are extracted (dumped) from the accelerator and disposed of on the dump blocks around IR6.

The statistics of the 2022 operation, as compared to 2018, are presented in Tab. 5.2. In a nutshell, operation in 2022 achieved approximately 60% what was delivered in 2018 in terms of integrated intensity or integrated experiment luminosity (62%). Therefore, the 2022 radiation levels in multiple locations in the LHC are expected to be approximately 60% of what was measured in 2018.

It's worth noting that as 2022 was a recommissioning year, and even if the number of injected protons was close to 2018's value (90%), a significant fraction of the operation was not devoted to physics. An example of this is the scrubbing operation (high-intensity at injection energy) aiming at improving the accelerator vacuum and surface quality, as reflected in the ratio (2022 vs 2018) of a total number of protons dumped (0.96, i.e. 96%) or lost in collimation regions (81%). In 2022, fills with collisions at the experiments corresponded to 63% of 2018's injected intensity.

During a fill with collisions the intensity in the accelerator decreases primarily due to i) p-p interactions at the experiments (luminosity burn-off, σ =72 mb [149]), and ii) beam cleaning at the collimators in IR7 (dominating) and IR3, as given by Eq. (5.2.1). The other losses, e.g. due to beam-residual interactions are minor and are shadowed by the luminosity burn-off/collimation losses.

$$\text{injected} - \text{dumped} \approx \text{luminosity burn-off} + \text{cleaned in IR7(3)} \tag{5.2.1}$$

Table 5.2: Selected statistics of the LHC operation in 2018 and in 2022 [62, 148].

Quantity	2018	2022	unit	2022/2018 ratio
protons' energy	6.5	6.8	TeV	1.05
Duration with beam	141	101	days	0.72
incl. collisions only	79	44	days	0.55
Injected protons	15.0	13.5	10^{16} p	0.90
incl. collision fills only	10.7	6.7	10^{16} p	0.63
Dumped protons	11.5	11.0	10^{16} p	0.96
incl. collision fills only	7.4	4.8	10^{16} p	0.65
Protons lost due to luminosity burn-off	1.9	1.2	10^{16} p	0.63
Time-integrated intensity	30.6	17.9	10^{20} ps	0.58
incl. collision fills only	29.1	15.8	10^{20} ps	0.54
Lost in IR3 and IR7	1.6	1.3	10^{16} p	0.81
incl. collision fills only	1.3	0.64	10^{16} p	0.49
Total experiment integrated delivered luminosity	134	85	fb^{-1}	0.63
incl. CMS experiment	68	42	fb^{-1}	0.62

5.2.3 Beam Loss Mechanisms

Depending on the accelerator region the beam loss mechanism behind the radiation varies. In the experimental IRs (and sometimes in the neighboring arcs), the dominating beam loss source is collision debris, which is lost or intercepted by collimators in the experimental IRs. In such regions, the dose rates scale with the luminosity of experiments. An example of the dose rates measured in the various LHC locations, affected by different beam loss mechanisms, are depicted in Fig. 5.9. Close to the CMS experiment (or more generally the LHC experiments), dose rates scale with the respective experiment luminosity as they originate from the lost collision debris. In the long term, the related dose scales with the integrated luminosity of the experiment, as illustrated in Fig. 5.10. In the injection regions, the losses occur mostly during beam injections, at 450 GeV. Losses at the collimation region depend on the operation of the collimators (aperture) that might vary within an LHC fill. In the arc sectors, the losses are, in relative terms, low, and they rise during acceleration, with the increasing beam energy.

Another significant mechanism of beam loss is collimation, a procedure aiming at removing the particles that, due to scattering, do not meet the desired parameters. They are intercepted in these specially designed regions, such as in IR7 or IR3, that are able to withstand annual radiation levels of a few hundreds of kGy. For constant energy, the dose scaling in the collimation regions is, in first approximation, proportional to the number of protons that are intercepted, as depicted in Fig. 5.10.

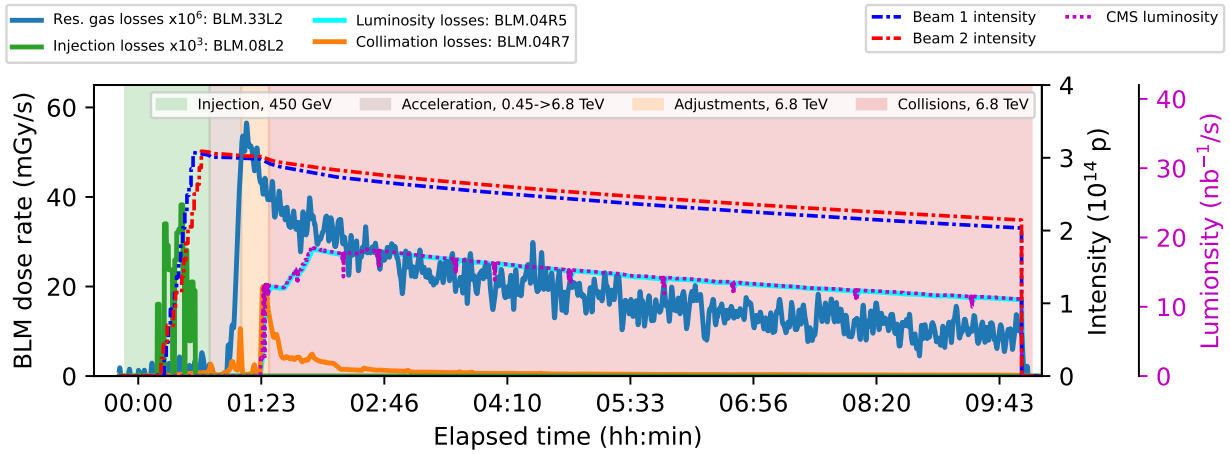

Figure 5.9: Dose rate over the LHC fill #8228 (2022-10-04 18:09:14 to 2022-10-05 09:52:13 UTC) measured by BLMs in the selected LHC regions, affected by the different beam loss mechanisms, together with the CMS experiment luminosity, beam intensities, with highlighted accelerator state. The long-term dose evolution for the selected monitors is depicted in Fig. 5.10. LHC CMS experimental region, collimation region, and in the LHC arc.

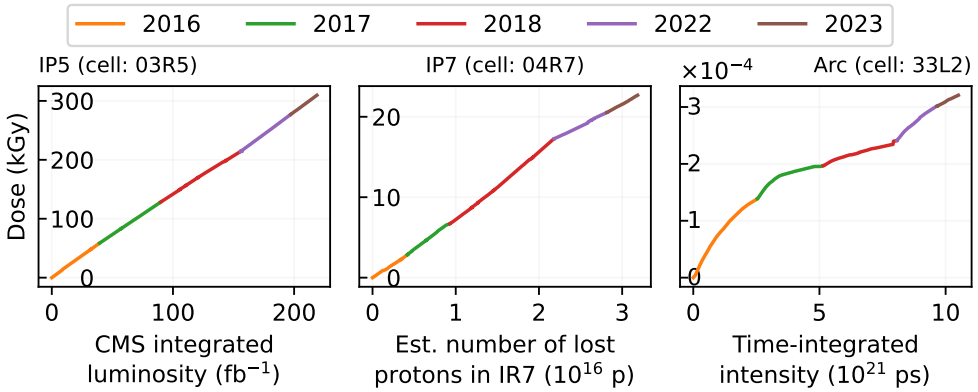

Figure 5.10: Examples of dose evolution over i) CMS experiment integrated luminosity (left side), ii) the estimated number of lost particles in the collimation regions (center), iii) time-integrated beam intensity; as measured by the BLMs in different locations of the LHC during 2016-2023 operation, illustrating the impact of different beam loss mechanisms (collision debris, collimation, beam-residual gas interactions) on the dose measurements.

In the arc sectors, the dose levels are driven by the interactions of the beam with residual gas molecules. The levels are proportional to the residual gas density and the time-integrated beam intensity. As the residual gas density varies with time [4], the linearity between dose and time-integrated beam intensity is not preserved over long periods, as shown in Fig. 5.10.

5.2.4 Radiation levels in 2022

5.2.4.1 Long Straight Sections

Radiation Levels in the IRs are driven by the functionality of each region. In the case of experimental IRs (1,2,5,8), the dominating radiation sources are the off-momentum particles and collision debris that are intercepted by the collimators and other aperture restrictions, leading to radiation showers.

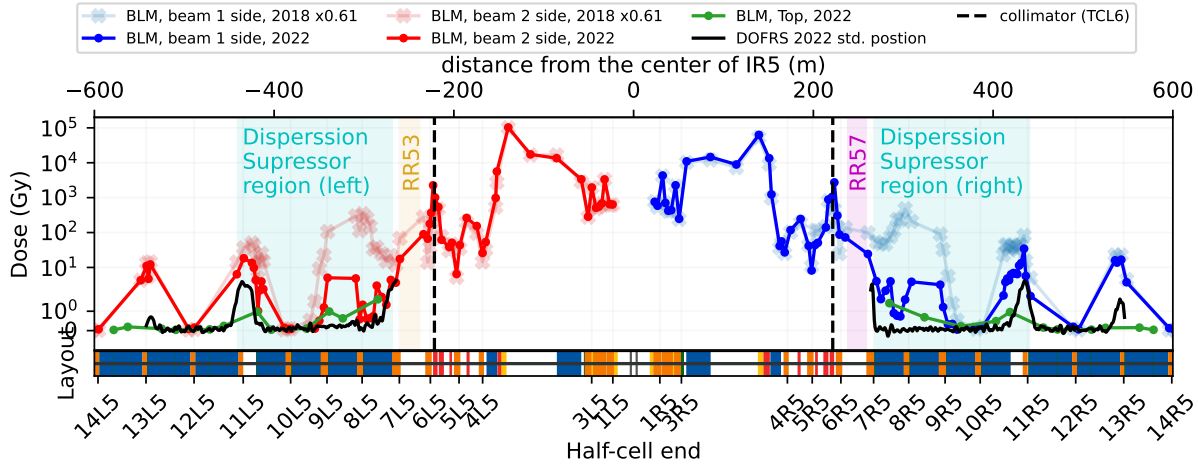

Figure 5.11: TID levels in the IR5 (region of the CMS experiment, highlighted in Fig. 5.8), as measured in 2018 and 2022 by the BLMs. The smaller aperture of TCL6 collimators led to higher local losses (once normalized, increase in dose by a factor 20) and significant loss reduction in the half-cells of DSs (reduction in normalized dose over a factor 400). dose levels measured in 2018 were multiplied by a factor of 0.62 which is equal to the ratio of the integrated luminosities between 2022 and 2018.

Focusing on the IR5 that hosts the CMS experiment, a comparison between integrated luminosity-normalized dose levels measured by BLMs is presented in Fig. 5.11. In the regions less than 200 m away from IP5, the normalized dose levels are fully comparable in 2018 and 2022. Then, around the TCL.6 collimators, designed to intercept the collision debris and particle showers, the normalized dose levels increased up to a factor of 20 due to their tighter aperture. In 2018, these collimators were fully open (no beam interception) [150], whereas in 2022 they were closed to ± 25 mm, corresponding to 17σ in terms of beam size [151]. This affected radiation levels in the shielded alcoves RR57 (right side of IP5, depicted in Fig. 5.14) and RR53. For example, as depicted in Fig. 5.15, the increase in luminosity-normalized HEHeq was about factor 3. Despite this local increase, there was a significant reduction in the DS regions, where multiple electronic systems are installed. Similar conclusions can be drawn for IR1, depicted Fig. 5.12, where the ATLAS experiment is located.

As depicted in Fig. 5.13, the dose levels measured during collision time by BLMs in IR7, as a function of the protons lost at the collimator regions (IR7 and IR3) slightly decreased. This is also illustrated in Fig. 5.10. The comparison of the entire annual operation between 2018 and 2022 is not representative, as during 2022 collimators have been extensively used due to recommissioning, e.g. during scrubbing.

The ALICE region (IR2) is mainly dedicated to the operation involving heavy ions, therefore during

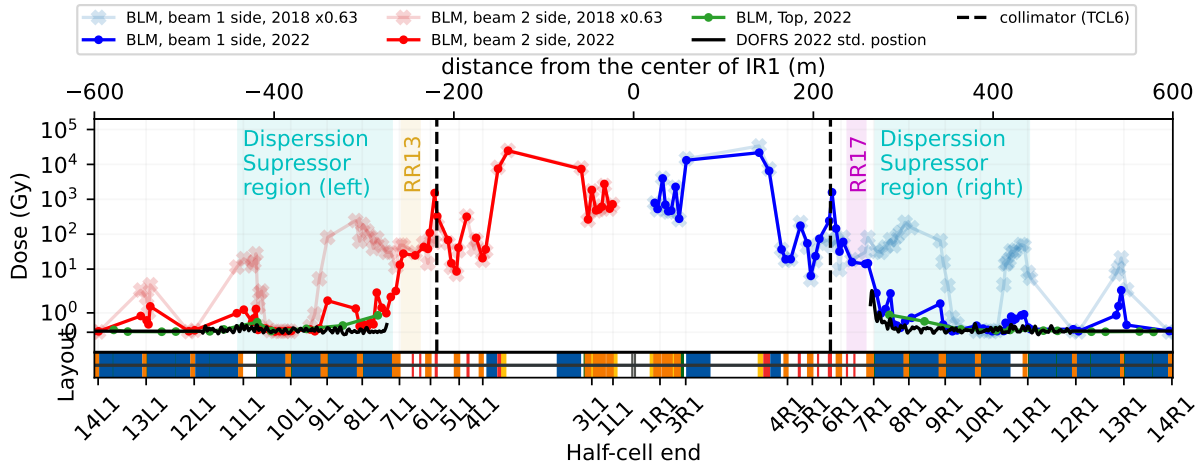

Figure 5.12: TID levels in the IR1 (region of the ATLAS experiment), as measured in 2018 and 2022. The smaller aperture of TCL6 collimators lead to higher local losses (once normalized, increase in dose by a factor 20) and significant loss reduction in the half-cells of DSs (reduction in normalized dose over a factor 400). dose levels measured in 2018 were multiplied by a factor of 0.63 which is equal to the ratio of the integrated luminosities between 2022 and 2018.

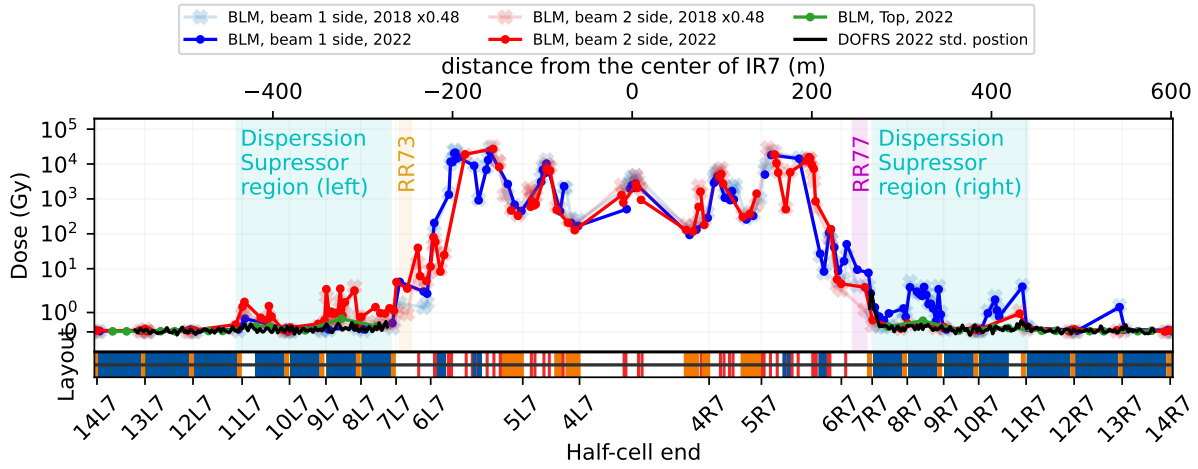

Figure 5.13: TID levels in the IR7 (one of the collimation regions), as measured in 2018 and 2022 by BLMs during collision time. The smaller aperture of TCL6 collimators led to higher local losses (once normalized, increase in dose by a factor 20) and significant loss reduction in the half-cells of DSs (reduction in normalized dose over a factor 400). dose levels measured in 2018 were multiplied by a factor of 0.48 which is equal to the ratio of the integrated luminosities between 2022 and 2018.

(a) LHC's tunnel and RR57 alcove **(b)** electronics at the ground floor of RR57

Figure 5.14: RR57 shielded alcove in the proximity of the LHC, consisting of two floors: ground one is shielded with concrete wall as opposed to the unshielded first floor. The alcove is equipped with several electronic systems, including PCs and RadMons. Similar alcoves are on the opposite side of IP5, in IR1 and IR7. Image source: CERN Geographic Information System.

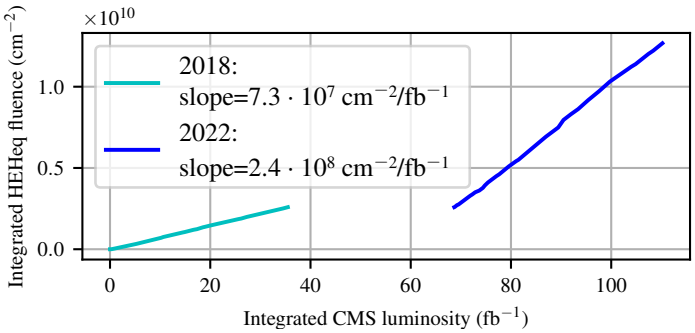

Figure 5.15: Evolution of the HEHeq fluence measured by RadMon deployed in the LHC tunnel, at the wall of the RR57 shielded alcove (highlighted in Fig. 5.14a), as a function of the integrated luminosity of the nearby experiment, i.e. CMS. The change in the slope between 2018 and 2022 is caused by a tighter collimator aperture (TCL6), leading to higher local losses. The gap between the curves is due to the unavailability of the RadMon data at the end of the 2018 operation.

standard p-p operation the measured dose levels are low, below 260 Gy in 2022 BLM measurements. Moreover, IR2 is a region where Beam 1 is injected into the LHC.

The LHCb region (IR8) was upgraded during the LS2, aiming to increase the experiment luminosity (number of collisions) in Run 3. In 2022 no significant changes in dose profiles were observed. The ratio between annual values of integrated luminosities for LHCb was 0.43. With the planned luminosity increase as of 2023, higher radiation levels are expected [152]. In addition to the experiment, IR8 is an injection region for Beam 2.

Losses in the remaining IR4 and IR6 are mainly caused by the accelerator systems necessary for the operation. In particular, in IR4 the dominating radiation source term is Beam Instrumentation [153], for example, Beam Gas Vertex demonstrator [154]. In 2022, in the 6^{th} and 7^{th} half-cells of the right side of IR4, an increase of up to factor 12 with respect to 2018 was observed, likely due to vacuum issues. IR6, hosting

beam dump system, the dose levels are mostly due to halo particles induced in IR7 [155]. No significant changes in the dose profile were observed, with the maximum increase within factor 1.7.

5.2.4.2 Dispersion Supressors

DS regions are the first regions where radiation levels generally allow for the use of radiation-tolerant COTS-based custom electronics systems. The measured dose levels in the DS regions of IR1 and IR5 in 2022 were reduced by more than 2 orders of magnitude (x800 for a BLM with the highest reduction) with respect to 2018, as depicted in Fig. 5.11 due to the smaller aperture of TCL6 collimators, that intercept the radiation showers created in the IPs.

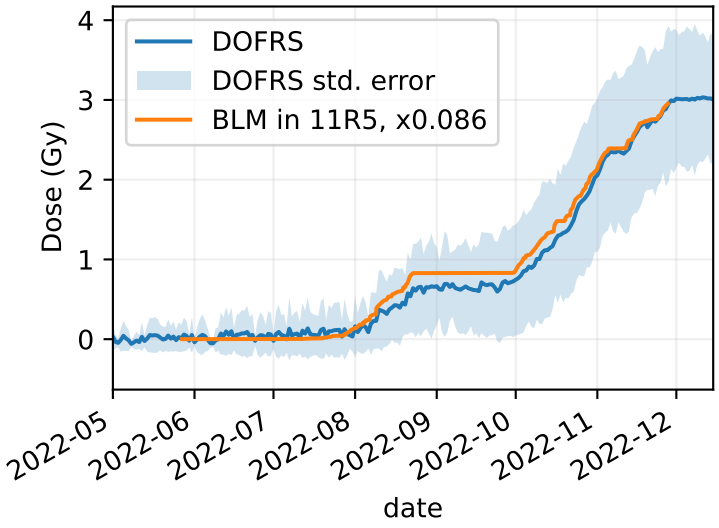

Figure 5.16: Evolution of the dose over time as measured by the "top" BLM installed in the 11$^{\text{th}}$ half-cell at the right side of IP5, and by the DOFRS system at the same location (2 m spatial resolution, averaged between 13 764 m $<$ dcum $<$ 13 774 m).

As of 2021, the DS regions of IR1,5 and 7 have the DOFRS system installed. Due to the aforementioned reduction, dose levels as measured by the fiber are below 10 Gy, as depicted in Fig. 5.11, Fig. 5.12 and Fig. 5.13. Focusing on the dose peak on the right side of IP5 (11$^{\text{th}}$ half-cell), Fig. 5.16 illustrates the dose evolution during 2022 operation, as compared with the BLM installed in the peak's proximity. The relative dose evolution for both sensors is in very good agreement. As opposed to IR, it can be observed (Fig. 5.12), that in the case of IR1, peaks in the 11$^{\text{th}}$ half-cells are below the fiber's detection limit. This is likely due to differences in the radiation profiles between IR1 and IR5, as similar conclusions can be drawn based on BLMs measurements, especially those installed on top of the dipole magnets, located approximately in the same plane as DOFRS.

Moreover as depicted before, the DOFRS system covers partially LSS1, LSS5, and LSS7, however with varying lateral sensor positions, and therefore resulting in a more challenging dose profile to interpret.

5.2.4.3 Arcs

In the LHC arc sections, the arrangement of both main magnets and radiation detectors is periodic, as illustrated in Fig. 5.17. The expected dominant beam loss mechanism is due to inelastic interactions of the

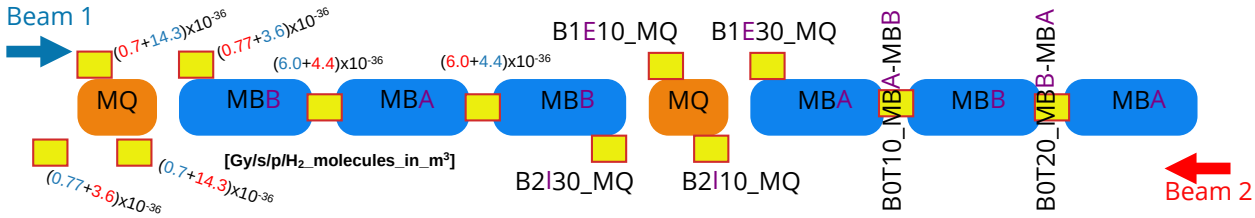

Figure 5.17: Schematic representation of the LHC arc FODO cell with the BLMs locations (yellow rectangles). MQ denotes quadrupole magnets whereas MB(B/A) dipole ones. There are six different locations (BLM families) of BLMs with respect to the half-cell: four on the beams plane (B1_10, B1_30, B2_10, B2_30), where B1s are located closer to the beam 1 and B2s closer to beam 2; and two on top of the interconnection between dipole magnets (B0T10, B0T20). Magenta colour letters vary depending on the half-cell. Additionally, FLUKA simulated values of BLM response due to beam-residual gas interactions have been added. For example, if $N_2 = 3 \times 10^{14}$ p circulated in the Beam 2 of the LHC with a residual gas density of $\rho = 10^{12}\,\mathrm{H_2}$ in m^3, B0T10 BLM would measure $\dot{D} = 4.4 \times 10^{-36} \cdot 3 \times 10^{14} \cdot 10^{12} = 1.3\,\mathrm{nGy/s}$. If at the same time, the same amount of intensity $N_1 = 3 \times 10^{14}$ p circulated in Beam 1, the BLM would measure $\dot{D} = 1.3 + 6 \times 10^{-36} \cdot 3 \times 10^{14} \cdot 10^{12} = 3.1\,\mathrm{nGy/s}$. Adapted from: [67].

beam with residual gas molecules present in the vacuum chamber. An example of the measured dose rate due to that mechanism is depicted in Fig. 5.9. The collision probability, over a path between coordinate s_1 and s_2, is given by Eq. (5.2.2), where i iterates over the gas constituents, σ_i stands for the respective cross-section and ρ_i for residual gas density (molecules in a given volume). It is assumed that the only gas present in the vacuum is $\mathsf{H_2}$. The real composition includes other gas molecules (CO, $\mathsf{CO_2}$, and $\mathsf{CH_4}$), however, their contribution can be converted to hydrogen equivalent density, through the ratio of nuclear-scattering cross sections, and in this study, all results are given in $\mathsf{H_2}$ equivalent density [156]. Moreover, it will be assumed that the residual gas density $\rho(s)$ is constant within each arc section, and hence the results will be an "average" arc behavior. Considering the assumption and expanding the exponential term of Eq. (5.2.2) into Maclaurin series, $p \approx \sigma\rho(s_2 - s_1)$. The collision rate will be therefore proportional to $p \cdot f \cdot N$, where N is the number of circulating protons (beam intensity), f is the revolution frequency (number of times each particle passes through the arc in one second), $d = s_2 - s_1$ is the arc's length, as per Eq. (5.2.3).

$$p = 1 - \exp\left(-\int_{s_1}^{s_2} \sum_{i}^{\mathrm{gas_i}} \sigma_i \rho_i(s')\mathrm{d}s'\right) \tag{5.2.2}$$

For a given energy (thus a given inelastic interaction cross-section σ), the related typical (*baseline*) dose rates ($\dot{D}$) in a fixed position are proportional to the beam intensity (N) and the residual gas density (ρ). The proportionality is through the LHC beam revolution frequency f and the length of interaction regions (d).

$$\dot{D} \propto \frac{\mathrm{d}N(t)}{\mathrm{d}t} = -f \cdot d \cdot \sigma(E) \cdot \rho(t) \cdot N(t) \tag{5.2.3}$$

It is assumed that inelastic $\sigma_{\mathrm{p-H}}$ in the case of 6.8 TeV scattering at a resting proton is $\sigma_{\mathrm{p-H}} \approx 40\,\mathrm{mb}$ [157], which is equal to $\sigma \equiv \sigma_{\mathrm{p-H_2}} \approx 80\,\mathrm{mb}$ for the hydrogen molecule. As it was previously shown [67], the

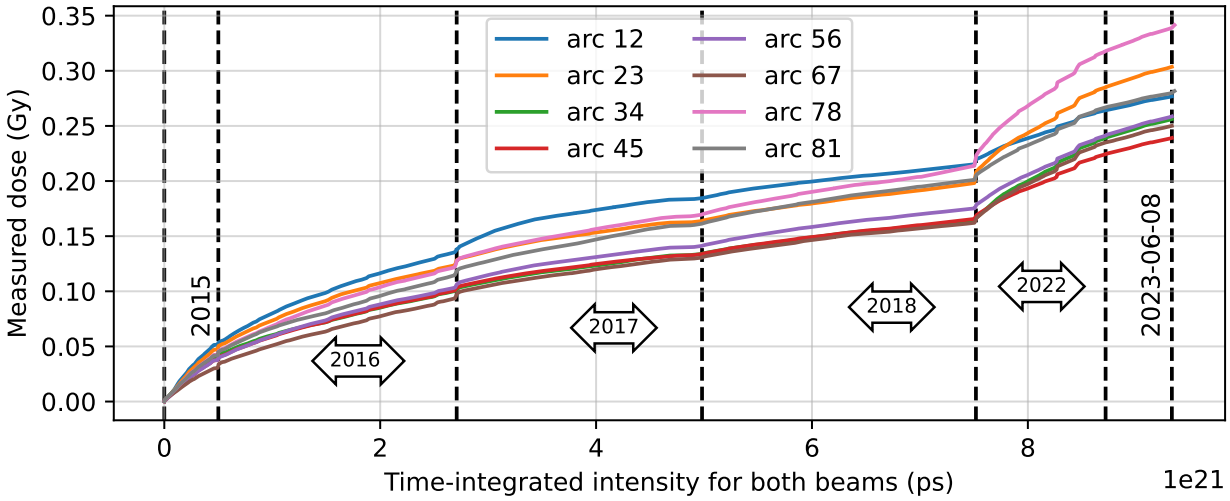

Figure 5.18: Evolution of the baseline dose level as measured by top BLMs (installed on top of the dipole magnets) as a function of the time-integrated beam intensity for both beams (top energy only).

majority of the BLMs in a given arc measures similar, low dose levels (in comparison due to other locations along LHC), that are denoted as *baseline*. These dose values are driven by the quality of the vacuum along the accelerator (ρ in Eq. (5.2.3)). Fig. 5.18 depicts the long-term (over a few years) evolution of the typical (median) dose levels ($\int \dot{D}\mathrm{d}t$) as a function of the time-integrated intensity ($\int N(t)\mathrm{d}t$) per arc sector. Only one detector family, i.e. having the same location with respect to a half-cell, was considered. Noteworthy, the slope is not constant, implying that ρ changes over time, as the other (f, d) parameters are fixed. In 2022 there is a factor 2.2 increase in the intensity-normalized dose versus 2018, likely due to the worse vacuum quality after the LS2 (years 2019-2021). The trend observed in 2022 is, however, still similar to 2015, the first year after LS 1 restart. It has to be pointed out that the proton's energy has been increased (from 6.5 TeV to 6.8 TeV) as of Run 3, however, this resulted in the negligible change of interaction cross-section $\sigma_{\mathrm{p-H}}$ and the related secondary shower. According to Eq. (5.2.3), the residual gas density is proportional to the intensity-normalized dose rate $\rho \propto \frac{\dot{D}}{N}$. In addition to the long-term conditioning, i.e. vacuum quality improvement observed indirectly in Fig. 5.18, within each LHC fill a dynamic decrease of residual gas was observed [4], as depicted in Fig. 5.19. As illustrated in Fig. 5.20, extending the analysis towards multiple LHC fills, one can identify two trends i) short-term, that manifests in the normalized dose rate (thus the dynamic density) decrease within each fill, and ii) long-term, resulting in the reduction of the normalized levels and the variability within the fills. An explanation could be one of the beam-vacuum chamber-related mechanisms, for example, the electron-cloud effect [158], leading to the production of secondary electrons that, after hitting the vacuum chamber, would result in the desorption of the molecules. However, this is highly unlikely as on the 4^{th} of September 2017 the LHC filling scheme was changed, increasing the spacing between some bunches, to reduce the e-cloud effect, hence the heat load on the cryogenic system [159]. This was accomplished and the related loads were reduced by about a factor 2 (Fig. 5.22). On the other hand, the change was transparent for the normalized dose rates, as depicted in Fig. 5.21.

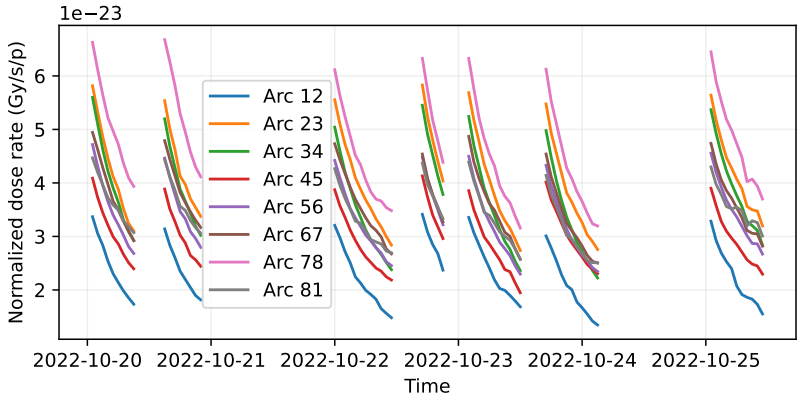

Figure 5.19: Baseline dose rate during physics production (beam collisions), normalized with the beam intensity, as a function of time for several LHC fills in 2022.

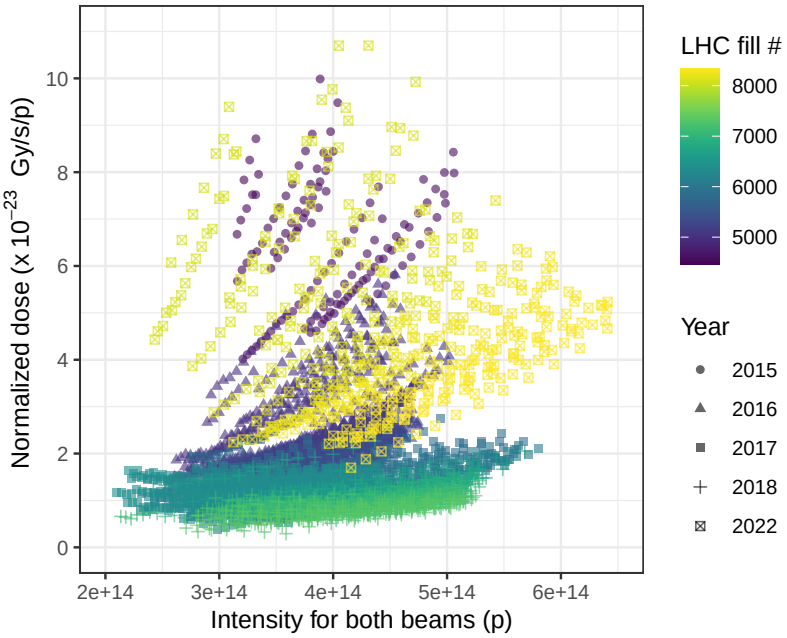

Figure 5.20: Normalized baseline dose rate (as calculated by the top BLMs) in Arc 34 of the LHC as a function of the intensity for both beams. Each point corresponds to the 1 h averaged value during physics collisions. The considered fills span between 2015 and 2022.

Another more likely explanation is synchrotron radiation [160], proportional to the beam intensity $N(t)$ which leads to the production of photoelectrons and secondary electrons, that lead to the desorption from the vacuum chamber surface, due to both photon and electron-stimulated desorptions [161, 162]. The observed effect could be also due to an ion-induced desorption [163]. In the case the proton ionizes the residual gas molecule, the created ion is accelerated towards the vacuum chamber wall by the beam's potential, leading to molecules' desorption. In all desorption types, yields of released molecules depend on the properties and treatment history of the vacuum chamber wall. This is described by the molecular desorption yield

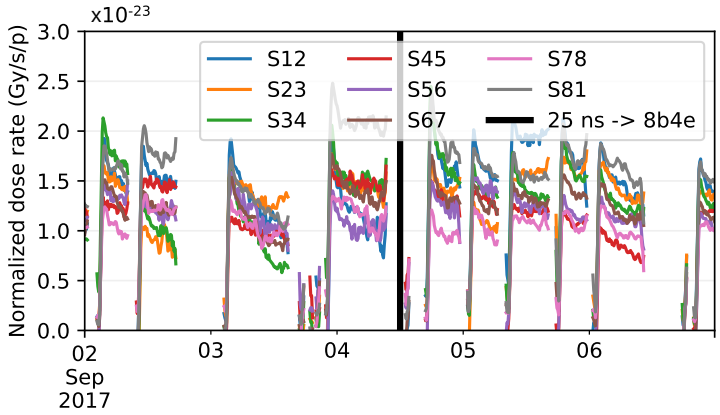

Figure 5.21: Evolution of the baseline dose rate normalized to the beam intensity over several fills in September 2017. On the 4th of September, the accelerator filling scheme was changed to reduce the impact of the e-cloud effect on the heat load of the cryogenic elements. Whereas this change reduced the heat load by more than a factor 2, as illustrated in Fig. 5.22, the baseline dose rates were not impacted, implying that they are not impacted significantly by losses due to e-cloud.

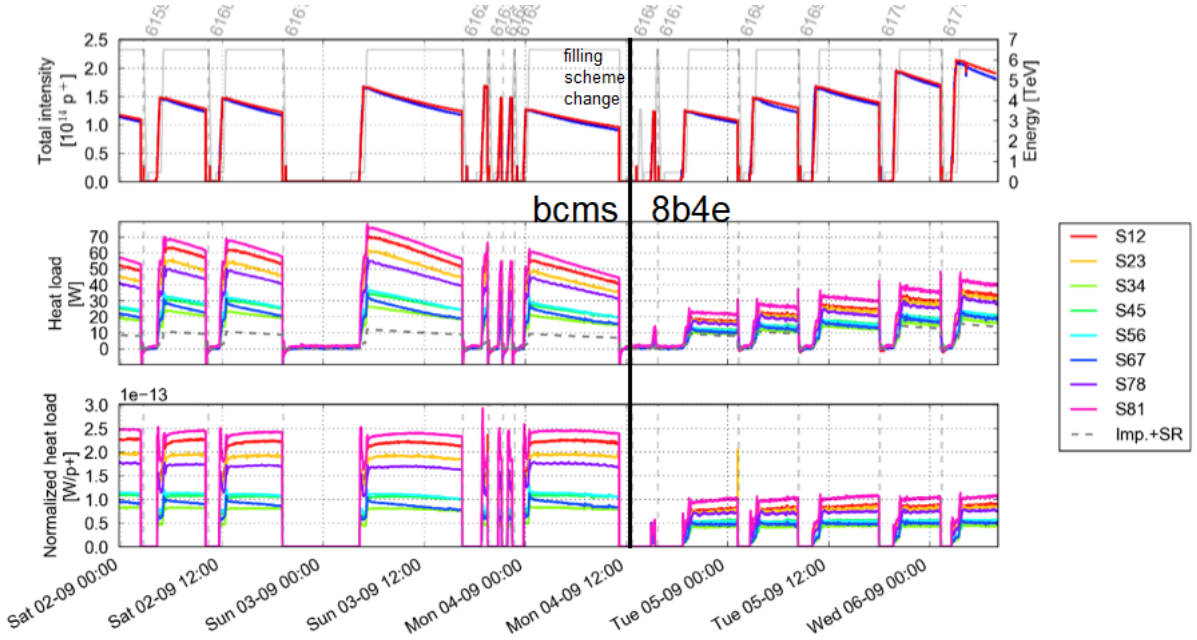

Figure 5.22: Evolution of the beam intensities (top), heat load to the cryogenic system (middle) and heat load normalised to the total intensity for the eight LHC arcs (bottom) over several fills in September 2017. On the 4th of September (black line), the accelerator filling scheme was changed to reduce the impact of the e-cloud effect on the heat load of the cryogenic elements [159]. Whereas this change reduced the heat load by more than a factor 2, the baseline dose rates, depicted in were not impacted, implying that the baseline dose rates are not impacted significantly by losses due to e-cloud. Image Credit: Giovanni Iadarola/CERN [159].

η. The respective yields are a power function (negative exponent α) of the number of impacting particles

and decrease with the accumulation of desorption events [162], i.e. $\eta \propto \left(\int_{start}^{now} N(t)\mathrm{d}t\right)^{-\alpha}$. The decrease in desorption yields is likely a qualitative explanation of the long-term vacuum conditioning, whereas the short-term variability within a fill is due to the proportionality of the desorption mechanisms to the beam intensity.

$$\dot{D}(T) \propto \rho N \propto N\eta N \propto NN\left(\int_{start}^{T} N(t)\mathrm{d}t\right)^{-\alpha} \tag{5.2.4}$$

$$D \propto a\int_{start}^{now} N^2(t)\left(\int_{start}^{t} N(t)\mathrm{d}t\right)^{-\alpha}\mathrm{d}t + c\cdot(now-start) \propto \int_{start}^{now} N^2(t)\left(\int_{start}^{t} N(t)\mathrm{d}t\right)^{-\alpha}\mathrm{d}t \tag{5.2.5}$$

Following considerations described in Chapter C, the evolution of the dose rate due to synchrotron radiation

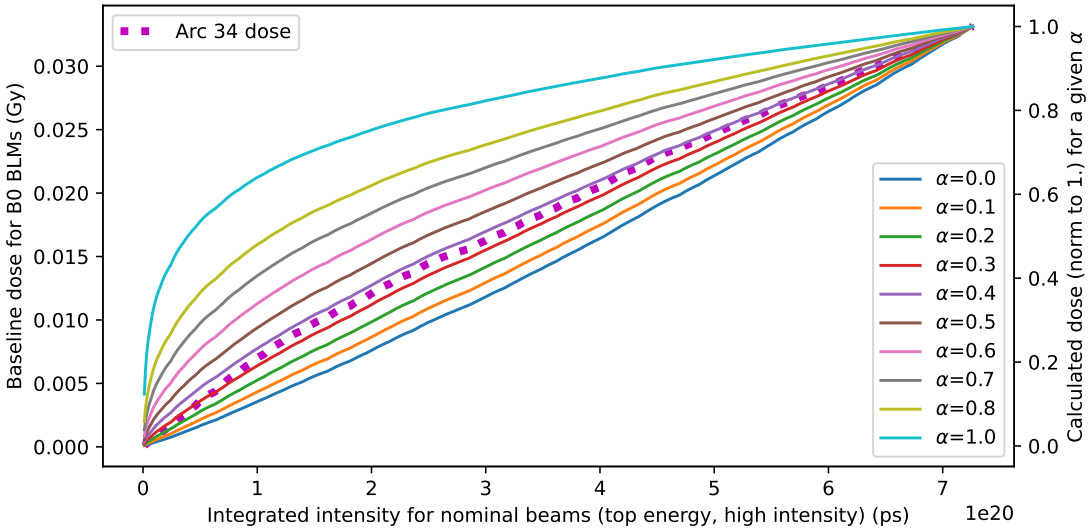

Figure 5.23: Evolution of measured dose in 2022 over the integrated intensity for both beams, together with relative dose modelled by Eq. (5.2.5) for different exponents ^{4}HeMeasurements at this plot are a subset (high intensity 2022 fills and arc 34) of measurements depicted in Fig. 5.18, corresponding to 2022 data points at Fig. 5.20.

and vacuum conditioning could be approximated with Eq. (5.2.4), where the first intensity factor comes from the linearity between given by Eq. (5.2.3), whereas the second is due to dynamic pressure increase due to photon-induced desorption. This simplification doesn't consider the effect of vacuum pumps, residual gas that is present without a beam, operation at different energies (e.g. scrubbing), and that the vacuum behaviour might be not due to one but multiple effects. Integrating Eq. (5.2.4) over time and neglecting time-dependent factor ($c = 0$ as dose needs to be dependent on intensity too), Eq. (5.2.5) can be obtained. It describes in relative terms the evolution of baseline dose as a function of the intensity-dependent integral. Focusing only on the 2022 operation with high intensity (over 2×10^{14} p per both beams) and top energy, depicted in Fig. 5.23, it can be observed that the measured value resembles the theoretical evolution given by Eq. (5.2.5) for $\alpha = 0.35$.

Similarly, as in the past studies [67], it is possible to indirectly retrieve the averaged annual residual gas density, by aligning the FLUKA simulations with the baseline BLM measurements [65, 67]. The simulation

geometry featured an LHC arc half-cell with the BLMs and provided radiation levels below the magnets, at the equipment height. The related profiles are illustrated in Fig. 5.25. Focusing only on BLMs installed on top of the dipoles' interconnectors, the simulations yielded a dose rate of 5.2×10^{-36} Gy/ps/H_2 molecules in m^3 (normalized to the intensity of both beams, i.e $N = N_1 + N_2$). As depicted in Fig. 5.24, in 2022 the densities increased by factors 3-5 compared to 2018's values. It is worth noting that, as opposed to Run 2, where arc 12 had the worst vacuum quality, in Run 3 arc 78 is the worst, a factor 2 worse with respect to arc 12 (that was the best in 2022). In 2022, the beam lifetime (time after the intensity decreases by a factor e) due to beam-residual gas interactions would be in the order of a few hundred days. At the end of Run 2, this value was around 4 years – 5 years. As anticipated, in 2023, the vacuum quality continues to improve, reaching 2016 values in June 2023.

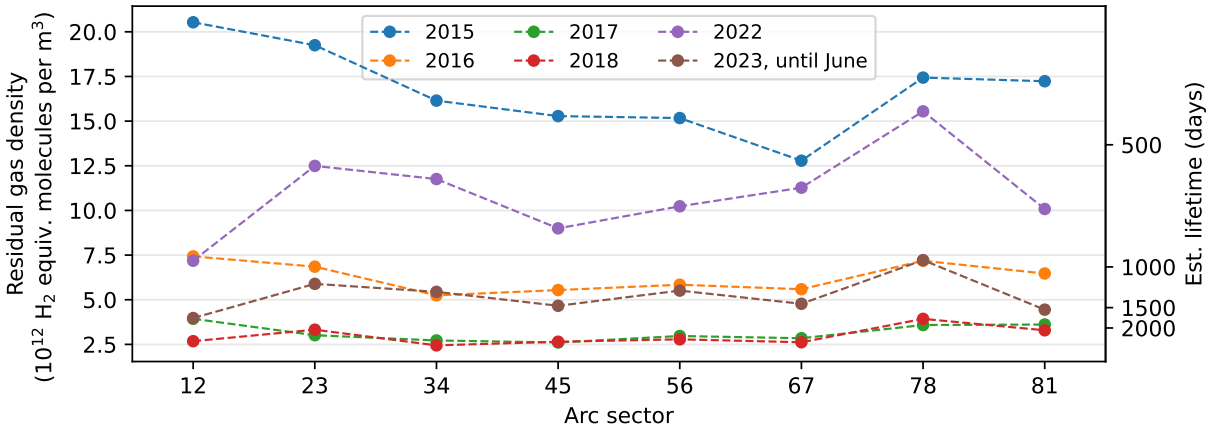

Figure 5.24: Annual residual gas densities averaged per arc sectors, as retrieved indirectly through FLUKA Monte Carlo simulations scaled to the dose measurements by top BLMs. The right y-axis represents the corresponding beam lifetime due to beam-residual gas interactions. Values for 2023 were retrieved based on the BLM data collected until 08.06.2022.

Profiting from past studies [67], depicted also in Fig. 5.25, it can be estimated that typical 60 A PC, installed below the middle dipole magnet, received a dose $D \approx 10^{13} \cdot 7 \times 10^{-36} \cdot 1.58 \times 10^{21} \approx 11$ mGy (assuming averaged residual gas density of 10^{13} H_2 equiv˙ molecules in m^3 and integrated intensity of 1.58×10^{21} ps). This dose is not a concern in terms of TID effects. However, analogous estimates for ϕ_{HEHeq} result in the annual value of 5.5×10^7 HEHeq/cm^2/year, posing a threat in terms of stochastic effects in the distributed accelerator systems.

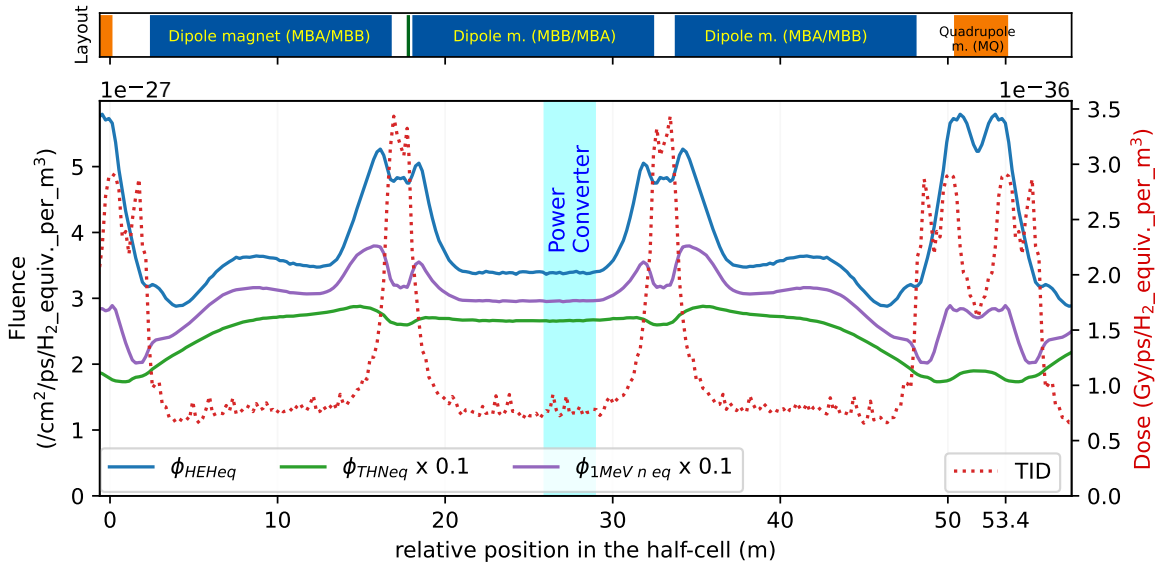

Figure 5.25: Particle fluences and dose below the LHC magnets (at the equipment level) as simulated using FLUKA Monte Carlo code, normalized to the H_2 equivalent gas density and to the integrated beam intensity (summed for both beams). Related studies presented in [67].

5.2.4.4 HEHeq and SEUs around the LHC

Underground areas at CERN, including those LHC-related, are equipped with RadMons. Fig. 5.26 illustrates the 2022 HEHeq-fluence measurements, focusing on the detectors installed in the DS (8^{th}<=half-cell<12^{th}) and arc (12^{th}>=half-cell) regions of the LHC. Additionally, measurements from the 16 detectors installed close to RR-shielded alcoves are presented. In the arc sectors, RadMons are installed close to the main quadrupole magnets, below the beamline, whereas around the shielded alcoves RadMons are installed at 3 possible locations (shielding wall, ground and first floors of an alcove).

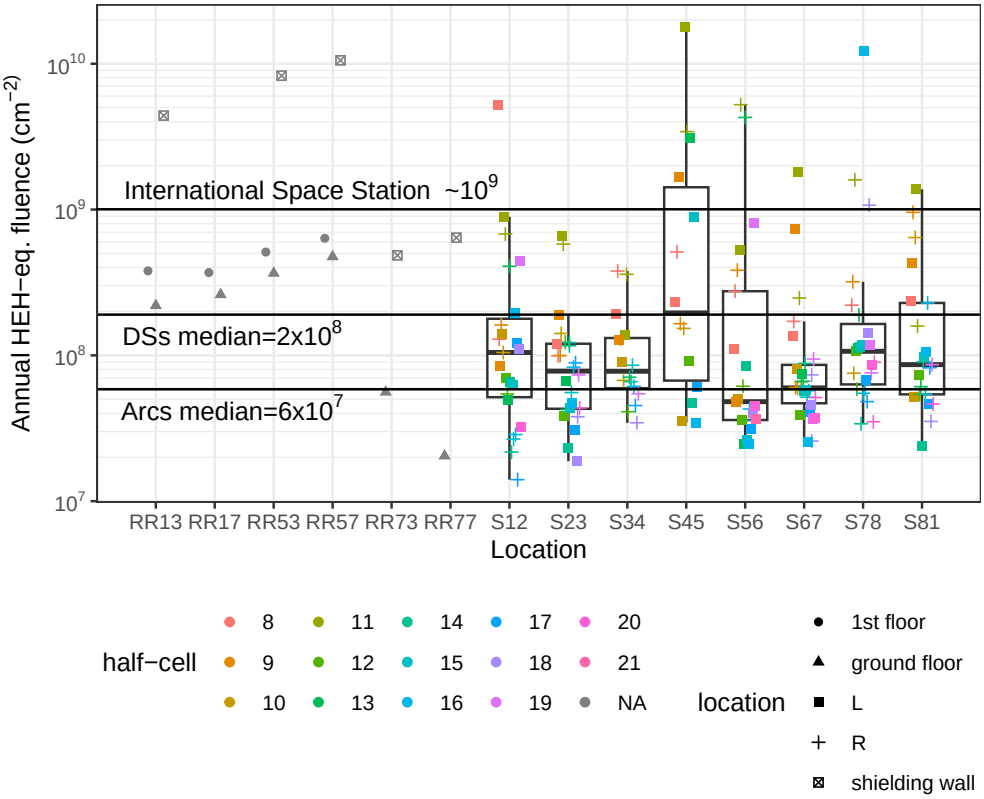

Figure 5.26: Annual HEHeq fluence measured by the CERN RadMons in 2022, in the DS/arc half-cells of the LHC tunnel and its shielded alcoves (RRs). Color denotes a half-cell number and the marker type refers to the side of an IP, in the case of RadMons under LHC magnets. For example, 16R in S78 corresponds to RadMon in the half-cell 16R8. In the case of RR alcoves, the marker type refers to 3 possible locations: the ground/first floors of the alcove or the LHC tunnel wall (in the proximity of the alcove).

Among considered detectors, the highest annual HEHeq levels were measured in the LHC tunnel, at the shielding wall of the RR53/RR57 alcoves ($\sim 10^{10}\,\text{cm}^{-2}/\text{year}$), in the 11^{th} half-cell of the left side of IR5, and in the 16^{th} half-cell of the left side of IR8. The median annual HEHeq measurement from the arc detectors is approximately equal to $6 \times 10^{7}\,\text{cm}^{-2}/\text{year}$, factor ~ 3 below the analogous value for monitors in the LHC DS regions. The majority of RadMon measurements is roughly one order of magnitude below the high-energy (>20 MeV) proton fluence values expected at the International Space Station ($\phi_{HEH} \approx 10^{9}\,\text{cm}^{-2}/\text{year}$ [24]). Yet, the ea level high-energy neutron fluxes are exceeded by the presented measurements by more than 2

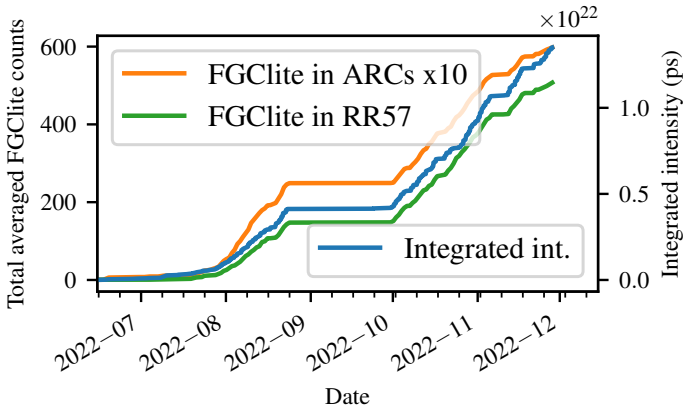

Figure 5.27: Averaged and integrated SEU counts as registered by the FGClite controller of the Power Converters located in the RR57 and in the arcs (multiplied by a factor 10 for visibility), together with the time-integrated beam intensity. Without a dedicated radiation-tolerant design a fraction of those events would have likely led to the R2E failures in the PC system.

orders of magnitude ($\phi_{HEH} \approx 2 \times 10^5\,\mathrm{cm}^{-2}/\mathrm{year}$ [164]).

In addition to RadMons, the LHC is equipped with another system capable of measuring SEUs, FGClite Power Converter (PC) controllers, although not being considered (yet) as a radiation monitor. The controllers are used to power the LHC magnets. Therefore, the PC type depends on the related magnet, and the magnet positions drive its deployment locations. The 752 units of 60 A-power-converter racks are installed along the LHC arc sectors, with 4 units installed in each half-cell, approximately 20 cm under the middle main bending dipoles, as depicted in Fig. 3.5b. The other power converter racks (120 A, 600 A, 4 kA, 6 kA) equipped with FGClite, 256 units, are installed in the 6 RR shielded alcoves, both at the beamline level and at the RR's first floor, as pictured in Fig. 5.14a. FGClite modules [165–167] feature 90 nm 8 Mbit Cypress SRAM (CY62157EV30LL-45ZSXI) onboard. This memory type is widely used for radiation-field characterization. The system is performing the SEU readout on a daily basis, providing a number of SEU/MBU counts per day. Whereas the primary system objective is not radiation monitoring, as will be demonstrated, the SEUs recorded by the FGClite controllers provide distributed information concerning the relative radiation environment.

As of 2022, Power Converters installed in the RR-shielded alcoves are equipped with FGClite controllers, featuring SRAM capable of measuring SEUs. An example of such a measurement is depicted in Fig. 5.27, where the averaged evolution of the counts over time is illustrated. The trend, as expected, is similar to the evolution of the integrated intensity, thus the integrated luminosity (although the two quantities might not be directly proportional to each other). As measured through the controllers, and depicted in Fig. 5.28, in 2022 radiation levels in shielded alcoves around IR7 (RR73 and RR77) were similar to the one observed in arc sectors. However, in the RR-shielded alcoves close to high-luminosity experiments, IR1 and IR5, the measured number of SEUs was more than a factor 10 higher with respect to the arc environment. Controllers in the shielded alcoves of IR1 (RR13 and RR17) had a slightly lower number of SEUs as compared with RRs of IR5 (RR53, RR57), which is consistent with the TID measured in the DSs of that IRs (Fig. 5.11,

Fig. 5.12).

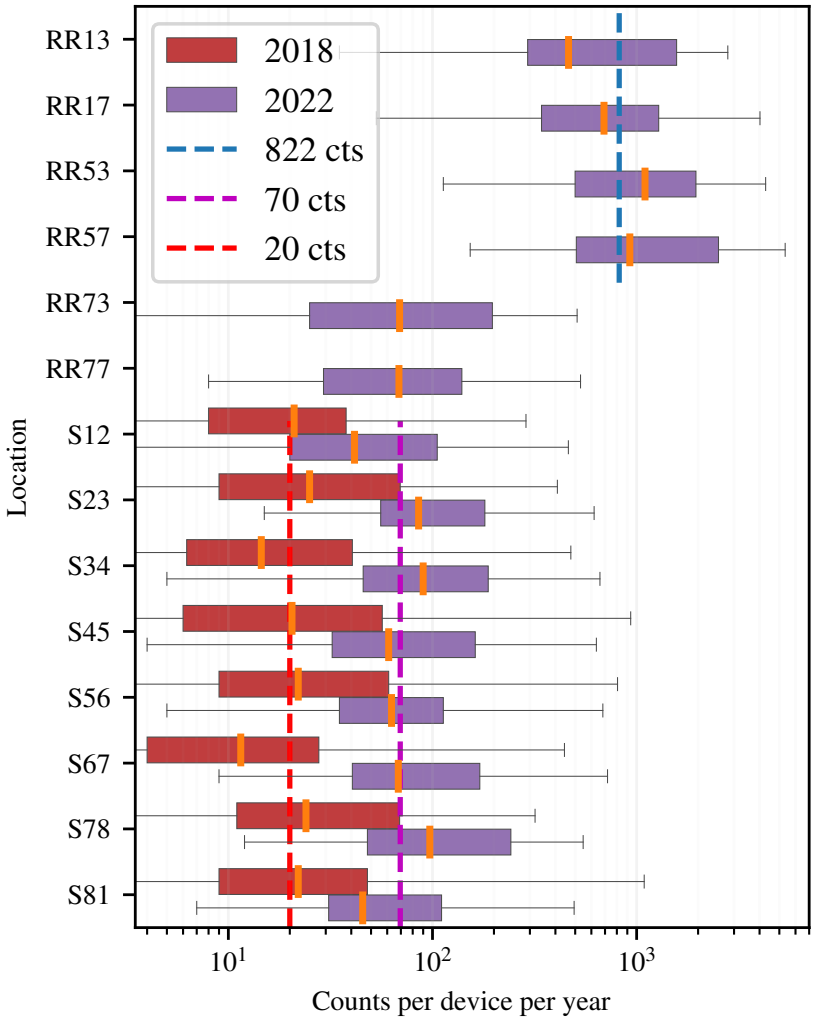

Figure 5.28: Boxplot representation of the annual 2022 SEU counts measured by the FGClite controllers of the Power Converters installed along arc sectors (S*NM*) and in the shielded alcoves (RR*NM*). Each arc region (arc/RR) is represented by a box that spans between the first and the third quartile, enclosing the middle 50% of measurements. The median value for each sector is denoted with orange bar and the whiskers correspond to the minimum/maximum measured value. Additionally, the median annual SEU count value for i) 2022 among racks in RR13/RR17/RR53/RR57, ii) 2018 among arc racks, and iii) 2022 among arc racks.

As depicted in Fig. 5.28, the degradation of the vacuum quality between 2018 and 2022 is reflected in the measurements from the FGClite controllers, distributed along the arc sections. The increase (median of the annual count of SEUs) of factor 3.5 between 2022 and 2018 is close to the dose increase (arc median value from "top" detectors) as measured by BLMs, equal to factor 2.1. Additionally, consistently with BLM-driven measurements, arc sector 12 had the lowest median value of SEU counts, and arc 78 the highest. Despite low radiation levels in terms of cumulative damage, HEH fluences are a threat to SEEs, especially in distributed

systems. However, in several locations, where other beam loss mechanisms dominate, the baseline dose levels are exceeded by up to 3 orders of magnitude [66].

Profiting from a large number of units of RadMons and 60 A-PCs in the arc sectors, it is possible to do very loose cross-calibration between both systems. As depicted in Fig. 5.26, the median measured annual HEHeq fluence was $6 \times 10^7\,\mathrm{cm}^{-2}$, which corresponded to the median value of 70 counts (Fig. 5.28) per year per PC. Assuming proportionality and into account the median value of SEU counts in RRs of IR1 and IR5, the estimated HEHeq value in the RRs would be $7 \times 10^8\,\mathrm{cm}^{-2}$/year that is close to the RadMon measured value (6 measurements between $2 \times 10^8\,\mathrm{cm}^{-2}$/year to $7 \times 10^8\,\mathrm{cm}^{-2}$/year following Fig. 5.26). Divagating further, one could estimate that if a single unit of PC was installed at the International Space Station, it would measure roughly 1200 counts annually.

5.2.5 Summary

- With the focus on the comparison of the measured radiation levels in 2018, the last year of Run 2, and 2022, the first year of Run 3, the analysis of dose across the entire LHC was presented. The differences were observed in the DS regions of ATLAS and CMS experiments, where the doses measured by BLMs were nearly 3 orders of magnitude lower in 2022. This was a result of the smaller effective collimator aperture, which intercepted more particles "before" the DSs. This reduction was beneficial for electronics systems located in that region. However, around the aforementioned collimators, locally higher radiation levels were observed, that propagated to nearby shielded alcoves (RRs). Fortunately, due to mitigation measures during the shutdown, i.e. deployment of radiation-tolerant controllers, this was transparent for the systems, namely PCs.
- In the LHC arcs the radiation is mainly driven by the beam-residual gas interactions. In the years 2015-2018, it was observed that the normalized dose levels decreased during the operation, which was attributed to the vacuum conditioning. In 2022, the first after the restart, related dynamics resembled the one observed in 2015, thus it is expected that in the following years vacuum quality will improve. Additionally, it was shown that the residual gas density changes within each fill, suggesting that additional processes such as synchrotron radiation or ion-induced desorption lead to the dynamic change of vacuum pressure.
- For the first time, SEU data from PCs were analysed, showing almost thousands of SEUs per device per year in RR alcoves. In 2022, the devices deployed in the arc sections measured about one order of magnitude less SEUs per device, however, still about factor 3-4 more than in 2018, due to vacuum quality degradation. The consistency of SEU measurements with other detectors, namely RadMons, suggest that PCs can be exploited for radiation measurements (at least in relative terms).
- Another novelty are the continuous dose profiles measured in some DS regions by recently deployed DOFRS. They were analysed for the first time in this work. However, as presented, in 2022 the radiation levels in DS regions were significantly reduced, therefore the potential of the system could not be fully exploited in 2022.

Chapter 6

Summary

6.1 Conclusions

The research presented in this study focused on two main areas: i) assessing the suitability and implementation of silicon solid-state detectors for beam and radiation monitoring, and ii) conducting comprehensive characterizations of the radiation environment within CERN's largest accelerators, namely the SPS and LHC. The first area utilized data collected from thirteen scientific experiments and bespoke software tools developed for efficient data analysis. The second branch benefited from multiple already-deployed radiation monitors including BLMs, DOFRS, and RadMon, which, after the development of the processing framework, collectively provided a comprehensive depiction of radiation levels along the accelerators and their temporal evolution, enabling their correlation to operational modes and the estimation of future radiation levels.

Profiting from the presented calibrations, the silicon detectors were exposed to various particle beams (protons, neutrons, heavy ions) in broad energy ranges, with the main goals of showing their versatile characterization capabilities and significantly enhanced sensitivity as compared with SRAM-based solutions, e.g. RadMon. Each solution has its advantages, however, it was demonstrated that in the low-intensity radiation environment, typical for locations where electronics systems are deployed, the improved sensitivity would accelerate the time required to collect meaningful statistics. This opens doors to measurements of radiation levels at the electronics locations during short slots, e.g. when the accelerator is operated with settings dedicated to future upgrades. The most profitable outcome was a cross-calibration of the Secondary Emission Chamber, within CHIMERA-HEARTS activity, allowing to provide beam intensity measurements to the internal (CERN) and external facility users (e.g. from European Space Agency). Another striking example of the detectors' potential was the discovery of a nonoptimal solution related to the LEIR accelerator, allowing for a complete beam loss within a ring, as opposed to beam extraction to a dedicated dump.

Regarding the second branch or research covered in this work, i.e. CERN's radiation environment, the key achievements relate to the SPS and the LHC. For the first time, prompt radiation levels in the SPS were analyzed in relation to the related beam loss mechanisms. This was possible due to a recent upgrade,

introducing BLM data logging with 5 ms resolution. This, focusing on the two most common machine modes, i.e. related to the North Area and LHC operations, allowed to investigate the origin of the losses. It was shown that, in the majority of the locations, the actual radiation is produced at the low (injection) energy. Another novelty was the exploitation of continuous dose profile data measured along the accelerator, revealing that there are multiple local radiation maxima, not covered by the other discrete monitors. In the related work [4], it was shown how the system can be used to anticipate radiation-induced issues with A Logarithmic Position System. Concerning the LHC, the most relevant findings related to the demonstration of similarities and differences between Run 2 (2015-2018) and Run 3 (2022 onwards) operations. In this respect, it was shown how the change of the collision debris collimator aperture and beam parameters resulted in the decreased dose levels along the dispersion suppressors, although at the cost of locally increased radiation in the proximity of the RR shielded alcoves. In the arc sections, it was observed that the vacuum quality decayed over the accelerator shutdown. However, the vacuum conditioning progresses similarly to what was observed in 2015 and 2016, after the previous shutdown. Moreover, it was shown that there are two trends related to vacuum conditioning, one observed in the long term, where vacuum quality improves along the operation, and the second within each fill, where one can observe a decrease in residual gas density with the decreasing beam intensity. The studies showed, for the first time, measurements from DOFRS system and SEU measurements from hundreds of SRAMs distributed across the LHC and its RR alcoves, hosting large quantities of electronics, showing how the Power Converters could have suffered if radiation tolerance had not been taken into account at the design phase. Moreover, the system provides an analogous time evolution as RadMon, therefore could be considered as a complimentary solution for assessment of radiation along LHC (in relative terms).

Before the start of the project, two open objectives were laid ahead. The first one aimed at investigating the capabilities and applicability of the silicon solid-state radiation detectors for CERN-R2E applications. The second one referred to the analysis of LHC radiation levels in the first year (2022) after the maintenance break, with a focus on comparisons with the levels measured before the break. Both points were accomplished, even beyond the initial goals, e.g. by including analysis of SPS radiation data.

All the research findings were successfully disseminated through the five main authored peer-reviewed articles (plus a few coauthored), one conference proceeding, and six conference presentations (two talks, and four posters), reaching not only CERN audience but the entire radiation-effects community.

Nevertheless, the defined scope of the thesis was broad, the priority was application-oriented, and several accessibility constraints prevented from covering some aspects profoundly. One of the examples is the silicon detector's backend, which is not radiation tolerant and is not compatible with data transmission protocols. Therefore, performing measurements in the environment of the two largest accelerators was not feasible. Within the R2E activity there are ongoing studies dedicated to overcoming this issue, by designing a custom, radiation-tolerant backend. However, that was not accomplished within this work time frame. With a scientific spirit, this author hopes that the ideas highlighted in Chapter 6.2 will inspire follow-up research.

The findings presented in this work contributed to CERN's RHA through the detailed studies of the radiation environment in the two largest CERN accelerators and by proposing a commercial detector to

improve the test beam and radiation environment characterization even more. This might result in a further reduction of radiation-induced accelerator failures. The cost of the scientific LHC output cannot be estimated. Yet, a single hour of machine operation would have an average cost of about 7000 euros (given the annual electricity operation cost of operation 19 million Euros [168] and 2632 h of time with beam in 2015 [62]). A single beam dump, not requiring human onsite intervention, would result in at least 2 h and up to 6 h needed to bring back particle collisions back [169]. That results in tens of thousands of euros per beam dump, neglecting other costs, such as personnel. Considering CERN's 2022 budget related to the LHC accelerator programme (121 MCHF [170]) and the number of fills involving beams' collisions (around 170 fills), cost of a single fill would exceed 700 kCHF/fill. Apart from ambitious physics objectives, this provides a brief insight into how relevant the reduction of radiation effects is. Whereas the large fraction of the presented work is linked to CERN-R2E needs and applications, it is not the only activity that will benefit from it. For example, thanks to the studies a great potential of the DOFRS was brought to the attention of the team operating accelerators, e.g. to provide indications of beam losses at previously uncovered sections of the SPS. Another example is the improvement in the beam dump strategy of LEIR accelerator. The accurate flux measurements might contribute to the successes of space missions, through the electronics testings within CHIMERA-HEARTS activity.

6.2 Outlook

The activities within the PhD project covered several aspects related to the radiation environment, its characterization, and beam monitoring. Therefore, there are multiple engineering projects, ideas, and research directions that could be built on top of this work, and which, due to various limitations, could not be delivered within this work, some of them are highlighted below.

Silicon solid-state detectors:

- As demonstrated in LEIR, the detectors are sensitive (e.g. large detector measured on average 19 high energy deposition events per day) and can be exploited to characterize low-intensity radiation, e.g. close to the electronic systems. This would facilitate the collection of meaningful statistics in a reasonable time, e.g. during a few hours slots dedicated to the development of the accelerator settings used in future operations. The deployment could be done in one of the shielded alcoves of the LHC, in one of the LHC arcs, or in the low-radiation arc of the SPS. The current blocking point is the lack of the radiation-tolerant detector's back end (digitizer, power supplies, laptop). Within R2E there are ongoing studies to overcome this limitation by integrating the detectors with a future version of RadMon.
- One of the limitations, particularly in the case of large detector, is related to high noise levels in the proximity of high-frequency components, such as pulsing magnets. Investigations and reduction of that noise type would enable operation closer to beamlines.
- Related to the energy calibration of the detectors, given access to proton/neutron/electron facilities and a vacuum chamber with an alpha source, it would be relevant to study how the calibration factors k change with the accumulation of DD and TID.

- In the topic of detector calibration, it has to be pointed out that calibration performed in a controlled environment does not always lead to accurate results, due to additional attenuation from different cables or a vacuum feedthrough. Moreover, the cable attenuation is not only a function of length but also signal frequency. Therefore, ideally, the detectors should be calibrated before each test, in the respective environment. The most straightforward way would be to use an alpha source, such as ^{241}Am, ^{226}Ra or ^{239}Pu, that is tested as close as possible to the detector's surface, at a fixed distance, achieved by a prepared sample and detector holder. However, usually the use of radionuclides, if at all available, involves multiple formalities, both during material shipment and the test itself. Thus, it would be relevant to check if a pulsed laser system could be used for that purpose.
- As presented, the small detector together with ^{6}Li converter could be exploited for the characterization of the thermal neutron flux. This method and the setup were not benchmarked against other measurements, e.g. obtained with golden foil activation. If the cross-benchmark yields a reasonable agreement, the setup could be deployed in the LHC-shielded alcoves.
- The richness of CHARM configurations in terms of the testing locations, shielding and target materials, would allow the collection of the various energy deposition spectra that could be benchmarked against FLUKA simulations.
- Although this topic has been studied in detail in literature, following up on the atmospheric measurements, it would be interesting to show how the measured event rate increases with altitude, by performing measurements in the high-mountain environment or planes, using the presented silicon detectors. Additionally, carrying out the acquisition over longer periods would increase the chance of observing an increase due to Solar Particle Events.

CERN's radiation environment:

- One of the most useful engineering projects would be the development of a fully automated detection of anomalies, that could profit from all the implemented analysis tools and the variety of radiation monitors.
- As shown, during the LHC operation, the dynamic residual gas pressure decreases, both within a single fill and in longer periods. This is, however, a complex problem, due to the impact of the operation history (total injected intensity, operation time, energy, pumping efficiency, etc.) on the vacuum parameters. It is worth investigating if that, with several assumptions, could be modeled and with what results.
- FGClite provided a cumulative number of counts per each day of operation. Increasing the frequency of logging would enable to correlate SEUs directly with the beam losses. Additionally, the system relies on the well-known Cypress SRAMs. It would be worth investigating to what extent the system could be used for distributed HEHeq measurements.
- This thesis focused on the radiation levels in the two largest CERN accelerators. The third largest, PS, is equipped with 100 LHC-type BLMs, several RadMons and DOFRS. This provides the highest detector density, i.e. a number of detectors per unit length of an accelerator, that could be exploited to provide a comprehensive analysis of radiation levels, similarly as in the larger accelerators.

References

[1] Lyndon Evans and Philip Bryant. "LHC Machine". en. In: *Journal of Instrumentation* 3.08 (Aug. 2008). Art. no. S08001. ISSN: 1748-0221. DOI: 10.1088/1748-0221/3/08/S08001. (Visited on 10/02/2023) (cit. on pp. 1, 2).

[2] R. García Alía et al. "LHC and HL-LHC: Present and Future Radiation Environment in the High-Luminosity Collision Points and RHA Implications". In: *IEEE Transactions on Nuclear Science* 65.1 (Jan. 2018), pp. 448–456. DOI: 10.1109/TNS.2017.2776107 (cit. on pp. 1, 10).

[3] R Billen. *SPS remanent radiation: the warm spots*. Tech. rep. Geneva: CERN, Mar. 1998. URL: http://cds.cern.ch/record/702440 (cit. on p. 1).

[4] Kacper Biłko et al. "CERN Super Proton Synchrotron Radiation Environment and Related Radiation Hardness Assurance Implications". In: *IEEE Transactions on Nuclear Science* 70.8 (Aug. 2023), pp. 1606–1615. ISSN: 1558-1578. DOI: 10.1109/TNS.2023.3261181 (cit. on pp. 1, 4, 5, 70, 83, 89, 100).

[5] Ewa Lopienska. *The CERN accelerator complex, layout in 2022. Complexe des accélérateurs du CERN en janvier 2022*. 2022. URL: https://cds.cern.ch/record/2800984 (visited on 08/09/2023) (cit. on p. 2).

[6] Luigi Di Lella and Carlo Rubbia. "The Discovery of the W and Z Particles". en. In: *Advanced Series on Directions in High Energy Physics*. Vol. 23. WORLD SCIENTIFIC, Sept. 2015, pp. 137–163. ISBN: 978-981-4644-14-3. URL: https://doi.org/10.1142/9789814644150_0006 (visited on 01/31/2024) (cit. on p. 2).

[7] G. Arnison et al. "Experimental observation of isolated large transverse energy electrons with associated missing energy at s=540 GeV". In: *Physics Letters B* 122.1 (Feb. 1983), pp. 103–116. ISSN: 0370-2693. DOI: 10.1016/0370-2693(83)91177-2. (Visited on 02/01/2024) (cit. on p. 2).

[8] G. Arnison et al. "Experimental observation of lepton pairs of invariant mass around 95 GeV/c2 at the CERN SPS collider". In: *Physics Letters B* 126.5 (July 1983), pp. 398–410. ISSN: 0370-2693. DOI: 10.1016/0370-2693(83)90188-0. (Visited on 02/01/2024) (cit. on p. 2).

[9] M. Banner et al. "Observation of single isolated electrons of high transverse momentum in events with missing transverse energy at the CERN pp collider". In: *Physics Letters B* 122.5 (Mar. 1983), pp. 476–485. ISSN: 0370-2693. DOI: 10.1016/0370-2693(83)91605-2. (Visited on 02/01/2024) (cit. on p. 2).

[10] P. Bagnaia et al. "Evidence for Z0→e+e- at the CERN pp collider". In: *Physics Letters B* 129.1 (Sept. 1983), pp. 130–140. ISSN: 0370-2693. DOI: 10.1016/0370-2693(83)90744-X. (Visited on 02/01/2024) (cit. on p. 2).

[11] E. Adli et al. "Acceleration of electrons in the plasma wakefield of a proton bunch". en. In: *Nature* 561.7723 (Sept. 2018). Number: 7723 Publisher: Nature Publishing Group, pp. 363–367. ISSN: 1476-4687. DOI: 10.1038/s41586-018-0485-4. (Visited on 07/05/2023) (cit. on pp. 2, 71).

[12] I Efthymiopoulos et al. "HiRadMat: A New Irradiation Facility for Material Testing at CERN". In: *Proc. 2nd IPAC*. JACoW Publishing, Geneva, Switzerland, Nov. 2011, p. 1665 (cit. on pp. 2, 71).

[13] Dipanwita Banerjee et al. *The North Experimental Area at the CERN Super Proton Synchrotron*. July 2021. URL: https://cds.cern.ch/record/2774716 (cit. on pp. 2, 70).

[14] C. Bahamonde Castro et al. "Power Deposition in LHC Magnets Due to Bound-Free Pair Production in the Experimental Insertions". In: *Proc. of International Particle Accelerator Conference (IPAC'16), Busan, Korea, May 8-13, 2016*. International Particle Accelerator Conference. Issue: 7. Geneva, Switzerland: JACoW, June 2016, pp. 1418–1421. ISBN: 978-3-95450-147-2. DOI: doi:10.18429/JACoW-IPAC2016-TUPMW006 (cit. on p. 2).

[15] A L Macpherson. "2011 availability analysis". In: (2012). DOI: 10.5170/CERN-2012-006.60. (Visited on 03/27/2024) (cit. on p. 3).

[16] M Brugger et al. "R2E - experience and outlook for 2012". In: (2012). DOI: 10.5170/CERN-2012-006.163. (Visited on 03/27/2024) (cit. on p. 3).

[17] M Brugger. "R2E and Availability". In: *Proc. LHC Performance Workshop (Chamonix 2014)*. CERN, May 2015, pp. 149–160. DOI: 10.5170/CERN-2015-002.149 (cit. on pp. 3, 10).

[18] A Perrot. "R2E strategy and activities during LS1". In: (2012). DOI: 10.5170/CERN-2012-006.225. (Visited on 03/27/2024) (cit. on p. 3).

[19] S Uznanski et al. "Qualification of electronic components for a radiation environment: When standards do not exist — high-energy physics". en. In: *2017 17th European Conference on Radiation and Its Effects on Components and Systems (RADECS): Short course*. Publisher: CERN Document Server. Geneva, Switzerland: CERN, Oct. 2017. DOI: 10.17181/CERN.WZJB.7NTT. (Visited on 10/02/2023) (cit. on pp. 3, 4).

[20] Ygor Aguiar et al. "Radiation to Electronics Impact on CERN LHC Operation: Run 2 Overview and HL-LHC Outlook". en. In: *Proceedings of the 12th International Particle Accelerator Conference*. JACOW Publishing, Geneva, Switzerland, Aug. 2021, pp. 80–83. ISBN: 978-3-95450-214-1. DOI: 10.18429/JACoW-IPAC2021-MOPAB013. (Visited on 07/10/2023) (cit. on p. 3).

[21] Y. Q. Aguiar et al. "Implications and Mitigation of Radiation Effects on the CERN SPS Operation during 2021". In: *Proc. 13th IPAC*. International Particle Accelerator Conference. JACoW Publishing, Geneva, Switzerland, July 2022, pp. 740–743. ISBN: 978-3-95450-227-1. DOI: 10.18429/JACoW-IPAC2022-MOPOMS044 (cit. on pp. 3, 42).

[22] Manfred Wendt et al. "Upgrade of the CERN SPS Beam Position Measurement System". en. In: JACOW Publishing, Geneva, Switzerland, June 2018, pp. 2047–2050. ISBN: 978-3-95450-184-7. DOI: 10.18429/JACoW-IPAC2018-WEPAF085. (Visited on 08/22/2023) (cit. on p. 3).

[23] Andrea Coronetti. "Relevance and Guidelines of Radiation Effect Testing Beyond the Standards for Electronic Devices and Systems Used in Space and at Accelerators". PhD thesis. University of Jyvaskyla (FI), 2021. URL: https://cds.cern.ch/record/2799812 (visited on 02/01/2024) (cit. on p. 4).

[24] J. Mekki et al. "CHARM: A Mixed Field Facility at CERN for Radiation Tests in Ground, Atmospheric, Space and Accelerator Representative Environments". In: *IEEE Transactions on Nuclear Science* 63.4 (Aug. 2016), pp. 2106–2114. ISSN: 1558-1578. DOI: 10.1109/TNS.2016.2528289 (cit. on pp. 4, 10, 66, 95).

[25] Eva Barbara Holzer et al. "Beam Loss Monitoring for LHC Machine Protection". en. In: *Physics Procedia*. Proceedings of the 2nd International Conference on Technology and Instrumentation in Particle Physics (TIPP 2011) 37 (Jan. 2012), pp. 2055–2062. ISSN: 1875-3892. DOI: 10.1016/j.phpro.2012.04.110. (Visited on 07/05/2023) (cit. on pp. 5, 18).

[26] Giovanni Spiezia et al. "Operational Experience of the LHC RADiation MONitoring (RADMON) System". en. In: *Proceedings of 10th International Conference on Large Scale Applications and Radiation Hardness of Semiconductor Detectors — PoS(RD11)*. Art. no. 024. Florence, Italy: Sissa Medialab, Oct. 2012, p. 024. DOI: 10.22323/1.143.0024. (Visited on 10/02/2023) (cit. on pp. 5, 21).

[27] G. Spiezia et al. "A New RadMon Version for the LHC and its Injection Lines". In: *IEEE Transactions on Nuclear Science* 61.6 (Dec. 2014), pp. 3424–3431. ISSN: 1558-1578. DOI: 10.1109/TNS.2014.2365046 (cit. on pp. 5, 21).

[28] Diego Di Francesca et al. "Radiation-Induced Attenuation in Single-Mode Phosphosilicate Optical Fibers for Radiation Detection". In: *IEEE Transactions on Nuclear Science* 65.1 (Jan. 2018), pp. 126–131. DOI: 10.1109/TNS.2017.2778314 (cit. on pp. 5, 19).

[29] D. Di Francesca et al. "Distributed Optical Fiber Radiation Sensing in the Proton Synchrotron Booster at CERN". In: *IEEE Transactions on Nuclear Science* 65.8 (Mar. 2018), pp. 1639–1644. DOI: 10.1109/TNS.2018.2818760 (cit. on pp. 5, 20).

[30] Kacper Bilko et al. "CHARM High-energy Ions for Micro Electronics Reliability Assurance (CHIMERA)". In: *IEEE Transactions on Nuclear Science* (2024), pp. 1–1. ISSN: 0018-9499, 1558-1578. DOI: 10.1109/TNS.2024.3358376. (Visited on 01/29/2024) (cit. on pp. 5, 6, 28, 38, 46, 51, 52).

[31] Kacper Biłko et al. "Mixed-Field Radiation Monitoring and Beam Characterization Through Silicon Diode Detectors". In: *IEEE Transactions on Nuclear Science* 71.4 (Apr. 2024), pp. 777–784. ISSN: 0018-9499, 1558-1578. DOI: 10.1109/TNS.2024.3350342. (Visited on 04/22/2024) (cit. on pp. 5, 28).

[32] Kacper Biłko et al. "Ultra-Large Silicon Diode for Characterizing Low-Intensity Radiation Environments". In: *IEEE Transactions on Nuclear Science* 71.4 (Apr. 2024), pp. 770–776. ISSN: 0018-9499, 1558-1578. DOI: 10.1109/TNS.2023.3337839. (Visited on 04/22/2024) (cit. on pp. 5, 28).

[33] K. Bilko et al. "Overview of Total Ionizing Dose Levels in the Large Hadron Collider during 2022 restart". In: *Proc. IPAC'23*. IPAC'23 - 14th International Particle Accelerator Conference. JACoW Publishing, Geneva, Switzerland, May 2023, pp. 4008–4011. ISBN: 978-3-95450-231-8. DOI: 10.18429/jacow-ipac2023-thpa047 (cit. on p. 5).

[34] Kacper Biłko et al. "Radiation Environment in the Large Hadron Collider During the 2022 Restart and Related RHA Implications". In: *IEEE Transactions on Nuclear Science* 71.4 (Apr. 2024), pp. 607–617. ISSN: 0018-9499, 1558-1578. DOI: 10.1109/TNS.2023.3328145. (Visited on 04/22/2024) (cit. on pp. 5, 70).

[35] Kacper Biłko et al. "Silicon solid-state detectors for monitoring high-energy accelerator mixed field radiation environments". In: *2021 21th European Conference on Radiation and Its Effects on Components and Systems (RADECS)*. Sept. 2021, pp. 179–183. DOI: 10.1109/RADECS53308.2021.9954498 (cit. on p. 5).

[36] C. Cazzaniga et al. "Study of the Deposited Energy Spectra in Silicon by High-Energy Neutron and Mixed Fields". In: *IEEE Transactions on Nuclear Science* 67.1 (2020), pp. 175–180. DOI: 10.1109/TNS.2019.2944657 (cit. on pp. 6, 7, 66).

[37] M. Bagatin et al. "Characterizing High-Energy Ion Beams With PIPS Detectors". In: *IEEE Transactions on Nuclear Science* 67.7 (July 2020), pp. 1421–1427. ISSN: 1558-1578. DOI: 10.1109/TNS.2019.2958746 (cit. on pp. 6–8, 23, 34, 38).

[38] Matthew Fraser et al. "Feasibility of Slow-Extracted High-Energy Ions From the CERN Proton Synchrotron for CHARM". en. In: JACOW Publishing, Geneva, Switzerland, July 2022, pp. 1703–1706. ISBN: 978-3-95450-227-1. DOI: 10.18429/JACoW-IPAC2022-WEPOST012. (Visited on 07/30/2023) (cit. on p. 6).

[39] M. Delrieux, Kacper Bilko, et al. "Production of slow extracted beams for CERN's East Area at the Proton Synchrotron". In: *Proc. IPAC'23*. IPAC'23 - 14th International Particle Accelerator Conference. JACoW Publishing, Geneva, Switzerland, May 2023, pp. 257–260. ISBN: 978-3-95450-231-8. DOI: doi:10.18429/jacow-ipac2023-mopa099 (cit. on p. 6).

[40] E. Johnson, Kacper Bilko, et al. "Beam delivery of high-energy ion beams for irradiation experiments at the CERN Proton Synchrotron". In: *Proc. IPAC'23*. IPAC'23 - 14th International Particle Accelerator Conference. JACoW Publishing, Geneva, Switzerland, May 2023, pp. 297–300. ISBN: 978-3-95450-231-8. DOI: 10.18429/jacow-ipac2023-mopa115 (cit. on p. 6).

[41] N. A. Dodds et al. "Charge Generation by Secondary Particles From Nuclear Reactions in BEOL Materials". In: *IEEE Transactions on Nuclear Science* 56.6 (Dec. 2009). Conference Name: IEEE Transactions on Nuclear Science, pp. 3172–3179. ISSN: 1558-1578. DOI: 10.1109/TNS.2009.2034160. (Visited on 03/28/2024) (cit. on p. 7).

[42] Michael Andrew Clemens et al. "The Effects of Neutron Energy and High-Z Materials on Single Event Upsets and Multiple Cell Upsets". In: *IEEE Transactions on Nuclear Science* 58.6 (Dec. 2011). Conference Name: IEEE Transactions on Nuclear Science, pp. 2591–2598. ISSN: 1558-1578. DOI: 10.1109/TNS.2011.2171716. (Visited on 03/28/2024) (cit. on p. 7).

[43] Pat Sangsingkeow et al. "Advances in germanium detector technology". en. In: *Nuclear Instruments and Methods in Physics Research Section A: Accelerators, Spectrometers, Detectors and Associated Equipment* 505.1-2 (June 2003), pp. 183–186. ISSN: 01689002. DOI: 10.1016/S0168-9002(03)01047-7. (Visited on 01/31/2024) (cit. on p. 7).

[44] D. R. Kania et al. "Diamond radiation detectors". In: *Diamond and Related Materials*. Diamond 1992 2.5 (Apr. 1993), pp. 1012–1019. ISSN: 0925-9635. DOI: 10.1016/0925-9635(93)90266-5. (Visited on 01/31/2024) (cit. on p. 7).

[45] Maria Kastriotou et al. "Single Event Effect Testing With Ultrahigh Energy Heavy Ion Beams". In: *IEEE Transactions on Nuclear Science* 67.1 (Jan. 2020), pp. 63–70. ISSN: 1558-1578. DOI: 10.1109/TNS.2019.2961801 (cit. on p. 7).

[46] Frédéric Wrobel et al. "A Silicon Diode-Based Detector for Investigations of Atmospheric Radiation". In: *IEEE Transactions on Nuclear Science* 60.5 (Oct. 2013), pp. 3603–3608. ISSN: 1558-1578. DOI: 10.1109/TNS.2013.2264957 (cit. on p. 7).

[47] Adrian Ildefonso et al. "Quantitative Laser Testing for Predicting Heavy-Ion SEE Response – Part 1: Metrics for Assessing Response Agreement". In: *IEEE Transactions on Nuclear Science* (2023). Conference Name: IEEE Transactions on Nuclear Science, pp. 1–1. ISSN: 1558-1578. DOI: 10.1109/TNS.2023.3346215. (Visited on 03/28/2024) (cit. on p. 8).

[48] G. Augustin et al. "Cross-Calibration of Various SEE Test Methods Including Pulsed X-rays and Application to SEL and SEU". In: *2019 19th European Conference on Radiation and Its Effects on Components and Systems (RADECS)*. ISSN: 1609-0438. Sept. 2019, pp. 1–4. DOI: 10.1109/RADECS47380.2019.9745662. (Visited on 03/27/2024) (cit. on p. 8).

[49] Simon Rocheman et al. "Neutron Induced Energy Deposition in a Silicon Diode". In: *IEEE Transactions on Nuclear Science* 55.6 (Dec. 2008), pp. 3146–3150. ISSN: 0018-9499. DOI: 10.1109/TNS.2008.2006264. (Visited on 03/06/2024) (cit. on p. 8).

[50] P. Truscott et al. "Assessment of neutron- and proton-induced nuclear interaction and ionization models in Geant4 for Simulating single event effects". In: *IEEE Transactions on Nuclear Science* 51.6 (Dec. 2004). Conference Name: IEEE Transactions on Nuclear Science, pp. 3369–3374. ISSN: 1558-1578. DOI: 10.1109/TNS.2004.839517. (Visited on 03/06/2024) (cit. on p. 8).

[51] Dávid Lucsányi et al. "G4SEE: A Geant4-Based Single Event Effect Simulation Toolkit and Its Validation Through Monoenergetic Neutron Measurements". In: *IEEE Transactions on Nuclear Science* 69.3 (2022), pp. 273–281. DOI: 10.1109/TNS.2022.3149989 (cit. on pp. 8, 27, 56).

[52] H. Chabane et al. "Comparison of Experimental and Simulated Am/Be Neutron Source Energy Spectra Obtained in Silicon Detector". In: *2005 8th European Conference on Radiation and Its Effects on Components and Systems*. ISSN: 0379-6566. Sept. 2005, LN2–1–LN2–4. DOI: 10.1109/RADECS.2005.4365657. (Visited on 03/28/2024) (cit. on p. 8).

[53] Carlo Cazzaniga et al. "Measurements of ultra-high energy lead ions using silicon and diamond detectors". en. In: *Nuclear Instruments and Methods in Physics Research Section A: Accelerators, Spectrometers, Detectors and Associated Equipment* 985 (Jan. 2021). Art. no. 164671. ISSN: 01689002. DOI: 10.1016/j.nima.2020.164671. (Visited on 08/16/2023) (cit. on pp. 8, 53).

[54] Carlo Cazzaniga et al. "Measurements of Low-Energy Protons Using a Silicon Detector for Application to SEE Testing". In: *IEEE Transactions on Nuclear Science* 69.3 (Mar. 2022), pp. 485–490. ISSN: 1558-1578. DOI: 10.1109/TNS.2021.3123814 (cit. on pp. 8, 29).

[55] Thomas Borel et al. "PIPS Diode Test Setup for Heavy Ion Beam Spectral Characterization". In: *IEEE Transactions on Nuclear Science* 70.8 (Aug. 2023), pp. 1732–1739. ISSN: 0018-9499, 1558-1578. DOI: 10.1109/TNS.2023.3284225. (Visited on 11/12/2023) (cit. on p. 8).

[56] Rubén García Alía et al. "Fragmented High-Energy Heavy-Ion Beams for Electronics Testing". In: *IEEE Transactions on Nuclear Science* 70.4 (Apr. 2023), pp. 486–495. ISSN: 1558-1578. DOI: 10.1109/TNS.2022.3210403 (cit. on p. 8).

[57] Rubén García Alía et al. "Heavy Ion Energy Deposition and SEE Intercomparison Within the RADNEXT Irradiation Facility Network". In: *IEEE Transactions on Nuclear Science* 70.8 (Aug. 2023), pp. 1596–1605. ISSN: 1558-1578. DOI: 10.1109/TNS.2023.3260309 (cit. on pp. 8, 23, 34, 38, 56).

[58] Daniel M. Fleetwood, Peter S. Winokur, and Paul E. Dodd. "An overview of radiation effects on electronics in the space telecommunications environment". In: *Microelectronics Reliability* 40.1 (Jan. 2000), pp. 17–26. ISSN: 0026-2714. DOI: 10.1016/S0026-2714(99)00225-5. (Visited on 02/21/2024) (cit. on p. 9).

[59] R. A. Mewaldt. "Galactic cosmic ray composition and energy spectra". In: *Advances in Space Research* 14.10 (Oct. 1994), pp. 737–747. ISSN: 0273-1177. DOI: 10.1016/0273-1177(94)90536-3. (Visited on 11/04/2023) (cit. on p. 9).

[60] Piers Jiggens et al. "The magnitude and effects of extreme solar particle events". en. In: *Journal of Space Weather and Space Climate* 4 (2014). Publisher: EDP Sciences, A20. ISSN: 2115-7251. DOI: 10.1051/swsc/2014017. (Visited on 02/21/2024) (cit. on p. 9).

[61] W. Li and M.K. Hudson. "Earth's Van Allen Radiation Belts: From Discovery to the Van Allen Probes Era". en. In: *Journal of Geophysical Research: Space Physics* 124.11 (Nov. 2019), pp. 8319–8351. ISSN: 2169-9380, 2169-9402. DOI: 10.1029/2018JA025940. (Visited on 02/21/2024) (cit. on p. 9).

[62] Kacper Biłko and Oliver Stein. *Report on the Prompt Dose Distribution Along the LHC Based on BLM Data for proton-proton operation in Run 2.* Tech. rep. CERN-ACC-NOTE-2019-0040. CERN, Sept. 2019 (cit. on pp. 10, 82, 101).

[63] Corinna Martinella. *High Energy Hadrons Fluence Measurements in the LHC during 2015, 2016 and 2017 Proton Physics Operations.* Tech. rep. CERN-ACC-NOTE-2018-0088. CERN, Dec. 2018. URL: http://cds.cern.ch/record/2652458 (cit. on p. 10).

[64] Oliver Stein et al. "A Systematic Analysis of the Prompt Dose Distribution at the Large Hadron Collider". en. In: *Proc. 9th International Particle Accelerator Conference (IPAC'18), Vancouver, BC, Canada, April 29-May 4, 2018*. JACOW Publishing, Geneva, Switzerland, June 2018, pp. 2036–2038. ISBN: 978-3-95450-184-7. DOI: 10.18429/JACoW-IPAC2018-WEPAF082. (Visited on 07/05/2023) (cit. on p. 10).

[65] Kacper Bilko. "Detailed analysis of the evolution and distribution of the total ionising dose in the LHC arc sections during the accelerator operation". MA thesis. AGH University of Science and Technology, Dec. 2018. URL: http://cds.cern.ch/record/2652979 (cit. on pp. 10, 18, 92).

[66] Kacper Bilko et al. "Detailed Analysis Of The Baseline Dose Levels And Localized Radiation Spikes In The Arc Sections Of The Large Hadron Collider During Run 2". en. In: *Proc. 10th International Particle Accelerator Conference (IPAC'19), Melbourne, Australia, 19-24 May 2019*. JACOW Publishing, Geneva, Switzerland, June 2019, pp. 4009–4012. ISBN: 978-3-95450-208-0. DOI: 10.18429/JACoW-IPAC2019-THPRB083. (Visited on 07/06/2023) (cit. on pp. 10, 18, 98).

[67] K. Biłko et al. "Radiation Environment in the LHC Arc Sections During Run 2 and Future HL-LHC Operations". In: *IEEE Transactions on Nuclear Science* 67.7 (July 2020), pp. 1682–1690 (cit. on pp. 10, 77, 88, 89, 92–94).

[68] A. Lechner et al. "Validation of energy deposition simulations for proton and heavy ion losses in the CERN Large Hadron Collider". In: *Phys. Rev. Accel. Beams* 22.7 (July 2019). Publisher: American Physical Society, p. 071003 (cit. on p. 10).

[69] Eleftherios Skordis. "Radiation impact of collimation beam losses in the LHC and HL-LHC". In: *University of Liverpool Repository* (2020). DOI: 10.17638/03083483 (cit. on p. 10).

[70] Ketil Roed et al. "FLUKA Simulations for SEE Studies of Critical LHC Underground Areas". In: *IEEE Transactions on Nuclear Science* 58.3 (2011), pp. 932–938. DOI: 10.1109/TNS.2010.2097605 (cit. on p. 10).

[71] Ketil Roeed et al. "Method for Measuring Mixed Field Radiation Levels Relevant for SEEs at the LHC". In: *IEEE Transactions on Nuclear Science* 59.4 (Aug. 2012), pp. 1040–1047. ISSN: 0018-9499, 1558-1578. DOI: 10.1109/TNS.2012.2183677. (Visited on 08/16/2023) (cit. on pp. 10, 15).

[72] Dejan Pramberger et al. "Characterization of Radio-Photo-Luminescence (RPL) Dosimeters as Radiation Monitors in the CERN Accelerator Complex". In: *IEEE Transactions on Nuclear Science* 69.7 (July 2022), pp. 1618–1624. ISSN: 0018-9499, 1558-1578. DOI: 10.1109/TNS.2022.3174784. (Visited on 02/01/2024) (cit. on p. 11).

[73] Elisa Guillermain. *Study of the SPS radiation environment*. Tech. rep. SPS-SI-EN-0001 (EDMS id 1739976). May 2019. URL: https://edms.cern.ch/document/1739976/1.1 (cit. on p. 11).

[74] Joao Pedro De Carvalho Saraiva and Markus Brugger. "Radiation Environments and their Impact at the CERN's Injector Chain". In: (Dec. 2015). URL: https://cds.cern.ch/record/2114889 (cit. on p. 11).

[75] G. Arduini et al. *REPORT OF THE BEAM LOSSES AND RADIATION WORKING GROUP*. Tech. rep. CERN-AB-2006-ABP. Jan. 2017. URL: https://edms.cern.ch/ui/file/1160274/2/BLRWG_Report_v14_GA.pdf (cit. on pp. 11, 73).

[76] International Atomic Energy Agency. *ENDF: Evaluated Nuclear Data File*. Aug. 2023. URL: https://www-nds.iaea.org/exfor/endf.htm (visited on 03/07/2024) (cit. on p. 13).

[77] Francis Berghmans et al. "An Introduction to Radiation Effects on Optical Components and Fiber Optic Sensors". en. In: *Optical Waveguide Sensing and Imaging*. Ed. by Wojtek J. Bock, Israel Gannot, and Stoyan Tanev. Series Title: NATO Science for Peace and Security Series. Dordrecht: Springer Netherlands, 2008, pp. 127–165. ISBN: 978-1-4020-6950-5. DOI: 10.1007/978-1-4020-6952-9_6. (Visited on 02/17/2024) (cit. on p. 15).

[78] E. Cavalo, Effinger E, and C. Zamantzas. *Renaming of Beam Loss Monitors in the SPS during LS2*. Tech. rep. EDMS Id. 2381720 v.1. Oct. 2021. URL: https://edms.cern.ch/document/2381720/1.0 (cit. on pp. 18, 19).

[79] C Zamantzas et al. *System Architecture for measuring and monitoring Beam Losses in the Injector Complex at CERN*. Tech. rep. Geneva: CERN, 2012. URL: https://cds.cern.ch/record/1627308 (cit. on p. 18).

[80] B. Dehning et al. "The LHC beam loss measurement system". In: *2007 IEEE Particle Accelerator Conference (PAC)*. June 2007, pp. 4192–4194. DOI: 10.1109/PAC.2007.4439980 (cit. on p. 18).

[81] Kacper Biłko, Ruben García Alía, and Jean-Baptiste Potoine. "Automated Analysis of the Prompt Radiation Levels in the CERN Accelerator Complex". en. In: *Proc. 13th International Particle Accelerator Conference (IPAC'22), Bangkok, Thailand, 12-17 June 2022*. JACOW Publishing, Geneva, Switzerland, July 2022, pp. 736–739. ISBN: 978-3-95450-227-1. DOI: 10.18429/JACoW-IPAC2022-MOPOMS043. (Visited on 07/05/2023) (cit. on pp. 18, 25).

[82] Diego Di Francesca et al. "Qualification and Calibration of Single-Mode Phosphosilicate Optical Fiber for Dosimetry at CERN". In: *Journal of Lightwave Technology* 37.18 (Sept. 2019), pp. 4643–4649. ISSN: 1558-2213. DOI: 10.1109/JLT.2019.2915510 (cit. on p. 19).

[83] Diego Di Francesca et al. "Dosimetry Mapping of Mixed-Field Radiation Environment Through Combined Distributed Optical Fiber Sensing and FLUKA Simulation". In: *IEEE Transactions on Nuclear Science* 66.1 (Nov. 2019), pp. 299–305. DOI: 10.1109/TNS.2018.2882135 (cit. on p. 19).

[84] M. Brucoli et al. "Floating Gate Dosimeter Suitability for Accelerator-Like Environments". In: *IEEE Transactions on Nuclear Science* 64.8 (Aug. 2017), pp. 2054–2060. ISSN: 1558-1578. DOI: 10.1109/TNS.2017.2681651 (cit. on pp. 21, 61).

[85] Matteo Marzo et al. "RadFET dose response in the CHARM mixed-field: FLUKA MC simulations". en. In: *EPJ Nuclear Sciences & Technologies* 3 (2017). Art. no. 24. ISSN: 2491-9292. DOI: 10.1051/epjn/2017016. (Visited on 11/11/2023) (cit. on p. 21).

[86] Kacper Bilko. *Canberra PIPS detector FD 50-14-300 RM (aka Vanessa I): performance data*. Publisher: Zenodo. Apr. 2024. DOI: 10.5281/zenodo.10953558. (Visited on 04/11/2024) (cit. on p. 23).

[87] Kacper Bilko. *Canberra PIPS detector FD 50-14-300 RM (aka Vanessa II): performance data*. Apr. 2024. DOI: 10.5281/ZENODO.10973056. (Visited on 04/15/2024) (cit. on p. 23).

[88] Kacper Bilko. *Canberra PIPS detector FD 50-14-300 RM (aka Vanessa III): performance data*. Apr. 2024. DOI: 10.5281/zenodo.10953511. (Visited on 04/10/2024) (cit. on p. 23).

[89] Kacper Bilko. *Canberra PIPS detector PD 5000-75-500 AM (aka Mario I): performance data*. Apr. 2024. DOI: 10.5281/zenodo.12653477. (Visited on 07/04/2024) (cit. on p. 23).

[90] Jakub Wozniak and Chris Roderick. "NXCALS - Architecture and Challenges of the Next CERN Accelerator Logging Service". In: (2020), WEPHA163. DOI: 10.18429/JACoW-ICALEPCS2019-WEPHA163. (Visited on 08/16/2023) (cit. on p. 24).

[91] Matei Zaharia et al. "Apache Spark: a unified engine for big data processing". In: *Communications of the ACM* 59.11 (Oct. 2016), pp. 56–65. ISSN: 0001-0782. DOI: 10.1145/2934664. (Visited on 08/16/2023) (cit. on p. 24).

[92] Wes McKinney. "Data Structures for Statistical Computing in Python". In: *Proceedings of the 9th Python in Science Conference* (2010), pp. 56–61. DOI: 10.25080/Majora-92bf1922-00a. (Visited on 08/16/2023) (cit. on p. 25).

[93] Charles R. Harris et al. "Array programming with NumPy". en. In: *Nature* 585.7825 (Sept. 2020). Number: 7825 Publisher: Nature Publishing Group, pp. 357–362. ISSN: 1476-4687. DOI: 10.1038/s41586-020-2649-2. (Visited on 08/16/2023) (cit. on p. 25).

[94] A. Ferrari et al. *FLUKA: A Multi-Particle Transport Code*. en. Tech. rep. SLAC-R-773. SLAC, Dec. 2005. URL: https://doi.org/10.2172/877507 (visited on 12/26/2023) (cit. on p. 27).

[95] T.T. Bohlen et al. "The FLUKA Code: Developments and Challenges for High Energy and Medical Applications". In: *Nuclear Data Sheets* 120 (June 2014), pp. 211–214. DOI: 10.1016/j.nds.2014.07.049 (cit. on p. 27).

[96] C. Ahdida et al. "New Capabilities of the FLUKA Multi-Purpose Code". In: *Frontiers in Physics* 9 (Jan. 2022). Art. no. 788253. ISSN: 2296-424X. DOI: 10.3389/fphy.2021.788253. (Visited on 08/16/2023) (cit. on p. 27).

[97] Vasilis Vlachoudis. *Flair: A powerful but user friendly graphical interface for FLUKA*. Pages: 790-800. 2009. URL: https://cds.cern.ch/record/2749540 (visited on 01/26/2024) (cit. on p. 27).

[98] Y. Morilla et al. "Progress of CNA to become the Spanish facility for combined irradiation testing in aerospace". In: *2018 18th European Conference on Radiation and Its Effects on Components and Systems (RADECS)*. 2018, pp. 250–254. DOI: 10.1109/RADECS45761.2018.9328656 (cit. on p. 29).

[99] J. Gómez-Camacho et al. "Research facilities and highlights at the Centro Nacional de Aceleradores (CNA)". en. In: *The European Physical Journal Plus* 136.3 (Mar. 2021). art. no. 273. ISSN: 2190-5444. DOI: 10.1140/epjp/s13360-021-01253-x. (Visited on 12/26/2023) (cit. on p. 29).

[100] H. Chabane et al. "Determination of the deposited energy in a silicon volume by n-Si nuclear interaction". In: *Journal of Applied Physics* 99.12 (June 2006). Art. no. 124916. ISSN: 0021-8979. DOI: 10.1063/1.2209088. (Visited on 08/31/2023) (cit. on p. 29).

[101] Michael Moll. "Displacement Damage in Silicon Detectors for High Energy Physics". In: *IEEE Transactions on Nuclear Science* 65.8 (Aug. 2018). Conference Name: IEEE Transactions on Nuclear Science, pp. 1561–1582. ISSN: 1558-1578. DOI: 10.1109/TNS.2018.2819506. (Visited on 03/28/2024) (cit. on p. 30).

[102] UK Atomic Energy Authority. *U235 - thermal neutron fission yield*. URL: https://fispact.ukaea.uk/ND/fission_yields/ENDFB-7.1/ENDFB-7.1_92_235_2.53E-2.png (visited on 02/22/2024) (cit. on p. 35).

[103] P. Armbruster et al. "The recoil separator Lohengrin: Performance and special features for experiments". In: *Nuclear Instruments and Methods* 139 (Dec. 1976), pp. 213–222. ISSN: 0029-554X. DOI: 10.1016/0029-554X(76)90677-7. (Visited on 02/22/2024) (cit. on p. 35).

[104] Institut Laue-Langevin. *ILL PN1 Fission-product spectrometer*. URL: https://www.ill.eu/users/instruments/instruments-list/pn1/description/instrument-layout (visited on 02/22/2024) (cit. on p. 35).

[105] BILKO Kacper et al. *Calibration of a silicon solid state detector and pulse shape discrimination with low-energy heavy ions*. DOI: 10.5291/ILL-DATA.3-01-709. (Visited on 07/13/2023) (cit. on p. 35).

[106] U. Köster et al. "Experience with in-pile fission targets at LOHENGRIN". In: *Nuclear Instruments and Methods in Physics Research Section A: Accelerators, Spectrometers, Detectors and Associated Equipment*. Target and Stripper Foil Technologies for High Intensity Beams 613.3 (Feb. 2010), pp. 363–370. ISSN: 0168-9002. DOI: 10.1016/j.nima.2009.09.078. (Visited on 02/22/2024) (cit. on p. 35).

[107] U Köster. "Yields and spectroscopy of radioactive isotopes at LOHENGRIN and ISOLDE. Ausbeuten und Spektroskopie radioaktiver Isotope bei LOHENGRIN und ISOLDE". PhD thesis. Tech. U. Mnchen, 1999. URL: https://cds.cern.ch/record/494272 (visited on 01/30/2024) (cit. on p. 35).

[108] J. B. Moulton. *A NEW METHOD FOR CALIBRATING THE PULSE HEIGHT DEFECT IN SOLID STATE DETECTORS*. en. Tech. rep. LBL-7101. Lawrence Berkeley National Laboratory, Oct. 1977. URL: https://escholarship.org/uc/item/35z6r93s (visited on 01/31/2024) (cit. on p. 37).

[109] R. C. Axtmann and D. Kedem. "The pulse height defect in semiconductor detectors". In: *Nuclear Instruments and Methods* 32.1 (Jan. 1965), pp. 70–76. ISSN: 0029-554X. DOI: 10.1016/0029-554X(65)90477-5. (Visited on 01/31/2024) (cit. on p. 37).

[110] Ari Virtanen et al. "Upgrades for the RADEF Facility". In: *2007 IEEE Radiation Effects Data Workshop*. ISSN: 2154-0535. July 2007, pp. 38–41. DOI: 10.1109/REDW.2007.4342538. (Visited on 02/01/2024) (cit. on p. 38).

[111] Matteo Cecchetto et al. "Thermal Neutron-Induced SEUs in the LHC Accelerator Environment". In: *IEEE Transactions on Nuclear Science* 67.7 (July 2020), pp. 1412–1420. DOI: 10.1109/TNS.2020.2997992 (cit. on p. 42).

[112] Agatino Musumarra et al. "Silicon detectors for the neutron flux and beam profile measurements of the n_TOF facility at CERN". en. In: *International Journal of Modern Physics: Conference Series* 44 (Jan. 2016), p. 1660210. ISSN: 2010-1945. DOI: 10.1142/S2010194516602106. (Visited on 02/01/2024) (cit. on pp. 42, 43).

[113] S. Amaducci et al. "Measurement of the 235U(n, f) cross section relative to the 6Li(n, t) and 10B(n,$ \alpha$) standards from thermal to 170 keV neutron energy range at n_TOF". en. In: *The European Physical Journal A* 55.7 (July 2019), p. 120. ISSN: 1434-6001, 1434-601X. DOI: 10.1140/epja/i2019-12802-7. (Visited on 02/01/2024) (cit. on pp. 42, 43).

[114] S. Raman et al. "Thermal-neutron capture by silicon isotopes". In: *Physical Review C* 46.3 (Sept. 1992). Publisher: American Physical Society, pp. 972–983. DOI: 10.1103/PhysRevC.46.972. (Visited on 02/09/2024) (cit. on p. 42).

[115] V. Agoritsas. "Secondary emission chambers for monitoring the CERN Proton Synchrotron ejected beams". In: *Symposium on Beam Intensity Measurement*. Daresbury, UK, Apr. 1968, pp. 117–151. URL: https://cds.cern.ch/record/299104/files/CERN-MPS-Int-co-68-9.pdf (cit. on p. 46).

[116] "Stopping-Power & Range Tables for Electrons, Protons, and Helium Ions". en. In: *NIST* (Oct. 2009). URL: https://www.nist.gov/pml/stopping-power-range-tables-electrons-protons-and-helium-ions (visited on 07/20/2023) (cit. on p. 50).

[117] G. Pausch et al. "Identification of light charged particles and heavy ions in silicon detectors by means of pulse-shape discrimination". In: *1995 IEEE Nuclear Science Symposium and Medical Imaging Conference Record*. Vol. 1. Oct. 1995, 23–27 vol.1. DOI: 10.1109/NSSMIC.1995.504169 (cit. on p. 53).

[118] W. Seibt, K. E. Sundström, and P. A. Tove. "Charge collection in silicon detectors for strongly ionizing particles". In: *Nuclear Instruments and Methods* 113.3 (Dec. 1973), pp. 317–324. ISSN: 0029-554X. DOI: 10.1016/0029-554X(73)90496-5. (Visited on 02/09/2024) (cit. on p. 53).

[119] Ana M. Gómez et al. "Determination of the Plasma Delay Time in PIPS detectors for fission fragments at the LOHENGRIN spectrometer". en. In: *EPJ Web of Conferences* 284 (2023). Publisher: EDP Sciences, p. 04012. ISSN: 2100-014X. DOI: 10.1051/epjconf/202328404012. (Visited on 11/07/2023) (cit. on p. 53).

[120] Francesca Ferrulli et al. "A thermal neutron source for the CERN radiation Calibration Laboratory". In: *Applied Radiation and Isotopes* 178 (Dec. 2021), p. 109977. ISSN: 0969-8043. DOI: 10.1016/j.apradiso.2021.109977. (Visited on 04/08/2024) (cit. on p. 55).

[121] Fabio Pozzi et al. "CERN irradiation facilities". In: *Radiation Protection Dosimetry*. Vol. 180. Sept. 2017. DOI: 10.1093/rpd/ncx187 (cit. on p. 55).

[122] E.W. Blackmore. "Operation of the TRIUMF (20-500 MeV) proton irradiation facility". In: *2000 IEEE Radiation Effects Data Workshop*. Reno, NV, USA: IEEE, 2000, pp. 1–5. ISBN: 978-0-7803-6474-5. DOI: 10.1109/REDW.2000.896260. (Visited on 12/26/2023) (cit. on pp. 55, 58).

[123] E.W. Blackmore, P.E. Dodd, and M.R. Shaneyfelt. "Improved capabilities for proton and neutron irradiations at TRIUMF". In: *2003 IEEE Radiation Effects Data Workshop*. 2003, pp. 149–155. DOI: 10.1109/REDW.2003.1281368 (cit. on p. 55).

[124] Ewart W. Blackmore. "Development of a Large Area Neutron Beam for System Testing at TRIUMF". In: *2009 IEEE Radiation Effects Data Workshop*. 2009, pp. 157–160. DOI: 10.1109/REDW.2009.5336297 (cit. on p. 55).

[125] Ewart W. Blackmore and Michael Trinczek. "Intensity Upgrade to the TRIUMF 500 MeV Large-Area Neutron Beam". In: *2014 IEEE Radiation Effects Data Workshop (REDW)*. 2014, pp. 130–134. DOI: 10.1109/REDW.2014.7004574 (cit. on p. 55).

[126] Nicolo Biancacci et al. "Linac3, LEIR and PS Performance with Ions in 2021 and Prospects for 2022". In: *JACoW IPAC* 2022 (2022), pp. 1983–1986. DOI: 10.18429/JACoW-IPAC2022-WEPOPT055. (Visited on 07/12/2023) (cit. on p. 55).

[127] M. Cecchetto et al. "Impact of Thermal and Intermediate Energy Neutrons on SRAM SEE Rates in the LHC Accelerator". In: *IEEE Transactions on Nuclear Science* 65.8 (Aug. 2018), pp. 1800–1806. DOI: 10.1109/TNS.2018.2831786 (cit. on p. 55).

[128] TRIUMF. *NIF Beam Specifications*. URL: https://www.triumf.ca/nif-beam-specifications (cit. on p. 55).

[129] RadMod Research. *MAIRE*. URL: https://www.radmod.co.uk/maire (visited on 05/02/2021) (cit. on p. 55).

[130] Michel Chanel. "LEIR: the low energy ion ring at CERN". In: *Nuclear Instruments and Methods in Physics Research Section A: Accelerators, Spectrometers, Detectors and Associated Equipment*. International Workshop on Beam Cooling and Related Topics 532.1 (Oct. 2004), pp. 137–143. ISSN: 0168-9002. DOI: 10.1016/j.nima.2004.06.040. (Visited on 08/17/2023) (cit. on p. 62).

[131] Maciej Slupecki et al. *LHC Oxygen Run Preparation in the CERN Injector Complex*. Tech. rep. CERN-ACC-NOTE-2024-0001. Geneva, Switzerland: CERN, Mar. 2024. URL: https://cds.cern.ch/record/2888741 (visited on 03/11/2024) (cit. on p. 62).

[132] Eva Montbarbon et al. "The New CERN East Area Primary and Secondary Beams". en. In: JACOW Publishing, Geneva, Switzerland, June 2019, pp. 3730–3733. ISBN: 978-3-95450-208-0. DOI: 10.18429/JACoW-IPAC2019-THPGW062. (Visited on 07/20/2023) (cit. on p. 66).

[133] Daniel Prelipcean et al. "Benchmark Between Measured and Simulated Radiation Level Data at the Mixed-Field CHARM Facility at CERN". In: *IEEE Transactions on Nuclear Science* 69.7 (July 2022), pp. 1557–1564. ISSN: 1558-1578. DOI: 10.1109/TNS.2022.3169756 (cit. on p. 66).

[134] Angelo Infantino. *FLUKA Monte Carlo Modelling of the CHARM Facility's Test Area: Update of the Radiation Field Assessment*. 2017. URL: https://cds.cern.ch/record/2291683 (visited on 02/23/2024) (cit. on p. 66).

[135] P. Collier and B. Goddard. "The SPS as LHC injector". In: *PACS2001. Proceedings of the 2001 Particle Accelerator Conference*. Vol. 4. 2001, pp. 3150–3152. DOI: 10.1109/PAC.2001.988034 (cit. on p. 70).

[136] Pieter Van Trappen et al. "SPS Beam Dump System (SBDS) Commissioning After Relocation and Upgrade". In: *JACoW IPAC 2022* (2022), pp. 2530–2532. DOI: 10.18429/JACoW-IPAC2022-THPOST039. (Visited on 03/11/2024) (cit. on p. 71).

[137] M. Schwarz et al. "Studies of Capture and Flat-Bottom Losses in the SPS". In: *Proc. 61st ICFA Advanced Beam Dynamics Workshop (HB'18), Daejeon, Korea, 17-22 June 2018*. ICFA Advanced Beam Dynamics Workshop. Issue: 61. Geneva, Switzerland: JACoW Publishing, July 2018, pp. 180–185. ISBN: 978-3-95450-202-8. DOI: doi:10.18429/JACoW-HB2018-TUP2WA03 (cit. on p. 73).

[138] V. Kain et al. "Identification and Removal of SPS Aperture Limitations". In: *Proc. 9th IPAC, Vancouver, BC, Canada, April 29-May 4, 2018*. International Particle Accelerator Conference. Issue: 9. Geneva, Switzerland: JACoW Publishing, June 2018, pp. 709–712. ISBN: 978-3-95450-184-7. DOI: doi:10.18429/JACoW-IPAC2018-TUPAF021 (cit. on pp. 73, 77).

[139] B.J. Holzer. "Introduction to Transverse Beam Dynamics". In: (2014). _eprint: 1404.0923, pp. 27–45. DOI: 10.5170/CERN-2013-007.27. (Visited on 08/17/2023) (cit. on p. 73).

[140] Oliver Sim Bruning and and others and. *LHC Design Report*. CERN Yellow Reports: Monographs. Geneva: CERN, June 2004. ISBN: 978-92-9083-224-9. DOI: 10.5170/CERN-2004-003-V-1 (cit. on p. 80).

[141] The ATLAS Collaboration et al. "The ATLAS Experiment at the CERN Large Hadron Collider". en. In: *Journal of Instrumentation* 3.08 (Aug. 2008). Art. no. S08003. ISSN: 1748-0221. DOI: 10.1088/1748-0221/3/08/S08003. (Visited on 07/06/2023) (cit. on p. 81).

[142] The CMS Collaboration et al. "The CMS experiment at the CERN LHC". en. In: *Journal of Instrumentation* 3.08 (Aug. 2008). Art. no. S08004. ISSN: 1748-0221. DOI: 10.1088/1748-0221/3/08/S08004. (Visited on 07/06/2023) (cit. on p. 81).

[143] The ALICE Collaboration et al. "The ALICE experiment at the CERN LHC". en. In: *Journal of Instrumentation* 3.08 (Aug. 2008). Art. no. S08002. ISSN: 1748-0221. DOI: 10.1088/1748-0221/3/08/S08002. (Visited on 07/06/2023) (cit. on p. 81).

[144] The LHCb Collaboration et al. "The LHCb Detector at the LHC". en. In: *Journal of Instrumentation* 3.08 (Aug. 2008). Art. no. S08005. ISSN: 1748-0221. DOI: 10.1088/1748-0221/3/08/S08005. (Visited on 07/06/2023) (cit. on p. 81).

[145] S. Redaelli. "Beam Cleaning and Collimation Systems". en. In: *CERN Yellow Reports* 2 (Jan. 2016), pp. 403–403. ISSN: 0007-8328. DOI: 10.5170/CERN-2016-002.403. (Visited on 07/05/2023) (cit. on p. 81).

[146] D. Boussard et al. "The LHC superconducting cavities". In: *Proceedings of the 1999 Particle Accelerator Conference*. Vol. 2. New York, NY, USA: IEEE, Apr. 1999, pp. 946–948. ISBN: 978-0-7803-5573-6. DOI: 10.1109/PAC.1999.795409. (Visited on 10/02/2023) (cit. on p. 81).

[147] R. Harboe-Sorensen, F.- Guerre, and A. Roseng. "Design, Testing and Calibration of a "Reference SEU Monitor" System". In: *2005 8th European Conference on Radiation and Its Effects on Components and Systems*. 2005, B3–1–B3–7. DOI: 10.1109/RADECS.2005.4365561 (cit. on p. 81).

[148] The CMS Collaboration. *Delivered luminosity versus time for 2015-2018 and 2022-2023 (pp data only)*. July 2023. URL: https://twiki.cern.ch/twiki/bin/view/CMSPublic/LumiPublicResults#2022_proton_proton_collisions_at (cit. on p. 82).

[149] M Lamont. *Estimates of Annual Proton Doses in the LHC*. Place: Geneva. June 2005. URL: http://cds.cern.ch/record/893060 (visited on 07/07/2023) (cit. on p. 81).

[150] N. Fuster Martinez et al. "Run 2 Collimation Overview". In: *Proc. 9th Evian Workshop on LHC beam operation*. Evian Les Bains, France: CERN, Feb. 2019, pp. 149–164. URL: https://cds.cern.ch/record/2750291 (cit. on p. 84).

[151] D. Mirarchi, R. Bruce, et al. *Collimator setting strategy for 2022 commissioning and run (with p)*. Apr. 2022. URL: https://indico.cern.ch/event/1147643/contributions/4817101/attachments/2425091/4186876/CollSettings_DM.pdf (cit. on p. 84).

[152] Alessia Ciccotelli et al. "Energy deposition studies for the LHCb insertion region of the CERN Large Hadron Collider". In: *Physical Review Accelerators and Beams* 26.6 (June 2023). Art. no. 061002. DOI: 10.1103/PhysRevAccelBeams.26.061002. (Visited on 07/05/2023) (cit. on p. 86).

[153] Kacper Bilko and Ruben Garcia Alia. *Overview of Radiation Levels in IR4*. May 2020. DOI: 10.5281/zenodo.8253071. (Visited on 08/16/2023) (cit. on p. 86).

[154] D. Prelipcean et al. "Radiation levels produced by the operation of the Beam Gas Vertex monitor in the LHC tunnel at IR4". In: *Proc. IPAC'23*. IPAC'23 - 14th International Particle Accelerator Conference. JACoW Publishing, Geneva, Switzerland, May 2023, pp. 4578–4581. ISBN: 978-3-95450-231-8. DOI: doi:10.18429/jacow-ipac2023-thpl082 (cit. on p. 86).

[155] Jean-Baptiste Potoine et al. "Risk of Halo-Induced Magnet Quenches in the HL-LHC Beam Dump Insertion". In: *Proceedings of the 12th International Particle Accelerator Conference*. Aug. 2021. DOI: 10.18429/JACOW-IPAC2021-MOPAB002. (Visited on 08/16/2023) (cit. on p. 87).

[156] A Rossi. "Estimates of Residual Gas Density in the LHC". In: *Proc. LHC Workshop on Experimental Conditions and Beam Induced Detector Backgrounds*. Geneva: CERN, 2009, pp. 26–29. DOI: 10.5170/CERN-2009-003.26 (cit. on p. 88).

[157] C. Patrignani. "Review of Particle Physics". en. In: *Chinese Physics C* 40.10 (Oct. 2016), p. 100001. ISSN: 1674-1137. DOI: 10.1088/1674-1137/40/10/100001. (Visited on 03/14/2024) (cit. on p. 89).

[158] P. Chiggiato et al. "Observations of Electron Cloud Effects with the LHC Vacuum System". In: *Proc. 2nd International Particle Accelerator Conference (IPAC)*. San Sebastian, Spain, Sept. 2011, pp. 1560–1562. URL: https://accelconf.web.cern.ch/ipac2011/papers/tups018.pdf (cit. on p. 89).

[159] Jorg Wenninger. *LHC Report: operation with holes*. Image credit: G. Iadarola (CERN). Sept. 2017. URL: https://home.cern/news/news/accelerators/lhc-report-operation-holes (cit. on pp. 89, 91).

[160] V Baglin et al. "Synchrotron Radiation in the LHC Vacuum System". en. In: *Proc. 2nd International Particle Accelerator Conference (IPAC)*. San Sebastian, Spain, Sept. 2011. URL: https://accelconf.web.cern.ch/IPAC2011/papers/TUPS019.pdf (cit. on p. 90).

[161] Oleg B. Malyshev. "Gas dynamics modelling for particle accelerators". In: *Vacuum*. Vacuum Gas Dynamics: Theory, experiments and practical applications 86.11 (May 2012), pp. 1669–1681. ISSN: 0042-207X. DOI: 10.1016/j.vacuum.2012.03.047. (Visited on 03/14/2024) (cit. on p. 90).

[162] Oswald Gröbner. "Dynamic outgassing". en. In: (1999). Publisher: [object Object]. DOI: 10.5170/CERN-1999-005.127. (Visited on 03/12/2024) (cit. on pp. 90, 92, 133).

[163] Malyshev, Oleg. *Beam induced desorption*. Glumslov, Sweden, June 2017. URL: https://indico.cern.ch/event/565314/contributions/2285763/attachments/1465820/2282466/Oleg_Malyshev_-_Beam_Induced_Desorption.pdf (cit. on p. 90).

[164] R. Garcia Alia et al. "SEU Measurements and Simulations in a Mixed Field Environment". In: *IEEE Transactions on Nuclear Science* 60.4 (Aug. 2013), pp. 2469–2476. DOI: 10.1109/TNS.2013.2249096 (cit. on p. 96).

[165] Benjamin Todd et al. "Radiation tolerant power converter controls". In: *Journal of Instrumentation* 7 (Nov. 2012). Art. no. C11012. DOI: 10.1088/1748-0221/7/11/C11012 (cit. on p. 96).

[166] S. Uznanski et al. "Radiation Hardness Assurance Methodology of Radiation Tolerant Power Converter Controls for Large Hadron Collider". In: *IEEE Transactions on Nuclear Science* 61.6 (Dec. 2014), pp. 3694–3700. DOI: 10.1109/TNS.2014.2368149 (cit. on p. 96).

[167] Slawosz Uznanski et al. "Qualification of Electronic Systems for Radiation Environments of High Energy Accelerator". In: *Proc. 25th International Conference on Mixed Design of Integrated Circuits and System*. June 2018, pp. 34–38. DOI: 10.23919/MIXDES.2018.8436726 (cit. on p. 96).

[168] Education Communications and Outreach Group. *FAQ-LHC The guide*. Feb. 2017. URL: https://cds.cern.ch/record/2255762 (visited on 03/12/2024) (cit. on p. 101).

[169] M. Solfaroli Camillocci. "LHC nominal cycle". In: *6th Evian Workshop on LHC beam operation*. Geneva: CERN, 2016, pp. 45–48 (cit. on p. 101).

[170] *Final budget of the Organization for the sixty-eighth financial year 2022. Video-meeting: Finance Committee - Three-Hundred-and-Seventy-Ninth Meeting*. Tech. rep. CERN/FC/6531. Geneva, Switzerland: CERN, Dec. 2021. URL: https://cds.cern.ch/record/2799091/files/English.pdf (visited on 07/04/2024) (cit. on p. 101).

Appendix A

Silicon detector data processing software

Source Code A.1: Frame.hpp

```
#include <vector>
#include <memory>
#include <numeric>
#include <algorithm>
#include <functional>
#include <optional>
#include <utility>
#include <cmath>
#include <iostream>
#include <string>
#ifndef __FRAME__
#define __FRAME__
using Timestamp = double;
using dType = short;
using FrameElements = std::vector<dType>;
using Polarity = short;

const unsigned INTITIAL_POINTS_AS_A_BASELINE = 20;
const unsigned PULSE_THRESHOLD = 10;
const unsigned VARIANCE_THRESHOLD = 100;
const unsigned PULSE_EXTENSION = 3;
const double DROP_RATIO = .1;
const std::string CSV_DELIMITER = ",";
const unsigned SATURATION_ADC_VALUE = 1023;
const double NANO = 1e-9;
```

```
26  const double MILI = 1e-3;
27  const double CHANELS_IN_1V = 1024;
28  const double e_CHARGE = 1.602176634e-19;
29
30  class Frame
31  {
32  private:
33      std::unique_ptr<FrameElements> m_elements;
34      Timestamp m_timestamp;
35      std::optional<Timestamp> m_timestamp_corrected;
36      Polarity m_polarity;
37      double m_amplification, m_resistance;
38      std::optional<double> m_area;
39      std::optional<unsigned> m_fall_time;
40      std::optional<unsigned> m_multiplicity;
41      std::optional<double> m_baseline;
42      std::optional<unsigned> m_saturated_count;
43      std::optional<unsigned> m_extreme_value;
44      std::optional<unsigned> m_extreme_index;
45      std::optional<unsigned> m_start_index;
46      std::optional<unsigned> m_end_index;
47
48
49      bool isPulse(dType val, double baseline) const {return m_polarity*(val - baseline) >
        ↪  PULSE_THRESHOLD; }
50      auto getPulseIt() const;
51      unsigned getExtremeIdxInPulse() const;
52      auto getMeanWhereVarianceBelowThreshold() const;
53      void setArea(){m_area = getArea();}
54      void setPulseWidth(){m_fall_time = getPulseWidth();}
55      void setMultiplicity(){m_multiplicity = getMultiplicity();}
56      void setBaseline(){ m_baseline = getBaselineValue();}
57      void setStartAndEndIndices();
58      void setNumberOfSaturatedEntriesInThePulse(){ m_saturated_count =
        ↪  getNumberOfSaturatedEntriesInThePulse();}
59      void setExtremeValueInPulse(){ m_extreme_value = getExtremeValueInPulse();}
60      void setExtremeIdxInPulse(){ m_extreme_index = getExtremeIdxInPulse();}
61
62      void removeData() {m_elements.reset();}
63
64
65
66  public:
67      Frame(Timestamp t, std::unique_ptr<FrameElements> && data, Polarity polarity, double
        ↪  amplification, double resistance);
```

```
68      ~Frame() = default;
69      double getArea() const;
70      double getNumberOfCharges(double amplification, double resistance) const {return (getArea() *
        ↪  NANO )/ (e_CHARGE * CHANELS_IN_1V * std::pow(10.,amplification/20) *resistance );}
71
72      int getMultiplicity() const;
73      int getPulseWidth() const;
74      int getNumberOfSaturatedEntriesInThePulse() const;
75      int getExtremeValueInPulse() const;
76      void setTimestamp(Timestamp t){m_timestamp = t;}
77      void setTimestampCorrected(Timestamp t){m_timestamp_corrected = t;}
78
79      Timestamp getTimestamp() const {return m_timestamp;}
80      Timestamp getTimestampCorrected() const;
81
82      double getBaselineValue() const;
83      std::string toString() const;
84      std::string headerString() const;
85
86  };
87  #endif
```

Source Code A.2: FramesProcessor.hpp

```
1
2   #ifndef __FRAMES_PROCESSOR__
3   #define __FRAMES_PROCESSOR__
4   #include <vector>
5   #include <memory>
6   #include "Frame.hpp"
7   // #include <T1HD.h>
8
9   const unsigned MAX_PULSE_WIDTH = 100;
10  const double MAX_AREA = 10000;
11  const unsigned ENERGY_SPECTRUM_BINS = 2000;
12  const unsigned WIDTH_SPECTRUM_BINS = 100;
13  const unsigned MULTIPLICITY_SPECTRUM_BINS = 100;
14  const unsigned MAX_MULTIPLICITY = 100;
15
16  const double ENERGY_CONVERSION_OFFSET_MeV = 0;
17  const double ENERGY_CONVERSION_FACTOR_eV_per_charge = 3.6;
18
19  const double AREA_HIST_WIDTH = double(MAX_AREA)/ENERGY_SPECTRUM_BINS;
```

```

const unsigned RESET_TIME = (1 << 31);

const double TIMESTAMP_DEVICE_RESOLUTION_NS = 8;

const unsigned WIDTH_THRESHOLD_FOR_ENERGY_SPECTRUM = 20;


using Histogram = std::vector<unsigned>;
using Frames = std::vector<std::unique_ptr<Frame>>;

class FramesProcessor
{
private:
    std::shared_ptr<Frames> m_frames;

    void correctTimestamps();


public:

    FramesProcessor(std::shared_ptr<Frames> & frames);
    ~FramesProcessor() = default;

    unsigned getTotalCount() const;
    double getDuration() const;
};
#endif
```

Source Code A.3: Frame.cpp

```
#include "Frame.hpp"
Frame::Frame(Timestamp t, std::unique_ptr<FrameElements> && data, Polarity polarity,double
↪  amplification, double resistance) : m_timestamp(t),
m_polarity(polarity), m_amplification(amplification), m_resistance(resistance)
{
    m_elements = std::move(data);
    setStartAndEndIndices();
    setBaseline();
    setArea();
    setMultiplicity();
    setPulseWidth();
    setNumberOfSaturatedEntriesInThePulse();
```

```
    setExtremeValueInPulse();
    setExtremeIdxInPulse();
    removeData();
}

auto Frame::getPulseIt() const{
        if(m_end_index.has_value() and m_start_index.has_value())
            return std::make_pair( m_elements->begin() + m_start_index.value(),
             m_elements->begin() + m_end_index.value());
        double baseline = getBaselineValue();
        auto func = [&](auto a) {return isPulse(a, baseline);};
        auto pulse_start_idx = std::find_if(m_elements->begin(), m_elements->end(), func);
        auto pulse_end_idx = std::find_if_not(pulse_start_idx, m_elements->end(), func);
        auto pulse_start_idx_extended = std::max(pulse_start_idx - PULSE_EXTENSION,
        ↪  m_elements->begin());
        auto pulse_end_idx_extended = std::min(pulse_end_idx + PULSE_EXTENSION,
        ↪  m_elements->end());
        return std::make_pair(pulse_start_idx_extended, pulse_end_idx_extended);
}
void Frame::setStartAndEndIndices(){
    const auto pulse_iterators = getPulseIt();
    m_start_index = pulse_iterators.first - m_elements->begin();
    m_end_index = pulse_iterators.second- m_elements->begin();
}
double Frame::getArea() const{
    if(m_area.has_value())
        return m_area.value();
    const auto pulse_iterators = getPulseIt();
    const double baseline = getBaselineValue();
    return std::max(m_polarity * (std::accumulate(pulse_iterators.first,
    pulse_iterators.second, 0.) - (pulse_iterators.second - pulse_iterators.first)*baseline),
    0.);
}

int Frame::getNumberOfSaturatedEntriesInThePulse() const{
    if (m_saturated_count.has_value())
        return m_saturated_count.value();
    const auto pulse_iterators = getPulseIt();
    return std::count(pulse_iterators.first, pulse_iterators.second, SATURATION_ADC_VALUE);
}


unsigned Frame::getExtremeIdxInPulse() const{
    const auto pulse_iterators = getPulseIt();
```

```
54      if (m_polarity > 0){
55          return std::max_element(pulse_iterators.first, pulse_iterators.second) -
            ↪  m_elements->begin();
56      }
57      else
58      {
59          return std::min_element(pulse_iterators.first, pulse_iterators.second) -
            ↪  m_elements->begin();
60      }
61  }
62
63  int Frame::getExtremeValueInPulse() const{
64      if (m_extreme_value.has_value())
65          return m_extreme_value.value();
66      return *(m_elements->begin() + getExtremeIdxInPulse());
67  }
68
69  double Frame::getBaselineValue() const{
70      if (m_baseline.has_value())
71          return m_baseline.value();
72      return std::accumulate(m_elements->begin(), m_elements->begin()+INTITIAL_POINTS_AS_A_BASELINE,
        ↪  0.)
73       / double(INTITIAL_POINTS_AS_A_BASELINE);
74  }
75
76  int Frame::getPulseWidth() const{
77      if (m_fall_time.has_value())
78          return m_fall_time.value();
79      const auto pulse_iterators = getPulseIt();
80      const auto baseline = getBaselineValue();
81      auto maximum_in_pulse_it = std::max_element(pulse_iterators.first, pulse_iterators.second);
82      if(m_polarity < 0){
83          maximum_in_pulse_it = std::min_element(pulse_iterators.first, pulse_iterators.second);
84      }
85      return std::find_if(maximum_in_pulse_it, pulse_iterators.second,
86      [&](auto x){return m_polarity*(x - baseline) < m_polarity*(*maximum_in_pulse_it -
        ↪  baseline)*DROP_RATIO;}) - maximum_in_pulse_it;
87  }
88
89  auto Frame::getMeanWhereVarianceBelowThreshold() const{
90      auto it = m_elements->begin();
91          for(; it<m_elements->end(); it+=INTITIAL_POINTS_AS_A_BASELINE){
92              auto baseline = std::accumulate(it, it+INTITIAL_POINTS_AS_A_BASELINE, 0.) /
                ↪  double(INTITIAL_POINTS_AS_A_BASELINE);
```

```
93              auto variance_of_baseline = std::accumulate(it, it+INTITIAL_POINTS_AS_A_BASELINE, 0.,
                ↪  [&](auto x, auto y){return x + std::pow(y - baseline, 2.);}) /
                ↪  double(INTITIAL_POINTS_AS_A_BASELINE);
94              if(variance_of_baseline < VARIANCE_THRESHOLD){
95                  return it;
96              }
97          }
98          return it - INTITIAL_POINTS_AS_A_BASELINE;
99      }
100
101 int Frame::getMultiplicity() const{
102     if (m_multiplicity.has_value())
103         return m_multiplicity.value();
104      auto baseline = getBaselineValue();
105      auto is_pulse = false;
106      auto threshold = 10;
107      auto trigger_counter = 0;
108      auto is_above_threshold = [&](auto x){return std::pow(x-baseline, 2.) >
         ↪  threshold*threshold;};
109
110      for(auto i= m_elements->begin() + INTITIAL_POINTS_AS_A_BASELINE; i < m_elements->end(); ++i){
111         if(is_above_threshold(*i) && !is_pulse){
112             ++trigger_counter;
113             is_pulse = true;
114         }
115         else if (!is_above_threshold(*i) && is_pulse)
116         {
117             is_pulse = false;
118         }
119      }
120      return trigger_counter;
121
122 }
123
124
125 std::string Frame::toString() const{
126     auto s = std::to_string(m_timestamp) + CSV_DELIMITER
127     + std::to_string(getNumberOfCharges(m_amplification, m_resistance)) + CSV_DELIMITER
128     + std::to_string(getPulseWidth()) + CSV_DELIMITER
129     + std::to_string(getMultiplicity()) + CSV_DELIMITER
130     + std::to_string(getBaselineValue()) + CSV_DELIMITER
131     + std::to_string(getExtremeValueInPulse())+ CSV_DELIMITER
132     + std::to_string(getNumberOfSaturatedEntriesInThePulse()) + CSV_DELIMITER
133     + std::to_string(m_start_index.value()) + CSV_DELIMITER
```

```
    + std::to_string(m_end_index.value()) + CSV_DELIMITER
    + std::to_string(m_extreme_index.value())+ CSV_DELIMITER;
    if (m_timestamp_corrected.has_value()){
        s+=std::to_string(m_timestamp_corrected.value());
    }
    return s;
}

Timestamp Frame::getTimestampCorrected() const {
    if (m_timestamp_corrected.has_value())
        return m_timestamp_corrected.value();
    return Timestamp();
}

std::string Frame::headerString() const{
    auto s = "timestamp" + CSV_DELIMITER
    + "charges_number" + CSV_DELIMITER
    + "fall_time_ns" + CSV_DELIMITER
    + "multiplicity" + CSV_DELIMITER
    + "baseline" + CSV_DELIMITER
    + "extreme_value" + CSV_DELIMITER
    + "saturated_count" + CSV_DELIMITER
    + "pulse_start_index" + CSV_DELIMITER
    + "pulse_end_index" + CSV_DELIMITER
    + "pulse_extreme_index" + CSV_DELIMITER
    + "timestamp_corrected"
    ;
    return s;
}
```

Source Code A.4: FramesProcessor.cpp

```
#include "FramesProcessor.hpp"

FramesProcessor::FramesProcessor(std::shared_ptr<Frames> & frames) : m_frames(frames)
{
    correctTimestamps();

}

void FramesProcessor::correctTimestamps(){
    unsigned counter = 0;
    std::for_each(m_frames->begin(), m_frames->end(), [&](auto &
    ↪  frame){frame->setTimestampCorrected(frame->getTimestamp());});
```

```
12      auto previous_timestamp_before_correction = (*(m_frames->begin()))->getTimestamp();
13      for(auto it=(m_frames->begin()); it < m_frames->end(); ++it){
14          if((*it)->getTimestamp() < previous_timestamp_before_correction){
15              ++counter;
16          }
17          previous_timestamp_before_correction = (*it)->getTimestamp();
18          (*it)->setTimestampCorrected((counter * double(RESET_TIME) +
            ↪  previous_timestamp_before_correction )*NANO*TIMESTAMP_DEVICE_RESOLUTION_NS);
19      }
20
21  }
22  unsigned FramesProcessor::getTotalCount() const{
23      return std::accumulate(m_frames->begin(), m_frames->end(), 0, [](auto y, auto const  &
        ↪  frame_ptr){return y+frame_ptr->getMultiplicity();});
24  }
```

Source Code A.5: main.cpp

```
1   // #include "constants.hpp"
2   #include "Frame.hpp"
3   #include<iostream>
4   #include<ostream>
5   #include<fstream>
6   #include <stdlib.h>
7   #include <string>
8   #include <string>          // std::string
9   #include <cstddef>          // std::size_t
10  #include <string>
11
12  std::string SplitFilename (const std::string& str)
13  {
14    std::size_t found = str.find_last_of("/\\");
15    return str.substr(found+1);
16  }
17
18  std::string replace_dir_sign (std::string str)
19  {
20    str.replace( str.begin(), str.end(), "/\\", "_");
21    return str;
22  }
23  #include "FramesProcessor.hpp"
24  const unsigned HEADER_TIMESTAMP_IDX = 5;
25  const unsigned HEADER_FRAME_BYTE_SIZE_IDX = 0;
```

```
26 Polarity POLARITY;
27 const unsigned HEADER_ELEMENTS = 6;
28 const unsigned HEADER_ELEMENT_SIZE_BYTES = 4;
29 const unsigned FRAME_ELEMENT_SIZE_BYTES = 2;
30
31 std::ostream& operator<<(std::ostream& os, const Frames & frames)
32 {
33     if (frames.size())
34         os << frames.at(0)->headerString() << std::endl;
35     for(auto const& frame: frames)
36         os << frame->toString() << std::endl;
37     return os;
38 }
39
40
41 int main(int argc, char** argv){
42     auto file_path = std::string(argv[1]);
43     POLARITY = std::stod(std::string(argv[2]));
44     double amplification = std::stod(std::string(argv[3]));
45     double resistance = 50;
46
47
48     std::ifstream file(file_path, std::ios::in | std::ios::binary);
49     if(!file) {
50         std::cout << "Cannot find the file:\t" << file_path << std::endl;
51         return 1;
52     }
53     std::vector<unsigned> header(HEADER_ELEMENTS);
54     Frames frames;
55
56     while(true)
57     {
58         file.read((char*)&header.at(HEADER_FRAME_BYTE_SIZE_IDX), HEADER_ELEMENTS *
        ↪  HEADER_ELEMENT_SIZE_BYTES);
59         if (!file)
60             break;
61         Timestamp t  = header.at(HEADER_TIMESTAMP_IDX);
62         unsigned frame_element_number = (header.at(HEADER_FRAME_BYTE_SIZE_IDX) -
        ↪  HEADER_ELEMENTS*HEADER_ELEMENT_SIZE_BYTES) / FRAME_ELEMENT_SIZE_BYTES;
63         auto frame_elements = std::make_unique<FrameElements>(frame_element_number);
64         file.read((char*)&frame_elements->at(0), frame_element_number*FRAME_ELEMENT_SIZE_BYTES);
        ↪
65         auto x = std::make_unique<Frame>(t, std::move(frame_elements), POLARITY, amplification,
        ↪  resistance);
```

```
66          frames.push_back(std::move(x));
67      }
68      file.close();
69
70
71      auto frames_ptr = std::make_shared<Frames>(std::move(frames));
72      FramesProcessor frames_processor (frames_ptr);
73
74      std::ofstream myfile;
75      if (true){
76          std::ofstream frames_file;
77          frames_file.open ("frames_preprocessed.csv");
78          frames_file << *frames_ptr;
79          frames_file.close();
80      }
81
82
83  }
```

Appendix B

Analytical calculation of the thermal neutron flux

■ Modifiable parameters:

```
T = 1258143; (* number of events caused by Tritium in silicon *)
t = 44; (* acquistion duration of Tritium run in s*)
distanceConverterSilicon = 0.21;(* distance between silicon surface and converter in cm *)
aperture = π * (0.16 / 2) ^2;
(* apreture of collimator in cm2 *)
```

■ Fixed parameters:

```
In[43]:= ρ = 2.6; (* density of LiF g/cm3*)
mLi = 6;(* molar mass of Li g/mol*)
mF = 19;(* molar mass of F g/mol*)
detectorActiveSurface = 0.5 ;(* surface in cm2 *)
σ = 940.4 * 10^ (-24); (* XS for Li6(n, T)alpha reacion 940 b in cm2*)
Na = 6.02 * 10^ (23); (* Avogadro number *)
ρSurface = 500 * 10^ (-6) ;(* converter surface density 500ug/cm2 [g/cm2]*)
```

■ Calculations:

```
M = mLi + mF; (* molar mass of Li6F g/mol*)
ω = mLi / M; (* fraction of mass of Li in LiF *)
l = ρSurface / ρ; (* thickness of LiF converter *)
rSilicon = Sqrt[detectorActiveSurface / π]; (* radius of exposed Si surface in cm *)
θ = ArcTan[rSilicon / distanceConverterSilicon];
λ = 1 / (ρ * Na * σ * ω / mLi); (* inelastic length in LiF *)
k = (2 * π * r^2 * (1 - Cos[θ])) / (4 * π * r^2); (* fraction of T ions that might reach silicon, from geometry, asuming isotropic production *)
p = 1 - Exp[-l / (λ)]; (* interaction probability that thermal neutron will interact within length l *)
```

■ Result:

```
In[54]:= ϕ = T / (t * p * aperture * k) (* calculated flux of th-n-equivalnent /s/cm2 *)
Out[54]= 4.72923 × 10^8
```

Figure B.1: Semi-analytical calculation of the THNeq flux based on the measured event rate induced by tritium, as performed in the Wolfram Mathematica software.

Appendix C

Residual gas density considerations

The following calculations were inspired by [162]. The infinitesimal change in the vacuum density $\mathrm{d}\rho$ is the effect of several factors, and is given by:

$$\mathrm{d}\rho = \mathrm{d}\rho_{\text{synch.}} + \mathrm{d}\rho_{\text{ion.des.}} - \mathrm{d}\rho_{\text{pump.}} - \mathrm{d}\rho_{\text{abs.}} + \mathrm{d}\rho_{therm.} - \mathrm{d}\rho_{leaks} \tag{C.0.1}$$

- $\mathrm{d}\rho$ - change in the residual gas density,
- $\mathrm{d}\rho_{\text{synch.}}$ - an infinitesimal increase of gas density due to photoinduced desorption (due to synchrotron radiation), depends on molecular desorption yield (desorbed molecules per photon), beam intensity $\mathrm{d}N$ and accelerator parameters (beam energy E, bending radius, vacuum temperature). For a fixed accelerator settings:
$$\mathrm{d}\rho_{\text{synch.}} \propto \eta \mathrm{d}N$$
- $\mathrm{d}\rho_{\text{ion.des.}}$ - an infinitesimal increase in gas density due to ion-induced desorption, proportional to the actual residual gas density ρ, molecular desorption yield χ (desorbed molecules per ion), and beam intensity $\mathrm{d}N$
$$\mathrm{d}\rho_{\text{ion.des.}} \propto \chi\rho \mathrm{d}N$$
- $\mathrm{d}\rho_{\text{pump.}}$ - decrease in the gas density due to the active pumping system, depends on the pumping speed (pressure dependent) and pressure in the system, hence the residual gas density:
$$\mathrm{d}\rho_{\text{pump.}} \propto \rho \mathrm{d}t$$
- $\mathrm{d}\rho_{\text{therm.}}$ - increase of gas density due to thermal outgassing,
- $\mathrm{d}\rho_{\text{abs.}}$ - decrease of gas density due to spontaneous absorption,
- $\mathrm{d}\rho_{\text{leaks}}$ - decrease of gas density due to chamber leaks and permeation,

The molecular desorption yields decrease with the cumulative number of impacting gas molecules:

$$\eta(t) \propto \left(\int_{t_0}^{t} N(t')\mathrm{d}t' \right)^{-\alpha} \tag{C.0.2}$$

$$\chi(t) \propto \left(\int_{t_0}^{t} N(t')\mathrm{d}t' \right)^{-\alpha'} \tag{C.0.3}$$

Focussing only on the term arising from synchrotron radiation, change in vacuum pressure in infinitesimal time is equal to:

$$\mathrm{d}\rho = A\eta N = A' \left(\int_{t_0}^{t} N(t')\mathrm{d}t' \right)^{-\alpha} \mathrm{d}N \tag{C.0.4}$$

$$\rho = \rho_0 + A' \int \left(\int_{t_0}^{t} N(t')\mathrm{d}t' \right)^{-\alpha} \mathrm{d}N = \rho_0 + A' \left(\int_{t_0}^{t} N(t')\mathrm{d}t' \right)^{-\alpha} \tag{C.0.5}$$

In the unconditioned vacuum system, it is assumed that the second term dominates the first one.

$$\rho \approx A'N \left(\int_{t_0}^{t} N(t')\mathrm{d}t' \right)^{-\alpha} \propto N \left(\int_{t_0}^{t} N(t')\mathrm{d}t' \right)^{-\alpha} \tag{C.0.6}$$

Therefore, the dose rate is proportional to the square of intensity and molecular desorption yield.

$$\dot{D} \propto \rho N \propto N^2 \left(\int_{t_0}^{t} N(t')\mathrm{d}t' \right)^{-\alpha} \tag{C.0.7}$$

Abstract

This thesis focuses on the aspects related to the protection of electronics in the CERN radiation environment, also known as Radiation Hardness Assurance. In particular, the two core pillars are investigated, namely i) characterization of the CERN's radiation environment through the currently available radiation monitors, ii) applications of commercial silicon solid-state detectors for monitoring radiation fields and particle beams (relevant for electronics testing). In the first thesis branch, the focus is on the two largest CERN accelerators, the Super Proton Synchrotron (SPS) and the Large Hadron Collider (LHC). Thanks to multiple complementary radiation monitors, such as Beam Loss Monitors, Optical Fibers, and RadMons, and developed data analysis software solutions, the comprehensive view of the radiation spatial distribution and its time evolution. In the case of the SPS, the focus is on the 2021 operation and related beam loss mechanisms. For LHC, the accelerator restart in 2022 is covered. The second branch covers a silicon solid-state detector calibration and applications. Within the calibration, the detector response in proton-, neutron-, and heavy-ion beams is demonstrated. Furthermore, it is shown how the detector can be used for complete beam monitoring, in terms of flux, energy, and spatial distribution. The silicon detector-related work is concluded with the applications for radiation field characterization, such as atmospheric or accelerator one. The work covers also engineering aspects that enabled the synthesis of the related huge datasets.

Résumé

Cette thèse se concentre sur les aspects liés à la protection de l'électronique dans l'environnement radiatif du CERN, également connu sous le nom assurance durcissement aux radiations. En particulier, les deux piliers principaux sont étudiés, à savoir i) la caractérisation de l'environnement radiatif du CERN à travers les moniteurs de radiations actuellement disponibles, ii) les applications des détecteurs à semi-conducteurs en silicium commerciaux pour la surveillance des champs de radiation et des faisceaux de particules (pertinents pour les tests électroniques).

Dans la première branche de la thèse, l'accent est mis sur les deux plus grands accélérateurs du CERN, le SPS et le LHC. Grâce à plusieurs moniteurs de radiations complémentaires, tels que les moniteurs de perte de faisceau, les fibers optiques et les RadMons, ainsi que des solutions logicielles d'analyse de données développées, une vue d'ensemble de la distribution spatiale du radiations et de son évolution temporelle est obtenue. Dans le cas du SPS, l'accent est mis sur le fonctionnement de 2021 et les mécanismes de perte de faisceau associés. Pour le LHC, le redémarrage de l'accélérateur en 2022 est couvert.